technische universität
dortmund

Measurement of top-quark involved CKM matrix elements in single-top-quark events using the full Run 2 dataset with the ATLAS experiment

Dissertation
submitted in partial fulfillment of the requirements for the degree of
Doctor rerum naturalium

by
M.Sc. Benedikt Gocke
born in Dortmund

Department of Physics
TU Dortmund University
2025

Von der Fakultät Physik zur Veröffentlichung angenommene Dissertation zur Erlangung des akademischen Grades eines Doktors der Naturwissenschaften (Doctor rerum naturalium).

Die Dissertation wurde am 28.04.2025 eingereicht.
Die Verteidigung fand am 09.07.2025 statt.

Erstgutachter:	Prof. Dr. Kevin Alexander Kröninger
Zweitgutachter:	Prof. Dr. Johannes Albrecht
Vorsitz der Prüfungskomission:	Prof. Dr. Matthias Schneider
Vertretung der wiss. Mitarbeiter:	Prof. Dr. Zhe Wang

Abstract
In this thesis, an interpretation of an ATLAS single top-quark t-channel cross section measurement to constrain the top-quark involved CKM matrix elements, $|V_{tb}|$, $|V_{td}|$ and $|V_{ts}|$, as well as feasibility studies for a dedicated measurement are presented. The data used in this thesis corresponds to the full Run 2 dataset from proton-proton collisions at the LHC at $\sqrt{s} = 13\,\text{TeV}$ recorded by the ATLAS experiment. For the interpretation, all three different top-quark production modes and decay modes are considered. For the first time in ATLAS, single top-quark t-channel events with top-quark decays to light quarks are simulated. 2D profile likelihood scans are performed to constrain the CKM matrix elements at 95% CL: $f_{LV} \cdot |V_{tb}| < 1.048$, $f_{LV} \cdot |V_{td}| < 0.133$, and $f_{LV} \cdot |V_{ts}| < 0.306$, with f_{LV} being the left-handed form factor. A two-step neural network approach is applied in feasibility studies to improve sensitivity to the relevant CKM matrix elements: the first network separates signal events from background events, while the second distinguishes between different signal processes.
Furthermore, a calibration of the charm mis-tag rate of the flavor tagging algorithm in Run 2 using W+c-jets is presented, exploiting semileptonic c-hadron decays by identifying jets with a muon inside. Likelihood fits are used to derive data-to-MC scale factors for jets with $20 < p_{\text{T}} < 140\,\text{GeV}$. The derived scale factors are found to be mostly within unity and reduced uncertainties for jets with lower p_{T} are observed compared to the standard calibration in ATLAS. An extrapolation was done to generalize the results to all c-jets.

Kurzfassung
Diese Dissertation befasst sich mit einer Interpretation des Wirkungsquerschnitts der Einzel-Top-Quark-Produktion im t-Kanal zur Bestimmung der CKM-Matrixelemente $|V_{tb}|$, $|V_{td}|$ und $|V_{ts}|$ und Studien, welche explizit einer direkten Messung dieser CKM-Matrixelemente gewidmet sind. Alle Analysen in dieser Arbeit basieren auf dem vollständigen Run 2 Datensatz, aufgezeichnet mit dem ATLAS Detektor am LHC bei einer Schwerpunktsenergie von $\sqrt{s} = 13\,\text{TeV}$. Erstmals wurden in ATLAS dazu explizit t-Kanal Ereignisse simuliert, in denen das Top-Quark in leichte Quarks zerfällt. 2D-Likelihood-Scans werden in drei verschiedenen Szenarien durchgeführt, durch welche 95% CL Grenzen gesetzt werden: $f_{LV} \cdot |V_{tb}| < 1.048$, $f_{LV} \cdot |V_{td}| < 0,133$, und $f_{LV} \cdot |V_{ts}| < 0,306$, wobei f_{LV} der linkshändige Formfaktor ist. Darüber hinaus wurden Machbarkeitsstudien unter Verwendung neuronaler Netze durchgeführt, um die Sensitivität für diese CKM-Elemente zu erhöhen.
Weiterhin wird eine Kalibrierung der Charm-Fehlerkennungsrate des Flavor Tagging Algorithmus in Run 2 unter Verwendung von W+c-Jets vorgestellt. Dabei werden semileptonische c-Hadron-Zerfälle verwendet, bei denen ein im Jet vorkommende Myon zur Identifikation genutzt wird. Eine Likelihood Anpassung wurde angewendet, um Daten-zu-MC-Skalierungsfaktoren für Jets mit $20 < p_{\text{T}} < 140\,\text{GeV}$ zu erhalten. Die berechneten Skalierungsfaktoren stimmen größtenteils mit eins überein und es werden geringere Unsicherheiten für Jets mit kleinerem p_{T} beobachtet im Vergleich zur Standard-Kalibrierung in ATLAS. Eine Extrapolation wurde durchgeführt, um die Ergebnisse für alle c-Jets zu verallgemeinern.

"Nothing in this world that's worth having comes easy."

— Dr. Bob Kelso, *Scrubs*

"There's always one more way to do things and that's your way and you have a right to try it at least once."

— Waylon Jennings

Contents

List of Abbreviations

AFII	AtlFastII
AUC	area under the ROC curve
BOOSTER	Proton Synchrotron Booster
BSM	Beyond the Standard model
CB	combined
CCA	connected component analysis
CERN	European Organisation for Nuclear Research
CKM	Cabbibo-Kobayashi-Maskawa
CL	confidence level
CR	control region
CSC	Cathode strip chambers
DAQ	Data Acquisition
DCS	Detector Control System
EM	electromagnetic
FCal	Forward Calorimeter
fJVT	forward jet vertex tagging
FPR	false positive rate
HEC	hadronic end-cap calorimeter
HL	high-luminosity
HLT	High-Level trigger
IBL	Insertable B-Layer
ID	Inner Detector
IP	interaction point
IRC	infrared and colinear
ISR	initial state radiation
JER	jet energy resolution
JES	jet energy scale
JVT	jet vertex tagging
LAr	liquid-argon
LEP	Large Electron–Positron Collider
LHC	Large Hadron Collider
LO	leading order
MC	Monte Carlo
MDT	Monitored Drift Tubes
ME	matrix element
MS	Muon spectrometer
NLO	Next-to-leading order
NN	neural network
NNLL	next-to-next-to-leading logarithmic

NNLO next-to-next-to-leading order

NP nuisance parameter

OS opposite-sign

PCBT *pseudo-continuous b-tagging*

PDF parton distribution function

pdf probability density function

PDG Particle Data Group

PFlow particle-flow

POI parameters of interest

PS Proton synchrotron

QCD quantum chromodynamics

QFT quantum field theory

ReLu Rectified Linear Unit

ROC Receiver operating characteristic

ROD Readout Driver

RoI Region-of-Interest

ROL Readout Link

RPC Resistive Plate Chambers

SCT Silicon Microstrip Tracker

SF scale factor

SM Standard model of particle physics

SMT soft muon tagged

SPS Super proton synchrotron

SR signal region

SS same-sign

SVF secondary vertex finder

TDAQ Trigger and Data Acquisition

TGC Thin Gap Chambers

TPR true positive rate

TRT Transition Radiation Tracker

WLCG Worldwide LHC Computing Grid

WP working point

List of Figures

List of Tables

1 Introduction

Particle physicists aim to understand and describe the fundamental constituents of matter and their interactions. The most successful theoretical framework describing these interactions is the Standard model of particle physics (SM). While the SM has been heavily scrutinized and is able to successfully explain a wide range of experimental results, it is not regarded a complete theory, as it does not account for phenomena such as dark matter, neutrino masses, or the gravitational interaction. Therefore, it is still tested with increasing precision to search for possible deviations from predictions that could hint at a more complex theory which could involve new particles. In Chapter 2, a brief overview of the SM including the elementary particles and fundamental forces are given. A more detailed overview in this chapter is given to flavor changing interactions and the Cabbibo-Kobayashi-Maskawa (CKM) matrix, as well as the top-quark. Both of these topics are the primary focus of this thesis. The CKM matrix elements, which are experimentally accessible, are parametrized in the SM by three mixing angles and one complex phase. These three angles and the phase are so-called free parameters of the SM, i.e. parameters which need to be measured, as there is no theory prediction. Constraining those parameters helps to probe the SM and additionally provides crucial input for theoretical models, enabling more precise tests of potential deviations from the SM. The top-quark plays a crucial role, particularly as it is the heaviest particle in the SM, and therefore assumed to be a key particle in the search for Beyond the Standard model (BSM) physics.

In order to experimentally test the SM, data from hard scattering experiments are analyzed. At the Large Hadron Collider (LHC), proton-proton collisions provide such a unique environment. Four main experiments are utilized to record the data of these collisions. The ATLAS detector is one of these experiments. The recorded data used in this thesis correspond to the full Run 2 data set, recorded with the ATLAS detector between 2015 and 2018. This data set allows for highly precise measurements of different SM processes as well as searches for BSM physics. The LHC, as well as the ATLAS detector with its different components is described in Chapter 3. The reconstructed objects corresponding to particles originated in the collisions are described in Chapter 4, the used simulations and data samples are explained in Chapter 5.
Theoretical calculations and predictions as well as the measurement itself and the used analysis techniques introduce systematic uncertainties, which need to be accounted for. A description of all uncertainties incorporated in the measurements presented in this thesis are given in Chapter 6.

The work in this thesis focuses on two key aspects of Run 2 data analysis: Flavor tagging

and top-quark physics.
Flavor tagging plays a crucial role in identifying so-called heavy-flavor jets. Jets are physics objects originating from quarks or gluons, which are reconstructed in the detector. The jets originating from heavy-flavor quarks - mostly bottom quarks, but also charm quarks - are of particular interest, as these can be distringuished from other jets and are essential for many physics analyses. Therefore, dedicated flavor tagging algorithms are developed. As the development employs Monte Carlo (MC) simulated events, it is crucial to calibrate these algorithms using data events. In the ATLAS experiment, several calibrations are done with different approaches and goals. The tagging efficiency, i.e. the number of correctly tagged jets divided by all identified jets in an event, is important to be known. Another important measure is the mis-tagging efficiency, i.e. the tagging efficiency for non b-jets. A set of calibrations is used to estimate the tagging efficiency of different jet flavors. In this thesis, a charm-quark mis-tag calibration for the utilized flavor tagging algorithm in Run 2 is presented in Chapter 7. At the time of writing this thesis, a public note of the ATLAS experiment for this calibration is planned.

Flavor tagging is especially relevant for top-quark analyses, as the top-quark primarily decays into a bottom quark. Of particular interest in this thesis are also the top-quark decays into a down quark or a strange quark, as these decays are very rare compared to decays into a bottom quark. The corresponding CKM matrix elements are small, thus a precise determination is needed in order to probe the properties of the CKM matrix in the SM. Due to the properties of the top-quark, direct measurements of top-quarks decaying into down quarks or strange quarks would require less theoretical assumptions than the current best measurements of these CKM elements, using B-hadron decays. Nevertheless, a direct measurement in the environment of the ALTAS detector is very challenging. Hence, an interpretation of already existing measurement is performed first, using results from the measurement of the top-quark t-channel cross section measurement performed by the Wuppertal group.A parametrization of all events is used in a profile likelihood fit setup in order to obtain limits on all top-quark involved CKM matrix elements using three different scenarios. This interpretation is presented in Chapter 8. The results of this work are part of the publication of the single-top-quark t-channel analysis, were published in Ref. [1].

Building on the results and findings during the different steps of the interpretation, a proof-of-concept analysis is developed to further investigate potential improvements in precision measurements of the top-quark involved CKM matrix elements. An optimized event selection is developed to target all different top-quark production and decay processes. In order to distinguish between the signal events and the background events, a machine learning based approach using a feed-forward neural network (NN) is utilized. Additionally, to further enhance the precision, further NN studies are performed to distinguish between the different top-quark t-channel processes. Finally, a profile likelihood fit, independent of specific scenarios used in the previous interpretation, is employed to assess the feasibility of such a measurement. The studies of the proof-of-concept analysis are explained in detail in Chapter 9.
The overall conclusions of the work presented in this thesis is written down in Chapter 10.

2 Brief introduction of the Standard Model of particle physics and the role of the top-quark

The scientific field of particle physics explores the fundamental building blocks of the universe and the fundamental interaction between these. Starting in the early 20th century, the application of quantum physics became necessary as classical concepts were no longer able to describe all phenomena observed in experiments. Based on an increasing number of experimental discoveries including those of subatomic particles, a theoretical framework was developed that is known today as SM. The SM comprises the mathematical formulation of the known fundamental building blocks, the elementary particles, their properties and consequently their interactions. The SM is one of the most thoroughly tested and validated theoretical frameworks in physics. Although many experiments have successfully tested its predictions and demonstrated reproducible observations, it is not regarded as a complete theory. Thus, the goal of particle physics remains one comprehensive fundamental theory, describing all aspects of the elementary particles and all of their interactions. The analyses presented in this thesis contribute testing and improving the SM in order to advance the understanding of particle physics.

2.1 Overview of the Standard Model of particle physics

Symmetries play a fundamental role in physics and the mathematical description of it, as symmetries are related to conserved quantities as established by Noether's theorem [2]. In the context of quantum field theory (QFT), symmetries are naturally described by mathematical structures, the *groups*. In particle physics, groups form the basis for the description of the fundamental interactions, which are associated with gauge symmetries. The theory is required to be invariant under local symmetry transformations, so-called *gauge transformations*, of the fields, hence the corresponding groups are gauge symmetry groups. Further, gauge transformations form a Lie-group, often referred to as symmetry group of the theory. Its generators correspond to the independent directions in the transformation space and define the structure of the group. For each generator of a gauge group, a corresponding field, called the *gauge field*, inherently arises. These gauge fields are also included in the Lagrange density, $\mathcal{L}(\psi(x), \partial_\mu \psi(x))$, also referred to as the Lagrangian, of the QFT to ensure its *gauge invariance*. Consequently, the Lagrangian, which describes the dynamics and kinematics of a field $\psi(x)$, is invariant under gauge transformations,

however it restricts the number of potential terms permitted in the Lagrangian. Due to the requirement of local gauge invariance, interactions between fields related to the symmetry group occur. Hereby, gauge fields give rise to mediator particles of the respective interaction. Additionally, requiring gauge invariance ensures the *renormalizability* of the theory under the restriction, that the Lagrangian only includes interactions between three (fermion or boson) or four (boson) fields, respectively. A QFT is called renormalizable if all physical observables, e.g. cross sections or decay rates, can be uniquely determined from a finite number of measurements of a finite set of observables.

The SM is formulated as a renormalizable QFT [3, 4] with a gauge structure defined by three gauge groups, which represent the strong, electroweak interactions between elementary particles: $\mathrm{SU(3)_C} \times \mathrm{SU(2)_L} \times \mathrm{U(1)_Y}$. Similarly to the mediator particles, each elementary particle corresponds to a field in the Lagrangian of the SM. The transformation properties of these fields under gauge symmetries, determined by different charges, also called *quantum numbers*, of each field, specify which interaction each particle participates in. The elementary particles in the SM are fermions with spin 1/2, the mediators of the three interactions are vector bosons, i.e. spin 1 particles.

The gauge symmetry group $\mathrm{SU(3)_C}$ [5–8] is the underlying structure for quantum chromodynamics (QCD), which describes the strong interaction. The index C denotes the quantum number indicating the *color* charge. Historically, its three values are referred to as red, blue and green. The SM contains six fields which transform as triplets under $\mathrm{SU(3)_C}$ transformations and thus carry color charge and are subject to the strong interaction. These fields are referred to as *quarks*. In contrast, *leptons* do not interact due to the strong interaction, as the corresponding fields transform as $\mathrm{SU(3)_C}$ singlets. The gauge field of the $\mathrm{SU(3)_C}$ corresponds to eight kinds of vector bosons, the *gluons*. Since the gluon field belongs to the adjoint representation of the group, i.e. it transforms under the $\mathrm{SU(3)_C}$ in the same way as its generators, gluons themselves carry color charge. In addition, the $\mathrm{SU(3)_C}$ is a non-abelian group, hence gluons also interact with themselves.
The strong interaction preserves the charge conjugation-symmetry, C, i.e. the interaction is not altered when the electric charge of a fermion is reversed. Furthermore is also preserves the parity symmetry, P, ensuring that the interaction remains invariant under the inversion of the spatial coordinates of a particle. In the Lagrangian of the strong interaction, CP-symmetry is not necessarily broken, however, experimental observations suggest that any potential violation is extremely small or even absent.

The electroweak sector of the SM is described by the underlying product of the symmetry groups $\mathrm{SU(2)_L} \times \mathrm{U(1)_Y}$ [9–12]. Hereby, the gauge group $\mathrm{SU(2)_L}$ is the gauge group for the weak interaction. The index L indicates that the three gauge bosons of the $\mathrm{SU(2)_L}$, $\hat{W}_1, \hat{W}_2$ and $\hat{W}_3$ only couple to *left-handed* fermions. Left-handed fermions are eigenstates of the chirality operator, γ^5, with an eigenvalue of -1, while right-handed particles have an eigenvalue of $+1$. For massless fermions, the chirality coincides with the helicity, i.e. the projection of the spin of the particle onto the direction of motion. There are three doublets transforming under the $\mathrm{SU(2)_L}$, $L_{i,\mathrm{L}} = (\nu_\ell, \ell)^\intercal, \quad i = 1, 2, 3$, each containing a

massive[1] left-handed lepton, ℓ, and a corresponding left-handed massless lepton, called neutrino, ν_ℓ. In addition, there are right-handed singlets for the massive leptons, ℓ_{R}, however no right-handed neutrinos are included in the SM[2]. For quarks, there are three $\mathrm{SU(2)_L}$ doublets, $Q_{i,\mathrm{L}} = (u_{\mathrm{L}}, d_{\mathrm{L}})^{\intercal}, \quad i = 1, 2, 3$, consisting of a left-handed up-type quark, u_{L}, and a left-handed down-type quark, d'_{L}. Further, there are six singlets, q_{R}, each describing a right-handed up- or down-type quark.
All particles that transform as $\mathrm{SU(2)_L}$ doublets carry a quantum number, the weak isospin I^W, which is corresponding charge of the weak interaction. It is evident from the doublet structure, that these particles have a weak isospin of $I^W = \frac{1}{2}$, with the third component being $I_3^W = +\frac{1}{2}$ for the upper component, while for the lower component it is $I_3^W = -\frac{1}{2}$. Consequently, for the particles in $\mathrm{SU(2)_L}$ singlets, $I^W = 0$ applies.

The $\mathrm{U(1)_Y}$ denotes the symmetry group, which in combination with the $\mathrm{SU(2)_L}$, determines the electromagnetic interaction. The gauge boson of the $\mathrm{U(1)}_Y$ symmetry group is the $\hat{B}$, which couples to the *weak hypercharge*, Y_W. Contrary to the strong interaction, the weak interaction violates both, the charge conjugation-symmetry and the parity symmetry. In the SM Lagrangian, the electromagnetic part is CP-symmetric.

In the most general possible Lagrangian of the SM, free parameters called *coupling constants* for each interaction occur. These parameters determine the strength of the interaction. The coupling constant for the strong interaction is denoted as g_s, while the corresponding coupling constants for the $\mathrm{SU(2)_L}$ and $\mathrm{U(1)}_Y$ are given by g' and g, respectively. In contrast to their nomenclature, the coupling constants do in fact depend on the energy- and momentum-scale at which the interaction occurs. Due to the imposed $\mathrm{SU(3)_C}$ gauge invariance, g_s increases for small energy- or momentum scales, i.e the interaction strength between two color charged particles increases largely. While there is no mathematical proof, this behavior qualitatively explains the existence of color-neutral boundstates, *hadrons*, build by two or three quarks, and the *confinement* of quarks and gluons inside these boundstates. Confinement further describes the effect when separating two color-charged particles, the energy added to the system leads to the creation of quark-antiquark pairs. As a result, instead of two separate color charges, multiple color-less hadrons are formed. Subsequently, g_s decreases with increasing energy scale. Accordingly, the interaction strength between two color charged particles becomes smaller the smaller their distance. Consequently, at sufficiently high energies, quarks and gluons can be treated as free particles. This characteristic is called *asymptotic freedom* [6, 7]. An important implication of this phenomenon is that pertubation theory, used in calculations for the QCD, is valid only for asymptotic free quarks and gluons. Both of these phenomena have therefore implications for high energy particle physics experiments. The effect of asymptotic freedom also exists mathematically in other non-abelian gauge theories, such as the $\mathrm{SU(2)_L}$.

Due to the $\mathrm{SU(2)_L} \times \mathrm{U(1)_Y}$ symmetry of the electroweak interaction, the aforementioned

[1] More on particle masses in the last paragraph of this chapter.
[2] Right-handed chirality states of neutrinos have not been observed, hence they are not considered a part of the SM in order to stick to a minimal formulation of the theory.

four gauge bosons, $\mathrm{SU(2)_L}$, $\hat{W}_1, \hat{W}_2$, $\hat{W}_3$ and $\hat{B}$, are massless in the SM formulated thus far. Moreover, the SM Lagrangian formulated thus far, does not include direct mass terms for fermions as well, as these would violate the gauge invariance. However, this presents a contradiction with experiments which measured massive fermions and massive vector bosons.

A central aspect of the SM to solve this contradiction is the concept of *spontaneous symmetry breaking*. This principle follows from the Brout-Englert-Higgs mechanism [13–15], which introduces another field, the Higgs field, $\hat{\phi}$, into the SM Lagrangian. The Higgs field is a scalar boson field, i.e. it has spin 0, with a hypercharge of $Y = \frac{1}{2}$. An important feature of the Higgs field, is displayed by its transformation as a $\mathrm{SU(2)_L}$ doublet: $\phi = (\phi^+, \phi^0)^\intercal$. As both scalar fields, ϕ^+ and ϕ^0 are complex fields, this yields in four degrees of freedom. Further, when the Higgs potential, $V(\phi)$, is constructed such that it leads to a nonzero vacuum expectation value, v, the $\mathrm{SU(2)_L \times U(1)_Y}$ symmetry is broken[3]. Since this effect is not caused by a term in the Lagrangian, it is called spontaneous symmetry breaking. Of the four degrees of freedom, three correspond to three massless Goldstone bosons, while one real scalar field corresponds to another particle, the Higgs boson, h^0. The three Goldstone bosons are not observed, since together with the W and B bosons they give rise to the masses of the physical $W^\pm$ and Z^0 bosons. Addtionally, the Lagrangian with the Higgs field is characterized by two free parameters, λ and μ. The former is a coupling constant for self-interactions of the Higgs boson, while μ^2 describes the form of the Higgs potential. Both are free parameters of the SM and connected to the non-vanishing vacuum expectation value via $\lambda v = \sqrt{\lambda \mu^2}$. Similarly to the vacuum expectation value, the mass of the Higgs boson is a free parameter of the SM, as the relation $m_{h^0} = \sqrt{2\lambda v^2}$ applies. The ATLAS and CMS experiments, which observed the Higgs boson for the first time in 2012 [17, 18] have measured both values to be $v \approx 246\,\mathrm{GeV}$ and $m_h \approx 125\,\mathrm{GeV}$.

A consequence of the Broud-Englert-Higgs mechanism, the *mass eigenstates*, i.e. physical bosons, emerge from a superposition of the *interaction eigenstates*, the aforementioned W and B bosons. Mass eigenstates correspond to the physical particles with a well-defined mass which propagate freely. In contrast, interaction eigenstates describe how particles couple to the fundamental interactions. As visible in Equations (2.1) (2.2) (2.3), both states are not required to coincide, and thus superpositions of interaction eigenstates can create a mass eigenstate. In the electroweak sector of the SM, the particles observed experimentally are the $W^\pm$ bosons, the Z^0 boson and the photon, γ:

$$W^\pm = \frac{1}{\sqrt{2}} \hat{W}_1 \mp i \hat{W}_2, \tag{2.1}$$

$$Z = \cos(\theta_W)\, \hat{W}_3 - \sin(\theta_W)\, \hat{B}, \tag{2.2}$$

$$\gamma = \sin(\theta_W)\, \hat{W}_3 + \cos(\theta_W)\, \hat{B}. \tag{2.3}$$

Here, θ_W denotes the electroweak mixing angle, also referred to Weinberg angle [10]. It is defined as $\tan(\theta_W) = \frac{g'}{g}$. The masses of the $W^\pm$ boson and the Z^0 result in $m_W \equiv \frac{gv}{2}$ and

[3] Note, the Lagrangian is still invariant under $\mathrm{SU(2)_L \times U(1)_Y}$, but the physical fields do not reflect the symmetry. See Ref. [16]

$m_Z = \frac{\sqrt{g^2+g'^2}v}{2}$, respectively, while the photon remains massless. The photon mediates the electromagnetic interaction in the SM, as it couples to the electric charge, Q, of a particle. The electric charge of a particle is connected with its weak isospin and the weak hypercharge, by the relation $Q = T_3^W + Y_W$. Up-type quarks have an electric charge of $Q = +\frac{2}{3}$, whereas down-type quarks have an electric charge of $Q = -13$. The massive leptons in the SM carry an electric charge of $Q = -1$, in contrast the neutrinos do not carry an electric charge.
For both, the vector bosons and the fermions, mass terms occur in the SM Lagrangian after the Higgs field acquires a vacuum expectation value, thus quarks, leptons and mediator bosons gain mass via interactions with the Higgs field. In the SM, the interactions between fermions and scaler fields, such as the Higgs field, is the so-called *Yukawa*-interaction. The masses of the fermions are proportional to the value of the coupling constant, h_f: $m_f = h_f v/\sqrt{2}$. However, neutrinos remain massless, as the formulation of mass terms in the SM Lagrangian requires the existence of right-handed chirality states. For every fermion in the SM, there exists a corresponding anti-fermion with reversed electric charge and opposite quantum numbers under the interactions, while the mass, spin, and overall interaction strength remain the same. A schematic overview of all fermions and bosons including important properties and the interactions they are subject to or mediate, respectively, is given in Figure 2.1.

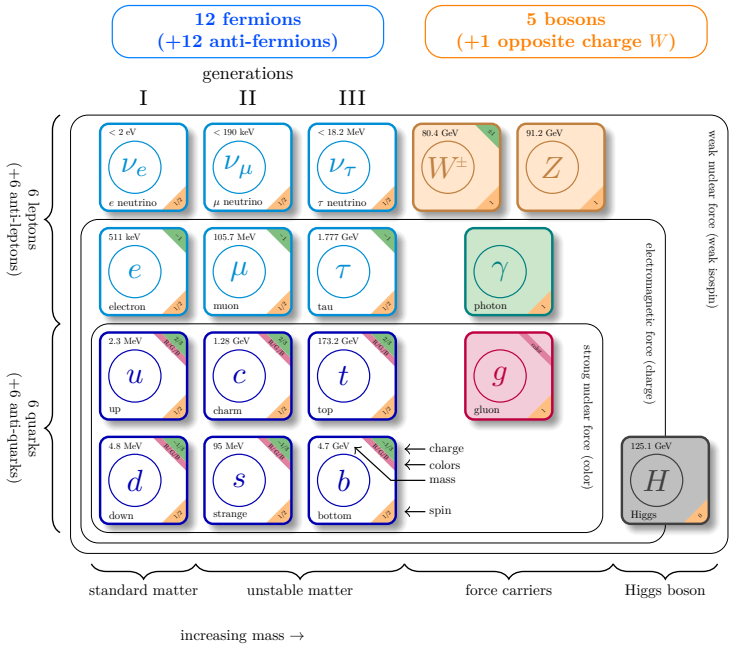

Figure 2.1: Schematic overview of the particles of the SM. The leptons and quarks are sorted by their third component of the weak isospin. The mass values are taken from Ref. [19]. Grapic adapted from Ref. [20].

The two types of fermions in the SM, the leptons and the quarks, are each ordered in three generations. For the leptons, each generation consists of one electricly charged massive lepton and its corresponding neutrino. The first generation includes the electron (e) and the electron neutrino (ν_ℓ), while the second generation contains the muon (μ) and the muon neutrino (ν_μ). Lastly the third generation consists of the tau lepton (τ) and the tau neutrino (τ).
Quarks are classified into six flavors, split into three up-type quarks, specifically the up-quark (u), the charm quark (c) and the top-quark (t), and three down-type quarks, namely the down-quark (d), the strange quark (s) and the bottom quark (b), with one quark of each type forming a generation. The up-quark and down-quark build the first generation, the charm quark and strange quark the second generation, and the top-quark and the bottom quark the third generation.
The hierachy of these fermion generations is arranged by the mass values of the fermions, with the lightest ones populating the first generation and the heaviest ones the third generation. All fermion masses are free parameters in the SM and hence, need to be measured experimentally. The determined masses follow the sequence: $m_u < m_c < m_t, m_d < m_s < m_b$ and $m_e < m_\mu < m_\tau$ [19]. Regardless of the flavor, all fermions across different generations interact identically in the SM, hence this phenomenon is referred to as *flavour universality* of the SM. In addition, interactions between fermions across different generations are realized via *charged currents*. These interactions, especially between quarks, and their implications are discussed in the following chapter.

2.2 Flavor changing currents and the CKM matrix

The weak interaction in the SM uniquely allows for transitions between different generations of fermions. These interactions occur by charged current interactions mediated by the $W^\pm$ bosons. The flavor changing nature of the charged current interactions is a direct consequence of the weak isospin structure: The weak interaction acts on $\mathrm{SU(2)_L}$ fermion doublets, in such a way that the charged current is associated with the ladder operators $I_\pm = I_1 \pm iI_2$, inducing a transition of the weak isospin projection I_3 by ± 1, respectively, and thus, changing the flavor of the fermion.

As discussed in the previous section in the context of the electroweak interaction, the mass and interaction eigenstates of particles do not necessarily align. In the case of the quarks, both, their masses and mixing between certain quark eigenstates arise from the Yukawa interactions. The relevant part of the SM Lagrangian describing the Yukawa interaction between quarks and the Higgs field before the spontaneous symmetry breaking is given by

$$\mathcal{L}_y^{\text{quarks}} = -\left(\sum_{i,j} Y_{ij}^d \overline{Q_{i,\mathrm{L}}^I}\phi d_{j,\mathrm{R}}^I + Y_{ij}^u \overline{Q_{i,\mathrm{L}}^I}\epsilon\phi^* u_{j,\mathrm{R}}^I + \text{h.c.}\right). \tag{2.4}$$

Specifically, the Yukawa interaction is represented by the 3×3 complex matrices $Y^{u,d}$, the Higgs field is denoted as ϕ and $\epsilon = i\sigma$ is the 2×2 antisymmetric tensor, with σ being

the Pauli matrices. The left-handed quark doublets in the weak eigenstate basis are given by Q_L^I, whereas d_R^I and u_R^I correspond to the right-handed up- and down-type quark singlets, respectively. After spontaneous symmetry breaking, with ϕ acquiring its vacuum expectation value, the Lagrangian yields mass terms for the quarks:

$$\mathcal{L}_y^{\text{quarks}} = -\frac{v}{\sqrt{2}} \sum_{i,j} \left(Y_{ij}^d \overline{d_{i,\text{L}}^I} d_{j,\text{R}}^I + Y_{ij}^u \overline{u_{i,\text{L}}^I} u_{j,\text{R}}^I + \text{h.c.} \right). \tag{2.5}$$

These terms result in the quark mass matrices, $\tilde{M}^{u,d} = \frac{v}{\sqrt{2}} Y^{u,d}$. The Yukawa matrices and thus the mass matrices are in general not diagonal - in fact, in the SM both matrices are not diagonal. Thus, the physical states of the quarks observed need to be obtained by singular value decomposition of $Y^{u,d}$ using unitary transformations, $V_\text{L}^u, V_\text{L}^u, V_\text{L}^u, V_\text{L}^u \in \text{U}(3)$:

$$\tilde{M}_{\text{diag.}}^u = \frac{v}{\sqrt{2}} V_\text{L}^u Y^u V_\text{R}^{u\dagger}, \tag{2.6}$$

$$\tilde{M}_{\text{diag.}}^d = \frac{v}{\sqrt{2}} V_\text{L}^d Y^d V_\text{R}^{d\dagger}. \tag{2.7}$$

Hereby, $V_\text{L}^{u,d}$ are independent unitary matrices, i.e. $V_{\text{R,L}}^{u,d} V_{\text{R,L}}^{u,d\dagger} = \mathbb{1}$. The mass matrices $\tilde{M}^{u,d}$ are independent and, in general, cannot be brought to diagonal form simultaneously with one matrix, but four different unitary matrices are needed which each corresponding to a quark field of the weak interaction. Transformation of each quark field into a new base, the mass eigenstates, is given by $u_\text{L}^{(\text{mass})} = V_\text{L}^u u_\text{L}^I$ and $d_\text{L}^{(\text{mass})} = V_\text{L}^d d_\text{L}^I$, respectively. The most terms of the SM Lagrangian is symmetric under this quark field transformation and the newly introduced transformation matrices, $V_{\text{R,L}}^{u,d}$, cancel out because of their unitary properties. The charged current Lagrangian of the SM, however, is not symmetric under the quark field transformation:

$$\mathcal{L}_{CC} = -\frac{g}{\sqrt{2}} \left(\overline{\tilde{u}}_\text{L} V_\text{L}^u \gamma^\mu W_\mu^+ V_\text{L}^{d\dagger} \tilde{d}_\text{L} + \overline{\tilde{d}}_\text{L} V_\text{L}^d \gamma^\mu W_\mu^- V_\text{L}^{u\dagger} \tilde{u}_\text{L} \right) \tag{2.8}$$

$$= -\frac{g}{\sqrt{2}} (\overline{\tilde{u}}_\text{L} \gamma^\mu W_\mu^+ \underbrace{V_\text{L}^u V_\text{L}^{d\dagger}}_{V_\text{CKM}} \tilde{d}_\text{L} + \overline{\tilde{d}}_\text{L} \gamma^\mu W_\mu^- \underbrace{V_\text{L}^d V_\text{L}^{u\dagger}}_{V_\text{CKM}^\dagger} \tilde{u}_\text{L}) \tag{2.9}$$

The matrix V_CKM is the CKM matrix [21, 22]:

$$V_\text{CKM} = \begin{pmatrix} V_{ud} & V_{us} & V_{ub} \\ V_{cd} & V_{cs} & V_{cb} \\ V_{td} & V_{ts} & V_{tb} \end{pmatrix} \tag{2.10}$$

Hence, each element $V_{\text{CKM},(ij)}$ connects a left-handed up-type quark of the i-th generation with a left-handed down-type quark of the j-generation. Thus, the quark field transformation introduces transitions between different generations. In the SM, conventionally, the weak interaction eigenstates correspond to the mass eigenstates for the up-type-quarks. The CKM matrix is then utilized to obtain the eigenstates to the weak interaction for the down-type quarks, $(d', s', b')^\intercal$, from the corresponding mass eigenstates, $(d, s, b)^\intercal$:

$$\begin{pmatrix} d' \\ s' \\ b' \end{pmatrix} = V_\text{CKM} \begin{pmatrix} d \\ s \\ b \end{pmatrix} \tag{2.11}$$

Each element of the CKM matrix corresponds to an imaginary number, all of these being free parameters of the SM which values can be measured. All matrix elements are labelled according to both quark flavors instead of the generation index.

As a unitary 3×3 matrix, the CKM matrix is determined by nine real parameters and nine imaginary parameters. From the unitarity condition, $V_{\mathrm{CKM}} V_{\mathrm{CKM}}^{\dagger} = \mathbb{1}$, follows that all lines and all columns need to be orthonormal:

$$\sum_i = V_{ij} V_{ik}^* = \delta_{jk}, \qquad \text{and} \qquad \sum_j V_{ij} V_{kj}^* = \delta_{ik} \qquad \text{for all } j, k, \tag{2.12}$$

with V_{ij} being the CKM matrix element of the i-th line and j-th column, and V_{ik}^* being the complex conjugated CKM matrix elements. As a result of these conditions, six real (phases) and three complex (angles) unitary constraints are imposed on the matrix elements. These nine constraints reduce the total number of independent parameters from eighteen to nine. Another five parameters can be absorbed by relative quark phases: Since there are $N = 3$ quark generations in the SM, there are $2 \cdot N = 6$ freely definable phases for the quark fields. i.e. quark fields can independently be redefined by multiplying them with complex phase factors. Each quark field has a corresponding complex phase that can be freely chosen, e.g. $u_{\mathrm{L}} \to e^{i\alpha(u)} u_{\mathrm{L}}$. However, one global phase for all quark fields exists with $V_{ij} = e^{\alpha(j) - \alpha(i)} V_{ij}$. This global phase does not have any physical significance as it cannot be observed and thus, can be factored out, leaving $2 \cdot N - 1 = 5$ independent phases. Consequently, the number of free parameters of the CKM matrix further reduces from nine to four free parameters.
Therefore, the CKM matrix can be parametrized by three mixing angles and one phase. A conventional parametrization choice is given by (2.13) [23]:

$$\begin{aligned} V_{\mathrm{CKM}} &= \begin{pmatrix} 1 & 0 & 0 \\ 0 & c_{23} & s_{23} \\ 0 & -s_{23} & c_{23} \end{pmatrix} \begin{pmatrix} c_{13} & 0 & s_{13} e^{-i\delta} \\ 0 & 1 & 0 \\ -s_{13} e^{i\delta} & 0 & c_{13} \end{pmatrix} \begin{pmatrix} c_{12} & s_{12} & 0 \\ -s_{12} & c_{12} & 0 \\ 0 & 0 & 1 \end{pmatrix} \\ &= \begin{pmatrix} c_{12} c_{13} & s_{12} c_{13} & s_{13} e^{-i\delta} \\ -s_{12} c_{23} - c_{c2} s_{23} s_{13} e^{i\delta} & c_{12} c_{23} - s_{12} s_{23} s_{13} e^{i\delta} & s_{23} c_{13} \\ s_{12} s_{23} - c_{12} c_{23} s_{13} e^{i\delta} & -c_{12} s_{23} - s_{12} c_{23} s_{13} e^{i\delta} & c_{23} c_{13} \end{pmatrix}. \end{aligned} \tag{2.13}$$

The complex phase is denoted as δ, the three mixing angles, θ_{12}, θ_{13} and θ_{23} appear in $s_{ij} = \sin\theta_{ij}$ and $c_{ij} = \cos\theta_{ij}$, respectively.

Historically, before a third quark generation was considered, a mixing of the weak eigenstates of the first two quark generations was proposed by Cabibbo [21].

$$\begin{pmatrix} d\prime \\ s\prime \end{pmatrix} = \begin{pmatrix} \cos\theta_C & \sin\theta_C \\ -\sin\theta_C & \cos\theta_C \end{pmatrix} \begin{pmatrix} d \\ s \end{pmatrix}. \tag{2.14}$$

The Cabibbo angle, θ_C, describes the mixing in this rotation matrix and determines its structure. With the extension to three quark generations, it was observed that the hierachical structure of the elements was retained, and further, that all CKM matrix elements exhibit a certain pattern. While the diagonal elements were measured to be

close to unity, the off-diagonal elements decrease in magnitude with increasing distance between the generations, i.e. with increasing distance from the diagonal. The Wolfenstein parametrization has become a convenient parametrization of the CKM matrix to reflect its hierachy [24]. In the Wolfenstein parameterization, the CKM matrix is expressed in terms of four real parameters, λ, A, ρ and η, which are defined from [24–26]

$$\lambda = s_{12}, \qquad A\lambda^2 = s_{23}, \tag{2.15}$$

$$A\lambda^3 (\rho + i\eta) = s_{13} e^{i\delta}, \tag{2.16}$$

with the parametrization being expanded in orders of λ. Thus, the Wolfenstein parametrization of the CKM matrix is used as an approximation of the standard parametrization in Equation (2.13). In equation (2.17), the traditional form of the Wolfenstein parameterization, up to the order λ^3, is given[4]:

$$V_{\mathrm{CKM}} = \begin{pmatrix} 1 - \frac{\lambda^2}{2} & \lambda & A\lambda^3(\rho - i\eta) \\ -\lambda & 1 - \frac{\lambda^2}{2} & A\lambda^2 \\ A\lambda^3(1 - \rho - i\eta) & -A\lambda^2 & 1 \end{pmatrix} + \mathcal{O}(\lambda^4). \tag{2.17}$$

Both, the Wolfenstein parametrization (2.17) and the standard parametrization (2.13) contain the complex phase which is responsible for CP-violating phenomena in flavor-changing interactions. In fact, the extension to three generations was necessary in order to explain observed CP-violation in the SM, as with only two generations of quarks, CP-violation is not allowed due to the absence of a complex phase. In the standard parametrization δ exhibits the CP-violation, while equivalently in the Wolfenstein parametrization the rates of CP-violation correspond to ρ and η.
A phase-convention-independent quantity directly related to the CKM matrix and its parameters is the Jarlskog invariant $\mathcal{J}$ [27]. It is defined as

$$\begin{aligned} \mathcal{J} &= \mathrm{Im}(V_{ij} V_{kl} V_{il}^* V_{kj}^*), \qquad \text{with} \quad i \neq j, k \neq l \\ &= s_{12} s_{13} s_{23} c_{12} c_{23} c_{13} \sin\delta = \lambda^6 A^2 \eta \end{aligned} \tag{2.18}$$

and serves as a measure of CP violation. A vanishing of $\mathcal{J}$ would correspond to the absence of CP-violation. In addition, $\mathcal{J}$ is directly related to the differences of the quark masses. The commutator algebra of the mass matrices, $\tilde{M}^{u,d}$, yields

$$C = \left[\tilde{M}_u \tilde{M}_u^\dagger, \tilde{M}_d \tilde{M}_d^\dagger\right] = \tilde{M}_u \tilde{M}_u^\dagger \tilde{M}_d \tilde{M}_d^\dagger - \tilde{M}_d \tilde{M}_d^\dagger \tilde{M}_u \tilde{M}_u^\dagger, \tag{2.19}$$

with $C \neq 0$ since $\tilde{M}_d$ and $\tilde{M}_u$ cannot be diagonalized simultaneously. For its determinant follows that

$$\det(C) \propto \mathcal{J} \prod_{k>l} \left(m_{i,k}^2 - m_{i,l}^2\right) \left(m_{j,k}^2 - m_{j,l}^2\right), \tag{2.20}$$

with $m_{i,j}$ being the entries of the mass matrices. In the case that two quarks are degenerate in their masses, the determinant would vanish. Analogously, the determinant would vanish

[4] The Wolfenstein parametrization is exact at high enough orders. Furthermore, it ensures unitarity to all orders in λ.

if all quarks would have no masses[5]. Consequently, an analogous mixing in the lepton sector is not realized, since neutrinos are massless in the SM.

Experimentally, $\mathcal{J}$ is determined to be at the order of $\mathcal{O}\left(10^{-5}\right)$ [19]. Hence, the CP-violation is considered small in the SM.

2.2.1 Determination of CKM matrix elements

Precise measurements to determine the magnitudes of the CKM matrix elements are essential to verify SM, as all CKM matrix elements are free parameters of the SM. Further, the fundamental parameters, δ and the three mixing angles, θ_{12},θ_{13} and θ_{23} are obtained using the measured CKM matrix elements. Experimentally, the entries of the CKM matrix are determined through measurements of quark transition rates and ratios.
The most precise determination for the CKM matrix elements is obtained using a global fit to all available measurements[6]. The fit results for the Wolfenstein parameters, which are used by state-of-the-art MC generators (see Chapter 5) are [19]

$$\begin{aligned} \lambda &= 0.22501 \pm 0.00068, & A &= 0.826^{+0.016}_{-0.015} & , \\ \rho &= 0.1591 \pm 0.0094, & \eta &= 0.3523^{+0.0073}_{-0.0071} & . \end{aligned} \tag{2.21}$$

The magnitudes of all nine CKM matrix elements is determined as [19]

$$|V_{\mathrm{CKM}}| = \begin{pmatrix} 0.97435 \pm 0.00016 & 0.22501 \pm 0.00068 & 0.003732^{+0.000090}_{-0.000085} \\ 0.22487 \pm 0.00068 & 0.97349 \pm 0.00016 & 0.04183^{+0.00078}_{-0.00069} \\ 0.00858^{+0.00019}_{-0.00017} & 0.04111^{+0.00077}_{-0.00068} & 0.999118^{+0.000029}_{-0.000034} \end{pmatrix} \tag{2.22}$$

Hereby, the off-diagonal CKM matrix elements investigated in this thesis, V_{td} and V_{ts}, are measured in B^0-$\bar{B}^0$ mixing processes, which are dominated by Feynman box-diagrams including virtual[7] top-quarks, and by loop-mediated kaon and B-meson decays, also including virtual top-quarks. Hence, theoretical uncertainties in the description of hadronic effects in these processes limit the accuracy of the current determinations [19]. On the other hand, single-top-quark and top-quark pair cross section measurements are utilized to obtain V_{tb}. The differences arise from the properties of the top-quark, which are examined in the following chapter.

2.3 Properties of the top-quark

The top-quark belongs to the third generation of quarks in the SM, which was predicted in order to explain the observed phenomena of flavor-changing interactions and CP-violating

[5] This relation is also consistent with the requirement of three quark generations in the SM since just two existing quark generations would again lead to $C = 0$ and therefore no CP-violation.
[6] And imposing SM constraints, i.e. unitarity
[7] Particles not produced on the mass-shell are called virtual.

processes. The hypothesis of a third generation was reinforced when the bottom quark was discovered in 1977 [28], providing the first experimental evidence for a third generation of quarks. Its weak isospin partner, the top-quark, was discovered nearly two decades later, in 1995, at the Tevatron at Fermilab in proton-antiproton collisions by the DØ [29] and CDF collaboration [30]. The left-handed top-quark in the $\mathrm{SU}(2)_L$ doublet has an electric charge of $Q = 2/3$ and a projection of the weak isospin of $T_3 = +1/2$, whereas the right-handed top-quark is evidently an $\mathrm{SU}(2)_L$ singlet.

It is the heaviest elementary particle measured to date with its mass being ≈ 40 times larger than the mass of the b-quark, the second heaviest particle in the SM. At Tevatron, the CDF and DØ experiments measured its mass, as well as currently the ATLAS and CMS experiments. The average top-quark mass value from the latter two experiments, combining several measurements, yields $m_t = 172.52 \pm 0.14\,(\text{stat.}) \pm 0.30\,(\text{syst.})\,\text{GeV}$ [19]. The measured mass corresponds approximately to $m_t \simeq \frac{v}{\sqrt{2}}$, i.e it is the only particle in the SM which Yukawa-coupling is on the order of unity. Further, since m_t is larger than the W-boson mass, the top-quark is the only quark that decays into a W-boson on mass shell and another down-type quark.

As indicated in the previous chapter, it was found that the top-quark nearly exclusively decays into a b-quark. Thus, its *decay width*, Γ_t, is expected to be characterized primarily by the $t \to Wb$ decay. The decay width of the top-quark at Next-to-leading order (NLO) accuracy is given by [31]

$$\Gamma_t = \frac{G_F m_t^3}{8\pi\sqrt{2}} \left(1 - \frac{m_W^2}{m_t^2}\right)^2 \left(1 + 2\frac{m_W^2}{m_t^2}\right) \left[1 - \frac{2\alpha_S}{3\pi}\left(\frac{2\pi^2}{3} - \frac{5}{2}\right)\right]. \tag{2.23}$$

Using the world average for the W-boson mass, $m_W = 80377 \pm 12\,\text{MeV}$ [19], and $G_F = 1.1663788(6) \cdot 10^{-5}\text{GeV}^{-2}$ [19], the top-quark decay width yields $\Gamma_t = 1.326\,\text{GeV}$ [19] with a theoretical precision of better than 1%. For the calculation, a top-quark mass reference value of $m_t = 172.5\,\text{GeV}$ is inserted. A direct measurement of the top-quark decay width was done by the ATLAS experiment, resulting in $\Gamma_t = (1.9 \pm 0.5)\,\text{GeV}/c^2$.

The corresponding lifetime of the top-quark is $\tau = \frac{1}{\Gamma_t} \approx 0.5 \cdot 10^{-24}\text{s}$. Consequently, this lifetime is too short for strong interactions to alter the properties of the top-quark or confine it within a hadron. As a result, the top-quark is the only quark that effectively remains free during its existence. This property distinguishes the top-quark from all other quarks in the SM, which form hadrons prior to their decay.

In the proton-proton collisions at the LHC, top-quarks are produced mainly in pairs ($t\bar{t}$). The production cross section is measured by both, ATLAS and CMS, with the most precise measurements to-date resulting in $\sigma_{t\bar{t}} = 829 \pm 1\,(\text{stat.}) \pm 13\,(\text{syst.}) \pm 8\,(\text{lumi.}) \pm 2\,(\text{beam})\,\text{pb}$ [32] and $\sigma_{t\bar{t}} = 791 \pm 1\,(\text{stat.}) \pm 21\,(\text{syst.}) \pm 14\,(\text{lumi})\,\text{pb}$ [33], respectively. These results are in agreement with theoretical predictions at next-to-next-to-leading order (NNLO)+next-to-next-to-leading logarithmic (NNLL) [34] resummations. In contrast, single-top-quark production in the t-channel, tW-channel or s-channel cross sections yield in smaller values. For the s-channel production the most recent measurement at the LHC from ATLAS measured $\sigma_{s\text{-chan}} = 8.2^{+3.5}_{-2.9}\,\text{pb}$ [35], for the tW-channel CMS measured

$\sigma_{tW} = 79.2 \pm 0.9\,(\text{stat.})^{+7.7}_{-8.0}\,(\text{syst.}) \pm 1.2(\,\text{lumi.})\,\text{pb}$ [36]. All results are again in agreement with theoretical predictions of the SM. The most recent t-channel cross section measurement in ATLAS was done by Joshua Reidelstürz et.al [1] and an overview is given in Chapter 8.1. This measurement was utilized in order to obtain a measurement, not just of $|V_{tb}|$, but also $|V_{td}|$ and $|V_{ts}|$. Due to the unique property of its short lifetime, this direct measurement of CKM matrix elements involving the top-quark is particularly well-motivated. Since the top-quark does not hadronize, it decays solely by the electroweak interaction, allowing in principle for a direct extraction of the top-quark involved CKM elements without additional hadronic uncertainties. The average value of $|V_{tb}|$ calculated using ATLAS and CMS single-top-quark measurements is estimated to be $|V_{tb}| = 1.007 \pm 0.030$, with a world average using also measurements at the Tevatron resulting in $|V_{tb}| = 1.01 \pm 0.027$. Therefore, due to the unitarity assumption in the SM, the values of V_{td} and V_{ts} are much smaller, and thus are not likely to be precisely measured from top-quark decays. As discussed in the previous chapter, determinations of V_{td} and V_{ts} are primarily obtained from B^0-$\bar{B}^0$ mixing. However, these measurements rely on theoretical assumptions to account for hadronic effects, which introduce uncertainties that limit the precision of the extracted CKM elements. A direct measurement of V_{td} and V_{ts} in top-quark decays would thus provide an alternative approach, reducing model dependencies and improving the understanding of flavor transitions in the SM. The work presented in this thesis contributes to this effort.

2.4 The top-quark and physics beyond the Standard model of particle physics

Despite the great success of the SM in describing fundamental particles and their interactions, it is not considered a complete theory. Numerous unanswered questions arose from experimental observations during its origin and construction in the last decades and some questions still remain. In the search for a more profound theoretical framework describing particles and their interactions, extensions of the SM, BSM theories, are explored. Some of the most significant open key questions to date concern the nature of dark matter, which is estimated to be responsible for about 27% of the energy content in the universe. Observations regarding the motion of galaxies and galaxy clusters suggest that most matter in the universe is not visible and does not interact via any force described by the SM. Dark matter is theorized to be a form of exotic matter that interacts primarily through gravity, which is also not included in the SM, and possibly the weak force. There exist multiple BSM theories providing frameworks for the description of dark matter. Prominent samples are supersymmetry models [37–39], which proposes that for every known particle, there exists a partner particle with different spin properties, aim to provide a framework to describe dark matter.
Further, the SM does not explain the reason for the observed matter-antimatter asymmetry in the universe, with an observed predominance of matter over antimatter in the universe. While the SM does predict and explain CP-violation, the amount of it predicted is insufficient to account for the observed asymmetry.

Similarly, the discovery of neutrino oscillations, i.e. the mixing of different neutrino flavors, is observed. Hence, neutrinos are expected to have mass. The SM, however, does not include any mechanism for neutrinos obtaining mass.

The top-quark plays a pivotal role in many areas of particle physics, not only due to its unique properties within the SM but also because of its potential implications for BSM physics.

One of the most significant properties of the top-quark is its coupling to the Higgs boson, as it is the largest among all particles in the SM. This large coupling implies that the top-quark has a crucial role in further understanding the mechanism of electroweak symmetry breaking. In particular, two keys aspects of BSM physics include the top-quark.
First, the top-quark is crucial in the hierachy problem in the SM, which arises from large quadratic radiative corrections to the Higgs boson mass. The dominant contribution to these corrections comes from top-quark loops due to its large Yukawa coupling. In the SM, these corrections push the Higgs mass toward much higher energy scales, than the experimentally observed value. Large adjustments of the theory's parameters, due the need for a cancellation between large quantum corrections and an assumed bare Higgs boson mass to achieve the measured mass, is regarded highly unnatural. Therefore, additional mechanisms or symmetries, such as supersymmetry or compositeness [40], are suggested in order to stabilize the calculations by introducing additional particles that cancel these corrections.
Second, the large coupling strength between the top-quark and the Higgs boson makes it a sensitive probe for new physics at higher energy scales than the SM. Many BSM theories predict deviations in Higgs-top-quark interactions, such as modifications of the top-quark Yukawa coupling or the presence of additional Higgs-like states [41–44]. Furthermore, new particles associated with the electroweak symmetry breaking could preferentially couple to the top-quark due to its large mass, leading to measurable effects in processes involving top-quark-Higgs interactions.

These examples highlight some of the most pressing challenges in theoretical particle physics and demonstrate why investigating the top-quark's properties and its interactions in and beyond the Standard Model is essential. Examining processes involving the top-quark, leads to a more complete understanding of the universe and its fundamental forces.

3 The ATLAS Detector at the Large Hadron Collider

In order to probe the SM at the highest accessible energies and with increasing precision, large-scale experiments were build and developed. Particle accelerators play a central role in these experiments. They enable high-energy particle collisions that are necessary to recreate conditions similar to those of the early universe and therefore to investigate fundamental interactions predicted by the SM. Over the past decades, increasingly powerful accelerators were constructed to extend the accessible energy frontier. The largest particle accelerator to date is the LHC [45–47] at European Organisation for Nuclear Research (CERN). Among these, the ATLAS detector was designed to investigate a wide range of physics processes, performing precision measurements as well as searches for BSM physics. In this chapter, first the LHC is introduced and afterwards, a detailed overview of the ATLAS detector is provided with a focus on its key components and capabilities.

3.1 The Large Hadron Collider

The LHC is a circular accelerator with a circumference of 27 km. It is situated in the former Large Electron–Positron Collider (LEP) tunnel at CERN. As successor of LEP, the LHC was built to study particle interactions using proton-proton collisions. For this reason, LHC can accelerate proton beams up to 6.8 TeV. Further, the LHC is used to accelerate lead ions[1] up to 2.51 TeV. In Figure 3.1, the LHC is shown as part of the CERN accelerator complex. The protons are obtained by ionizing hydrogen gas and then accelerated in several steps. First, a linear accelerator[2] (Linac2) gets the protons to 50 MeV. As a second step, the protons are injected into the Proton Synchrotron Booster (BOOSTER), which accelerates them to an energy of 1.4 GeV and splits them into bunches. Each proton beam consists of more than 2500 bunches, with 10^{11} protons per bunch [49]. The used bunch spacing is 25 ns. Afterwards, the proton bunches are sequentially injected in the Proton synchrotron (PS), which accelerates them to 25 GeV, and the Super proton synchrotron (SPS), which increases their energy further to 450 GeV. At this point, the protons are injected into two separate beam pipes in the LHC. The beams circulate in opposite directions. Superconducting magnets are used to hold the protons on their tracks,

[1] In addition, runs with xenon and oxygen nuclei were performed.

[2] Linac2 operated until the end of Run 2 in 2018. For Run 3 it was repaced by Linac3 in 2020, which can accelerate the protons to 160 MeV.

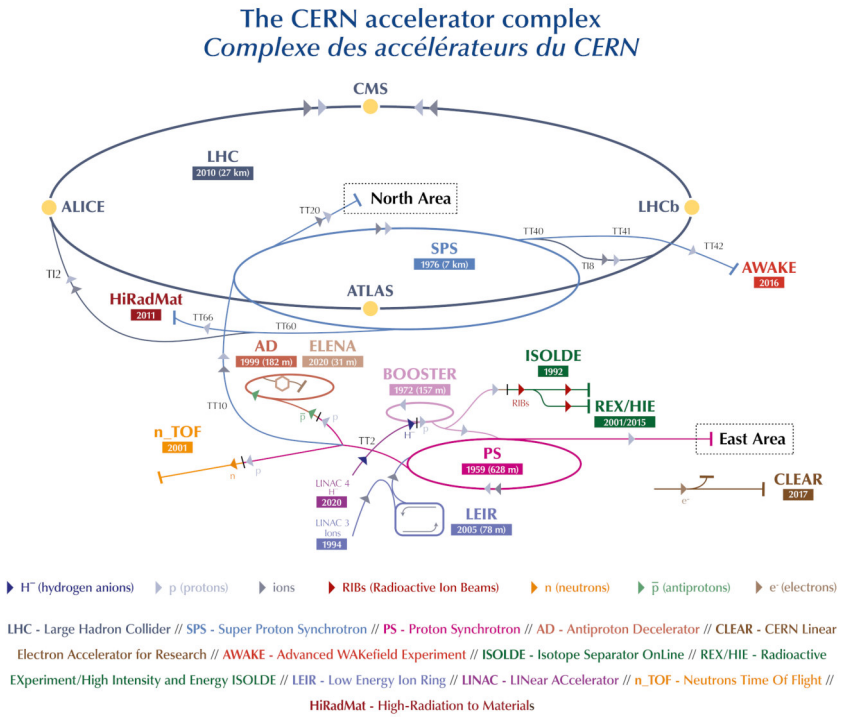

Figure 3.1: Overview of the CERN accelator complex [48]. All pre-accelerators are shown, as well as the experiments at the four interaction points and smaller experiments at CERN.

whereas superconducting cavities either keep the beams at a given energy or increase the energy slowly. Between 2015-2018 (Run 2) the reached centre-of-mass energy in proton-proton collisions was 13 TeV.
There are four interaction points (IPs), where the beams, either proton-proton, lead-lead or proton-lead, are brought to collision. At each, one of the large LHC experiments is located: ATLAS [50], CMS [51], LHCb [52] and ALICE [53]. The ALICE detector focuses its physics program on heavy-ion involved collisions to investigate high-density QCD states, e.g. the quark-gluon-plasma, while LHCb is build to precisely measure the properties of hadrons containing a b-quark. On the other hand, ATLAS and CMS are multi-purpose detectors, build to measure a variety of phenomena.
Due to the bunch spacing, the LHC was operated at a crossing rate of 40 MHz. The event rates, $\mathrm{d}N/\mathrm{d}t$, are determined by the instantaneous luminosity, $\mathcal{L}_{\text{inst}}$:

$$\frac{\mathrm{d}N}{\mathrm{d}t} = \mathcal{L}_{\text{inst}} \cdot \sigma, \tag{3.1}$$

with σ being the cross section of the physics process of interest in the collisions and N the number of originating events of that process.
The LHC was first operated from 2009 to 2013 (Run 1) at a centre-of-mass energy of $\sqrt{s} =$ 7 TeV and 8 TeV, achieving a peak instantaneous luminosity of $\mathcal{L}_{\text{inst}} = 8{\times}10^{32}\mathrm{cm}^{-2}\,\mathrm{s}^{-1}$ [54].

In Run 2, the achieved peak instantaneous luminosity was increased to $\mathcal{L}_{\text{inst}} = 2.1 \times 10^{34}\text{cm}^{-2}\,\text{s}^{-1}$ [55]. Taking the integral over Equation 3.1, leads to the integrated luminosity:

$$\mathcal{L}_{\text{int}} = \int \mathcal{L}_{\text{inst}} \text{d}t. \tag{3.2}$$

The integrated luminosity recorded by the ATLAS experiment in Run 2 amounts to $\mathcal{L}_{\text{int}} = 140.1 \pm 1.2\text{fb}^{-1}$ [56].
Currently, the LHC continues with Run 3, since 2022 and until the end of 2025. Data are collected at $\sqrt{s} = 13.6\,\text{TeV}$. The integrated luminosity is expected to be up to 200fb^{-1} [57].

3.2 The ATLAS Detector

The ATLAS detector [50] is built around one of the collision points of the LHC and nominally forward-backward symmetric with respect to the IP. It covers nearly the entire solid angle around the collision point, excluding the beam pipe and gaps in the detector construction, used for support structure and detector infrastructure. With a length of approximately 46 m and a diameter of approximately 25 m, the ATLAS detector is the largest detector at the LHC. A schematic view of the structure is shown in Figure 3.2.
Because of its geometry, the ATLAS detector is commonly described using a cylindrical coordinate system, in which the beam pipe is defined as the z-axis. The origin of this right-handed coordinate system is the nominal IP in the centre of the detector, with the

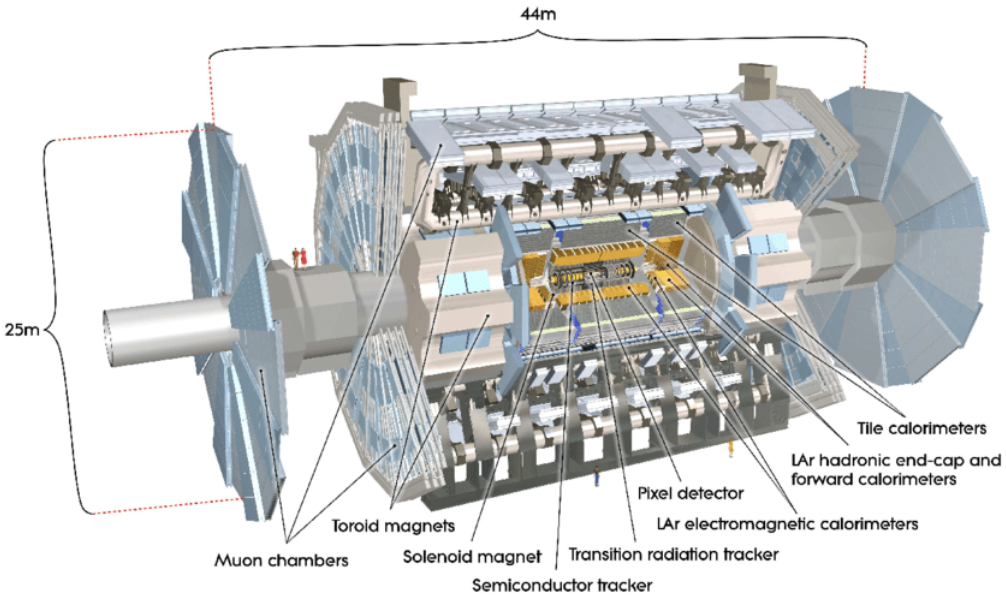

Figure 3.2: Cut-away view of the ATLAS detector [50]. The overall dimensions of the detector are shown, as well as the arrangement of its subdetectors.

x-axis pointing torwards the centre of the LHC ring and the y-axis standing vertically on the $x-y$-plane, pointing upwards. Hence, the radial coordinate r and the azimuthal angle around the z-axis, ϕ, are used as coordinates in the transverse plane ($x-y$ plane). The polar angle with respect to the beam axis, θ, is used to define the pseudorapidity $\eta = -\ln\tan\left(\frac{\theta}{2}\right)$. In the relativistic limit that particle masses are negligibly small with respect to their momenta, η approaches the true rapidity y, which is a Lorentz invariant measure. Thus, differences between two pseudorapidities are Lorentz invariant under boosts in z-direction. The angular distance between two objects in the $\eta-\phi$-plane is given by $\Delta R = \sqrt{(\Delta\phi)^2 + (\Delta\eta)^2}$. The transverse momentum of a particle is calculated by projecting the momentum of a particle to the transverse plane: $p_{\mathrm{T}} = \sqrt{p_x^2 + p_y^2}$.
In order to study the properties of particles generated in the proton-proton collisions, the ATLAS detector consists of several detector parts, all arranged in layers around the collision point. Each *sub-detector* is designed to fulfill specific tasks in measuring the properties of each type of particles, as individual particles leave distinct signatures in the different detector components. The sub-detectors are described in detail in the following.

3.2.1 The Inner Detector and tracking system

The innermost part of the ATLAS detector is the Inner Detector (ID) [58, 59], which itself is surrounded by a superconducting solenoid magnet [60]. The magnet field of the solenoid is 2 T. The ID is measuring the trajectories of charged particles and has a coverage of $|\eta| < 2.5$. The tasks of the ID are pattern recognition, momentum and vertex measurements, and electron identification. The momentum of charged particles is determined from the bending of their trajectories due to the applied magnetic field, with particles having a smaller momentum undergoing a stronger bending than particles with higher momentum. The general tracking resolution is $\sigma_{p_{\mathrm{T}}}/p_{\mathrm{T}} = 0.05\% \oplus 1\%$. The ID consists of three independent but complementary parts: The pixel detector [61, 62], the Silicon Microstrip Tracker (SCT) [63] and the Transition Radiation Tracker (TRT). The schematic layout in Figure 3.3 shows the arrangement.
The system of the ID closest to the IP is the pixel detector, which is arranged in three layers cocentrically around the IP in the *barrel* region and in two *end-caps*, each consisting of three disk layers perpendicular to the beam axis. There are 1744 silicon pixel sensors build in the pixel detector with 47232 pixels on each sensor. These pixel sensors measured the ionization energy deposited by charged particles from the proton-proton collisions. The pixel detector has approximately 80.4 million readout channels. The nominal pixel size is $50 \times 400\,\mu\mathrm{m}^2$, which is predefined by electronics design limitations. All pixel layers are segmented in $R-\phi$ and z, thereby the intrinsic resolution in the barrel region is 10 µm in $R-\phi$ and 115 µm in z, and for the end-cap region it is 10 µm in $R-\phi$ and 115 µm in R. An additional layer, the Insertable B-Layer (IBL) [64, 65] was inserted as the innermost layer of the ID before Run 2 of the LHC. It consists of 14 staves which hold 20 pixel sensor modules each.
The IBL has approximately 12.4 million readout channels. The size of the silicon pixel sensors is reduced to $50 \times 250\,\mu\mathrm{m}^2$ compared to the pixel detector. Hence, it provides

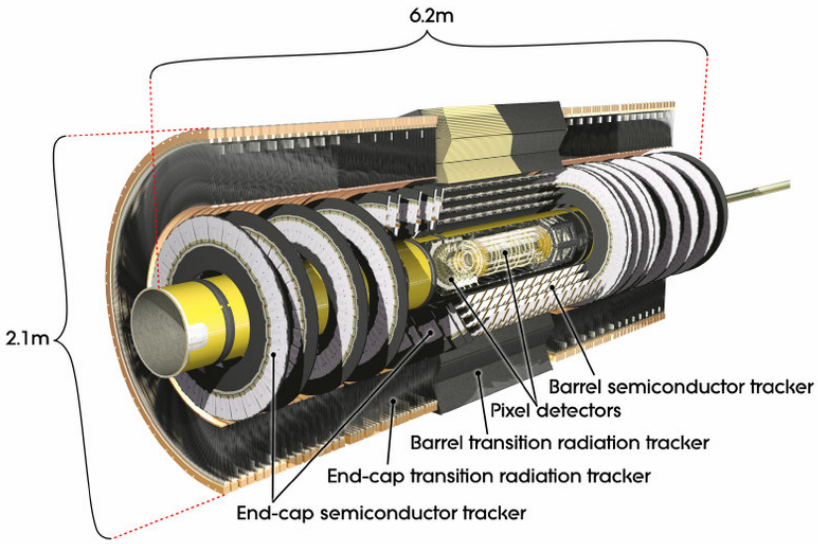

Figure 3.3: Illustration of the layout of the ID [50]. The cut-away view shows the overall dimensions, as well as all sub-systems in a cut-away view.

an additional high-precision measurement per track (*hit*), which improves the impact parameter measurement and also primary and secondary vertex reconstruction. These improvements directly translate into the performance of the ATLAS flavour-tagging algorithms. A detailed description of flavour-tagging in ATLAS is given in chapter 4.5.2. The SCT is placed around the pixel detector. It consists of eight strip layers, which are crossed by each track, ordered in four cylindrical layers around the barrel. Additionally, the two end-caps contain nine disk layers each. A total of 15912 sensors are built into the SCT, with each sensor comprising 768 active silicon strips, corresponding to approximately 6.3 million readout channels. The SCT uses stereo strips, which are offset by 40 mrad. In the barrel region, one set of strip modules per layer is parallel to the beam direction. In contrast, in the end-cap regions, one set is arranged radially to the beam pipe. Similar to the pixel detector, all SCT layers are segmented in $R-\phi$ and z. The intrinsic resolution in $R-\phi$ is 17 µm for both, barrel and end-cap region. The resolution in z is 580 µm in the barrel region, and for the end-cap discs it is 580 µm in R. This layout covers the whole fiducial coverage of the ID, yielding in at least four additional hits per track.
Surrounding the SCT for $|\eta| < 2.0$ is the TRT, which consists of 4 mm diameter straw tubes. These straws are either filled with a xenon-based gas mixture, or in case of straws belonging to modules with large gas leaks in Run 1, are filled with an Argon based gas mixture [66]. In general, the TRT operates as a drift chamber, with particles depositing energy in the active gas. In the barrel region, 52544 straws are aligned parallel to the z-direction, whereas in the end-cap region two sections with 122880 strays each, are aligned perpendicular to the beam axis, pointing outwards in the radial direction. The barrel region of the TRT consists of 73 layers of straw tubes, which are arranged in three clindrical rings, while both end-cap sections are composed of two sets of identical but independent wheels. The 350848 readout channels of the TRT also allow for a drift-time measurement

in each channel. The TRT can only provide $R-\phi$ information with an intrinsic resolution of 130 µm per straw. Although the TRT has lower precision compared to the silicon sensors in the pixel detector and SCT, its measurements enable continuous tracking and primary vertex reconstruction, with each charged track causing an average of 36 hits[3], significantly contributing to the momentum measurement due to this large number of hits compared to the pixel detector and SCT and the longer measured track lengths due to the straw tube hits at the outer radius. Further, the detection of transition-radiation photons in the gas mixtures of the straw tubes enhances the electron identification complementary to that of the electromagnetic calorimeter over a wide range of energies (see Chapter 3.2.2). Other than the SCT and pixel detector, which are cooled down to approximately -5 to $-10\,^{\circ}\mathrm{C}$ in order to maintain an adequate performance after radiation damage, the TRT is operated at room temperature.
In Figure 3.4, the radial position R and the $|z|$ of all sub-systems of the ID is shown.

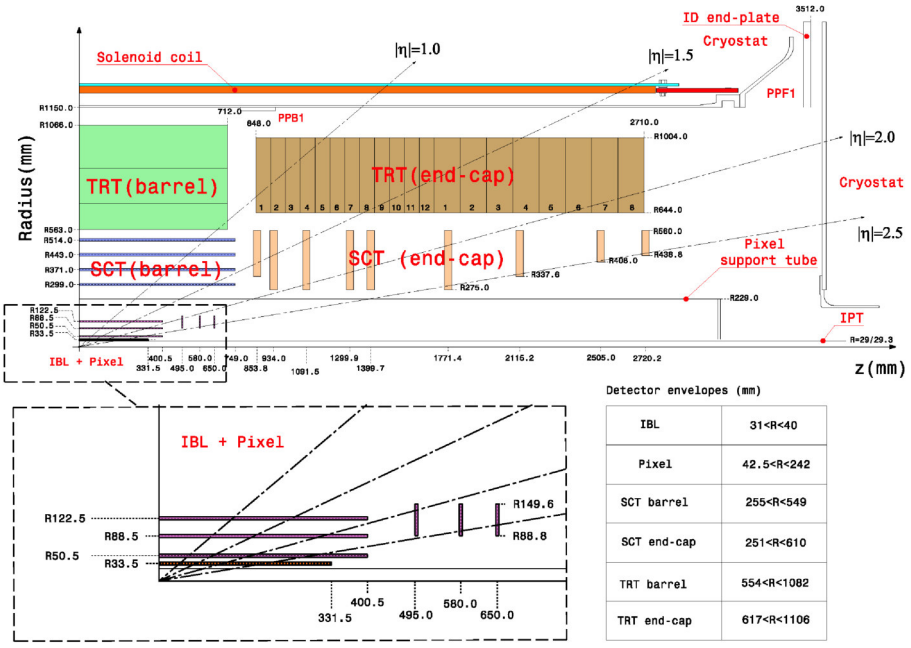

IBL	31<R<40
Pixel	42.5<R<242
SCT barrel	255<R<549
SCT end-cap	251<R<610
TRT barrel	554<R<1082
TRT end-cap	617<R<1106

Figure 3.4: Plan view of the layout of a quarter of the ATLAS inner tracking detector with the IBL layer [65].

Overall, combining the precision tracking measurements of the pixel detector and SCT at small radii from the IP with the measurements by the TRT at a larger radius yields in a very robust pattern recognition and high precision in both, the $R-\phi$ direction and z-direction. The tracking measurements from the inner detector system are corresponding to the precision measurements of the electromagnetic calorimeter, which is described in the next Section about the ATLAS calorimeter system.

[3]For charged tracks with $p_{\mathrm{T}} > 0.5\,\mathrm{GeV}$ and $|\eta| < 2.0$ at least 36 straw tubes are traversed, while in the barrel-end-cap transition region ($0.8 < |\eta| < 1.0$), at least 22 straws are crossed.

3.2.2 The calorimeters

The ATLAS calorimeter system [67] is composed of a liquid-argon (LAr) electromagnetic (EM) calorimeter and a hadronic calorimeter, consisting of a LAr hadronic end-cap calorimeter (HEC), a LAr Forward Calorimeter (FCal) and a scintillator tile calorimeter [68–72]. Figure 3.5 gives an overview over the arrangement of these four components.

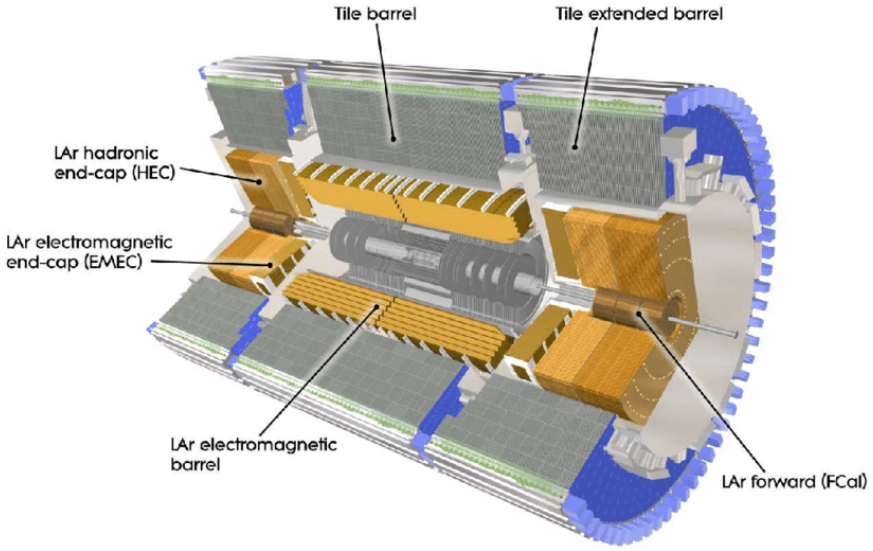

Figure 3.5: Illustration of the layout of the ATLAS calorimeter system [50]. The cut-away view shows the EM calorimeter and hadronic calorimeter sub-systems in a cut-away view.

Each calorimeter is a sampling detector, i.e. they consist of alternating layers of dense passive material, which induce particle interactions (*particle showers*), and active material, which detect ionization particles or photons, produced by the shower particles. An important aspect of the calorimeter design is to contain these electromagnetic and hadronic showers inside the calorimeter, in order to limit the *punch-through*[4] into the muon system. Hence, in the EM calorimeter the total thickness is at least 22 radiation lengths, X_0, and 24 X_0 in the barrel region and in the end-caps, respectively. Both, the EM calorimeter and the hadronic calorimeter, cover the range $|\eta| < 4.9$ around the beam axis. The pseudorapidity ranges of each component are listed in detail in Table 3.1.

The geometry of both calorimeter systems also provide a full azimuthal symmetry.
The EM calorimeter is the innermost calorimeter. It is a lead-LAr detector, with lead as passive material and LAr as the active layer material. The thickness of the lead absorber plates is optimized with respect to the energy resolution, which is $\sigma_E/E = 10\%/\sqrt{E} \oplus 0.7\%$. The EM calorimeter is divided into a barrel part, covering $|\eta| < 1.475$, and two end-cap

[4] Energy depositions going from the hadronic calorimeter into the Muon spectrometer (MS) are called punch-through contributions.

Table 3.1: Number of layers and the $|\eta|$ coverage of each calorimeter sub-system [50].

	Barrel		**End-cap**	
	Layers	Coverage	Layers	Coverage
EM calorimeter				
Presampler	1	$\|\eta\| < 1.52$	1	$1.5 < \|\eta\| < 1.8$
Calorimeter	3	$\|\eta\| < 1.35$	2	$1.375 < \|\eta\| < 1.5$
	2	$1.35 < \|\eta\| < 1.475$	3	$1.5 < \|\eta\| < 2.5$
			2	$2.5 < \|\eta\| < 3.2$
Hadronic calorimeter				
LAr hadronic end-cap	-	-	4	$1.5 < \|\eta\| < 3.2$
LAr forward calorimeter	-	-	3	$3.1 < \|\eta\| < 4.9$
	Barrel		**Extended barrel**	
Hadronic tile calorimeter	3	$\|\eta\| < 1.0$	3	$0.8 < \|\eta\| < 1.7$

regions, covering $1.375 < |\eta| < 3.2$, with the barrel calorimeter consisting of two identical half-barrels, while the end-cap calorimeter is divided into an outer wheel ($1.375 < |\eta| < 2.5$) and an inner wheel ($2.5 < |\eta| < 3.2$). Over the pseudorapidity region matched to the ID and aimed for precision measurements ($|\eta| < 2.5$), the EM calorimeter is segmented in three sections in depth, and its fine granularity benefits the measurements of electrons and photons. For this, each layer in the range of $|\eta| < 1.4$ is segmented into $\Delta\eta \times \Delta\phi$ regions of size 0.003×0.1, 0.025×0.025 and 0.05×0.025, respectively. Furthermore, in the region $|\eta| < 1.8$, the EM calorimeter is complemented by a presampler detector, which provides information about the energy loss of particles in front of the EM calorimeter. The presampling detector consists of one active LAr layer.
The tile calorimeter is the first part of the hadronic calorimeter and is located directly outside the EM calorimeter envelope. It consists of one barrel and two extended barrels, which cover the regions $|\eta| < 1.0$ and $0.8 < |\eta| < 1.7$, respectively. Each barrel consists of 64 modules, made of scintillating tiles as the active material and steel as absorbing medium. There are 5760 readout channels in the barrel and 4092 readout channels on each side of the extended barrels, all collecting the scintillation light using wavelength shifting fibres into two separate photomultiplier tubes.
The LAr HEC is situated directly behind the end-cap EM calorimeter and provides an extension to larger pseudorapidities ($1.5 < |\eta| < 3.2$). It is composed of two independent wheels per end-cap, each constructed from 32 identical wedge-shaped modules. Each wheel is segmented into two layers in depth, resulting in a total of four layers for each end-cap. Copper plates are used as the absorbing parts of the detector. The gaps between these plates are filled with liquid argon as active material.
Finally, the LAr FCal is situated between the beam pipe and the HEC. It provides both, electromagnetic and hadronic energy measurements. Hereby, it provides coverage over

$3.1 < |\eta| < 4.9$. It consists of three layers in each end-cap, with each layer featuring a metal matrix with longitudinal channels consisting of concentric rods and tubes, which are parallel to the beam axis. The first layer is optimized for electromagnetic measurements, while the other two are optimized predominantly for hadronic measurements. Therefore, the first layer uses copper as absorber material, the other two tungsten. LAr is used as active medium in the gaps between each rod and tube in all layers.
The resolution of the hadronic calorimeter is $\sigma_E/E = 50\%/\sqrt{E} \oplus 3\%$ in the barrel and end-cap parts, and $\sigma_E/E = 100/\sqrt{E} \oplus 10\%$ in the forward region. The thickness of the entire calorimeter system yields an interaction length (λ) of 9.7 in the barrel region and 10λ in the end-cap region. Together with the large η-coverage, this thickness also provides a precise measurement of missing transverse momentum ($E_{\mathrm{T}}^{\mathrm{miss}}$).

3.2.3 The Muon Spectrometer

The MS [73, 74], the largest ATLAS sub-detector, surrounds the whole calorimeter. Its design facilitates the detection of charged particles that exit the barrel and end-cap calorimeters, measuring their momentum in the pseudorapidity range of $|\eta| < 2.7$. Further, it is also designed to trigger on these particles in the range of $|\eta| < 2.4$. The conceptual layout of the MS is shown in Figure 3.6. The MS consists of four chambers, two are used for precision tracking and two are used for triggering. In the barrel region, these chambers are aligned in three concentric cylindrical shells surrounding the beam axis, while in the two end-cap regions and in the transition region inbetween, they are organized in large planes (*wheels*) perpendicular to the z-axis. Monitored Drift Tubes (MDT) are used for precise measurements of the muon tracks over a range of $|\eta| < 2.7$. They consist of three to eight layers of drift tubes, which provide an average resolution of about 35 µm per chamber in z direction, with 20 measurements per track in the barrel and the end-cap region each.

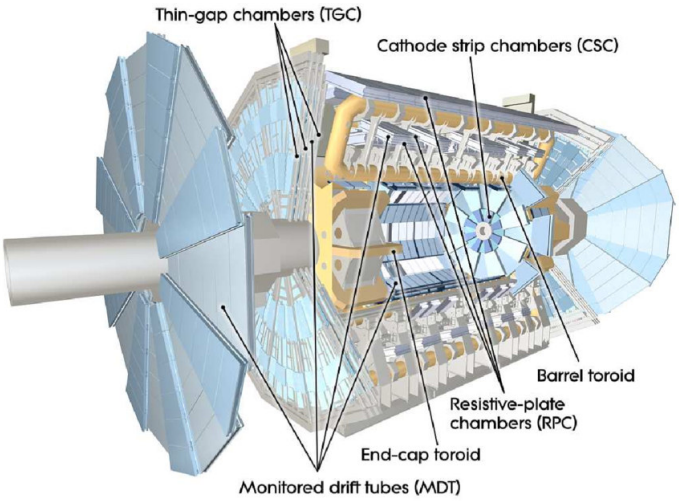

Figure 3.6: Cut-away overview of the ATLAS muon system [50].

Within the forward region of $2.0 < |\eta| < 2.7$, the Cathode strip chambers (CSC) are implemented in the innermost plane. They have a higher granularity than the MDT, thereby withstanding the larger rates and background conditions. CSC are multiwire proportional chambers with cathode planes segmented into strips in orthogonal directions, which average a resolution of 40 µm in R and 5 mm in ϕ. Additionally, 4 measurements per track ensure a timing resolution of 7 ns.
Since the measurement of charged particle tracks is based on magnetic reflection, three large superconducting air-core toroid magnets are build in the MS. A large barrel toroid [75] generates the magnetic field for the range $|\eta| < 1.4$. Two smaller end-cap toroids [76] are inserted into both ends of the barrel toroid, providing the magnetic field between $1.6 < |\eta| < 2.7$. In the transition region ($1.4 < |\eta| < 1.6$), a combination of barrel and end-cap fields is used. Each of the three toroids consists of eight coils assembled radially and symmetrically around the z-axis. This configuration offers the benefit of a magnetic field that is mostly orthogonal to the muon trajectories, while minimizing the loss of resolution due to multiple scattering. The bending power of this setup is 1.5 to 5.5 T m for $|\eta| < 1.4$, and approximately 1 to 7.5 T m in the range $1.6 < |\eta| < 2.7$. In the transition region, the bending power is lower due to the overlap of both magnets. In the barrel region, the MDT are located between and on the eight coils of the toroid. In the end-cap region, the CSC are placed in front and behind the toroids.
The precision tracking chambers of the MS are complemented by a trigger system, which consists of Resistive Plate Chambers (RPC) in the barrel region ($|\eta| < 1.05$) and Thin Gap Chambers (TGC) in the end-caps ($1.05 < |\eta| < 2.4$). Both trigger chambers provide bunch-crossing identification and well-defined p_{T} thresholds. Further, they measure the muon track coordinate perpendicular to the direction determined by the precision-tracking chambers. Both coordinates are matched such that the trigger chamber's coordinate works as second coordinate of the MDT measurement. The resolution of the RPC is 10 µm in z and 10 mm in ϕ, with a timing resolution of 1.5 ns. For the TGC, the chamber resolution is $2 - 6$ µm in R and $3 - 7$ mm in ϕ, with a timing resolution of 4 ns. The RPC provides on average 6 measurements per track, the TGC 9 measurements per track.
The CSC are mounted together with the MDT and TGC on a shielding disk, which is called *small wheel*. For LHC Run 3, this first station of the ATLAS MS end-cap system is replaced by the *New Small Wheel*. It uses Micromegas detectors as precision-tracking chambers, which are combined with small-strip TGC for the trigger [77].

3.2.4 Trigger and readout systems

With the proton-proton bunches colliding at a rate of 40 MHz at the IPs of the LHC, the size per event recorded with the ATLAS detector is around 1.5 MB, which needs to be saved for further analysis. Consequently, a minimum data rate of 40 TB s^{-1} would be necessary to store every event from the collisions. However, most readout systems of the different sub-detectors require longer than 25 ns for a full signal read-out and due to hardware limitations of the storage elements, the data rate needs to be adjusted accordingly. A two level trigger system is employed in ATLAS in order to decide on the most relevant events for the physics program to be stored: L1 [78] followed by L2 and the event filter, with

the latter two combining to form the High-Level trigger (HLT) [79]. At each trigger level, the decisions made at the previous level are refined and, as needed, additional selection criteria are applied. A schematic overview over the ATLAS Trigger and Data Acquisition (TDAQ) [50, 80, 81] system implemented in Run 2 is illustrated in Figure 3.7. The TDAQ systems, as well as the timing- and trigger-control logic are arranged into sub-systems, corresponding to the sub-detectors, which have the same logical components and building blocks.
To ensure a safe and coherent operation of the ATLAS detector, it is continuously monitored, with supervision of the detector hardware (e.g. gas systems, power-supply voltages etc.) being provided by the Detector Control System (DCS). Hereby, it archives all operational parameters (e.g. high- and low-voltage systems, temperatures, and humidity). The DCS also acts as an interface to all sub-detectors and to the technical infrastructure, in order to control the experiment. Furthermore, the DCS allows to take corrective actions (automatically or manually) in case any irregular behavior is signaled. A bi-directional communication with the Data Acquisition (DAQ) allows to synchronize the state of the detector with data-taking. Additionally, the DCS manages the communication between the sub-detectors and other independently controlled systems, such as the LHC accelerator, the CERN technical services, the ATLAS magnets, as well as the detector safety system. Like the TDAQ, the DCS is also partitioned into sub-systems, which are again corresponding to sub-detectors with similar logical components and building blocks.
The first level trigger, L1, reduces the initial event rate to less than about 75 kHz[5], which is the maximum accept rate which the detector readout systems can process. It is a hardware based trigger, concipated to identify high transverse-momentum signatures, including muons, electrons, photons, jets, and hadronically decaying τ-leptons. The trigger decisions are made based on information from a subset of detectors: muons are identified using the trigger chambers in the barrel and end-cap regions of the MS, while reduced-granularity information from all sub-systems of the calorimeter are used to detect electromagnetic clusters, jets, τ-leptons, and total missing transverse energy. The L1 trigger decision must be delivered to the front-end electronics within 2.5 µs of the associated bunch-crossing. In the front-end electronics the information is temporarily stored until the L1 trigger decides whether to accept or reject an event. Afterwards, the data are transferred off the detector to the Readout Drivers (RODs), which gather information from several front-end data streams. It digitizes the information, which is then formatted as raw data prior to being send to the DAQ system. The RODs are functional elements of the front-end systems of each detector, which are able to store and gather information from several front-end data streams. Subsequently, the DAQ receives and buffers the information from the RODs at the L1 trigger rate. Further data transmission down the trigger chain is performed and controlled over point-to-point Readout Links (ROL's). Additionally, the DAQ provides for the configuration, as well as control and monitoring of the ATLAS detector during data-taking. A central trigger processor processes the results from the L1 trigger using an implemented trigger *menu*, consisting of different combination of trigger selections. The L1 trigger also defines Regions-of-Interest (RoI's). These regions are geographical coordinates in η and ϕ, where the trigger has identified interesting objects within an event.

[5] upgradeable to 100 kHz

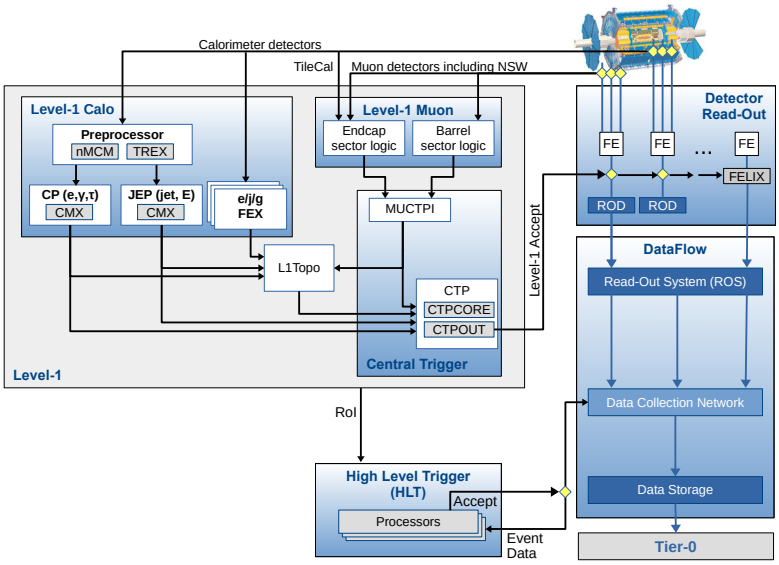

Figure 3.7: Schematic overview of the ATLAS TDAQ system in Run 2 showing both, the distinct trigger levels as well as the components of the DAQ system itself [82].

Events that pass the L1 trigger are processed by the HLT. In contrast to L1, the HLT is a software based trigger, based on algorithms running on farms of commercial computers. The event selection of the first part of the HLT, the L2 trigger is optimized for speed to reconstruct full events, whereas the event filter selection uses more complex offline analysis procedures on these reconstructed events. The selection at L2 is based on the RoI information provided by the L1 trigger and the full granularity and precision of all available detector data within the RoI's (approximately 2% of the total event data) are used. Hereby, the L2 trigger reduces the trigger rate to approximately 3.5 kHz, needing an average event processing time of about 40 ms. The final stage of the event selection is carried out by the second part of the HLT, the event filter. The L2 trigger menues are designed to reduce the event rate further to 200 Hz, which can be recorded in order to allow for subsequent offline analysis. The average event processing time of the event filter is four seconds.
Data passing the HLT are stored on CERN permanent storage and transferred to the CERN Data Center for full offline reconstruction. The CERN Data Center is the first level (Tier 0) of the Worldwide LHC Computing Grid (WLCG) [83], which is composed of four levels (Tiers) in total, which are used to process, store and analyze the data from the LHC. Tier 0 is also used to distribute the raw data and the reconstructed output to Tier 1, which consists of 13 computer centres around the world. Tier 2, typically scientific institutes, e.g. universities, receive data from Tier 1 and also produce and reconstruct simulated data. 155 Tier 2 sites exist to date. Local computer resources (e.g. local clusters in a university department) build Tier 3, although there is no formal engagement between the WLCG and these resources.

4 Object reconstruction

In order to use the recorded signals by the ATLAS detector in an analysis, several object reconstruction algorithms are needed. They translate the raw information into objects that represent either single final state particles (e.g. electrons, photons or muons) or particle *jets* (from final state quarks or gluons). For single particles *identification* criteria are placed on reconstructed objects in order to select and distinguish particular types of different physics objects. In addition, *isolation* criteria are applied to suppress background contamination and enhance the selection of physics objects which are presumed to have limited additional detector signals in their immediate vicinity. Each object needs to be calibrated in the end to account for possible differences due to detector-specific effects between the simulation and the recorded data.
The physics reconstruction of the particle objects, is based on the reconstruction of trajectories of charged particles (tracks) and calorimeter clusters. Moreover, primary and secondary vertex finding is performed to suppress additional contributions from pile-up vertices and, in Run 2, to elevate the flavor tagging of jets.
The main objects used in the charm mis-tag calibration and the single-top-quark t-channel analyses are electrons, muons, small-radius jets (with b-tagging information) and missing transverse momentum. This chapter describes the different object reconstruction processes for these objects, as well as the overlap removal applied to all objects in a reconstructed pp collision event.

4.1 Tracks

The trajectories of charged particles are reconstructed using the information of their energy deposits in the ID [84, 85]. For muons, additional information from the MS is used as described in Chapter 4.4.
The primary-track reconstruction follows an inside-out approach that begins from the Pixel detector and builds tracks while moving outwards through the ID, starting with a clusterization algorithm. There are two sorts of clusters, single-particle clusters, created by charge deposits from only one particle, and merged clusters, which are obtained from charge deposits by multiple particles. Afterwards, three space-points are used to form track seeds [85]. Subsequently, a combinatorial Kalman filter [86] is applied to three-dimensional combined clusters, so-called space-points, to build track candidates. In the process, it adds additional space-points from the remaining layers of the Pixel detector and the SCT, that are compatible with the preliminary trajectory estimated from the seeds. A stringent ambiguity-solver is applied to all track candidates, which compares each track candidate

by assigning a track score to it, in order to reject wrong combinations of uncorrelated clusters. The track score is determined using quantities that indicate the track quality. All track candidates need to have a transverse momentum greater than 400 MeV and be within the acceptance of the ID, $|\eta| < 2.5$. Moreover, a track candidate needs to fulfill selection criteria on the impact parameters[1], which ensure that they are compatible with the primary vertex. An artificial NN is employed for the identification of merged clusters [87, 88]. Finally, a fit to the estimated trajectory is performed and its χ^2 value is used in order to reduce the score of candidates with a poor fit.
Afterwards, a high-resolution fit is performed for all accepted track candidates from the ambiguity-solver. Tracks that fail the fit are discarded, while the surviving tracks are extended from the silicon detectors into the outer TRT by finding compatible sets of TRT hits. Another track fit is performed afterwards, as well as the same scoring mechanism of the ambiguity-solver. All track candidates which pass this step are added to the final track collection.
A secondary track reconstruction algorithm is used to reconstruct particle trajectories originating from decays further away from the IP, e.g. leptons from hadron decays or photon conversions, which may not have any hits in the ID. An outside-in approach is deployed which start the pattern recognition in the TRT opposed to the Pixel detector and SCT. Hereby, hits that are already assigned to track candidates in the primary track reconstruction are not taken into consideration. The identified TRT hits are followed back into the silicon detector (*backtracking*) and extended into track candidates. If the track candidates pass the ambiguity solving algorithm, they are added to the final track collection as well.
Tracking information are utilized in flavor tagging algorithms (see Chapter 4.5.2) to enhance their performance. Hereby, tracks are required to have $p_{\mathrm{T}} > 1\,\mathrm{GeV}$, $|\eta| < 2.5$ and at least seven hits in SCT and Pixel combined....

4.2 Vertex reconstruction

Given that proton bunches collide in the LHC, vertex reconstruction is essential for accurately determining the points of interaction, allowing for a precise identification of the origin of particles produced in the collisions. The knowledge of the position of the primary interaction point (*primary vertex*) is important for most analyses in order to identify the one related to the respective signal process. Further, *secondary vertices*, originating e.g. from heavy flavor hadron decays, are important input features to flavor tagging algorithms, which allow identification of b- and c-jets.
The reconstruction of primary vertices is divided into the primary vertex finding and the primary vertex fitting [89–91]. In the first step, a set of reconstructed tracks is associated to a particular primary vertex candidate, while in the second step, the actual position of this candidate is estimated using the adaptive vertex fitting algorithm [92]. Afterwards, tracks incompatible with the vertex candidate are removed. The remaining tracks can be reused

[1] The impact parameter is the distance of the closest approach of a charged particle track to the IP. It is described with a transverse (d_0) and a longitudinal (z_0) component.

by other vertex candidates and the fit procedure is repeated until no unassociated tracks are left or no further vertex candidate can be found. In the end, all candidates with at least two associated tracks are retained as vertex candidates. The primary vertex is determined as the one with the highest sum of squared transverse momenta $\left(\sum p_{\mathrm{T}}^2\right)$ of the associated tracks. This reflects the expectation that the hard scattering interactions produce particles with higher energies compared to those originating from pile-up interactions.
The secondary vertex finder (SVF), `SV1`, is used to reconstruct secondary vertices [93]. This algorithm also uses two stages: In the first, all two-track vertices are reconstructed and background tracks (e.g. tracks from hadronic interactions with the detector material) are filtered out. In the second stage, all two-track vertices which are close in space are merged together to form the secondary vertex. Outlier tracks are removed iteratively during this procedure.
Variables of different properties of the secondary vertex can be constructed, which are utilized as input variables to the flavor tagging algorithms. Two exemplary distributions are shown in Figure 4.1, as they illustrate differences for light and heavy flavor quarks.

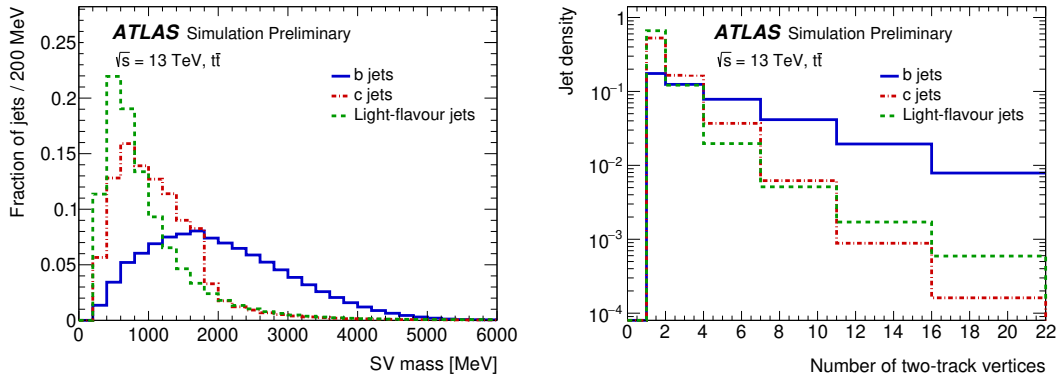

(a) (b)

Figure 4.1: Secondary vertex property distributions for (a) the secondary vertex mass and (b) the number of two-track vertices in an event. The distributions are shown for b-jets, c-jets and light-flavor jets. All distributions are normalized to one, and the over- and underflow bins are included [93].

4.3 Electrons

Electrons ($e^{\pm}$) are reconstructed in the range of $|\eta|_{\mathrm{cluster}} < 2.47$ with information from the ID and the EM calorimeter [94, 95]. This $|\eta|_{\mathrm{cluster}}$ range lies within the ID acceptance and covers the highly segmented area of the EM calorimeter. In all analyses in this thesis, electrons need to have a $p_{\mathrm{T}} > 27\,\mathrm{GeV}$. This requirement ensures that selected electron candidates are above the transitional region of the trigger turn-on curve[2], where the

[2]The analyses presented in this thesis are based on events selected using such single-lepton triggers.

trigger efficiency is not yet stable [96]. Further, electron candidates in the transition region between the barrel and end-cap calorimeter ($1.37 < |\eta|_{\text{cluster}} < 1.52$) are excluded.
In the first step of the reconstruction chain, the energy deposits in cells of both, the EM and hadronic calorimeter, are combined in order to build variable-sized topological clusters, so called *EM topo-clusters* [97]. One or more track candidates, either from the standard track reconstruction algorithm described in Chapter 4.1 or build by an alternative approach which accounts for energy losses due to bremsstrahlung [95], are matched to the EM topo-clusters [98]. All matched track candidates are fitted again to improve their accuracy. In case there are multiple tracks matching the cluster, a primary track of the electron candidate is chosen based on the measured momentum. Then, EM superclusters are assembled from all clusters matched to track candidates [95]. Hereby, nearby EM topo-clusters can be merged to account for bremsstrahlung effects [94]. Lastly, the electron objects are finalized after initial position corrections and energy calibrations [99] are performed to the superclusters and the track matching is repeated.
The calibration scheme for the energy response of electrons is done in multiple steps [94] [99]. In the first step, the energy resolution is optimized as a function of the η of the electron using a multivariate algorithm. The relative energy scale correction between different EM calorimeter layers is adjusted using muon energy deposits in the calorimeter and electron showers. While the resolution correction is applied to simulation, the corresponding energy scale correction is applied to data. Afterwards, the adjustment of the absolute energy scale is performed using $Z \to ee$ decays, a validation measurement uses radiative Z-boson decays and $J/\psi \to e^+e^-$ decays. In this step, reconstruction efficiencies are measured as a function of the electron η and E_{T} as well. With these, scale factors (SFs) to correct for differences between data and simulation are estimated that are applied to simulation.

Identification and isolation criteria are placed on the electron candidates between prompt electrons from the hard scattering process and background objects. Three types of discriminating variables are combined in a likelihood classifier: variables using properties of the track candidate, parameters of the shower in the EM calorimeter or the matching between the track candidate, and the superclusters [94]. Depending on the likelihood value, three categories of identification requirements, so called working points (WPs), are defined: *Loose*, *Medium*, and *Tight*. The likelihood threshold value for each WP depends on $|\eta|$ and the transverse energy E_{T} of the electron candidate. The three WPs invoke increasingly stricter selections, leading to greater background suppression but at the expense of a reduced acceptance of electron candidates. Electrons in all analyses in this thesis correspond to electron objects selected with the *Tight* WP.
Furthermore, two different isolation selection criteria, are applied. The electron calorimeter isolation, $E_{\text{T}}^{\text{cone}YY}$, is build by adding up the transverse energy of nearby topo-clusters, excluding the energy of the electron candidate itself and removing contributions from pileup events. Here, YY refers to the size of the employed cone in this procedure, $\Delta R = XX/100$, around the electron cluster center, which is set to 20 [95]. The second isolation variable is the track isolation, $p_{\text{T}}^{\text{cone}XX}$. It is determined as the scalar sum of the transverse momenta of all tracks[3] inside a variable cone of $\Delta R = \min\left(10\,\text{GeV}/p_{\text{T}}, \Delta R_{\text{max}}\right)$, around the electron

[3] Tracks need to fulfil minimum quality requirements, detailed in Ref. [94].

candidate track, again excluding said candidate track, with ΔR_{max} set to 0.2. There are several isolation selection criteria based on thresholds of both isolation variables. Electrons used in all analyses presented in this thesis use the *FixedCutTight* WP, where the isolation criteria are $E_{\text{T}}^{\text{cone20}} < 0.06$ and $p_{\text{T}}^{\text{cone}XX} < 0.06$.
Analogously to the reconstruction part, calibration analyses for the identification and isolation are performed [94]. For each operating point the identification and isolation efficiencies are extracted in data and compared to the predicitions from simulation. SFs are calculated as a function of η and E_{T}, which are applied to simulation.

4.4 Muons

Muons are reconstructed based on their characteristic as minimum-ionizing particles. Therefore, muon reconstruction is reliant primarily on information from the ID and MS [100, 101]. Further, information from the calorimeters are used in order to account for larger energy loss of muon candidates in the calorimeters. Muons in all analyses in this thesis are required to have a $p_{\text{T}} > 27\,\text{GeV}$.[4]
There are several *types* of muons, based on the complete information provided by the different sub-detectors. The muons used in all analyses in this thesis are *combined (CB) muons*, for that a combined track is constructed from tracks reconstructed independently in the ID and MS for the muon candidates. The majority of these muons are reconstructed using an outside-in approach, in which muon tracks reconstructed in the MS are extrapolated and matched to an ID track. Additionally, there is an inside-out pattern recognition used as a complementary approach. For the reconstruction of tracks in the MS, Short straight-line track segments are build from hits in one MS station. Then, multiple segments from different stations are combined into preliminary track candidates. Three dimensional track candidates are constructed by adding coordinate information from precise measurements from the MS trigger chambers. Preliminary muon candidates are obtained by performing a χ^2 fit of the trajectory through the magnetic field, considering the potential interactions occurring in the detector material and the possible misalignments among the different MS chambers. Subsequently, outlier hits are removed from this preliminary track and hits along the fitted trajectory are added, before the track fit is performed again. Next, overlapping tracks are removed and then, the final set of tracks is fitted once again, using calorimeter information about the energy loss in the calorimeter.
Analogous to electrons, identification and isolation criteria are applied to the muon candidates. The identification requirements are based on the number of hits in the different ID and MS subdetectors, as well as on the track fit properties and on variables comparing the compatibility of both individual track reconstruction procedures [100]. Several working points for each muon type are defined, each designed to meet the demands of different physics analysis in terms of prompt-muon identification efficiency, the resolution of the candidates momentum, and the rejection of background due to non-prompt muons. Since non-prompt muons are reconstructed as well, a differentiation is made between these

[4] Similar to electrons, this criterion ensures that selected muon candidates are above the transitional region of the trigger turn-on curve [102].

muons originating from semileptonic in-flight decays of light hadrons and from the decays of heavy flavor hadrons. The identification working points aim at a high rejection rate of muons from light hadrons, as muons from bottom or charm hadron decays produce good-quality tracks which can be distinguished from prompt-muon candidates. More information on these muons from heavy flavor hadron decays, called *soft muons*, are given in the Chapters 4.5.1. Similar to electrons, three identified working points are defined, *Loose*, *Medium* and *Tight*, with all analyses in this thesis using muons passing the Medium working point [100].
Isolation criteria help to distinguish prompt from muons from hadronic decays. Again, similar to electrons, track-based isolation requirements and calorimeter-based isolation requirements are utilized. In either a fixed cone of $\Delta R = 0.2$ around the candidate track or a variable size cone with $\Delta R = \min(10\,\text{GeV}/p_{\text{T}}, 0.3)$, the scalar sum of the transverse momenta of the ID tracks around the muon candidate, $p_{\text{T}}^{\text{cone20}}$ ($p_{\text{T}}^{\text{cone30}}$), is measured. For the sum of the transverse energy of topological cell cluster in the calorimeters, $E_{\text{T}}^{\text{topocone20}}$, a fixed cone of $\Delta R = 0.2$ is used.
The calibration of the muon reconstruction, identification and isolation efficiencies are done using $Z \to \mu^+\mu^-$ and $J/\psi \to \mu^+\mu^-$ events [100]. The reconstruction and identification efficiencies are calculated in data and compared to predictions of the simulation. SFs are derived as a function of η and p_{T}, which are applied to simulation, in order to correct for any mismodelling. Similarly, the isolation calibration is done, but here, SFs are obtained also as a function of the angular distance between the muon and the clostest reconstructed jet in the event, $\Delta R(\mu, j)$. All muons used in analyses in this thesis use the particle-flow (PFlow) algorithm based isolation working point, *PflowTight_FixedRad* [94]. This algorithm allows for removal of redundant measured hadronic activity by both, the calorimeters and the ID, because of the combination of track-based and calorimeter-based isolation criteria.

4.5 Jets

In pp collisions at the LHC, quarks and gluons are the predominantly produced particles. Except for the top-quark, all particles carrying color charge undergo fragmentation and hadronization to form energetic hadrons due to color confinement. Therefore, quarks and gluons cannot be observed - and reconstructed - as isolated particles, but rather collimated streams of hadrons, so called *jets* [103]. There are various algorithms to reconstruct jets that need to fulfill certain criteria such as infrared and colinear (IRC) safety, i.e. low-energy and collinear radiation must not change the resulting jet. In ATLAS, the anti-k_t algorithm [104] is most commonly used to reconstruct jets using a four-momentum recombination scheme. It is implemented in `FastJet` [105]. Using this clustering algorithm, the reconstructed jets tend to have a circular shape. *Small-radius* (small-R) jets are reconstructed using the anti-k_t algorithm with a radius parameter, which is equivalent to the jets' maximum radius, of $R = 0.4$. All jets used in analyses in this thesis are small-R jets. The inputs to the anti-k_t algorithm are particle flow objects, resulting in so called *PFlow jets*. In the particle flow algorithm [106] tracks reconstructed from the ID and topo-cluster [97] from the calorimeter are combined. This combination takes advantage of

the superior pile-up suppression and energy resolution of the ID at low momenta, and the excellent performance of the calorimeter at high energies.
In order to correct the energy of reconstructed jets to account for various effects during the reconstruction, e.g. energy deposited outside the jet cone, a mostly simulation based calibration chain is applied [103]. In a first step, a p_{T} correction accounting for pile-up contributions is performed. Afterwards, the jet energy scale (JES) is corrected on average to the particle-level[5] energy scale using dijet events. A *global sequential calibration* is applied next, reducing the flavor (quark or gluon) dependence of the jet energy response in the calorimeters, as well as effects due to punch-through. Finally, a residual *in situ* JES calibration chain is applied to data in order to correct for differences between data and simulation resulting from limitations in modeling both, the detector materials and the relevant physics processes [107]. As the first stage, the η-intercalibration is used to derive a correction for the JES of forward jets ($0.8 < |\eta| < 4.5$) from jets in the central region ($|\eta| < 0.8$), by matching the latter to the former using the p_{T} balance method in dijet events. Subsequently, a total of three *in situ* measurements are performed in order to correct differences in the JES of jets between data and MC simulation with respect to well-measured reference objects. The results of these calibrations getting combined in the end to cover the full p_{T} range. The first two *in situ* calibrations use a photon and Z-boson, respectively, as reference object, as the uncertainties in their energy scale are small, whereas in the last measurement, a system of well-calibrated jets is used to calibrate one single high-p_{T} jet [108] [109]. All *in situ* measurements are performed sequentially, with systematic uncertainties being propagated through each step. Further, only central jets are used in these calibrations, with the η-intercalibration ensuring that the results remain applicable to forward jets as well. The uncertainty on the JES is evaluated after this calibration as a function of the jet p_{T} and η.
Another *in situ* measurement is done to derive and calibrate the jet energy resolution (JER) [107]. The dependence of the relative JER on the p_{T} is parameterized as follows:

$$\sigma\left(p_{\mathrm{T}}\right)/p_{\mathrm{T}} = \frac{N}{p_{\mathrm{T}}} \oplus \frac{S}{\sqrt{p_{\mathrm{T}}}} \oplus C. \tag{4.1}$$

Here, the first term denotes the noise, N, which includes the contribution of electronic noise and pile-up to the signal measured in the detector. The second term, the stochastic term, S, accounts for statistical fluctuations in the energy deposition in the detector and primarily determines the resolution for jets up to a range of several hundred GeV. The constant term, C, describes fluctuations independent of the jet p_{T}, such as energy depositions in passive detector material or the starting point of the hadronic showers. The JER is important, as it also affects the missing transverse momentum calculation. Each term is estimated for the JER calibration. For the resolution, di-jet events are used in order to measure the recoil of one jet against the other whose momentum needs to be measured precisely. For the noise term, the random cones method is used [107]. In the end, an *in situ* combination is done, by applying a fit to the di-jet balance measurements with a constraint on the noise term. Analogously to the JES calibration, the uncertainties of

[5] Particle level denotes the objects in simulation after hadronizing and showering but without a detector simulation in place.

each measurement are propagated. The uncertainty of the JER measurement is evaluated in bins of the jet p_{T} and η.
In order to suppress jets from pile-up vertices, a dedicated jet vertex tagging (JVT) algorithm is applied for jets with $|\eta| < 2.4$ [110]. The algorithm incorporates track, jet and vertex information into a two-dimensional likelihood, from which the JVT discriminant is derived. Different working points are defined, with all jets used in analyses in this thesis are required to pass the *Tight* working point (JVT>0.5). For forward jets ($2.5 < |\eta| < 4.5$), a forward jet vertex tagging (fJVT) algorithm applied [111]. Hereby, track and vertex information are exploited to identify and reject pile-up jets in the forward region by extrapolating the JVT to the forward region. All analyses using forward jets in this thesis, require these to fulfill the *Tight* working point (fJVT<0.5).

4.5.1 Characteristics of bottom and charm jets

The features and properties of reconstructed jets differ depending on the flavor of the originating parton. There is a distinction made between b-jets, c-jets and light flavor jets (initiated by $u-$, $d-$, $s-$quarks or gluons). An overview of the three different jet characteristics is illustrated in Figure 4.2 and is outlined in the following. b-jets originate from the hadronization of b-quarks. One important property of b-hadrons is their relatively long lifetime ($\mathcal{O}(1.5\,\mathrm{ps})$ [19]) compared to other hadrons. As a result, they can travel distances of several mm after production, before they decay. The distance is depending on the momentum of the b-hadron from the hard scattering process. Thus, a secondary vertex, displaced from the primary vertex, is expected for b-jets. Its tracks have large impact parameters with respect to the tracks from the primary vertex of the collision. Another characteristic, is the large mass of the b-quark ($\sim 5\,\mathrm{GeV}$), compared to that of light flavor quarks. Therefore, the b-hadrons contain around 75% of the overall jet momentum and they decay by average into five charged particles. b-quarks also decay primarily into c-quarks. Hence, a tertiary vertex can occur inside the b-jet.
The c-hadrons from the primary vertex produce c-jets, which have similar properties as b-jets. The produced c-hadron is most commonly a D-meson. As the lifetime of a D-meson is shorter than that of any b-hadron, their travel distance is also shorter [19]. Still, D-mesons travel a few mm before they decay - most often into a kaon. Analogous, as the mass of a D-meson is also smaller compared to b-hadron masses, it carries a smaller momentum fraction of the entire jet. The average number of charged particles per decay is reduced to two on average. Consequently, it is more difficult to reconstruct the secondary vertex of c-jets than for b-jets.
For both, b-jets and c-jets, semileptonic decays of the originating hadrons are another feature that can be used to determine the jet flavor. These muons lie inside the jet and are called *soft muons* - with the jets being labeled accordingly as *soft muon tagged (SMT)*-jets. They have a sizeable transverse momentum, though their momenta are smaller than the typical p_{T} of leptons from electroweak boson decays, hence the label "soft". Soft muons have to satisfy the *Tight* quality identification criterion [101], and further need to be within $\Delta R < 0.4$ of a selected jet candidate. Minimal requirements on the transverse momentum and the pseudorapidity are also applied, based on the analysis needs. To account for the

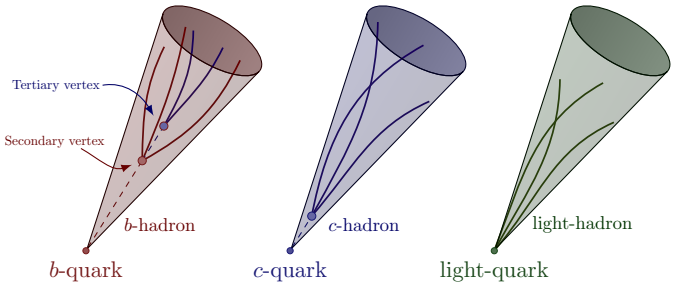

Figure 4.2: Schematic illustration of the different features between jets originated by b-quarks, c-quarks and light flavor quarks. Adapted illustration from Ref. [112]

contribution of the soft muon to the nearest jet, the jet p_{T} is re-calculated with the soft muon regarded as a part of the jet. Since the branching ratio for semileptonic decays is significantly larger for b-hadrons than for a c- or even light-flavor hadrons, the presence of a soft muon is enhanced in b-jets. Furthermore, even though these semileptonic decays are limited in general by their branching ratio, it was shown that these can improve the b-tagging algorithms in ATLAS [113], as they provide complementary information to track and vertex-based inputs, since the semileptonic decays reduce the aforementioned number of charged decay particles as well as the mass and energy of the jet overall. In this thesis, soft muons are used for the identification of c-jets (see Chapter 7.2 for details).
Light-flavor jets are not expected to exhibit a secondary vertex, as the hadronization of light-flavor quarks and gluons occurs nearly instantaneously.

4.5.2 Flavor-tagging

Dedicated algorithms, exploiting the differences and features of heavy flavor jets are used to identify and distinguish between different jet flavors. In general, charged particle tracks, primary vertex information and, naturally, reconstructed jets are the key inputs used for the identification. The procedure is called *flavor tagging* and is described in this chapter. The jet flavor tagging in ATLAS occurs in multiple stages, the first consisting of several *low-level b-taggers*, whereas the second stage includes one *high-level* tagger in Run 2 [114]. The low-level b-taggers consists of algorithms for two approaches: First, exploiting the large impact parameter values of b-jets, and secondly, reconstructing displaced vertices. In order to exploit the impact parameter information, two algorithms, `IP2D` and `IP3D` [115], are used. The `IP2D` tagger builds a discriminating variable using the signed transverse impact parameter significance, while the `IP3D` tagger incorporates both, the signed transverse and signed longitudinal impact parameter significances[6] in a two-dimensional template, leveraging the correlation between them. Three log-likelihood ratios are defined based on the estimated per-track probability ratios for each jet-flavor hypothesis. These are used as inputs to the high-level taggers.
A track-based recurrent NN (`RNNIP`) is used as a second algorithm in order to exploit the

[6]The significance is defined as the ratio of the track impact parameter to its uncertainty.

large impact parameter values. The advantage of this approach is the direct exploitation of more and arbitrary size of input variables and their sequential dependencies [116]. The outputs of this RNN are the different jet flavor probabilities, which are used as inputs to the high-level tagger and further, also combined into a discriminant.
In order to reconstruct secondary vertices, the SVF, `SV1`, described in Chapter 4.2 is used. The fourth low-level tagger is a topological multi-vertex finding algorithm, `JetFitter` [117]. It is used to reconstruct the full b-hadron decay chain by exploiting the topological structure of the weak b- and c-hadron decays inside the jet. Eight discriminating variables, including the track multiplicity at the `JetFitter` displaced vertices, the invariant mass of tracks associated with these vertices, their energy fraction and their average three-dimensional decay length significance, are used as inputs to the high-level taggers [114]. A set of nine additional variables [115], which include information on the number, the invariant mass and the energy of the tracks associated with the secondary vertex as well as their rapidity, computed with respect to the jet axis and the vector defined between the primary and secondary vertices, are used as inputs to the high-level algorithms as well [114].
The high-level tagger is the `DL1r` algorithm, a feed-forward NN, using the outputs of the four low-level taggers described above [114]. The DL1r tagger exploits the correlation between the different input features, which depend on the jet flavor and kinematic properties. Hence, the p_{T} and $|\eta|$ distributions of each jet are included in the training as well, in order to exploit also their correlations with the other input variables [114]. A resampling process is done for all jets in order to avoid a bias in the training due the usage of the kinematic distributions. In the training, a hybrid samples consisting of 70% $t\bar{t}$ events and 30% $Z' \to q\bar{q}$ events is used. The output of the `DL1r` tagger is a three-dimensional vector, including the probability for a jet to be a b-jet, a c-jet or a light-flavor jet. The final output discriminant is constructed using these probabilities and is defined as [114]:

$$D_{\mathrm{DL1r}} = \ln\left(\frac{p_b}{f_c \cdot p_c + (1 - f_c) \cdot p_{\mathrm{light}}}\right). \tag{4.2}$$

In this equation, p_b, p_c and p_{light} denote the respective probabilities, with f_c being the effective c-jet fraction in the background hypothesis. This approach allows to choose f_c after the training, in order to optimise the performance of the algorithm at the physics analysis level [114]. The value is chosen to be $f_c = 0.0018$. Similar, a discriminant can be defined for c-tagging:

$$D_{\mathrm{DL1r}} = \ln\left(\frac{p_c}{f_b \cdot p_b + (1 - f_b) \cdot p_{\mathrm{light}}}\right) \tag{4.3}$$

Here, the fraction of b-jets, f_b, is chosen to be 0.2 in order to maximize the b-jet rejection for given c-tagging efficiencies of 20% and 30%. In Figure 4.3, the light-flavor and charm rejection rates are shown as a function of the b-jet efficiency. It is shown that this algorithm is indeed improving the flavor tagging by incorporating the output information of the low-level tagger. Additionally, the improved rejection rates compared to the previously utilized `MV2c10` algorithm (see Chapter 7.2) is illustrated. There are four single-cut operating points (WPs) for the `DL1r` discriminant, each being based on a specific b-jet tagging efficiency. The efficiency is measured for the baseline $t\bar{t}$ sample. Further, the

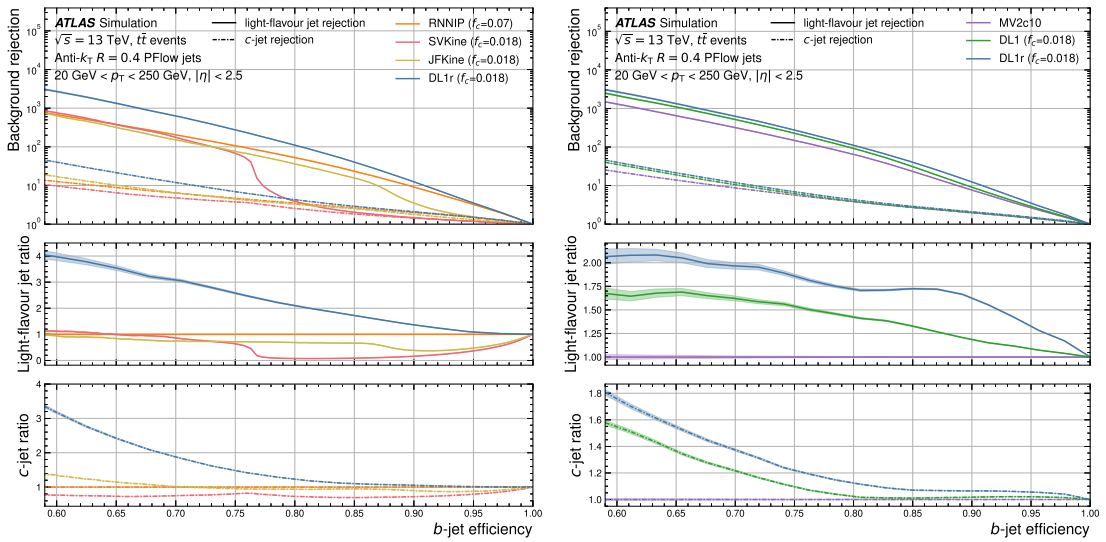

(a) (b)

Figure 4.3: The light-flavor jet and c-jet rejection factors as a function of the b-tagging efficiency, ϵ_b, (a) for `DL1r` as well as the low-level b-taggers `RNNIP`, `SVKine` and `JFKine`[7], and (b) for `DL1r` in comparison to previous flavor-tagging algorithms `MV2c10` [118], `DL1`. The lower two panels in each plot show the ratio of the algorithms. The statistical uncertainties are indicated as colored bands [114].

discriminating distribution is divided into five *pseudo-continuous* bins, delimited by the single-cut values for the four WPs (85%, 77%, 70% and 60%) and limited by the trivial 100% and 0% b-tagging efficiency cuts.

Both types of usage of the discriminant need to be calibrated. A detailed overview on the calibration strategy for each usage type is given in Chapter 7.1. For b-jet identification, dileptonic $t\bar{t}$ events are used, in which the two b-jets from the top-quark decays are targeted [118]. The b-jet efficiency on c-jets is calibrated using semileptonic $t\bar{t}$ events, aiming for the jets from the hadronically decaying W-boson [119]. Further, the mis-tag efficiency calibration for light-flavor jets is performed using $t\bar{t}$ events as well [120].
Another method to calibrate the `DL1r` tagger in terms of the c-jet mistagging efficiency is presented in this thesis in Chapter 7.2. Flavor tagging also plays a crucial part for the top-quark involved analyses presented in this thesis, and more details about the specific use of flavor tagging in the context of each analysis are provided in Chapters 7, 8 and 9.

4.6 Overlap removal

As the reconstruction of each physics object is done independently of one another in general, it might happen that objects are reconstructed in closeby detector areas and an

[7] `SVKine` and `JFKine` are trained NNs of the low-level tagger in order to be able to compare their results.

algorithm is used to resolve overlaps by removing all but one of the objects.
In a first step, electrons that share an ID track with a muon are removed. Next, jets within $\Delta R = 0.2$ of an electron are removed to avoid double-counting of electron energy deposits as jets. Afterwards, electrons within $\Delta R = 0.4$ of a remaining jet are also removed, before muons within $\Delta R = 0.4$ of a remaining jet are discarded. These cuts are done in order to remove any overlap between a jet and an electron and to suppress non-prompt leptons.
Usually, an overlap removal is applied to all reconstructed objects, but in order to enhance sensitivity or exploit event characteristics some cuts are omitted or additional cuts applied. In order to be able to use soft muons, the last cut, removing muons within $\Delta R = 0.4$ of a remaining jet, is not applied.

4.7 Missing transverse momentum

Undetected particles by the ATLAS detector, e.g. neutrinos, which do not interact with the detector material due to their small cross sections, produced in the pp collisions carry away some transverse momentum. The transverse momentum of the protons before the pp collisions is zero. In order to calculate the amount of missing transverse momentum, $p_{\mathrm{T}}^{\mathrm{miss}}$, after the collision, the two-dimensional momentum vector, $\vec{p_{\mathrm{T}}} = \left(p_x, p_y\right)$, which is defined transverse to the proton beam direction, is constructed [121]. The principle of momentum conservation allows the construction of $\vec{p}_{\mathrm{T}}^{\mathrm{miss}}$ from all reconstructed objects and tracks. Therefore, the missing transverse momentum vector $\vec{p}_{\mathrm{T}}^{\mathrm{miss}}$ is defined as:

$$\vec{p}_{\mathrm{T}}^{\mathrm{miss}} = -\left(\underbrace{\sum_{e} \vec{p_{\mathrm{T}}} + \sum_{\mu} \vec{p_{\mathrm{T}}} + \sum_{\mathrm{jets}} \vec{p_{\mathrm{T}}}}_{\text{hard term}} + \underbrace{\sum_{\text{unused tracks}} \vec{p_{\mathrm{T}}}}_{\text{soft term}} \right) \tag{4.4}$$

To be consistent in a given analysis, only the used objects contribute in the calculation of the $\vec{p}_{\mathrm{T}}^{\mathrm{miss}}$, hence photons and τ-leptons are not considered for this calculation in any analysis presented in this thesis, as no reconstructed photons and τ-leptons are used. The hard term in equation 4.4 includes the momenta of all fully reconstructed and calibrated objects, whereas the soft term incorporates any charged particle tracks which are not associated with any object, but only with the primary vertex. In order to avoid possible double counting an ambiguity resolution procedure is applied in the construction of $\vec{p}_{\mathrm{T}}^{\mathrm{miss}}$, making use of the different reconstruction features of each object, as well as overlap removal strategies [121].
The missing transverse momentum $p_{\mathrm{T}}^{\mathrm{miss}}$ is the magnitude $|\vec{p}_{\mathrm{T}}^{\mathrm{miss}}|$ of the missing transverse momentum vector, also referred to as $E_{\mathrm{T}}^{\mathrm{miss}}$. Another useful variable is the direction in the transverse plane of the $p_{\mathrm{T}}^{\mathrm{miss}}$, given by the azimuthal angle, $\phi^{\mathrm{miss}} = \tan^{-1}\left(p_x^{\mathrm{miss}}/p_y^{\mathrm{miss}}\right)$.
A non-zero value of $E_{\mathrm{T}}^{\mathrm{miss}}$ does not just indicate the production of SM neutrinos, but also potentially the occurrence of stable BSM particles. The $E_{\mathrm{T}}^{\mathrm{miss}}$ calculation is validated comparing simulated events with data, using events where $E_{\mathrm{T}}^{\mathrm{miss}} = 0$ is expected and events with expected $E_{\mathrm{T}}^{\mathrm{miss}} > 0$ due to neutrinos [121].

5 Data and Monte Carlo simulations

The measurements presented in this thesis utilize data recorded with the ATLAS detector and MC simulations for each contributing SM process. The MC samples are officially produced within the ATLAS software framework. Both, the W+c-jet charm mis-tag calibration analysis and the CKM measurements, use mostly the same samples. Therefore, if not stated otherwise, samples for a process are used in both types of analyses. A detailed description of the data studied for this thesis as well as the used MC simulations are given in the following.

5.1 Data

All analyses presented in this thesis use pp collision data recorded with the ATLAS detector in the years 2015 to 2018 at a centre-of-mass energy of $\sqrt{s} = 13\,\text{TeV}$. The data is subject to a set of data-quality requirements [122], ensuring that only events collected during periods of optimal detector performance, with all components functioning as expected, are included in the analyses. The full Run 2 data set corresponds to an integrated luminosity of $140\,\text{fb}^{-1}$ with a relative uncertainty of 0.83% [56]. The luminosity was measured with the LUCID2 detector [123] and complemented by ID and calorimeter information. In Table 5.1, the integrated luminosities and uncertainties per year, as well as the combined values are shown. All analyses presented in this thesis use single lepton triggers, either requiring a muon or electron to fire these.

5.2 Monte Carlo simulations

In order to analyze the data recorded with the ATLAS detector, simulations of all processes anticipated to contribute in an analysis are essential. An accurate description of reconstructed quantities in these simulations is crucial to enable precise measurements. The descriptions in this chapter are based mainly on Reference [1].
The matrix element (ME) calculations in the simulations are based on pertubation theory calculations to first generate events of a certain process on parton level. Hereby, the process' probability, which is given by its ME, is folded with the probability of the initial state particles of that given process being present in the protons in the initial state, given by the parton distribution function (PDF). Each hard scattering event is generated using specialized event generators, which are interfaced with algorithms that model parton

Table 5.1: Summary of the integrated luminosities (after ATLAS data-quality requirements [122]) and uncertainties for each individual year of Run 2, and the combined values [56].

Data sample	2015	2016	2017	2018	combined
Integrated luminosity [fb^{-1}]	3.24	33.40	44.63	58.79	140.07
Total uncertainty [fb^{-1}]	0.04	0.30	0.50	0.64	1.17

showering and hadronization as well as the underlying event. Various event generators and algorithms are utilized to leverage their specific advantages for modeling different processes.
After the first step, all events are passed through the ATLAS detector simulation [124], which is implemented in the GEANT4 toolkit [125], to simulate the response of the detector. The nominal setup, simulates the whole detector in very high detail (*full-sim*), while in an alternative setup the faster AtlFastII (AFII) simulation exploits a parametrization of the calorimeter response (*fast-sim*). The reconstruction after the detector simulation is done using the ATLAS offline reconstruction software.
The simulation of MC samples also includes the effects of multiple pp interactions per bunch crossing, as well as contributions from nearby bunch crossings that occur before or after the primary interaction (in- and out-of-time*pileup*, respectively). For this purpose, *minimum-bias* events, i.e. softer pp collisions with a larger cross section, are added to the hard scattering event. The minimum-bias events are simulated using the event generator PYTHIA 8.186 [126] with the tuned parameters from the A3 tune [127] and the NNPDF2.3LO PDF set [128]. The pileup effect is corrected by comparing the average number of interactions per bunch crossing, $\langle\mu\rangle$, in data and simulation, allowing for adjustments to better match the actual detector conditions. A *pileup reweighting* procedure is performed in which the $\langle\mu\rangle$ value in data is rescaled with a factor of 1.03 ± 0.04 [129].

The different settings and software setups for all simulated processes used in this thesis are described in detail in the following. The simulated processes used for the analyses presented in this thesis are largely identical, with the exception of the W+jets samples in the W+c calibration and additional single-top and $t\bar{t}$ samples for the interpretation and analysis of the CKM matrix elements. The latter samples are described specifically in Section 5.2.3. In general, for all top-quark and top-quark pair processes the parton shower and hadronization is modelled using PYTHIA 8.230 [130] with the A14 set of tuned parameters [131] and the NNPDF2.3LO set of PDFs [128]. The top-quark mass is set to $m_{\text{top}} = 172.5\,\text{GeV}$. Further, EVTGEN [132] is used to simulate the decays of heavy flavour hadrons for all samples which are not simulated using SHERPA.

5.2.1 Top-quark pair processes

Top-quark pair production ($t\bar{t}$) events are generated with NLO accuracy in the strong coupling constant α_s using POWHEG BOX v2 [133–136]. The five-flavor scheme is used and,

consequently, the NNPDF3.0NLO [137] PDF set. In the five-flavour scheme, the bottom quark is treated as a massless parton within the proton's structure, appearing in the parton distribution functions and participating in the hard scattering process. The h_{damp} parameter[1] is set to its standard value of $1.5\,m_{\text{top}}$ [138]. To estimate the uncertainty for this procedure, an alternative sample with $h_{\text{damp}} = 3\,m_{\text{top}}$ is used. Following the guidelines in Ref. [139], the renormalization and the factorization scales are set to $\sqrt{m_t^2 + p_{\text{T},t}^2}$. All $t\bar{t}$ samples are normalized to the theory cross section value of $\sigma_{t\bar{t}}^{\text{NNLO+NNLL}} = 834 \pm 33\,\text{pb}$. This cross section calculation is performed with TOP++ 2.0 [34, 140–145] at NNLO in QCD with the inclusion of NNLL soft-gluon terms. To estimate the impact of the choice of the parton shower and hadronization model, an alternative sample is generated in which PYTHIA 8.230 is exchanged with HERWIG 7.2.1 [146, 147].

5.2.2 Single-top-quark production

Three types of single-top-quark production are differentiated. The t-channel production, the s-channel production and the associated production of a top-quark and a W-boson (tW). For the simulation of t-channel events, the POWHEG BOX v2 [134–136, 139] generator at NLO in QCD is used with the corresponding NNPDF3.0NLO set of PDFs [137]. For the production, the four-flavour scheme is used. In contrast to the five-flavour scheme used for the $t\bar{t}$ production, the four-flavour scheme treats the bottom quark as a massive object that is not included in the proton's parton distribution functions but is instead produced explicitly in the hard scattering process. The renormalization and the factorization scales are set to $\sqrt{m_b^2 + p_{\text{T},b}^2}$. The decay of the top-quarks is modelled by MADSPIN [148, 149] at leading order (LO).
The s-channel process is simulated at NLO in QCD using the POWHEG BOX v2 [134–136, 150]. It uses the five-flavor scheme, and therefore the NNPDF3.0NLO [137] PDF set.
Similarly, the tW process is modelled by the POWHEG BOX v2 [134–136, 151] generator at NLO in QCD. It also uses the five-flavour scheme and the NNPDF3.0NLO set of PDFs [137]. In order to avoid interfering and overlapping events with $t\bar{t}$ production, a diagram removal scheme [152] is used and an alternative sample using the diagram subtraction scheme [138, 152] is generated to estimate the uncertainty on this approach.
The inclusive cross sections of all three single-top-quark processes are corrected to their theory predictions at highest order available. For the t-channel process, all events are normalized to $\sigma(t, t\text{-chan})_{\text{NLO}} = 134.02 \pm 2.2\,\text{pb}$ and $\sigma(\bar{t}, t\text{-chan})_{\text{NLO}} = 80.0 \pm 1.6\,\text{pb}$, respectively. The s-channel events are normalized to $\sigma(t, s\text{-chan})_{\text{NLO}} = 10.32 \pm 0.38\,\text{pb}$ and for associated tW production to $\sigma(tW)_{\text{NLO+NNLL}} = 79.3 \pm 2.9\,\text{pb}$. All cross sections are calculated at NLO in QCD, with additional NNLL soft gluon corrections for the association tW production [153, 154] using HATHOR 2.1 [155, 156].
For all single-top-quark processes, alternative samples with a modified value of the

[1] The h_{damp} parameter controls the matching of POWHEG BOX matrix elements to the parton shower and thus effectively regulates the high-p_{T} radiation against which the $t\bar{t}$ system recoils.

POWHEG :pThard parameter[2] are produced to estimate the uncertainty for the matching procedure between POWHEG BOX and PYTHIA. The $p_{\mathrm{T}}^{\mathrm{hard}}$ parameter controls the first radiation, e.g. of a gluon, and how it is combined with the parton shower. The uncertainty due to the choice of PYTHIA as the shower algorithm is assessed by another alternative sample which interfaces POWHEG BOX v2 with HERWIG 7.2.1.

5.2.3 Single-top-quark t-channel and $t\bar{t}$ CKM samples

The signal samples for the CKM interpretation in the single-top-quark t-channel cross section measurement and the CKM analysis are single-top-quark processes in which the top-quark originates and decays not only into the b-quark (as in the nominal samples described above) but also in the $s-$ and $d-$ quark. These t-channel samples are simulated with AMC@NLO v.2.9.9 with the NNPDF3.0NLO PDF set [137]. The four-flavour scheme is used for both processes, in which the top-quark originates from a b quark. All other processes are simulated with the five-flavour scheme. Only the leptonic decay of the top-quark is simulated in the production. MADSPIN [148, 149] is used to decay the top-quarks. The inclusive cross section calculated by AMC@NLO uses the Wolfenstein parametrisation [157]. Therefore, for each process, these cross section were used to calculate inclusive cross sections under the assumption $V_{tb} = 1$, $V_{td} = 1$, $V_{ts} = 1$ respectively, depending on the top-quark production vertex. Each sample is normalized to its calculated inclusive production cross section, the W-boson branching ratio is not include here. In Table 5.2, the different t-channel CKM samples, with their respective cross sections to which they are normalized to, are shown. In addition to the t-channel samples described above, for the CKM interpretation also $t\bar{t}$ events with all possible top-quark and anti top-quark decays, $t \to b, d, s$ and $\bar{t} \to \bar{b}, \bar{d}, \bar{s}$, are produced. These samples are required as the nominal $t\bar{t}$ process assumes $|V_{tb}| = 1$, and it is the dominant background contribution in this analysis. In order to take all possible processes into account in which a vertex including tWd or tWs occurs, eight samples are produced for the semileptonic decay mode and eight for the dileptonic decay mode, using a very similar setup to the nominal process simulation. POWHEG BOX v2 [133–136], employing the five-flavor scheme with the NNPDF3.0NLO [137] PDF set is used. The h_{damp} parameter is set to $1.5\, m_{\mathrm{top}}$ [138]. The decay of the top-quarks is modelled by MADSPIN [148, 149] at LO to allow for the decays into $d-$ and $s-$quarks and preserve the spin correlations of all particles.
The cross section of each sample depends on the occurring top-quark involved decays. The branching ratios for the top-quark and anti-top-quark decays to the respective quarks are set to 0.5 each, if both decay into different quarks. If both top-quarks decay into the same quark, the branching ratio to this quark is set to 1. The branching ratios of the W-boson decays into leptons and quarks, respectively, are also included in the calculated values. Hence, for semileptonic processes with both top-quarks decaying into different quarks, the cross section is $\sigma = 40.1\,\mathrm{pb}$ and for processes with both top-quarks decaying into the same quark, the cross section is $\sigma = 160.5\,\mathrm{pb}$. For the dileptonic modes, the cross section for processes with both top-quarks decaying into different quarks is $\sigma = 19.179\,\mathrm{pb}$ and for both top-quarks decaying into the same quark $\sigma = 76.7\,\mathrm{pb}$.

[2] The nominal value of POWHEG :pThard is zero, the alternative sample uses 1.

Table 5.2: All possible, simulated single-top-quark t-channel MC samples for the CKM interpretation with different top-quark production and decay vertices, and the calculated cross sections they are normalized to.

Process	cross section [pb]
$\bar{t}q$ $(\bar{b} \to \bar{t} \to \bar{d})$	76.1
tq $(b \to t \to d)$	127.2
$\bar{t}q$ $(\bar{b} \to \bar{t} \to s)$	76.1
tq $(b \to t \to s)$	127.2
$\bar{t}q$ $(\bar{d} \to \bar{t} \to b)$	168.6
tq $(d \to t \to b)$	445.7
$\bar{t}q$ $(\bar{d} \to \bar{t} \to d)$	168.6
tq $(d \to t \to d)$	445.7
$\bar{t}q$ $(\bar{d} \to \bar{t} \to s)$	168.6
tq $(d \to t \to s)$	445.7
$\bar{t}q$ $(\bar{s} \to \bar{t} \to b)$	111.3
tq $(s \to t \to b)$	155.6
$\bar{t}q$ $(\bar{s} \to \bar{t} \to d)$	111.3
tq $(s \to t \to d)$	155.6
$\bar{t}q$ $(\bar{s} \to \bar{t} \to s)$	111.3
tq $(s \to t \to s)$	155.6

5.2.4 Single vector boson processes

Single boson processes, i.e. the production of W and Z bosons in associated with additional QCD radiation (W+jets, Z+jets; together called V+jets) are important background processes for the single-top analyses. For the single-top-quark t-channel analysis with the CKM interpretation, V+jets processes are simulated with the Sherpa v2.2.1 [158] generator using the NNPDF3.0nnlo set of PDFs [137]. The computational accuracy is provided by NLO MEs for up to two partons and LO MEs for up to four partons calculated with the Comix [159] and OpenLoops [160–162] libraries, with all samples being normalized to a NNLO prediction [163]. All samples are interfaced with the Sherpa parton shower [164] using the MEPS@NLO prescription [165–168] and parameter tunes developed by the Sherpa authors.
In the $W + c$-jet calibration analysis, in which the signal consists of specific W+jets events, and the dedicated single-top-quark t-channel CKM measurement, V+jets samples are produced with the same setup but using a different Sherpa version. For these analyses, all V+jets samples are simulated using the Sherpa v2.2.11 [158] generator using the NNPDF3.0nnlo set of PDFs [137] and the standard Sherpa prescription [169].
In all analyses, different filters are applied to the V+jets samples in order to select a particular flavor composition for the associated jets. This allows for samples enriched in V+$b(b)$ or V+$c(c)$ with adequate number of MC simulated events when comparing with data.

5.2.5 Multiboson processes

Diboson (VV) processes are simulated with the Sherpa 2.2 [158] generator in all analyses presented in this thesis. These samples include off-shell effects and, where appropiate, also Higgs boson contributions. The generation of both fully leptonic and semileptonic final states, where one boson decays leptonically and the other hadronically, uses MEs at NLO accuracy in QCD for up to one additional parton and at LO accuracy for up to three additional parton emissions. For loop-induced processes $gg \to VV$, LO MEs are used for up to one additional parton emission for all final states. The ME interfaced to parton shower matching [165] and merging is based on Catani–Seymour dipole factorisation [159, 164] using the MEPS@NLO prescription [165–168]. For the parton-shower the dedicated set of tuned parameters by the Sherpa authors is used. Virtual QCD corrections for the MEs are supplied by the OpenLoops library [160–162]. Analoguos to the V+jets samples, the NNPDF3.0nnlo set of PDFs is used [137].
The electroweak production of two bosons in association with two jets ($VVjj$) is simulated with the Sherpa 2.2.2 [158] generator using the NNPDF3.0nnlo PDF set [137]. Similarly, the LO-accurate ME+parton shower matching [165] and merging is based on Catani–Seymour dipole factorisation [159, 164] using the MEPS@NLO prescription [165–168] and parton shower parameters tuned by the Sherpa authors are used.

5.2.6 Modelling of multijet production

In the single-top-quark t-channel analysis, additional samples are utilized in order to identify high-p_{T} multijet production. Events, in which jets are misidentified as an electron or muon, or real electron and muons originating from hadron decays inside a jet, contribute to this background. The latter contribution is called *non-prompt leptons*, whereas the former are called *fake leptons*. Additionally, electrons from photon conversions in the detector material are part of the fake lepton background.
In order to estimate the number and shape of multijet events with fake or non-prompt electrons, dijet samples are generated using Pythia 8.186 [126] with LO matrix elements and a p_{T} ordered parton shower. The A14 set of tuned parameters [131] and the NNPDF2.3lo set of PDFs [128] is used. Further, the scales μ_r and μ_f are set as $\mu_r = \mu_f = \sqrt[4]{(p_{\mathrm{T},1} + m_1^2)(p_{\mathrm{T},2} + m_2^2)}$, with the transverse masses, $m_{1,2}$, and the transverse momenta, $p_{\mathrm{T},1,2}$, of the two outgoing particles. Additionally, a filter requiring at least one jet with $p_{\mathrm{T}} > 17\,\mathrm{GeV}$ is applied using a jet clustering algorithm over all stable particles of the generated events. This dijet sample is used to model the kinematics of multijet events involving electrons, with the rate being estimated using a data-driven method [1]. Events with non-prompt muons are modelled using collision data, also described in detail in the publication in Ref. [1], while the number of events with fake muons was found to be negligible.

6 Systematic uncertainties

In all measurements carried out in this thesis, several sources of systematic uncertainties need to be considered. Systematic uncertainties characterize the uncertainties associated to the measurements which are not related to the statistical uncertainties of either the used simulations nor the observed data. Expected event yields from both, signal and background processes, as well as the shape of kinematic distributions and NN discriminants, can be affected by systematic uncertainties.

The sources of systematic uncertainties are grouped into two major categories. Experimental uncertainties include uncertainties for all used physics objects, e.g. due to calibration measurements, as well as uncertainties due to the experimental setup during data taking at the ATLAS detector. As for the second category, modelling uncertainties account for uncertainties related to the modelling of pp-scattering in simulations, including theory uncertainties.

In general, the uncertainties that are considered in each analysis depend on the physics objects involved. All uncertainties and their effects are propagated through all analyses presented in this thesis. If not stated otherwise, the uncertainties described in the following sections are present in each of these measurements. The $W+c$-jet mis-tag calibration has additional uncertainties which are described in detail in Chapter 7.4.

6.1 Experimental uncertainties

In the following, the sources of the experimental uncertainties are subdivided into the corresponding physics objects and other sources like pile-up or luminosity.

Jet related uncertainties

Systematic uncertainties related to jets correspond to the JES, the JER, JVT and fJVT. The overall JES uncertainties are estimated from different sources of uncertainties, propagated through the applied calibration chain including in-situ calibration steps [107]. These sources include the η intercalibration of forward jets ($0.8 < |\eta| < 4.5$) from central jets ($|\eta| < 0.8$), the jet flavor composition and response, the differences in the shape between jets from gluons or light-quarks and those originated by b-quarks, the effects of jets not fully absorbed in the calorimeter (punch-through) and uncertainties due to non-closure tests. Further considered sources are the differences in the response to high p_{T}

jets and to single-particles, as well as uncertainties accounting for the difference in the jet response between different detector modelling simulations. The uncertainties to the JES are decomposed into a set of 30 uncorrelated components for the single-top-quark t-channel analysis and interpretation, and into a set of 34 uncorrelated components for the charm mis-tag calibration.
The JER uncertainties are evaluated by smearing the measured jet energies according to a Gaussian function [107]. Depending on the difference of the measured resolution in data and simulation, the smearing is either applied to simulated events or pseudo-data, which are simulated events treated as data, in different bins of the jet p_{T} and η. The measured data remain unaltered. Thirteen orthogonal variations are used in the analyses described in this thesis.
Additional uncertainties related to the calibrations of the JVT and fJVT are also considered [110] [111].

Flavor Tagging uncertainties

The CKM interpretation of the single-top-quark t-channel analysis presented in this thesis, also includes flavor tagging uncertainties. There are three sources of uncertainties considered. Tagging efficiencies are calculated for b-jets [118], as well as mis-tagging efficiencies for c-jets [119] and light jets [120]. Differences in data and simulation are corrected by p_{T} dependent SFs, which are applied to simulation. For the b-tagging efficiency of true b-jets, the uncertainty in the scale factors is decomposed into 45 orthogonal components. For the mis-tag efficiencies of c-jets and light jets, the uncertainties on the respective scale factors is decomposed into 20 independent components each. Due to a limited range in jet p_{T} in the b-tagging calibration, the uncertainties are extrapolated from the last utilized jet p_{T} bin for higher p_{T} jets [170]. An additional uncertainty is assigned to account for this extrapolation procedure. All flavor tagging related uncertainties are propagated as weights in the analysis.

Lepton related uncertainties

In all analyses presented in this thesis, single lepton triggers are used to select events. For electrons, the statistical and systematic uncertainty of the trigger efficiency measurement [96], which is performed to correct the trigger efficiency in simulation to match the one in data, is combined into a single uncertainty. Contrary, for muons the statistical and systematic uncertainties of the measured trigger efficiency [102] are treated separately. Uncertainties related to the electron energy scale and energy resolution calibrations are considered [171]. For both calibrations, Z+jets events are utilized. In the case of the electron energy scale, the related uncertainties are negligible at the measured average transverse energy of the electrons, while at other energies these are kept. Similarly, the largest contribution to the uncertainty on the electron energy resolution is driven by the extrapolation to higher energies, which are negligible in the analyses in this thesis. Factors affecting the electron energy resolution include variations in energy loss before the calorimeter, shower

fluctuations in the calorimeter, as well as noise introduced by pileup and readout systems. In the energy scale calibration, a total of sixty different uncertainties are considered. For all analyses presented in this thesis, these are consolidated into one single variation. Analoguosly, the uncertainties related to the electron energy resolution calibration are grouped into a single variation.
Uncertainties related to the calibration measurements of the electron reconstruction, identification and isolation efficiencies are propagated to the analyses [94]. The respective efficiencies are measured in data and compared to simulated $Z \to e^+e^-$ and $J/\psi \to e^+e^-$ events. Uncertainties are derived separately for the respective reconstruction efficiency SFs, identification efficiency SFs and isolation efficiency SFs, as one variation each.

Uncertainties related to the muon momentum scale and resolution are evaluated using $Z \to \mu^+\mu^-$ and $J/\psi \to \mu^+\mu^-$ events [172]. In the calibration procedure, the respective efficiencies are measured in data and compared to simulation. The uncertainties in the corresponding energy scale and resolution SFs are included in the analyses, with one variation each, with a combined variation for the momentum resolution of the ID and the MS. For muons, uncertainties related to the reconstruction, identification and isolation calibrations are also available [100]. Two variations, one for the statistical and one for the systematic uncertainty of the respective calibration measurement, are included in the analyses.

In addition, an uncertainty is taken into account for the fake lepton background, also called *multijet* background, in the single-top t-channel cross section analysis. The selections in the corresponding control region (CRs) for the two chosen data-driven methods, which are described in Chapter 8.1 and explained in detail in the publication [1], are modified, resulting in alternative distributions, which are used in the statistical analysis of the measurement to estimate the uncertainty on these procedures. For the jet-electron method two alternative selections are defined by altering the criterion on the energy fraction recorded with the electromagnetic calorimeter. For the non-prompt muon method, a single alternative selection is applied with the variation of the required isolation criterion. Due to differences in the multijet rate between the used CRs and signal region (SRs), an additional uncertainty of 30% is applied to the multijet event rate in the SRs. Another uncertainty is the difference in the rates of the muon multijet between the positive lepton region and the negative lepton region.

Uncertainties related to $\boldsymbol{E_{\mathrm{T}}^{\mathrm{miss}}}$

As all analyses use leptonic W-boson decays, and therefore $E_{\mathrm{T}}^{\mathrm{miss}}$, uncertainties related to $E_{\mathrm{T}}^{\mathrm{miss}}$ have to be considered. The missing transverse momentum is calculated using all reconstructed objects, hence the uncertainties of the used objects are propagated to the $E_{\mathrm{T}}^{\mathrm{miss}}$ estimation and contribute to the total uncertainty of $E_{\mathrm{T}}^{\mathrm{miss}}$ [121]. In addition, uncertainties regarding the *soft term* of $E_{\mathrm{T}}^{\mathrm{miss}}$, which includes the p_{T} of tracks not associated to reconstructed objects, are evaluated. It displays the disagreement between the soft and hard terms in events without any true $E_{\mathrm{T}}^{\mathrm{miss}}$. The uncertainty is estimated by comparing the measured hard and soft terms in data and comparing these to simulation. The

maximum difference is taken as the uncertainty. Three components are distinguished for this uncertainty. One component describes the parallel scale uncertainty related to shifts in the soft term parallel to the axis of the $E_{\mathrm{T}}^{\mathrm{miss}}$. The two other components correspond to the resolution along and perpendicular to the $E_{\mathrm{T}}^{\mathrm{miss}}$ axis, respectively.

Other experimental uncertainties

The integrated luminosity of the full Run 2 proton-proton dataset is measured using van-der-Meer scans [56] and the uncertainty accumulates to 0.83%. This uncertainty is applied to all expected signal and background event yields, with exception of the multijet background in the single-top-quark t-channel analysis, as this background is estimated using data-driven methods.

Another uncertainty is implemented accounting for the procedure to correct differences in the pile-up profile distributions between simulation and data, where these differences are corrected by adjusting the pile-up profile in the simulation to match the one observed in data. A rescaling factor for data is calculated as 1.0/1.03 in this procedure [129], which is used to compute *pile-up weights* [173] which are applied to simulation. The uncertainty associated with this correction is computed by varying the nominal data rescaling factor up and down to 1.0/0.99 and 1.0/1.07, respectively. It is incorporated into the measurement by varying the applied pile-up weights accordingly.

6.2 Modelling uncertainties

Modelling uncertainties correspond to uncertainties from the used simulation. The MC simulation primarily relies on NLO ME calculations, which are interfaced with LO PS generators. Different generators are used, in which specific parameters are set through tuning. These choices introduce uncertainties in the final predictions. The additional samples produced with alternative parameter settings for different uncertainty evaluations are described in Chapter 5.

In both, the CKM interpretation and the charm mis-tag calibration, the following modelling uncertainties are considered. For the matrix element calculation, uncertainties related to the limited order of considered Feynman diagrams, as well as an uncertainty associated with the factorization of the PDFs and the ME calculation[1], are considered. Hereby, the renormalization scale, μ_R, controls the running of the strong coupling constant α_S, while the factorization scale, μ_F, separates perturbative and non-perturbative effects in the PDFs. Both scale uncertainties are estimated by varying each scale, μ_R and μ_F, independently by factors of 2.0 and 0.5, excluding the cases where both are varied in the opposite direction. This done for W+jets and all top-quark production processes. The derived uncertainties are obtained as generator weights, which are propagated through the full analysis chain.

[1] The factorization of the cross section into a perturbative matrix element and non-perturbative parton distribution functions follows from the factorization theorem in QCD [174].

Uncertainties related to the initial-state and final-state radiation in PYTHIA are evaluated by varying the `Var3c` parameter of the used A14 parton-shower tune within the given uncertainties of this tune. In addition, μ_R, at which the strong coupling constant α_S is evaluated, is varied by factors of 0.5 and 2.0 for an additional uncertainty estimation of the final-state radiation. These uncertainties are assessed for top-quark processes.
An overlap removal is performed between $t\bar{t}$ and tW events. The uncertainty of this procedure is evaluated by comparing the nominal sample, which uses the diagram removal scheme, with an alternative sample that uses the diagram subtraction scheme [152].
All alternative samples or reweighted samples used for the uncertainty evaluations described above, are normalized to the same cross sections as the nominal samples.

Both, the CKM interpretation and the charm mis-tag calibration, use the PDF4LHC prescription with 30 variations [175]. In simulation, events are reweighted for each variation and compared to the central PDF4LHC value. In the statistical analysis of the CKM interpretation and the underlying single-top-quark t-channel analysis, the PDF uncertainties are treated as correlated accross all top-quark production processes.

In this analysis, uncertainties related to the choice of the shower algorithm and hadronization model are evaluated by comparing the nominal simulation with an alternative setup for all top-quark involved processes, as described in Chapter 5. Specifically, different phenomenological models are used to describe the hadronization process, such as the cluster model [176] and the Lund string model [177] [178], which affect how the energy is distributed among the final-state particles. The latter is implemented in PYTHIA, while the former fragmentation model is used by SHERPA and HERWIG. Additionally, variations in the shower ordering (such as angular-ordered and p_{T}-ordered showers) are considered, as they influence the parton shower evolution and, consequently, the resulting final state kinematic distributions.
Furthermore, the uncertainty related to the matching of NLO matrix elements to the parton shower, is evaluated by comparing the nominal setup with an alternative setup for $t\bar{t}$ and t-channel events as described in Chapter 5. This evaluation utilizes variations in the hard-scattering scale, $p_{\mathrm{T}}^{\mathrm{hard}}$, which determines the energy scale at which the hard scattering process is matched to the parton shower.
Additionally, the choice of the h_{damp} parameter in the $t\bar{t}$ simulation is evaluated comparing the nominal simulation with an alternative $t\bar{t}$ sample produced with $h_{\mathrm{damp}} = 3 \times m_t$, while all other settings are kept the same.

Normalization uncertainties are placed on background processes, which are known to differ in data and in the used simulation. For W+$b\bar{b}$ production, where the b-quarks originate from gluon splitting ($g \to b\bar{b}$), an overall uncertainty of 40% is assigned to the expected rate. This uncertainty covers differences between the simulation and data, observed in previous measurements [179]. The same uncertainty is applied to W+light jet events, as these two processes are merged in the statistical analysis of this measurement. Another uncertainty of 20% is applied to the event rate of W+c-jet production, as well as on the combined rate of Z+jets and diboson production.
The uncertainties of the theoretical cross section calculations are evaluated for each sample as described in Chapter 5.

7 Calibration of charm mis-tag rate for *b*-tagging

Many analyses in ATLAS rely on the possibility to identify jets containing hadrons originating from b- or c-quarks. The algorithms used to identify these heavy-flavour originated jets are called b-tagging algorithms. These are fundamental components for precise analyses of physics processes involving b-quarks in the final state, such as Higgs-boson analyses as well as in BSM searches. Another field where b-tagging is essential are top-quark involved analyses. In all measurements involving top-quarks, b-tagging algorithms are used to identify the top-quarks, as it decays nearly exclusively into a b-quark and a W-boson. Therefore, it is crucial that the b-tagging algorithms achieve both, a high efficiency and a high accuracy in order to reliably identify potential b-jet candidates. An important step after the development of b-tagging algorithms, are calibration analyses. As the algorithms are developed using MC simulation, their performance is evaluated on actual data and thus, the simulations are corrected if needed. Usually, this is done by comparing the measured efficiency to select real b-jets in data and to the efficiency measured in MC events. The result of these calibration analyses are data-to-MC SFs, which are applied to all jet objects in analyses in order to correct for mismodelling in the simulations. For this purpose, so called *mis-tag* efficiency, i.e. the efficiency for c-jets or light jets to be tagged mistakenly is measured as well.
A more detailed description of calibration analyses is given in Section 7.1. In section 7.2, the charm mis-tag calibration for the flavor-tagging algorithm `DL1r`, is presented. The calibration procedure using W+c-jet events, including the event selection and the calculation of the SFs is described in detail. Furthermore, an extrapolation procedure needed to extract the final results is presented. Finally, the results of this calibration are compared with another charm mis-tag calibration analysis in ATLAS.

7.1 Calibrating the ATLAS `DL1r` flavour tagging algorithm in Run 2

One of the main flavor-tagging algorithms for Run 2 in ATLAS is the `DL1r` algorithm [114]. It is a high-level tagger, which uses information from several low-level tagging algorithms. The output is a tagger score for each jet in an event. Details on the low level algorithms and the build of the tagger score are described in Section 4.5.2.
To evaluate the `DL1r` performance on data, calibration analyses are performed with the goal to reweight the tagger score distribution for each jet type (b-, c-, and light-jets) present

in the MC samples to be more closely aligned with the tagger score distribution for the corresponding jet types in real data. As the tagger score is a continuous distribution, a direct reweighting, i.e. a process in which the weight of each individual jet is adjusted based on its value, is very difficult to do due to the infinite number of possible score values. Instead, the tagger score distribution is sub-divided by fixed single-cut WPs. Each WP is defined by the fraction of true b-jets passing the selection, the b-tagging efficiency. There are four efficiency WPs for the `DL1r` algorithm: $60\%, 70\%, 77\%$ and 85%.
In the so called fixed-cut scheme (SingleWP), a jet is either tagged or not tagged at a certain WP. The tagging efficiency typically depends on the kinematic properties of a jet and thus, a calibration analysis is done in several bins of the jet p_{T}[1]. Efficiency SFs are derived by building the ratio of the efficiency found in simulation and the efficiency observed in data:

$$SF\left(p_{\mathrm{T}}\right) = \frac{\epsilon^{\mathrm{data}}\left(p_{\mathrm{T}}\right)}{\epsilon^{\mathrm{MC}}\left(p_{\mathrm{T}}\right)} \tag{7.1}$$

Every tagged true b-jet in an event gets a weight $w_{b-\mathrm{tag}} = SF\left(p_{\mathrm{T}}\right)$ and every non-tagged true b-jet a so-called *inefficiency* SF, defined by

$$w_{\mathrm{untag}} = \frac{1-\epsilon^{\mathrm{data}}\left(p_{\mathrm{T}}\right)}{1-\epsilon^{\mathrm{MC}}\left(p_{\mathrm{T}}\right)} = \frac{1-SF\left(p_{\mathrm{T}}\right)\cdot\epsilon^{\mathrm{MC}}\left(p_{\mathrm{T}}\right)}{1-\epsilon^{\mathrm{MC}}\left(p_{\mathrm{T}}\right)}. \tag{7.2}$$

Two further WPs are the trivial 0% WP (no jet is tagged as a b-jet) and 100% WP (every jet is tagged as a b-jet). Using all efficiency WPs as bin-edges of so-called *tag-weight bins* then allows for a normalized tag-weight distribution in every p_{T} bin of the fixed-cut calibration, as the score for a jet must fall into one of the tag-weight bins. Using this method called *pseudo-continuous b-tagging* (PCBT), each jet is taken into account and therefore, more information from the continuous tagger score is maintained for further utilization in physics analyses.
The charm mis-tag calibration presented in the next section is performed for both methods, SingleWP and PCBT.

7.2 Calibration using $W+c$ events

The c-jet mis-tagging efficiency is measured since Run 1 in ATLAS. These calibrations need samples very pure in true c-jets in order to perform the efficiency measurement in data. Two methods were exploited in Run 1 in order to achieve high c-jet purity, both at $\sqrt{s} = 7\,\mathrm{GeV}$ and $\sqrt{s} = 8\,\mathrm{GeV}$: One technique is referred to as the D^* method [180, 181], which is based on c-jets containing $D^{*\pm}$ mesons, whereas the second technique uses c-jets produced in association with a W boson. The latter method is called $W+c$ method [182]. Both calibration methods in Run 1 were based on identifying the c-jet from semileptonic c-hadron decays. Therefore, both techniques needed an extrapolation procedure in order to extend the results to all possible c-hadron decays. While the $W+c$ method contains a c-jet sample with a mix of semileptonically decaying charm hadrons, the D^* method exploited

[1] Ideally one would include a binning in $|\eta|$ as well if enough data was available.

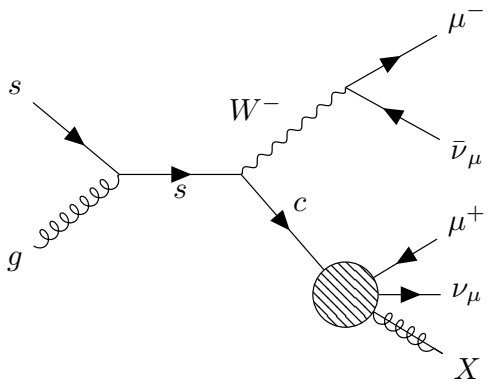

Figure 7.1: Feynman diagram illustrating one possible $W+c$-quark production mode, $gs \to W^-c$. The large circle at the c-quark decay vertex denotes a simplification of the hadronization process to illustrate the targeted decay mode of the formed c-hadron.

the possibility to reconstruct $D^{*\pm} \to D^0\pi^+$ decays, with $D^0 \to K^-\pi^+$ to get a very pure sample of c-jets. Since the uncertainties due to the applied extrapolation procedure to an inclusive c-jet sample are therefore smaller using the $W+c$ method compared to the D^* method, the latter method was not used anymore in Run 2.
Instead, another method was developed, which is based on semileptonically decaying $t\bar{t}$ events, in which the c-jet comes from the hadronically decaying W-boson from one of the top-quark decays [119]. The advantage of this so-called *$t\bar{t}$ method* is given by its inclusive sample of c-jets, thus not requiring an extrapolation procedure. As an alternative to the now standard calibration measurement using $t\bar{t}$ events, the $W+c$ method was used on a partial dataset corresponding to $36\,\text{fb}^{-1}$ to calibrate the charm mis-tag rate of the previous `MV2c10` tagging algorithm [118] at the beginning of Run 2 [183].

In order to derive the charm mis-tag efficiency of the `DL1r` tagging algorithm, the $W+c$ method is used as a reference measurement in Run 2. Analogously to the `MV2c10` calibration procedure, the c-jets in this procedure are identified by a muon coming from a semileptonic c-hadron decay. This muon is expected to be inside the jet cone and stemming from a tertiary vertex and is called *soft muon* (see Sections 4.4, 4.5.1), due to its usually lower p_T compared to prompt muons. As the two dominant production mechanisms for charm jets in association with a W boson are $gs \to W^-c$ and $g\bar{s} \to W^+\bar{c}$, the soft muon and the lepton coming from the W boson decay are expected to have an opposite electric charge. This correlation of the electric charges of the leptons is also exploited in order to extract a very pure c-jet sample for the calibration.
A schematic Feynman diagram, showing one possible $W+c$-quark production mode, is shown in Figure 7.1. It depicts the final state particles, visualizing the opposite-sign (OS) charged lepton pair. The large circle at the c-quark decay vertex denotes the simplification of the hadronization process to illustrate the semileptonic decay of the formed c-hadron.

7.2.1 Event selection

The charm mis-tag calibration of the `DL1r` algorithm uses the full Run 2 dataset corresponding to an integrated luminosity of $\mathcal{L} = 140\,\text{fb}^{-1}$. The largest assumed background processes are $W+b$-jets and $W+$light-flavour jets as well as processes involving top-quarks. In addition, $Z+$jets and diboson events are also expected to contribute to the overall number of events.
In contrast to the previous calibration, in which only events with $W \to e\nu_e$ were selected, in this calibration analysis, only events with $W \to \mu\nu_\mu$ are targeted. This choice was made due to technical reasons, as simulated samples were only available in the used ATLAS software release for this muon channel. Therefore, events are selected with exactly one prompt muon, expected to be coming from the W boson decay, and no electron candidate and no second prompt muon present. The prompt muon is required to have a $p_\text{T} > 27\,\text{GeV}$, since for this value the trigger efficiency reaches a plateau of 100%. As neutrinos are expected from the W-boson decay, a requirement was set on the missing transverse momentum of $E_\text{T}^\text{miss} > 35\,\text{GeV}$ in an event. In addition, events are required to have a transverse W-boson mass,

$$m_\text{T}^W = \sqrt{2p_\text{T}^\ell E_\text{T}^\text{miss} \cdot \left(1 - \cos\Delta\Phi\left(\vec{p}_\text{T}^\text{miss}, \ell\right)\right)}, \tag{7.3}$$

of $m_\text{T}^W > 40\,\text{GeV}$. The values of both, E_T^miss and m_T^W, are chosen in order to minimize the contributions due to wrongly identified leptons (fake leptons). Events are required to have exactly one jet in which exactly one soft muon is present. The jet needs to fulfill $p_\text{T}^\text{jet} > 20\,\text{GeV}$. In order to suppress $Z+$jet background events, two cuts involving both, the soft muon and the prompt muon, are introduced: The invariant mass of the two leptons is required to be outside the Z-boson mass window, thus events with $70 < m_{\mu\mu} < 100\,\text{GeV}$ are vetoed. This asymmetric window around the Z-boson mass peak was chosen to enhance the number of signal events over the number of background events. Furthermore, the distance in the detector between the muons is required to be $\Delta R(\mu,\mu) > 0.4$.
Due to a software bug present in the used ATLAS software release, non-leading muons were treated as pions and thus can subtract energy from the calorimeter in the reconstruction process and then form particle flow jets. These falsely reconstructed jets can alter the JES and JER systematic uncertainty determination for heavy flavor jets. Since events targeted in this calibration analysis do have the soft muon as a second muon in each event to the prompt muon, this bug is affecting the analysis heavily. To suppress events with (soft) muons falsely reconstructed as jets, which are mainly expected from the sub-leading muon in $Z+$jets events, requirements on the associated jet properties and the isolation of the soft muon are introduced. Soft muons are required to significantly exceed the calibrated *Loose* isolation working point, indicating a higher level of surrounding activity by other jet constituents. This isolation is calculated using the transverse momenta of nearby tracks and contributions from neutral particles within specific domains around the muon. Further, jets do either need to have two tracks associated to them or the fraction of the total jet energy measured in the electromagnetic calorimeter has to be lower than 80% of the total jet energy. Another requirement is set on the transverse momentum balance, p_T^bal, which

is defined by the ratio of the p_{T}^{Z}, with Z representing the soft muon and prompt muon, to the individual sum $p_{\mathrm{T}}^{\mu_{\mathrm{soft}}} + p_{\mathrm{T}}^{\mu}$, which has to be larger than 0.4. Finally, the ratio of the transverse momentum of the soft muon and the jet associated to the soft muon, has to be smaller than 0.5, as a value close to one indicates a wrongly reconstructed jet from that soft muon. All additional requirements were developed in studies done by the analysis team measuring the $W+c$ cross section and were adopted for the calibration measurement. As described before, for the signal two charged leptons of opposite charge are expected. In contrast, most of the background events are expected to be balanced in events with either OS or same-sign (SS) lepton pairs. For this reason, events with a SS lepton pair, N^{SS}, are subtracted from the events with an OS lepton pair, N^{OS}, in order to exploit this asymmetry for the $W+c$-jet events to realize a very pure OS-SS SR. This approach is confirmed by the event yields, which are shown in Table 7.1, with the number of signal events exceeding the number of expected background events. The purity in the OS-SS region for $W+c$ events is 89%, which is 6% larger than in the previous calibration [183]. In the MC simulated events, the flavor of the one present jet in events that pass the selection is determined on truth level, and corresponds to the quark flavor from which the soft muon originated.

Table 7.1: Number of events, N, in the OS region, SS region and the signal region, OS-SS. The total background is the sum of all individual background processes. The shown uncertainty is the MC statistical uncertainty.

Process	N^{OS}	N^{SS}	$N^{\mathrm{OS-SS}}$
W+light	$80\,000 \pm 1000$	$66\,900 \pm 900$	$13\,400 \pm 1300$
$W+b$	$16\,470 \pm 190$	$16\,800 \pm 190$	-340 ± 270
Z+jets	$15\,570 \pm 260$	8420 ± 140	7150 ± 290
VV	1600 ± 18	580 ± 10	1020 ± 20
$t\bar{t}$	5533 ± 28	4352 ± 25	1180 ± 40
t	$11\,329 \pm 27$	7793 ± 23	3540 ± 40
Total background	$131\,000 \pm 1000$	$104\,800 \pm 900$	$26\,000 \pm 1400$
$W+c$	$245\,000 \pm 1000$	$29\,900 \pm 400$	$215\,000 \pm 1000$
Total MC	$376\,000 \pm 1400$	$134\,700 \pm 1000$	$241\,300 \pm 1700$
Data	367144	130230	236914

In Figure 7.2, kinematic distributions illustrating the agreement between data and simulated events in the OS-SS region are shown. An overall reasonable agreement is observed, with no visible trend in any distribution and merely minor fluctuations within the statistical uncertainties. The kinematic distribution for each separate region are shown in Appendix A. For these distributions, the agreement between data and MC events is also reasonable. In order to perform the calibration, events are further divided by the p_{T} of the jet and its `DL1r` score. For the SingleWP calibration, events are categorized in five WP bins: untagged, tagged at 60% WP, tagged at 70% WP, tagged at 77% WP and tagged at 85% WP.

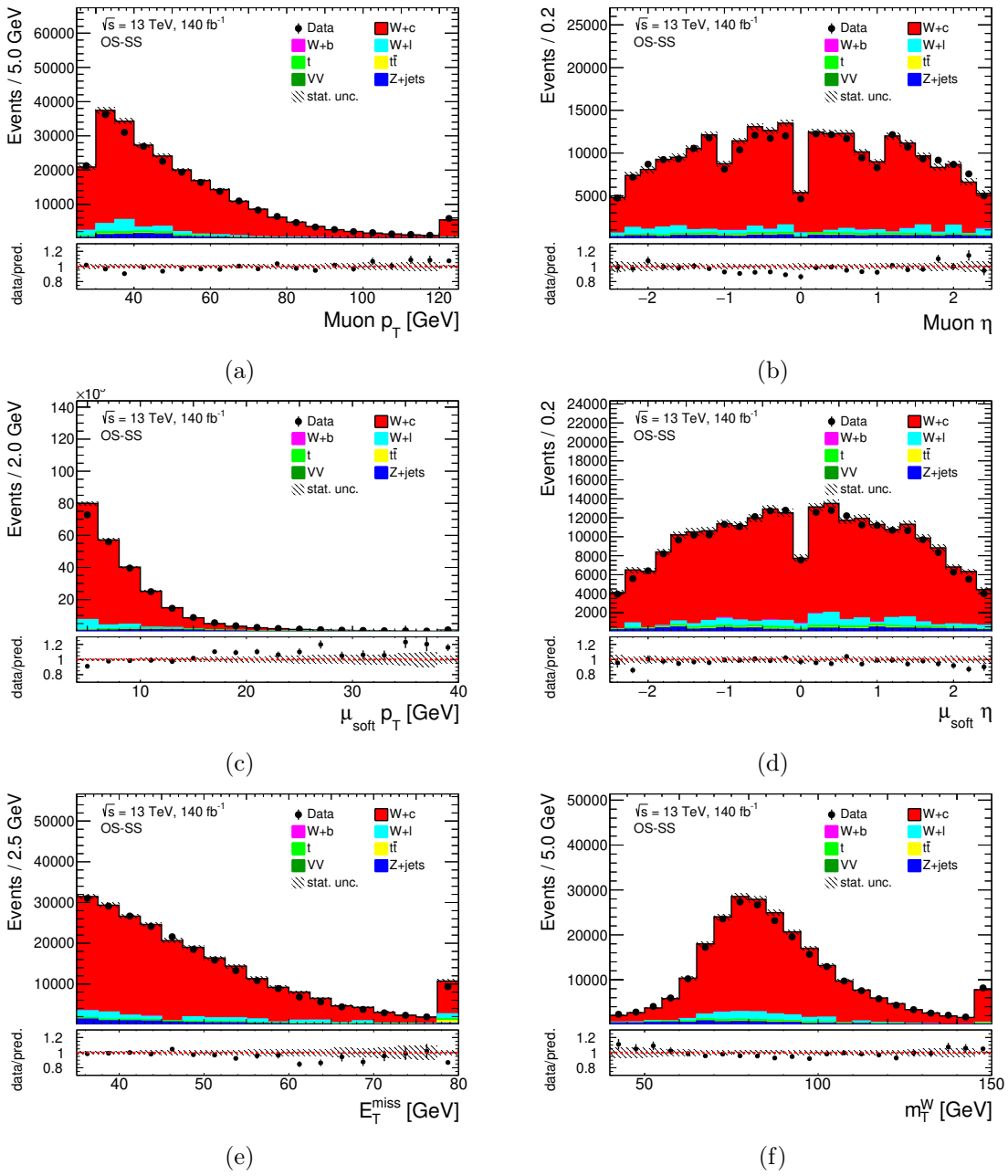

Figure 7.2: Kinematic distributions in the signal (OS-SS) region. (a) and (b) show the p_{T} and the pseudorapidity of the prompt muon in an event, respectively. (c) and (d) show the p_{T} and the pseudorapidity of the soft muon. In (e) the missing transverse momentum is shown and in (f) the transverse W-boson mass. The first and last bin of each distribution include the underflow and overflow bin, respectively. In the bottom panel of each plot, the ratio between observed and expected events is shown. All distributions show a good agreement between data and simulation. The depicted uncertainty bands indicate the MC statistical error, whereas the error bars on the black data points show the statistical uncertainty on the recorded data.

For the PCBT calibration, events are sorted in the five tag-weight bins: [85-100%], [77-85%], [70-77%], [60-70%] and [0-60%]. Additionally, events are categorized in three p_{T} bins ($20-40\,\mathrm{GeV}$, $40-65\,\mathrm{GeV}$ and $65-140\,\mathrm{GeV}$). These bins are chosen to be the same as the ones used in the standard $t\bar{t}$ based calibration, in order to allow the possibility to combine both calibrations in the end. A fourth p_{T} bin, $140-250\,\mathrm{GeV}$, used in the $t\bar{t}$ based calibration, was excluded from the $W+c$ calibration, as the event yields were not sufficient. Since the $W+c$ method was expected to be more suited for lower jet p_{T} values, this decision was made. In Figure 7.3, the jet p_{T} distribution is shown with the binning applied for each b-tagging WP, which illustrates the reason for the mentioned decision as well. The comparison between data and simulation shows a reasonable agreement. For all distributions, it is visible that in the range between 40-65 GeV fewer events are predicted by the simulation than recorded in data. The events in the different p_{T} and WP bins are used in a likelihood procedure to perform the calibration deriving data-to-MC SFs.

7.2.2 Likelihood fit procedure

In contrast to the previous charm mis-tag calibration, a likelihood fit procedure was performed in order to derive the data-to-MC scale factors in this calibration. The reason for this change is given by the higher c-jet rejection rate of the DL1r tagger with regard to the `MV2c10` tagger. The overall number of tagged events in data and simulation containing a charm jet is much lower. This is especially true for smaller efficiency working points and for jets with large p_{T}. Due to known mismodelling in simulated events for these phase spaces, the method using the ratio of two histograms, one filled with events in data and the other one filled with events from simulation, could lead to unphysical, negative SFs. In order to prevent these, a likelihood-based approach was developed. To avoid any potential bias arising from correlations between uncertainties solely occurring in this calibration, the systematic uncertainties are not included as nuisance parameters in the fit. Instead, the fitting procedure is repeated for each systematic uncertainty individually. The minimization of all likelihood functions is carried out by the `MINUIT` software library [184].

SingleWP

For the SingleWP calibration, a gaussian likelihood function is used, since the subtraction of OS-SS events cannot be treated with poissonian ansatz. The gaussian likelihood function for two regions, here realized by events with either a tagged or untagged jet, is given by

$$L = \prod_{i=\text{Tagged, Untagged}} \frac{1}{\sqrt{2\pi\sigma_i^2}} \exp\left(-\frac{(N_i-\lambda_i)^2}{2\sigma_i^2}\right), \tag{7.4}$$

with the expectation λ, the observed data, N, and the standard deviation σ. The logarithmic likelihood function is therefore given by

$$\ln(L) = \sum_{i=\text{Tagged, Untagged}} \left(-\frac{1}{2}\ln(2\pi) - \frac{1}{2}\ln\left(\sigma_i^2\right) - \frac{(N_i-\lambda_i)^2}{2\sigma_i^2}\right) \tag{7.5}$$

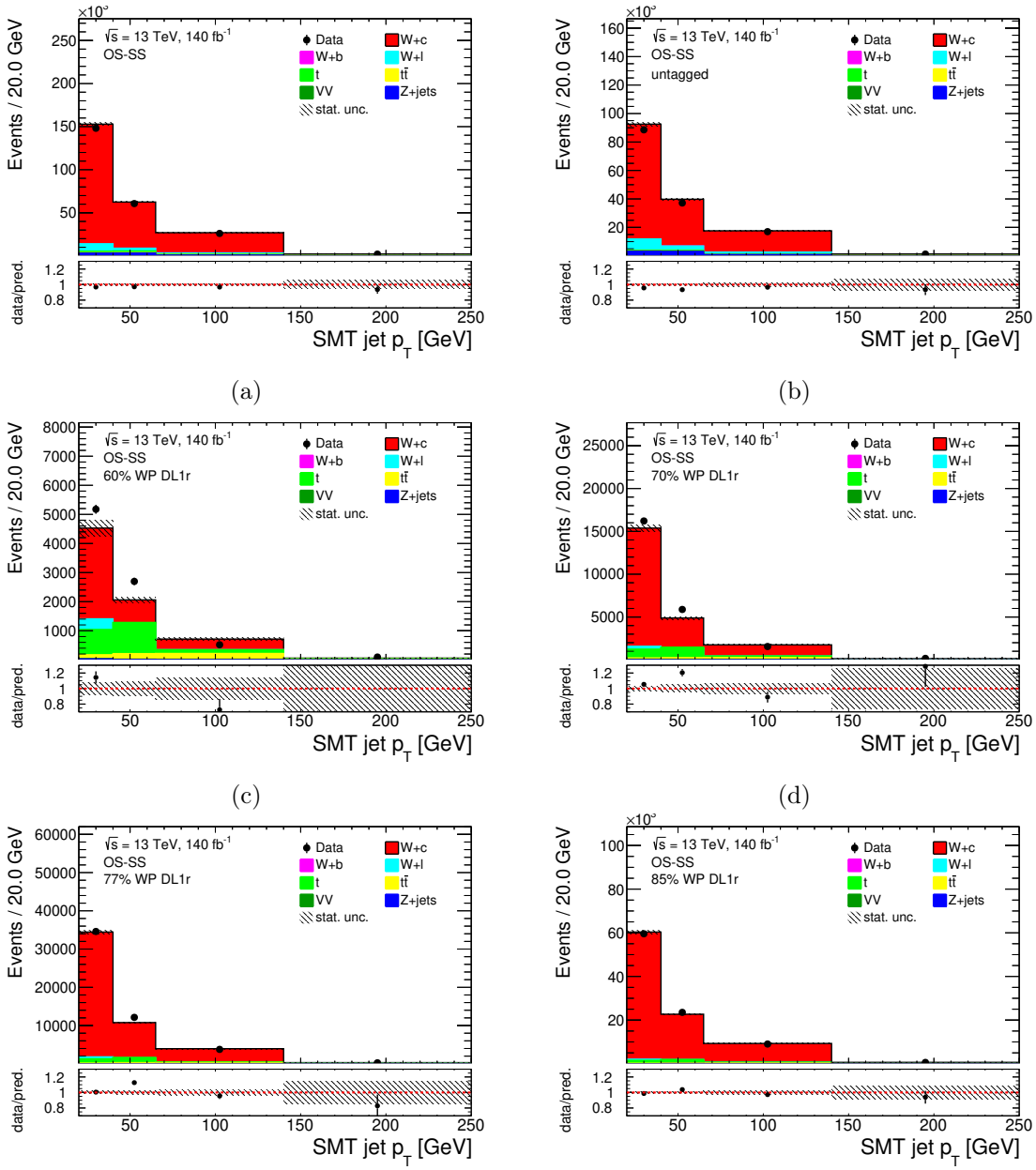

Figure 7.3: Different jet p_{T} distributions with the binning applied in which the calibration procedure is done. (a) the full jet p_{T} distribution, (b) p_{T} distribution for jets not tagged by the DL1r algorithm. The plots (c), (d), (e) and (f) show the p_{T} distribution for jets tagged at the 60%, 70%, 77% and 85%, respectively. All distributions show a reasonable agreement between data and simulation. The depicted uncertainty bands indicate the MC statistical error, whereas the error bars on the black data points show the statistical uncertainty on the recorded data.

The first two terms in the sum are neglected, as these are constant. Therefore, the logarithm of the likelihood function is obtained as

$$\ln(L) = -\sum_{i=\text{Tagged, Untagged}} \frac{\left((D^{\text{i}}_{\text{OS}} - D^{\text{i}}_{\text{SS}}) - (\text{MC}^{\text{i}}_{\text{OS}} - \text{MC}^{\text{i}}_{\text{SS}})\right)^2}{2 \cdot (D^{\text{i}}_{\text{OS}} + D^{\text{i}}_{\text{SS}})} \tag{7.6}$$

with $D_{\text{OS/SS}}$ and $\text{MC}_{\text{OS/SS}}$ denoting the events with the characteristic lepton pair in data and simulation, respectively. The MC events are parametrized as follows:

$$\text{MC}^{\text{Tagged}}_{\text{OS/SS}} = \left(N_{W+c} \cdot \text{SF} \cdot \epsilon_{\text{MC}} \cdot \left(S^{\text{Tagged}}_{\text{OS/SS}} + S^{\text{Untagged}}_{\text{OS/SS}}\right)\right) + B_{\text{Tagged}} \tag{7.7}$$

$$\text{MC}^{\text{Untagged}}_{\text{OS/SS}} = \left(N_{W+c} \cdot (1 - \text{SF}) \cdot \epsilon_{\text{MC}} \cdot \left(S^{\text{Tagged}}_{\text{OS/SS}} + S^{\text{Untagged}}_{\text{OS/SS}}\right)\right) \tag{7.8}$$

Here, S denotes the signal events and B the sum of all background events. The free floating parameters in the fit are the data-to-MC SF and the normalization of the signal events, N_{W+c}. Furthermore, ϵ_{MC} is the MC efficiency, which is given by the ratio of events in which the jet is tagged at a certain WP and all events overall after the event selection. The efficiencies for each p_{T} bin for all WPs are shown in Figure 7.4. The denominator in the likelihood function, σ^2, is obtained using error propagation for $f(\text{OS} - \text{SS}) = \text{OS} - \text{SS}$ events:

$$\sigma^2_f = \left(\frac{\partial f}{\text{OS}}\right)^2 \cdot \sigma^2_{\text{OS}} + \left(\frac{\partial f}{\text{SS}}\right)^2 \cdot \sigma^2_{\text{SS}} \tag{7.9}$$

$$= \sigma^2_{\text{OS}} + \sigma^2_{\text{SS}} \tag{7.10}$$

Since OS and SS are observed event yields, each individually follows the Poisson statistics. Further, the OS and SS events are uncorrelated and thus $\sigma^2 = \text{OS} + \text{SS}$. This likelihood function is used for each WP, for which the jet in each event either is tagged or untagged.

PCBT

For the PCBT case, a similar likelihood function is used. In contrast to the SingleWP procedure, the PCBT likelihood function is a product of gaussians for each tag-weight bin:

$$L = \prod_{i=0}^{4} \frac{1}{\sqrt{2\pi\sigma_i^2}} \exp\left(-\frac{(N_i - \lambda_i)^2}{2\sigma_i^2}\right), \tag{7.11}$$

with the expectation λ, the observed data, N, and the standard deviation σ. The 0-th bin corresponds to the events with a jet not being tagged, i.e. in the tag-weight bin of $85\% - 100\%$. Therefore, the fourth bin corresponds to the events with the jet having a `DL1r` score between $0\% - 60\%$. Consequently, the logarithmic likelihood is given by

$$\ln(L) = -\sum_{i=0}^{4} \frac{\left((D^{\text{i}}_{\text{OS}} - D^{\text{i}}_{\text{SS}}) - (\text{MC}^{\text{i}}_{\text{OS}} - \text{MC}^{\text{i}}_{\text{SS}})\right)^2}{2 \cdot (D^{\text{i}}_{\text{OS}} + D^{\text{i}}_{\text{SS}})}. \tag{7.12}$$

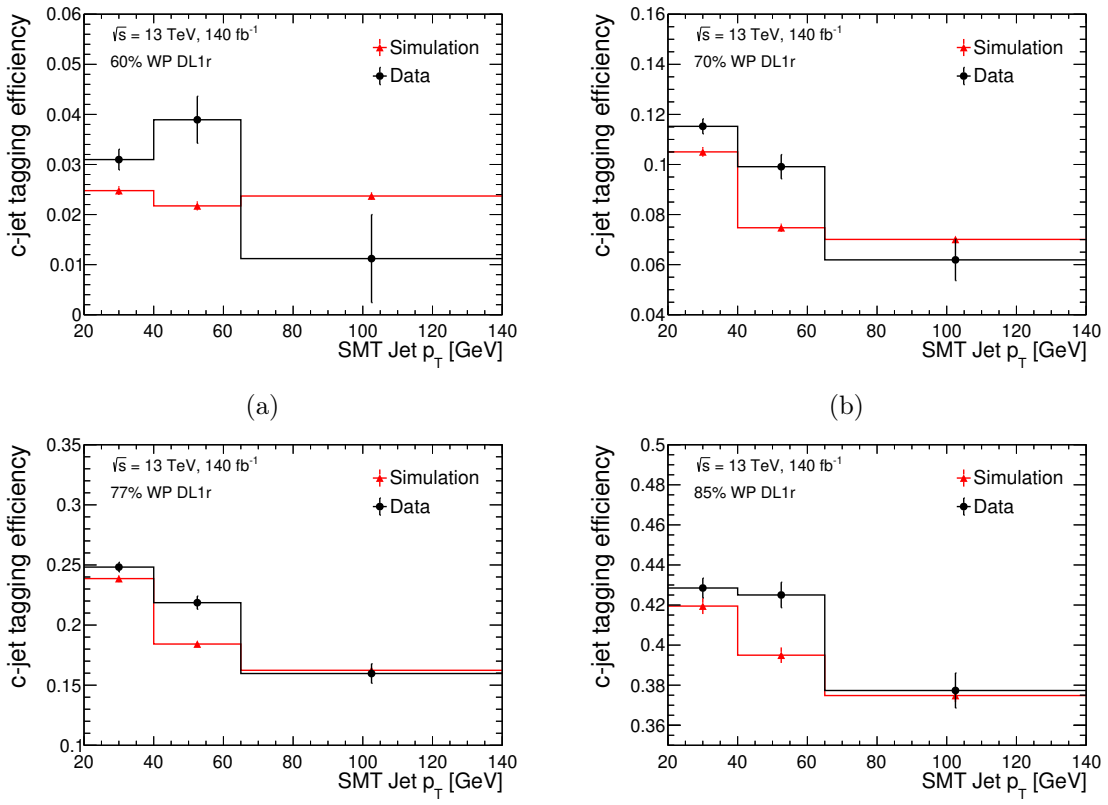

Figure 7.4: Tagging efficiency in simulation of $W+c$-jet signal events and data in all three jet p_{T} bins for (a) 60% `DL1r` WP, (b) 70% `DL1r` WP, (c) 77% `DL1r` WP and (d) 85% `DL1r` WP. The uncertainty given by the bars on the dots is the statistical uncertainty.

The MC events in the PCBT case are parametrized as follows:

$$\mathrm{MC}_0^{\mathrm{OS/SS}} = \left(N_{W+c} \cdot \mathrm{SF}_{\mathrm{ineff.}} \cdot \epsilon_0 \cdot S_{\mathrm{total}}^{\mathrm{OS/SS}}\right) + B_0^{\mathrm{OS/SS}} \tag{7.13}$$

$$\mathrm{MC}_{i>0}^{\mathrm{OS/SS}} = \left(N_{W+c} \cdot \mathrm{SF}_i \cdot \epsilon_i \cdot S_{\mathrm{total}}^{\mathrm{OS/SS}}\right) + B_i^{\mathrm{OS/SS}} \tag{7.14}$$

Again, the free floating parameters in the fit are the $W+c$-jet normalization correction, N_{W+c} and the SFs for each tag-weight bin, SF_i. The inefficiency SF is given as

$$\mathrm{SF}_{\mathrm{ineff.}} = \frac{\left(1 - \sum_{i=1}^{4} \mathrm{SF}_i \cdot \epsilon_i\right)}{\epsilon_0} \tag{7.15}$$

The efficiency, ϵ_i, for each tag-weight bin is calculated as the ratio of the signal events in that bin divided by all signal events. The efficiencies for each tag-weight bin for all p_{T} bins are shown in Figure 7.5. The denominator of the likelihood formula in Equation 7.12, is obtained analogously to the SingleWP case (see Equation 7.10).

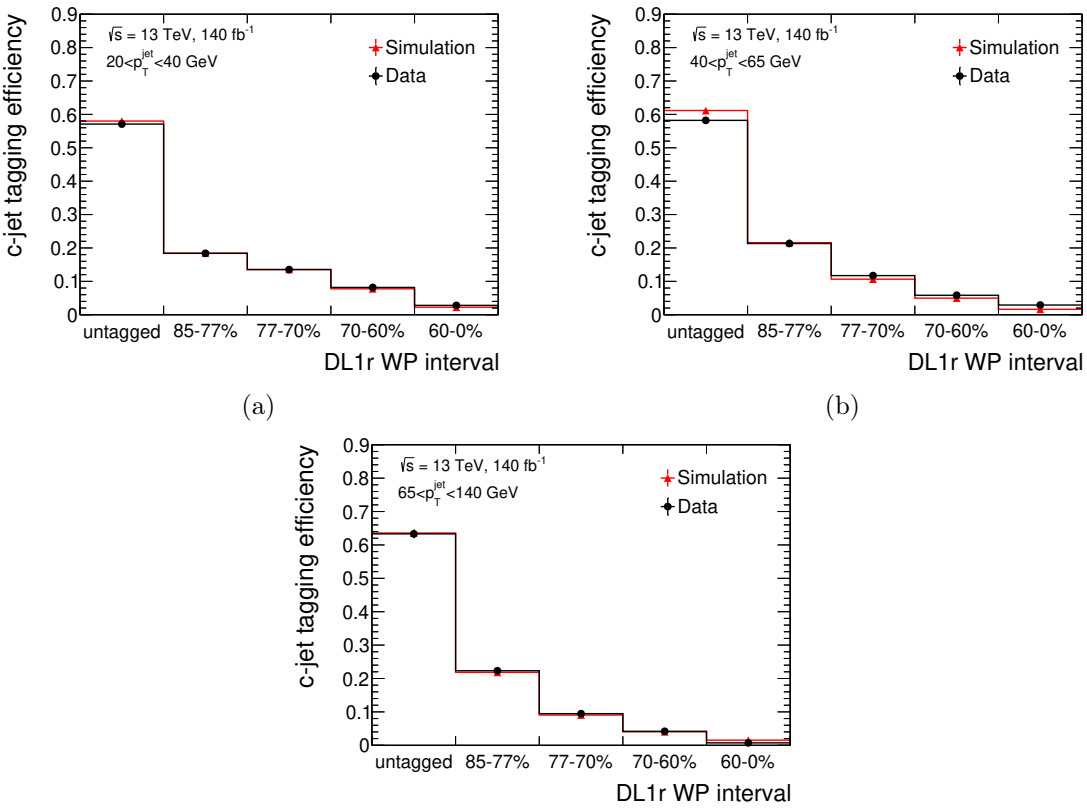

Figure 7.5: Tagging efficiency in data and simulation of W+c-jet signal events in all tag-weight bins for jets between (a) 20-40 GeV, (b) 40-65 GeV and (c) 65-140 GeV. The uncertainty given by the bars on the dots is the statistical uncertainty.

7.3 Resulting calibration data-to-MC scale-factors

SingleWP

The likelihood function is used to perform a fit of MC events to data for each WP of the `DL1r` algorithm. Example pre-fit and post-fit distributions for the 70% WP of the `DL1r` algorithm are shown in Figure 7.6 and 7.7. In all pre-fit plots, the high purity of W+c-jet events is visible, which underlines the advantage of this calibration method. A reasonable agreement between data and simulated events is observed in all post-fit plots. The pre-fit and post-fit plots for the three other WPs in all p_{T} bins are located in the Appendix B. These plots show overall a very similar agreement between data and MC events as well, but for the 60% WP, the purity in W+c-jet events is reduced due to single-top-quark and $t\bar{t}$ events. As mentioned above, the fit is done for each considered systematic uncertainty as well. Hereby, the observed data are replaced by pseudodata representing the nominal prediction, in order to obtain the difference due to the systematic uncertainty.

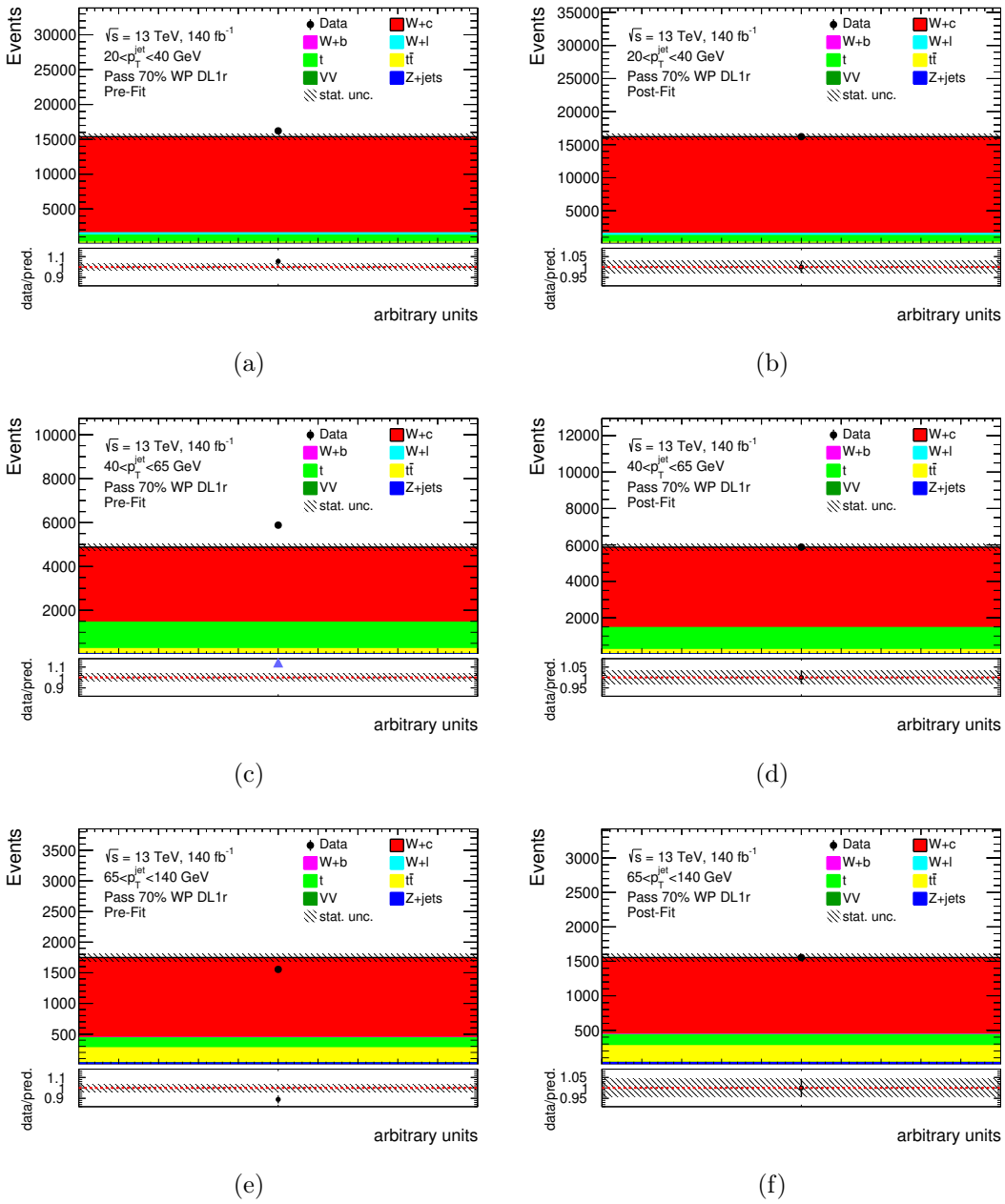

Figure 7.6: Pre-fit (left) and post-fit (right) plots for events in the OS-SS region with the jet being tagged at the 70% WP of the `DL1r` algorithm for the SingleWP calibration. (a) and (b) show the events with $20 <$ jet $p_{\mathrm{T}} < 40\,\mathrm{GeV}$, (c) and (d) show the events with $40 <$ jet $p_{\mathrm{T}} < 65\,\mathrm{GeV}$, and (e) and (f) show the events with $65 <$ jet $p_{\mathrm{T}} < 140\,\mathrm{GeV}$. In the bottom panel in each plot, the ratio between data and simulated events is shown. The MC statistical uncertainty is indicated by the black, shaded error band.

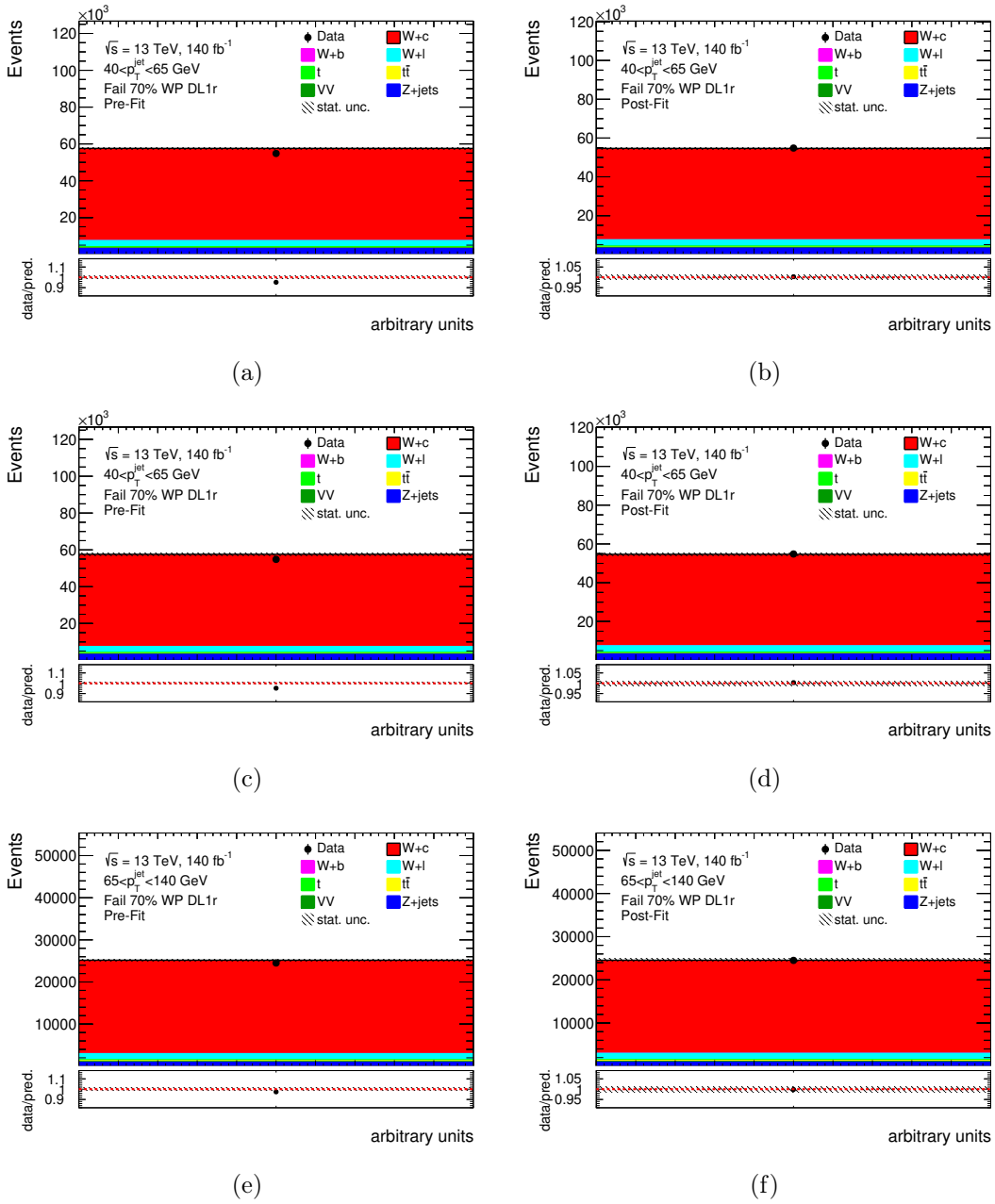

Figure 7.7: Pre-fit (left) and post-fit (right) plots for events in the OS-SS region with the jet not tagged at the 70% WP of the `DL1r` algorithm for the SingleWP calibration. (a) and (b) show the events with $20 <$ jet $p_{\mathrm{T}} < 40\,\mathrm{GeV}$, (c) and (d) show the events with $40 <$ jet $p_{\mathrm{T}} < 65\,\mathrm{GeV}$, and (e) and (f) show the events with $65 <$ jet $p_{\mathrm{T}} < 140\,\mathrm{GeV}$. In the bottom panel in each plot, the ratio between data and simulated events is shown. The MC statistical uncertainty is indicated by the black, shaded error band.

All differences are summed in quadrature in the end, including the statistical uncertainty, to derive the overall uncertainty on each SF. In Tables 7.2 and 7.3, the impact of different categories of systematic uncertainties on the resulting SFs is given for each WP and used p_{T} bin. For details on each different source of systematic uncertainties, see Chapter 6. The systematic uncertainty contributions are grouped based on their source. The uncertainties arising from the jet energy scale calibration are summarized under JES, whereas the uncertainties concerning the jet energy resolution are summarized under JER. Pileup, luminosity and JVT are summarized as experimental uncertainties. On the theory side, the uncertainties from each individual cross section uncertainty per sample are summarized, as well as the scale uncertainties and the electroweak corrections.
The largest systematic uncertainties arise from jet related uncertainties. Overall, this calibration is limited in precision by the systematic uncertainties. As the number of events with a tagged jet gets smaller for tighter `DL1r` WPs, the statistical uncertainty on the SFs is larger for these WPs.

The resulting data-to-MC SFs are shown in Figure 7.8. For all WPs a trend is visible, that the SF for jets between 40 and 65 GeV are further away from one than the SFs for

Table 7.2: Summary of the systematic and the statistical uncertainty contribution to the SingleWP data-to-MC scale factor calculation for the 60% and 70% `DL1r` WPs in all three p_{T} bins. All values are given in percent difference from the nominal result. The combined overall uncertainty is calculated by adding the corresponding sources in quadrature. If up and down variation of a source differ, the larger one is quoted here. No systematic uncertainties were symmetrized, thus adding up the uncertainties of each column might not result in the overall uncertainty quoted here. The "Experimental" category includes JVT, luminosity and pileup. If the impact is less than 0.05% it is shown as 0.0%.

	60% WP			70% WP		
Source	20-40 GeV	40-65 GeV	65-140 GeV	20-40 GeV	40-65 GeV	65-140 GeV
JES	8.6	22.7	82.0	4.4	12.4	10.9
JER	19.2	28.9	86.0	5.9	8.7	14.3
Muons	1.7	2.6	6.0	0.5	0.7	0.9
Electrons	0.0	0.0	0.0	0.0	0.0	0.0
$E_{\mathrm{T}}^{\mathrm{miss}}$	0.7	2.8	5.6	0.6	1.0	0.9
Experimental	0.2	0.6	1.5	0.0	0.1	0.2
Cross section	1.2	3.6	7.7	0.4	1.3	1.3
PDF	0.2	0.6	3.4	0.1	0.3	0.6
α_S variation	0.0	0.1	0.2	0.1	0.1	0.1
Scale	0.4	0.7	1.0	0.3	0.6	0.6
EW corrections	0.0	0.1	0.2	0.0	0.1	0.1
ISR / FSR	0.0	0.0	0.0	0.0	0.0	0.0
All systematic	19.3	29.3	86.8	7.4	13.0	14.5
Statistical	5.7	11.3	78.3	1.8	4.4	13.3

Table 7.3: Summary of the systematic and the statistical uncertainty contribution to the SingleWP data-to-MC scale factor calculation for the 77% and 85% `DL1r` WPs in all three p_{T} bins. All values are given in percent difference from the nominal result. The combined overall uncertainty is calculated by adding the corresponding sources in quadrature. If up and down variation of a source differ, the larger one is quoted here. No systematic uncertainties were symmetrized, thus adding up the uncertainties of each column might not result in the overall uncertainty quoted here. The "Experimental" category includes JVT, luminosity and pileup. If the impact is less than 0.05% it is shown as 0.0%.

	77% WP			85% WP		
Source	20-40 GeV	40-65 GeV	65-140 GeV	20-40 GeV	40-65 GeV	65-140 GeV
JES	3.3	8.3	5.2	1.3	4.0	3.0
JER	6.9	4.5	3.1	4.7	2.2	5.0
Muons	0.3	0.4	0.5	0.5	0.6	0.2
Electrons	0.0	0.0	0.0	0.0	0.0	0.0
$E_{\mathrm{T}}^{\mathrm{miss}}$	0.6	1.1	1.3	0.5	1.0	0.9
Experimental	0.0	0.0	0.0	0.1	0.1	0.1
Cross section	0.3	0.6	0.5	0.3	0.4	0.3
PDF	0.1	0.2	0.2	0.1	0.2	0.2
α_S variation	0.1	0.1	0.1	0.1	0.1	0.1
Scale	0.4	0.5	0.5	0.4	0.5	0.4
EW corrections	0.1	0.1	0.1	0.1	0.1	0.1
ISR / FSR	0.0	0.0	0.0	0.0	0.0	0.0
All systematic	7.7	8.7	6.2	3.8	4.7	5.9
Statistical	1.0	2.1	4.9	0.7	1.1	2.2

low p_{T} and high p_{T} jets in this calibration. Studies were done in order to investigate this observation. In these studies, the aforementioned p_{T} bin was split further into two bins, but the difference in data and simulated events, also visible e.g. in Figure 7.7, still persists. Therefore, the disagreement is treated as a MC modelling issue and thus as an effect which needs to be covered by this calibration. In general, the SFs obtained for tighter WPs have larger uncertainties compared to the SFs for looser WPs. This is expected, as less events are selected in these regions and the MC statistical uncertainty is larger. Most SFs are in agreement with unity within the overall uncertainties. In some bins, a large asymmetry of the effect of the systematic uncertainties is visible. This is overwhelmingly due to the jet related uncertainties. The reason for this behavior is driven by the calibration strategy to use different p_{T} bins and discard all events above 140 GeV. As the calibration procedures on jet objects are also done in different p_{T} bins, in some cases, both, up and down variations, of the corresponding uncertainties have the same effect, which is twice less or twice more events in a bin with respect to the nominal value. As this is a real physics effect, no symmetrization is applied. In Table 7.4, all data-to-simulation SFs are listed with statistical and systematic uncertainties. The fitted normalization values of the W+c-jet events are shown in Figure 7.9 for each fit. It is visible that in each fit, the

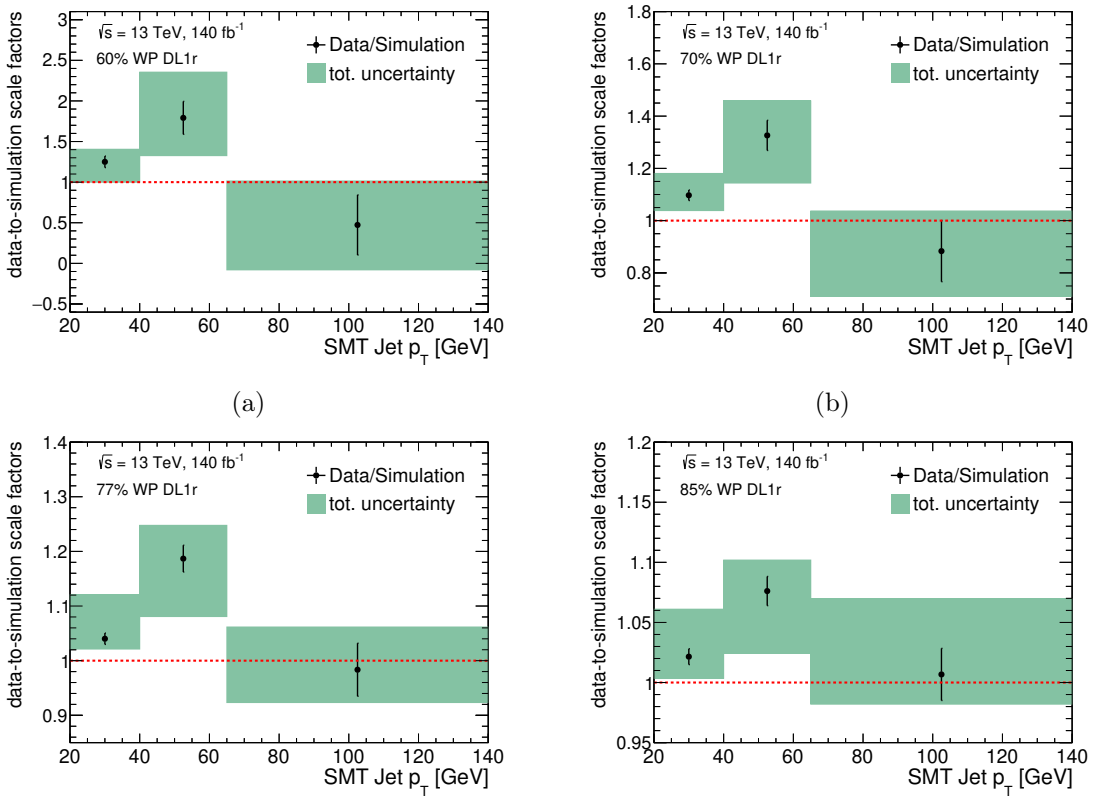

Figure 7.8: Resulting SingleWP data-to-MC scale factors in all three p_{T} bins for (a) 60% `DL1r` WP, (b) 70% `DL1r` WP, (c) 77% `DL1r` WP and (d) 85% `DL1r` WP. The black dots show the mean value, the black bars indicate the statistical uncertainty. The green boxes illustrate the total uncertainty, which is statistical and systematic uncertainties added in quadrature.

Table 7.4: Summary of the of the SingleWP data-to-MC scale factors for the `DL1r` algorithm in all three p_{T} bins.

`DL1r` / Jet p_{T}	20-40 GeV	40-65 GeV	65-140 GeV
60% WP	$1.25 \pm 0.07\,(\text{stat.})^{+0.14}_{-0.24}\,(\text{syst.})$	$1.79 \pm 0.20\,(\text{stat.})^{+0.52}_{-0.42}\,(\text{syst.})$	$0.47 \pm 0.37\,(\text{stat.})^{+0.39}_{-0.41}\,(\text{syst.})$
70% WP	$1.10 \pm 0.02\,(\text{stat.})^{+0.08}_{-0.05}\,(\text{syst.})$	$1.33 \pm 0.06\,(\text{stat.})^{+0.12}_{-0.17}\,(\text{syst.})$	$0.88 \pm 0.12\,(\text{stat.})^{+0.10}_{-0.13}\,(\text{syst.})$
77% WP	$1.04 \pm 0.01\,(\text{stat.})^{+0.08}_{-0.02}\,(\text{syst.})$	$1.19 \pm 0.02\,(\text{stat.})^{+0.06}_{-0.10}\,(\text{syst.})$	$0.98 \pm 0.05\,(\text{stat.})^{+0.06}_{-0.04}\,(\text{syst.})$
85% WP	$1.02 \pm 0.01\,(\text{stat.})^{+0.04}_{-0.02}\,(\text{syst.})$	$1.08 \pm 0.01\,(\text{stat.})^{+0.02}_{-0.05}\,(\text{syst.})$	$1.01 \pm 0.02\,(\text{stat.})^{+0.06}_{-0.01}\,(\text{syst.})$

normalization is the same for each p_{T} bin. This is expected since it is scaling both, the tagged and untagged events, in each p_{T} bin and thus, scales the same amount of events in each fit. The maximum correlation between a normalization factor, N_{W+c}, and a SF in a fit is 0.3, for the most p_{T} bins it is around 0.2.

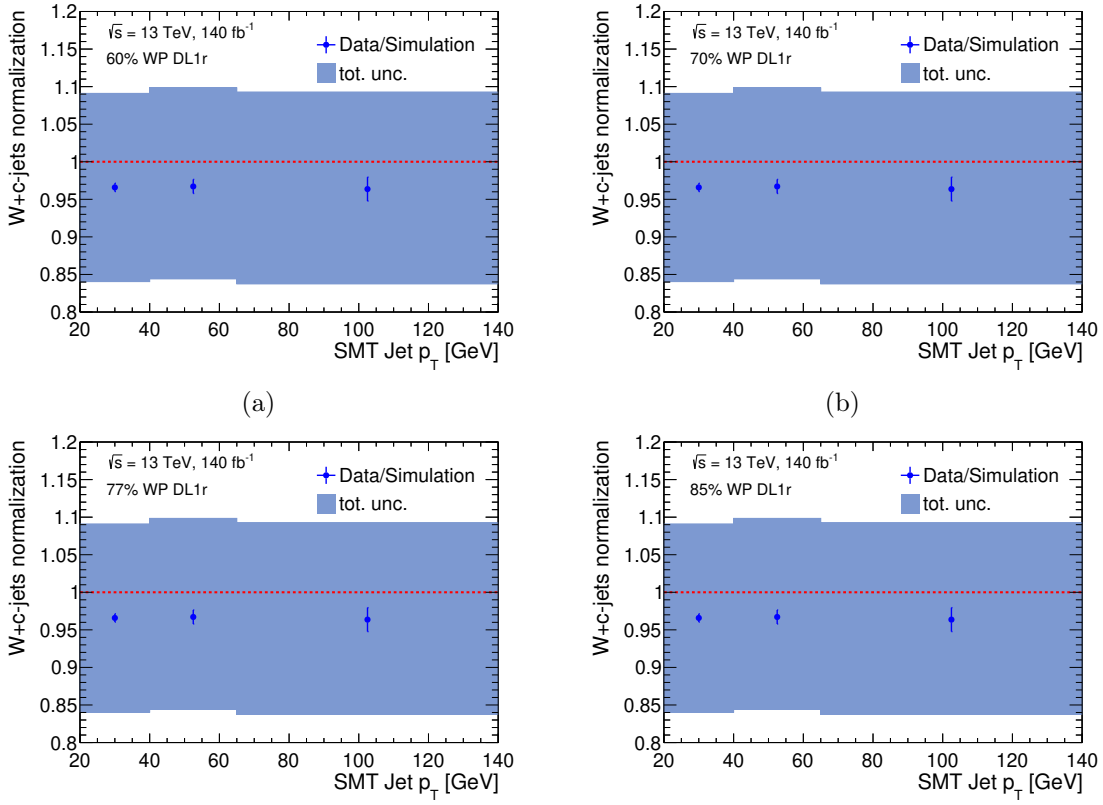

Figure 7.9: Resulting normalization factors for the W+c-jet signal events in all three p_{T} bins in the SingleWP fits for (a) 60% `DL1r` WP, (b) 70% `DL1r` WP, (c) 77% `DL1r` WP and (d) 85% `DL1r` WP. The blue dots show the mean value, the blue bars indicate the statistical uncertainty. The light blue boxes illustrate the total uncertainty, which is statistical and systematic uncertainties added in quadrature.

PCBT

The likelihood function is used to do a simultaneous fit of MC events to observed events for each tag-weight of the `DL1r` algorithm. This procedure is done for each aforementioned p_{T} bin. Example pre-fit and post-fit plots for the 20-40 GeV p_{T} bin are shown in Figure 7.10 and 7.11.

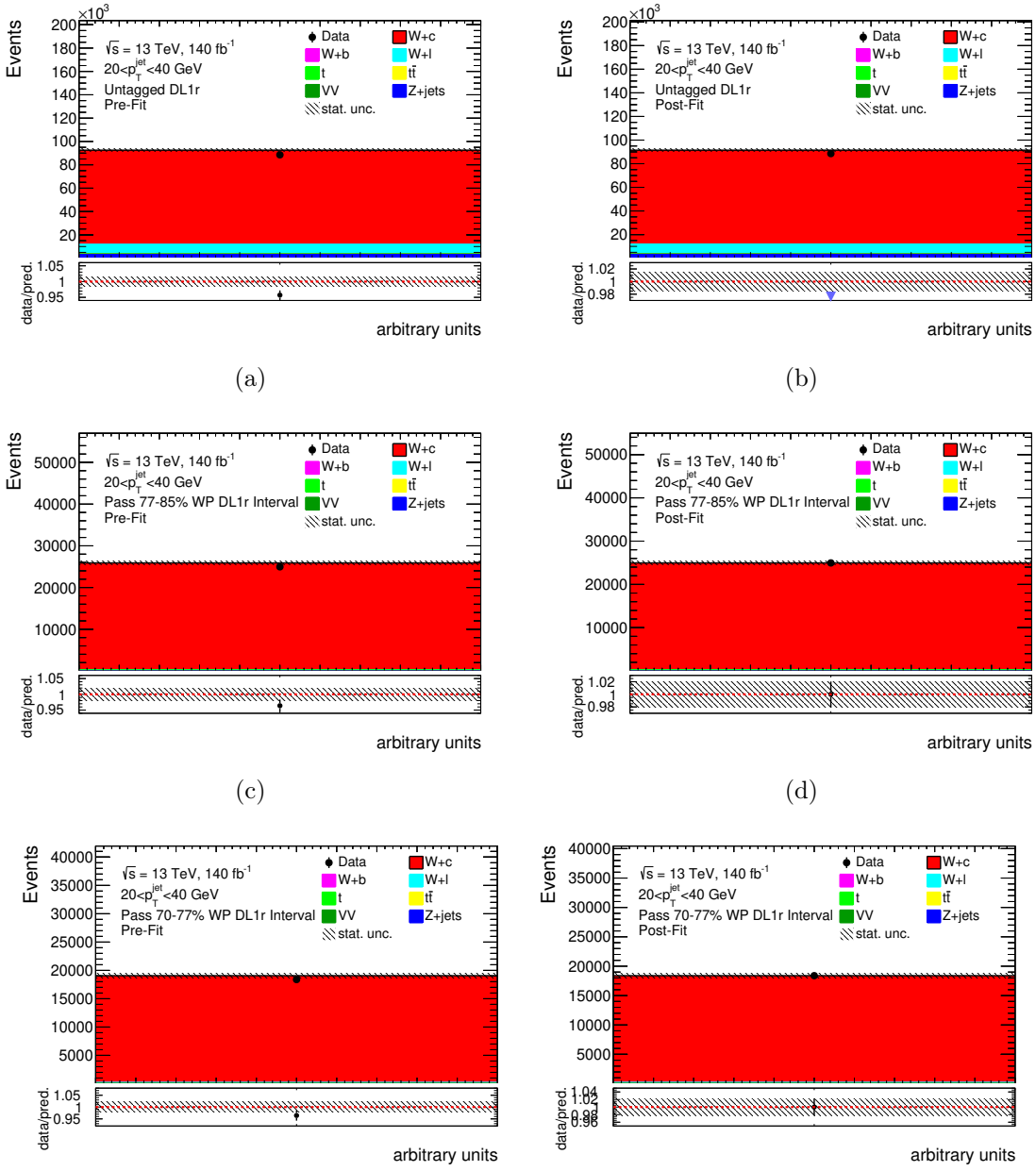

Figure 7.10: Pre-fit (left) and post-fit (right) plots for events in the OS-SS region with the p_{T} of the jet being within 20 and 40 GeV for the PCBT calibration. (a) and (b) show the events in the 0-th tag-weight bin (85%-100%), (c) and (d) the events in the first tag-weight bin and (e) and (f) the events in the second tag-weight bin. In the bottom panel in each plot, the ratio between data and simulated events is shown. The MC statistical uncertainty is indicated by the black, shaded error band.

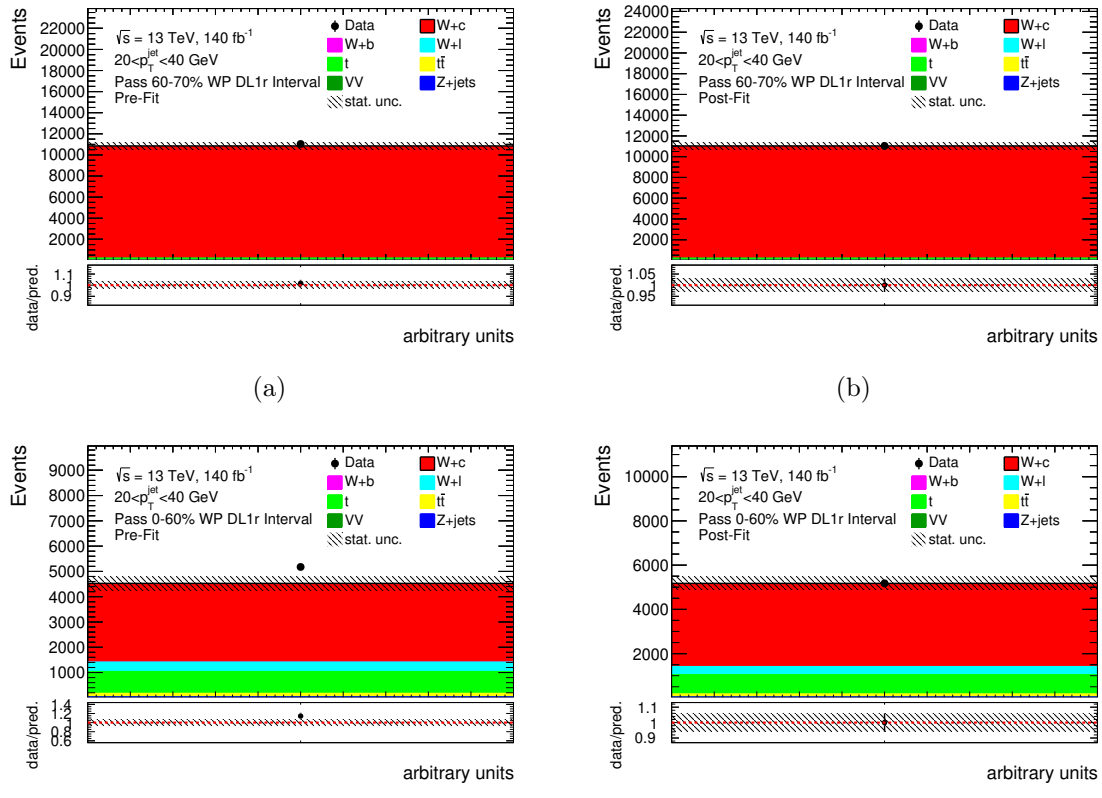

Figure 7.11: Pre-fit (left) and post-fit (right) plots for events in the OS-SS region with the p_{T} of the jet being within 20 and 40 GeV for the PCBT calibration. (a) and (b) show the events in the third tag-weight bin, and (c) and (d) the events in the fourth tag-weight bin. In the bottom panel in each plot, the ratio between data and simulated events is shown. The MC statistical uncertainty is indicated by the black, shaded error band.

The pre-fit and post-fit plots for the other two p_{T} bins are located in Appendix C. They show overall a very similar agreement between data and MC events.

In Tables 7.5 and 7.6, the impact of different categories of systematic uncertainties on the resulting SFs is given for each tag-weight bin and used p_{T} bin. A table with the uncertainty breakdown for the $85-100\%$ tag-weight bin is located in the Appendix D. Analogously to the SingleWP chapter, the systematic uncertainty contributions are grouped based on their source. As for the SingleWP case, for the PCBT case the largest systematic uncertainties arise from jet related uncertainties. Overall, this calibration is also limited in precision by the systematic uncertainties. As expected, since the number of events with a tagged jet gets smaller for tighter `DL1r` tag-weight bins, the statistical uncertainty on the SFs is larger in these bins.

Table 7.5: Summary of the systematic and the statistical uncertainty contribution to the PCBT data-to-MC SF calculation for the $0-60\%$ and $60-70\%$ `DL1r` tag-weight bin in all three p_{T} bins. All values are given in percent difference from the nominal result. The combined overall uncertainty is calculated by adding in quadrature the corresponding sources. If up and down variation of a source differ, the larger one is quoted here. No systematic uncertainties were symmetrized, hence why adding up the uncertainties of each column might not result in the overall uncertainty quoted here. The "Experimental" category includes JVT, luminosity and pileup. If the impact is less than 0.05% it is shown as 0.0%.

	0-60% WP			60-70% WP		
Source	20-40 GeV	40-65 GeV	65-140 GeV	20-40 GeV	40-65 GeV	65-140 GeV
JES	8.6	22.8	82.1	4.5	8.1	2.8
JER	19.2	28.9	86.0	7.1	8.9	4.9
Muons	1.7	2.6	6.0	0.5	0.5	0.6
Electrons	0.0	0.0	0.0	0.0	0.0	0.0
$E_{\mathrm{T}}^{\mathrm{miss}}$	0.7	2.8	5.5	0.7	0.9	2.3
Experimental	0.9	1.1	5.6	0.2	1.3	0.1
Cross section	1.2	3.7	7.7	0.4	0.4	0.3
PDF	0.2	0.6	3.4	0.2	0.2	0.2
α_S variation	0.0	0.1	0.4	0.1	0.1	0.1
Scale	0.4	0.7	1.0	0.4	0.5	0.5
EW corrections	0.0	0.1	0.1	0.1	0.1	0.1
ISR / FSR	0.0	0.0	0.0	0.0	0.0	0.0
All systematic	19.3	29.3	86.8	8.5	12.1	5.7
Statistical	5.7	11.3	78.3	1.7	3.7	8.0

In Table 7.7, all data-to-simulation SFs are listed with statistical and systematic uncertainties. In Figure 7.12, these data-to-MC SFs are shown for each tag-weight bin. As expected, the PCBT data-to-MC SFs in the 0-60% tag-weight bin are the exact same as the SFs for the 60% SingleWP fit. Further, most of the SFs are in agreement with unity within the overall uncertainties. The systematic and statistical uncertainties become larger for tighter tag-weight bins, as the purity in signal events is less and overall less events selected. Again, asymmetric uncertainties are visible for some SFs, these arise from the jet related uncertainties as explained in the SingleWP section. All normalization factors are in agreement with unity within the uncertainty.

Table 7.6: Summary of the systematic and the statistical uncertainty contribution to the PCBT data-to-MC SF calculation for the 70-77% and 77-85% `DL1r` tag-weight bin in all three p_{T} bins. All values are given in percent difference from the nominal result. The combined overall uncertainty is calculated by adding in quadrature the corresponding sources. If up and down variation of a source differ, the larger one is quoted here. No systematic uncertainties were symmetrized, hence why adding up the uncertainties of each column might not result in the overall uncertainty quoted here. The "Experimental" category includes JVT, luminosity and pileup. If the impact is less than 0.05% it is shown as 0.0%.

	70-77% WP			77-85% WP		
Source	20-40 GeV	40-65 GeV	65-140 GeV	20-40 GeV	40-65 GeV	65-140 GeV
JES	2.9	5.8	2.8	4.9	1.8	2.0
JER	8.8	3.8	7.0	4.1	5.4	7.7
Muons	0.8	0.6	0.3	0.9	0.6	0.6
Electrons	0.0	0.0	0.0	0.0	0.0	0.0
$E_{\mathrm{T}}^{\mathrm{miss}}$	0.8	1.3	2.3	1.1	1.3	0.7
Experimental	0.4	0.2	0.7	0.3	0.7	0.3
Cross section	0.3	0.4	0.4	0.3	0.4	0.3
PDF	0.1	0.2	0.1	0.1	0.2	0.1
α_S variation	0.1	0.1	0.1	0.1	0.1	0.1
Scale	0.4	0.7	0.6	0.2	0.4	0.3
EW corrections	0.1	0.1	0.1	0.1	0.1	0.1
ISR / FSR	0.0	0.0	0.0	0.0	0.0	0.0
All systematic	9.4	6.6	7.9	5.9	5.8	8.0
Statistical	1.2	2.2	4.2	1.1	1.6	2.5

Table 7.7: PCBT data-to-MC SFs for the `DL1r` algorithm in all three p_{T} bins.

`DL1r` / Jet p_{T}	20-40 GeV	40-65 GeV	65-140 GeV
$0-60\%$ WP	$1.25 \pm 0.07\,(\mathrm{stat.})^{+0.14}_{-0.24}\,(\mathrm{syst.})$	$1.79 \pm 0.20\,(\mathrm{stat.})^{+0.53}_{-0.42}\,(\mathrm{syst.})$	$0.47 \pm 0.37\,(\mathrm{stat.})^{+0.40}_{-0.41}\,(\mathrm{syst.})$
$60-70\%$ WP	$1.05 \pm 0.02\,(\mathrm{stat.})^{+0.09}_{-0.02}\,(\mathrm{syst.})$	$1.17 \pm 0.04\,(\mathrm{stat.})^{+0.06}_{-0.14}\,(\mathrm{syst.})$	$1.04 \pm 0.08\,(\mathrm{stat.})^{+0.03}_{-0.06}\,(\mathrm{syst.})$
$70-77\%$ WP	$1.00 \pm 0.01\,(\mathrm{stat.})^{+0.09}_{-0.01}\,(\mathrm{syst.})$	$1.10 \pm 0.02\,(\mathrm{stat.})^{+0.05}_{-0.07}\,(\mathrm{syst.})$	$1.04 \pm 0.04\,(\mathrm{stat.})^{+0.08}_{-0.03}\,(\mathrm{syst.})$
$77-85\%$ WP	$1.00 \pm 0.01\,(\mathrm{stat.})^{+0.04}_{-0.06}\,(\mathrm{syst.})$	$0.99 \pm 0.02\,(\mathrm{stat.})^{+0.02}_{-0.06}\,(\mathrm{syst.})$	$1.02 \pm 0.03\,(\mathrm{stat.})^{+0.08}_{-0.01}\,(\mathrm{syst.})$
$85-100\%$ WP	$0.98 \pm 0.01\,(\mathrm{stat.})^{+0.01}_{-0.03}\,(\mathrm{syst.})$	$0.95 \pm 0.01\,(\mathrm{stat.})^{+0.03}_{-0.01}\,(\mathrm{syst.})$	$1.00 \pm 0.02\,(\mathrm{stat.})^{+0.01}_{-0.03}\,(\mathrm{syst.})$

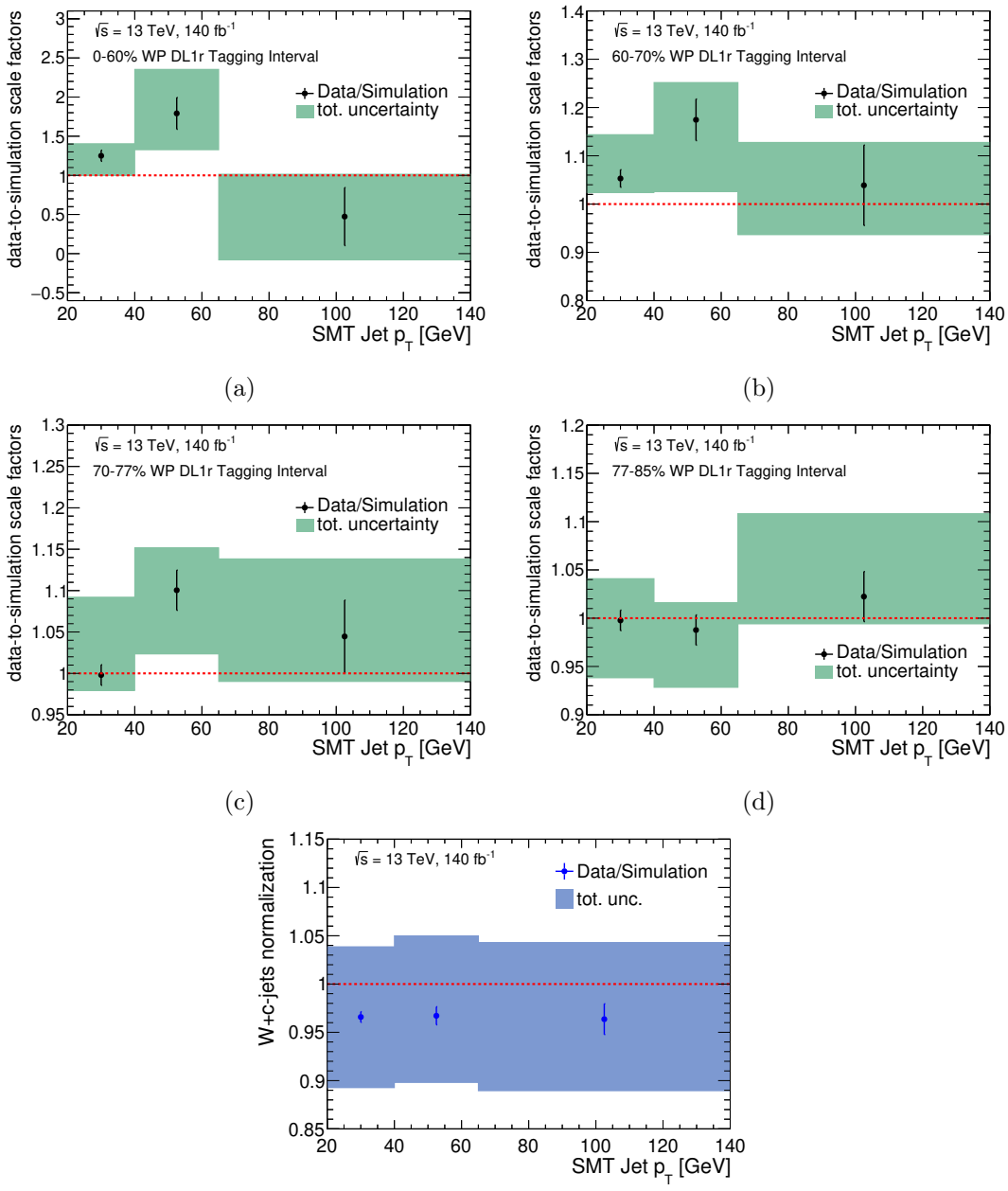

Figure 7.12: Resulting PCBT data-to-MC scale factors in all three p_{T} bins for (a) 0-60% `DL1r` tag-weight bin, (b) 60-70% `DL1r` tag-weight bin, (c) 70-77% `DL1r` tag-weight bin and (d) 77-85% `DL1r` tag-weight bin. (e) shows the resulting normalization factors for the W+c-jet signal events in all three p_{T} bins. The black and blue dots show the mean value, respectively. The black and blue bars indicate the statistical uncertainty, respectively. The green and light blue boxes illustrate the total uncertainty, respectively, which is statistical and systematic uncertainties added in quadrature.

7.4 Extrapolation from semileptonic to inclusive *c*-Hadron decays

As a soft muon is used to identify the c-jet in the W+c-jet method, the data-to-simulation SFs are obtained using solely semileptonically decaying c-hadrons. In order to avoid a bias in the SFs because the c-hadron composition due to the selection, an extrapolation procedure to an inclusive c-jet sample is needed.

In the previous calibration for the `MV2c10` algorithm, the then used MC sample was re-weighted based on the c-quark fragmentation fractions and branching ratios predicted in simulation compared with the measured ones by different experiments [185] [186]. The information regarding the c-hadrons were not contained in the used samples or other available samples, hence a new extrapolation strategy was introduced. The aim is to compare, and correct differences in SFs obtained with and without the usage of soft muons. Therefore, the selection strategy of the standard $t\bar{t}$ charm mis-tagging rate calibration [119] was chosen as a starting point. The extrapolation aims to obtain a very pure sample of semileptonic $t\bar{t}$ events, with a c- and light-jets from the hadronically decaying top-quark, which are distinguished between jets with and without a matched soft muon. As a result, ratio SFs are calculated to evaluate the difference between jets with and without a matched soft muon.

7.4.1 Event selection

The event selection requires events to have exactly one prompt electron with a $p_{\mathrm{T}} > 27\,\mathrm{GeV}$ and $E_{\mathrm{T}}^{\mathrm{miss}} > 20\,\mathrm{GeV}$. Further, at least 4 jets, each with a $p_{\mathrm{T}} > 25\,\mathrm{GeV}$ are required. A likelihood based $t\bar{t}$ event reconstruction algorithm, `KLFitter` [187], is used. It takes the four-vectors of the four highest p_{T} jets, the electron and the $E_{\mathrm{T}}^{\mathrm{miss}}$ of the event as inputs. The algorithm assigns one jet to the b-jet from the leptonically decaying top-quark, and another one to the b-jet from the hadronically decaying to quark. The remaining two jets are associated with the hadronic W-boson decay. It is important that this jet assignment does not employ any b-tagging information, but purely kinematic information. A likelihood value for each four-jet combination is calculated in order to find the best candidate for the $t\bar{t}$ reconstruction. In order to remove events in which the jets are wrongly assigned, events are required to have a negative logarithm of the likelihood value greater than -48. This value is chosen to be the same as the one used in the standard calibration [119]. Additionally, the two jets assigned to b-jets from both top-quarks are required to be tagged at the 60% efficiency WP of the `DL1r` algorithm. This requirement increases the purity in correctly assigned b-jets, and subsequently enhances the amount of correctly assigned c-jets and light jets from the hadronic W-boson decay. No b-tagging requirements are imposed on the two jets from the W-boson decay to not introduce a bias. In Table 7.8, the event numbers for all considered processes are shown after the selection. The overwhelming majority of selected events are $t\bar{t}$ events. Further, a difference of around 6% in the prediction and the measured data events is observed. As there are known mis-modelling effects in the p_{T} distribution of $t\bar{t}$ events, an overall normalization

Table 7.8: Event yields after the event selection for the extrapolation. The shown uncertainty is the MC statistical uncertainty. Values are rounded according to the particle data group guidelines for rounding.

Process	Yields
W+jets	1060 ± 60
Z+jets	636 ± 21
VV	62.9 ± 2.7
$t\bar{t}$	267 940 ± 190
t	5350 ± 25
Total MC	275 050 ± 210
Data	258772

correction for the MC estimation is calculated considering the MC statistical uncertaintes. The resulting correction factor is $\mathrm{NF}_{\mathrm{overall}} = 0.940 \pm 0.002$. This correction is applied in the fit procedure explained in the next section. After the initial event selection, the two jets associated to the W-boson are used for the extrapolation procedure. The jets are filled into histograms depending on their p_{T} and `DL1r` score. Jets are selected in the same p_{T} bins and `DL1r` requirements as in the primary calibration. Therefore, in some events not both but just one or even no jet are selected. In total 521314 jets out of possible 550100 jets are selected. In simulation, the flavor of each selected jet is determined on truth level based on the initial quark of the jet. The jets are categorized as a b-jet, c-jet or light jet. The majority of jets are light jets (77%), followed by a c-jet contribution of 21%. As expected, only a very minor contribution comes from b-jets (2%). A distinction between the different processes is not made, as the extrapolation procedure is aiming at differences between jets with and without a soft muon matched regardless of the origin of the jet. Further, jets are differentiated if they have a soft muon matched to it or not.

7.4.2 Profile likelihood approach

In contrast to the primary calibration, a binned profile likelihood procedure is utilized for the extrapolation. A detailed description of the used maximum likelihood method is given in Chapter 8.1.3. The goal of this approach is to obtain the ratio SFs which are defined as

$$\mathrm{SF}_{\mathrm{ratio}} = \frac{\mathrm{SF}_{\mathrm{matched}}}{\mathrm{SF}_{\mathrm{unmatched}}}, \tag{7.16}$$

with the SFs for jets with and without a matched soft muon.

SingleWP

For the SingleWP case, four regions are constructed for each `DL1r` WP, two where the jet is required to be tagged at a WP and two where the jet is required to not be tagged.

In both cases, one region contains the jets with a soft muon matched while the other contains the jets without a soft muon matched. Only the event yields in each region are considered, and no kinematic distributions, e.g. the secondary vertex mass, were examined where differences between the various quark flavors (b, c, light) could be observed, as those variables were not present in the MC samples used. The parametrization of the jet yields,N, in each region is as follows:

$$N^{\text{tagged}}_{\text{unmatched}} = \text{NF}_{\text{overall}} \cdot (\text{SF}_{\text{unmatched}} \cdot C_{\text{unmatched}} + B_{\text{unmatched}} + L_{\text{unmatched}}) \tag{7.17}$$

$$N^{\text{tagged}}_{\text{matched}} = \text{NF}_{\text{overall}} \cdot (\text{SF}_{\text{unmatched}} \cdot \text{SF}_{\text{ratio}} \cdot C_{\text{matched}} + B_{\text{matched}} + L_{\text{matched}}) \tag{7.18}$$

$$N^{\text{untagged}}_{\text{unmatched}} = \text{NF}_{\text{overall}} \cdot \left(\text{SF}^{\text{anti}}_{\text{unmatched}} \cdot C_{\text{unmatched}} + B_{\text{unmatched}} + L_{\text{unmatched}}\right) \tag{7.19}$$

$$N^{\text{untagged}}_{\text{matched}} = \text{NF}_{\text{overall}} \cdot \left(\text{SF}^{\text{anti}}_{\text{matched}} \cdot C_{\text{matched}} + B_{\text{matched}} + L_{\text{matched}}\right) \tag{7.20}$$

Parametrizing the jet yields with a soft muon matched to a jet in this way, allows for a correct estimate of the uncertainties on the ratio SF, taking into account all correlations between events in different regions. Further, jets with and without a soft muon matched to it are scaled with the desired SF. The inefficiency SFs are given by

$$\text{SF}^{\text{anti}}_{\text{unmatched}} = \frac{1 - \epsilon^{\text{MC}}_{\text{unmatched}} \cdot \text{SF}_{\text{unmatched}}}{1 - \epsilon^{\text{MC}}_{\text{unmatched}}} \tag{7.21}$$

$$\text{SF}^{\text{anti}}_{\text{matched}} = \frac{1 - \epsilon^{\text{MC}}_{\text{matched}} \cdot \text{SF}_{\text{matched}}}{1 - \epsilon^{\text{MC}}_{\text{matched}}} \tag{7.22}$$

with the MC efficiencies $\epsilon_{\text{MC}} = \text{MC}_{\text{(un)tagged}}\text{MC}_{\text{overall}}$ for jets tagged or untagged at a specific WP. The overall normalization correction, $\text{NF}_{\text{overall}}$, is fixed to 0.940, the value obtained beforehand. The free floating parameters, which are estimated by the fit, are the SF for jets not matched with a soft muon, $\text{SF}_{\text{unmatched}}$, and the ratio of SFs, SF_{ratio}.

Systematic uncertainties regarding the electron identification and isolation, jet related uncertainties as well as $t\bar{t}$ modelling and scale uncertainties, pileup and JVT uncertainties are considered. In addition, an uncertainty is placed on the light jet normalization. As there are no measurements of soft muon matched light jets in ATLAS, the uncertainties of the SFs from the light jet mis-tag calibration [120] are taken and increased by 50% in the fit.

Pre-fit and post-fit plots for the 60% `DL1r` WP for jets between 65 and 140 GeV are shown in Figures 7.13. In the regions, where a jet is tagged, simulation predicts less jets than there are observed in data. For regions, where the jet is not tagged, the opposite is true, as there are more predicted events than data. The visible trends in the agreement between data and simulation can also be seen for all other WPs and p_{T} bins. The pre-fit and post-fit plots of all regions are located in Appendix E. Further, in the post-fit plots, the overall uncertainty is much smaller compared to the pre-fit distributions. This is expected, as the overall uncertainty is calculated using the estimated correlations between the single uncertainties and different regions by the profile likelihood fit, which leads to the reduction of the overall uncertainty.

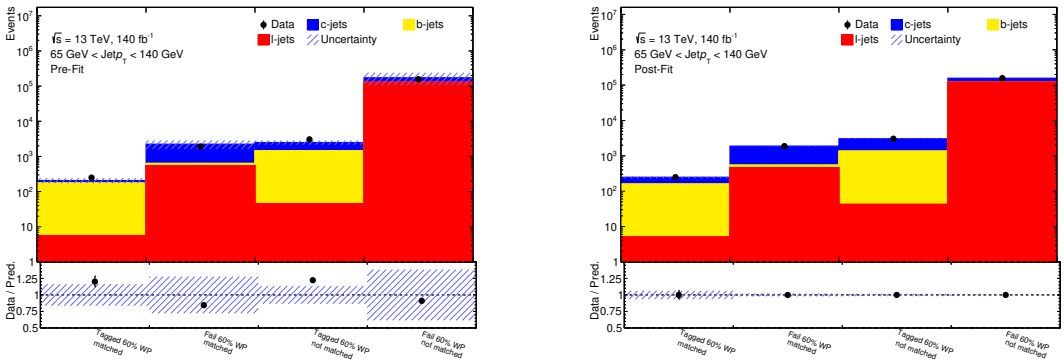

(a) (b)

Figure 7.13: Pre-fit (a) and post-fit (b) plots for events with the p_{T} of the jet being within 65 and 140 GeV for the inclusive c-hadron extrapolation in the SingleWP case. In the bottom panel in each plot, the ratio between data and simulated events is shown. The overall uncertainty is indicated by the blue, shaded error band.

The resulting ratio SFs for each SingleWP case are shown in Figure 7.14. It is visible, that for tighter WPs, the ratio SFs are further away from unity. In general, an agreement between the ratio SFs and unity, which would correspond to no difference between jets with and without a matched soft muon, is only given for the 85% `DL1r` WP and two p_{T} bins for the 77% `DL1r` WP.

In order to further investigate the large differences, the c-jet tagging efficiency for both, jets with and without a soft muon matched and the SFs for both jet types compared, are plotted. The c-jet tagging efficiency is shown in Figure 7.15. The efficiency gets smaller for tighter WPs, illustrating that the rejection rate for c-jets gets larger. For the 85% `DL1r` WP, the efficiency is larger for jets with a soft muon matched. This pattern changes into the opposite for more and more tight WPs. This can be explained as the existence of a soft muon is a strong indicator of a heavy flavor jet, but for tighter WPs, other criteria play a larger role for the `DL1r` score.

With the $\mathrm{SF}_{\mathrm{unmatched}}$ and the $\mathrm{SF}_{\mathrm{ratio}}$ obtained from the profile likelihood procedure, it is possible to calculate the $\mathrm{SF}_{\mathrm{matched}}$ using Equation 7.16. When comparing the SFs for jets matched and not matched to a soft muon, which are shown in Figure 7.16, it is visible that the difference between both gets larger for tighter WPs. Taken into account the agreement between data and simulation pre-fit and these plots, it is apparent, that mis-modelling in the simulation especially for the tighter WPs is present. An investigation would need more kinematic variables and further, variables in which differences between the different quark flavors are visible. Unfortunately, the timeline of this thesis did not permit to further look into this matter.

A comparison between the SFs with a soft muon matched to a jet and the SFs obtained in the primary calibration is shown in Figure 7.17. These plots also illustrate the discrepancy described above, as both SFs are expected to be very close, since both are obtained from

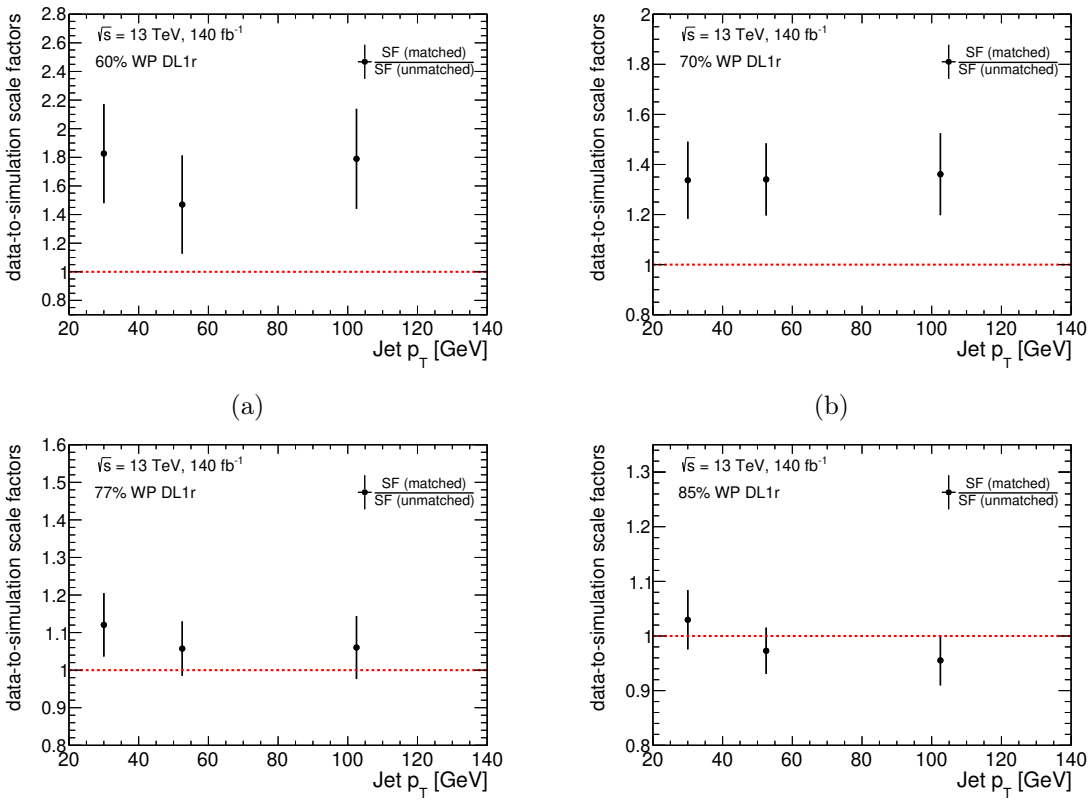

Figure 7.14: Resulting ratio SFs for the SingleWP case in all three p_{T} bins for (a) 60% `DL1r` WP, (b) 70% `DL1r` WP, (c) 77% `DL1r` WP and (d) 85% `DL1r` WP. The black dots show the mean value, the black bars indicate the total uncertainty.

charm jets with a matched soft muon. Further, the scale factors from the extrapolation procedure seem to be mirrored. Another study, which drops the inefficiency SFs in order to test the impact of the regions with the most events but less charm jet contribution. This study only yields small differences in the obtained SFs with comparable uncertainties and further confirms that the mis-modelling of the $t\bar{t}$ events in simulation causes the differences.

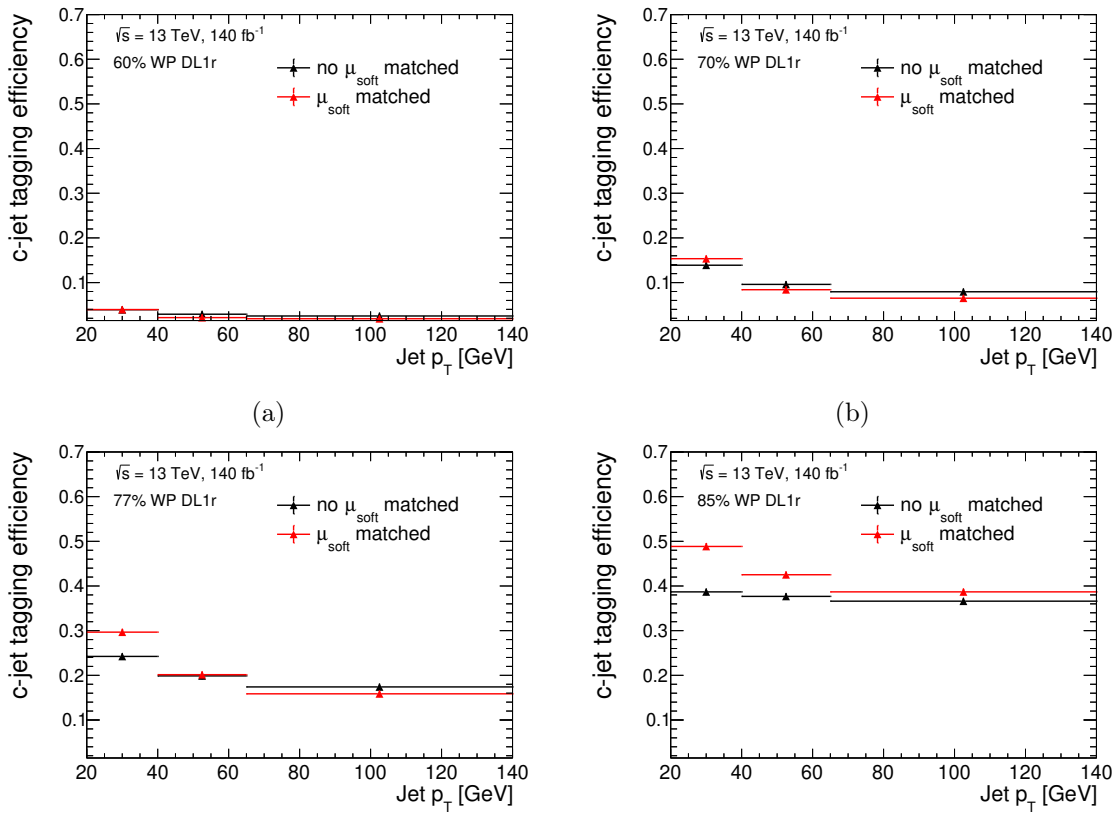

Figure 7.15: c-jet tagging efficiency for the SingleWP case in all p_{T} bins for (a) 60% `DL1r` WP, (b) 70% `DL1r` WP, (c) 77% `DL1r` WP and (d) 85% `DL1r` WP. The black and red dots show the mean value for jets with and without a soft muon matched, respectively. The black and red bars, respectively, indicate the total uncertainty.

PCBT

The extrapolation in the PCBT case is done analogously. Jets are categorized in the five tag-weight bins, i, depending on their `DL1r` score. Further, jets are distinguished by the occurance of a matched soft muon. Consequently, 10 regions are used in the profile likelihood fit. The parametrization of the events, N, in each region is as follows:

$$N^{0}_{\mathrm{unmatched}} = \mathrm{NF}_{\mathrm{overall}} \cdot \left(\mathrm{SF}^{\mathrm{anti},0}_{\mathrm{unmatched}} \cdot C^{0}_{\mathrm{unmatched}} + B^{0}_{\mathrm{unmatched}} + L^{0}_{\mathrm{unmatched}}\right) \tag{7.23}$$

$$N^{0}_{\mathrm{matched}} = \mathrm{NF}_{\mathrm{overall}} \cdot \left(\mathrm{SF}^{\mathrm{anti},0}_{\mathrm{matched}} \cdot C^{0}_{\mathrm{matched}} + B^{0}_{\mathrm{matched}} + L^{0}_{\mathrm{matched}}\right) \tag{7.24}$$

$$N^{i>0}_{\mathrm{unmatched}} = \mathrm{NF}_{\mathrm{overall}} \cdot \left(\mathrm{SF}^{i}_{\mathrm{unmatched}} \cdot C^{i}_{\mathrm{unmatched}} + B^{i}_{\mathrm{unmatched}} + L^{i}_{\mathrm{unmatched}}\right) \tag{7.25}$$

$$N^{i>0}_{\mathrm{matched}} = \mathrm{NF}_{\mathrm{overall}} \cdot \left(\mathrm{SF}^{i}_{\mathrm{unmatched}} \cdot \mathrm{SF}^{i}_{\mathrm{ratio}} \cdot C^{i}_{\mathrm{matched}} + B^{i}_{\mathrm{matched}} + L^{i}_{\mathrm{matched}}\right) \tag{7.26}$$

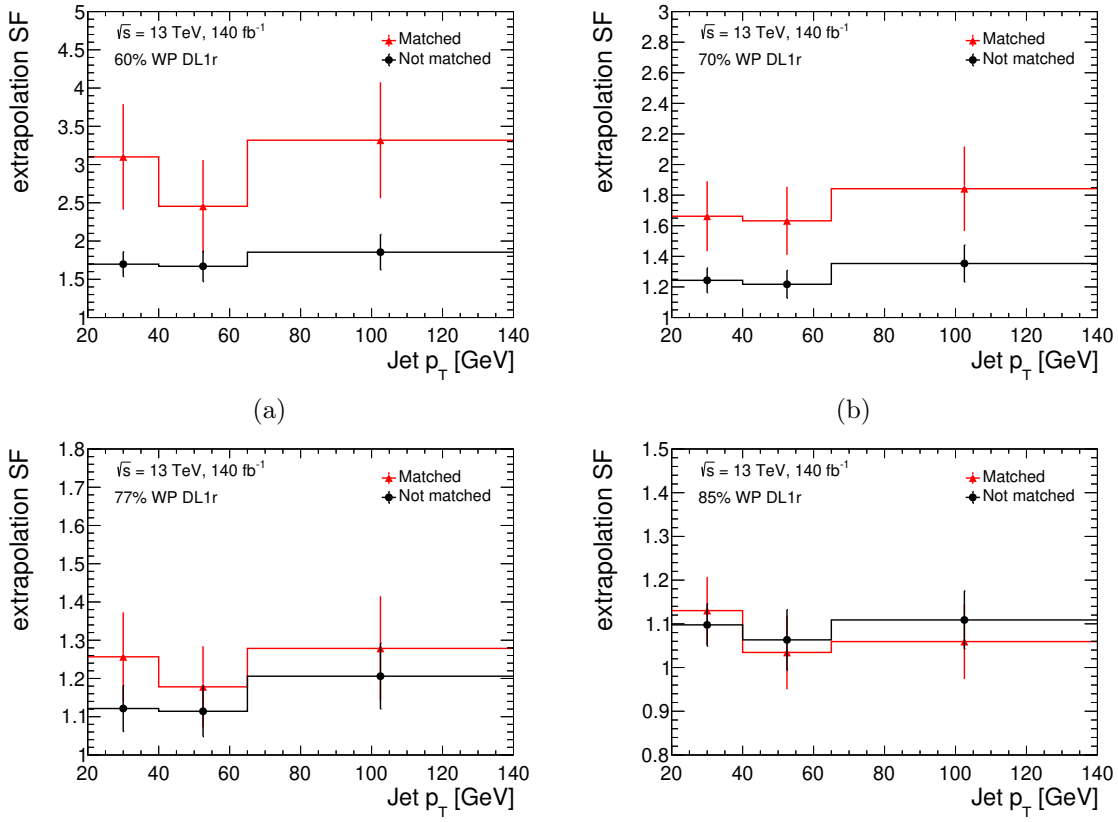

Figure 7.16: Comparison of resulting SFs for jets with and without a soft muon matched for the SingleWP case in all three p_{T} bins for (a) 60% `DL1r` WP, (b) 70% `DL1r` WP, (c) 77% `DL1r` WP and (d) 85% `DL1r` WP. The black and red dots show the mean value, respectively, with the black and red bars indicate the total uncertainty, respectively.

The inefficiency SFs are defined as:

$$\mathrm{SF}^{\mathrm{anti},i}_{\mathrm{unmatched}} = \frac{1-\epsilon^{\mathrm{MC},i}_{\mathrm{unmatched}} \cdot \mathrm{SF}^{i}_{\mathrm{unmatched}}}{1-\epsilon^{\mathrm{MC},i}_{\mathrm{unmatched}}} \tag{7.27}$$

$$\mathrm{SF}^{\mathrm{anti},i}_{\mathrm{matched}} = \frac{1-\epsilon^{\mathrm{MC},i}_{\mathrm{matched}} \cdot \mathrm{SF}^{i}_{\mathrm{matched}}}{1-\epsilon^{\mathrm{MC},i}_{\mathrm{matched}}} \tag{7.28}$$

The overall normalization correction, $\mathrm{NF}_{\mathrm{overall}}$, is fixed to 0.940 again. The free floating parameters in each fit, are the SF for jets not matched with a soft muon, $\mathrm{SF}^{i}_{\mathrm{unmatched}}$, and the ratio SF, $\mathrm{SF}^{i}_{\mathrm{ratio}}$, both for all tag-weight bins, i.e. $i = 0, ..., 5$.

As an example for the pre-fit and post-fit distributions, the jet yields for jets between 20 and 40 GeV are shown in Figure 7.18. Similarly to the primary calibration, the extrapolation

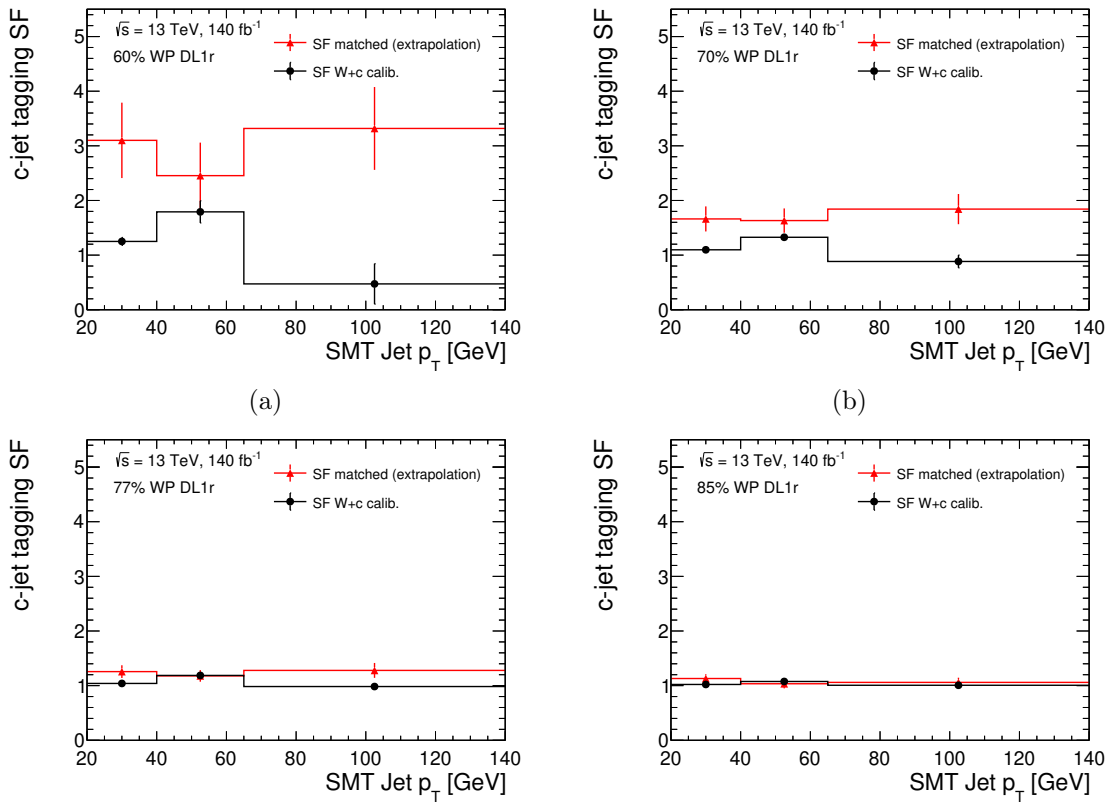

Figure 7.17: Comparison of resulting SFs for jets with a soft muon matched in the extrapolation and the SFs obtained in the primary calibration for the SingleWP case in all three p_{T} bins for (a) 60% `DL1r` WP, (b) 70% `DL1r` WP, (c) 77% `DL1r` WP and (d) 85% `DL1r` WP. The black and red dots show the mean value, respectively, with the black and red bars indicate the total uncertainty, respectively.

fit procedure is done in all tag-weight bins for each jet p_{T} bin. The resulting ratio SFs for each tag-weight bin case are shown in Figure 7.19.

7.5 Comparison with other calibration measurement techniques

As the primary charm mis-tag calibration using W+c-jet events is an alternative calibration to the standard calibration using $t\bar{t}$ events [119], a comparison of the obtained SFs in both calibrations is of significant interest.
In Figure 7.20, the SFs for the SingleWP calibration from both calibrations are shown. The plots reveal some notable differences: For the 70% and 77% `DL1r` WP in the p_{T} range

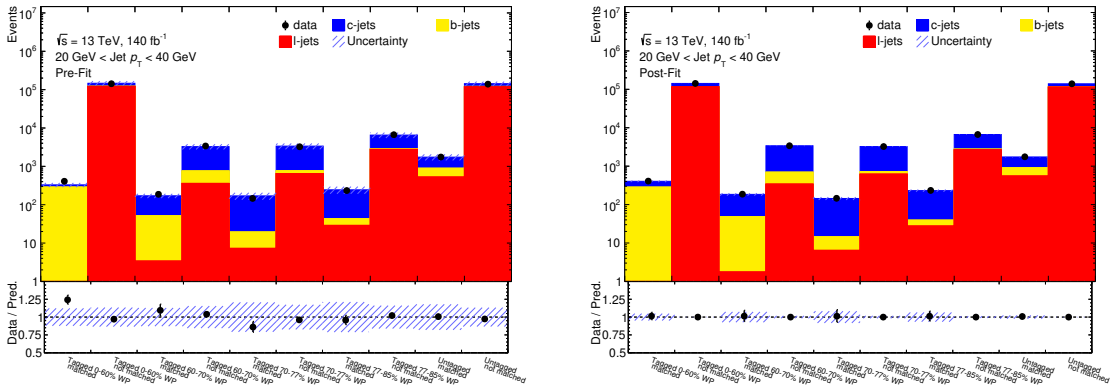

(a) (b)

Figure 7.18: Pre-fit (a) and post-fit (b) plots for events with the p_{T} of the jet being within 20 and 40 GeV for the inclusive c-hadron extrapolation in the PCBT case. In the bottom panel in each plot, the ratio between data and simulated events is shown. The overall uncertainty is indicated by the blue, shaded error band.

of 40 to 65 GeV as well as for the p_{T} bin between 65 and 140 GeV, the SFs from both calibrations are not in agreement within the respective uncertainties. Besides that, these plots show the expected differences with respect to the individual overall uncertainties on the SFs. For jets with a p_{T} between 20 and 40 GeV, the overall uncertainty is either comparable (e.g. for the 60% WP) or much reduced with respect to the $t\bar{t}$ standard calibration. The SFs from the standard calibration also show a smaller dependency on the p_{T}, whereas the SFs from the W+c-jet method show a very similar pattern for all four WPs.

In Figure 7.21, the SFs for the PCBT calibration from both calibrations are shown. All but two SFs are in agreement within the uncertainties. In the low p_{T} bin for jets between 20 and 40 GeV, the overall uncertainties are smaller for the W+c-jet method showing the importance of this calibration. Besides the 0-60% tag-weight bin, the uncertainties for all other p_{T} bins and tag-weight bins are either comparable or even smaller compared to the results obtained in the $t\bar{t}$ standard calibration, illustrating the competitiveness of this alternative calibration.

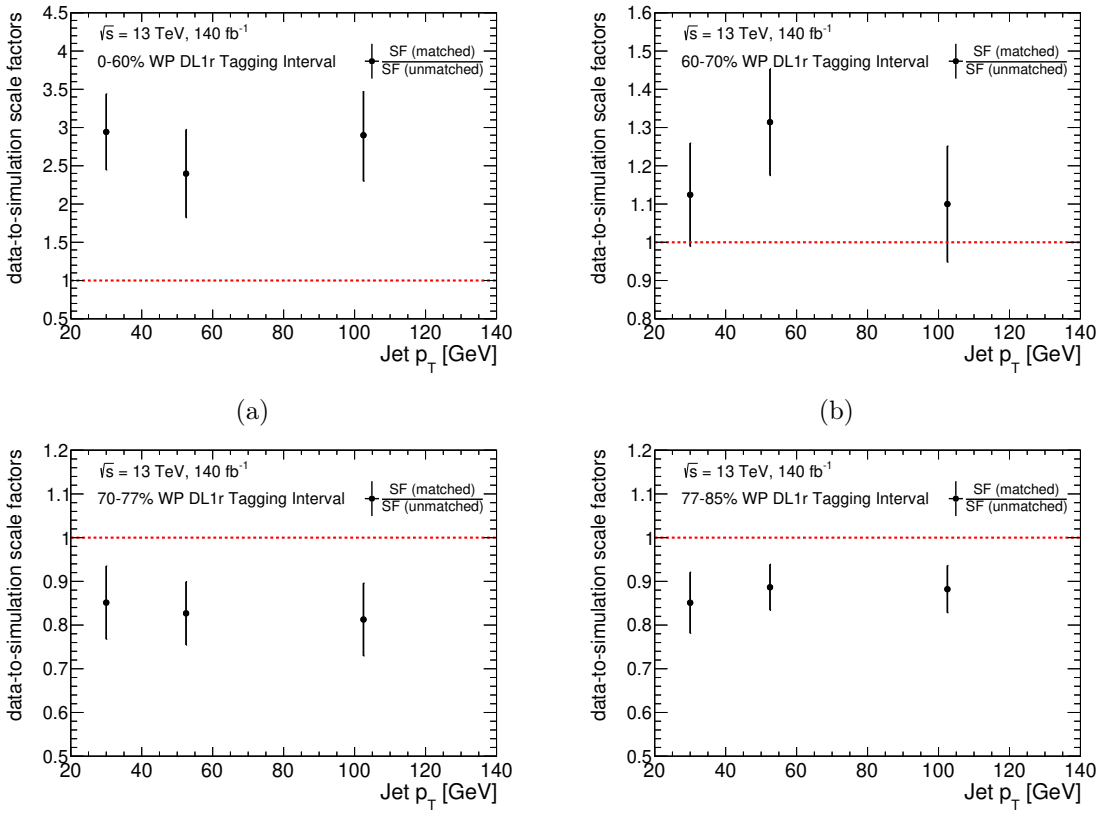

Figure 7.19: Resulting ratio SFs for the PCBT case in all three p_{T} bins for (a) 60% `DL1r` WP, (b) 70% `DL1r` WP, (c) 77% `DL1r` WP and (d) 85% `DL1r` WP. The black dots show the mean value, the black bars indicate the total uncertainty.

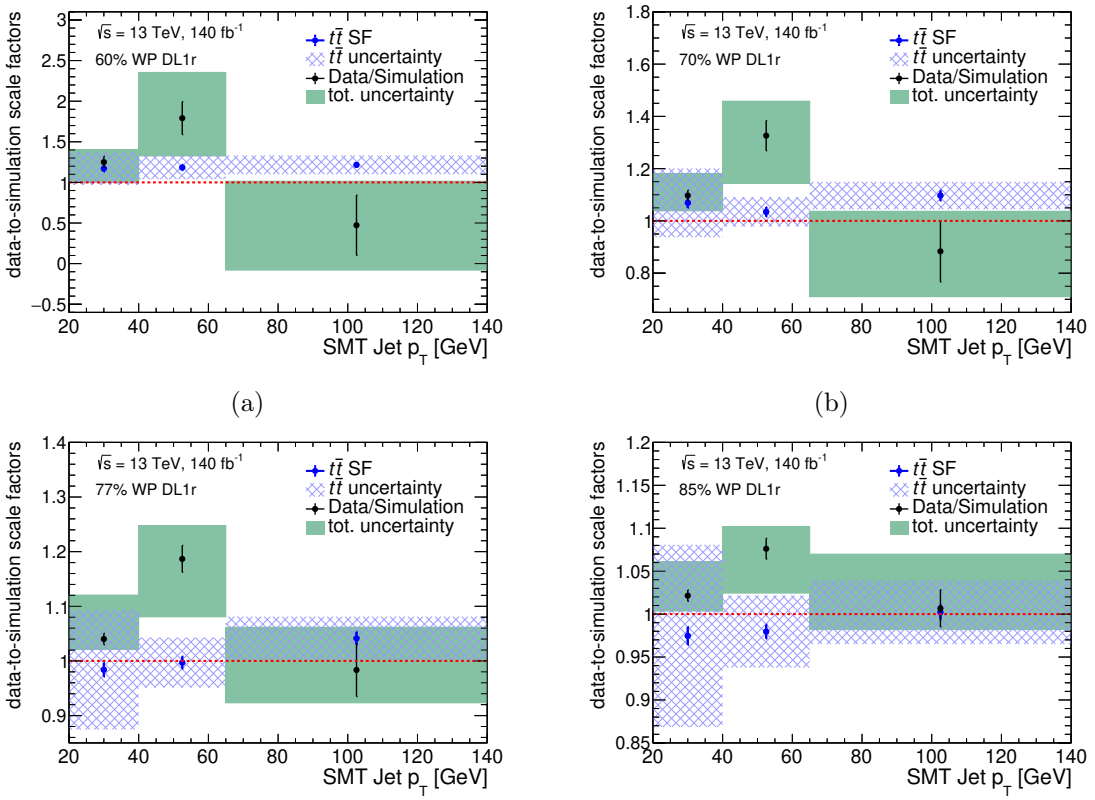

Figure 7.20: Comparison of the SFs obtained with the $t\bar{t}$ based standard calibration and the resulting SingleWP data-to-MC scale factors from the W+c-jet calibration in all three p_{T} bins for (a) 60% `DL1r` WP, (b) 70% `DL1r` WP, (c)77% `DL1r` WP and (d) 85% `DL1r` WP. The black dots show the mean value of the SFs from the W+c-jet method with the black bars indicating the statistical uncertainty. The green boxes illustrate the total uncertainty of the SFs from the W+c-jet method, which is statistical and systematic uncertainties added in quadrature. The blue dots represent the SFs obtained with the $t\bar{t}$ method, with the blue bars representing the statistical uncertainty, and the blue, shaded band showing the total uncertainty.

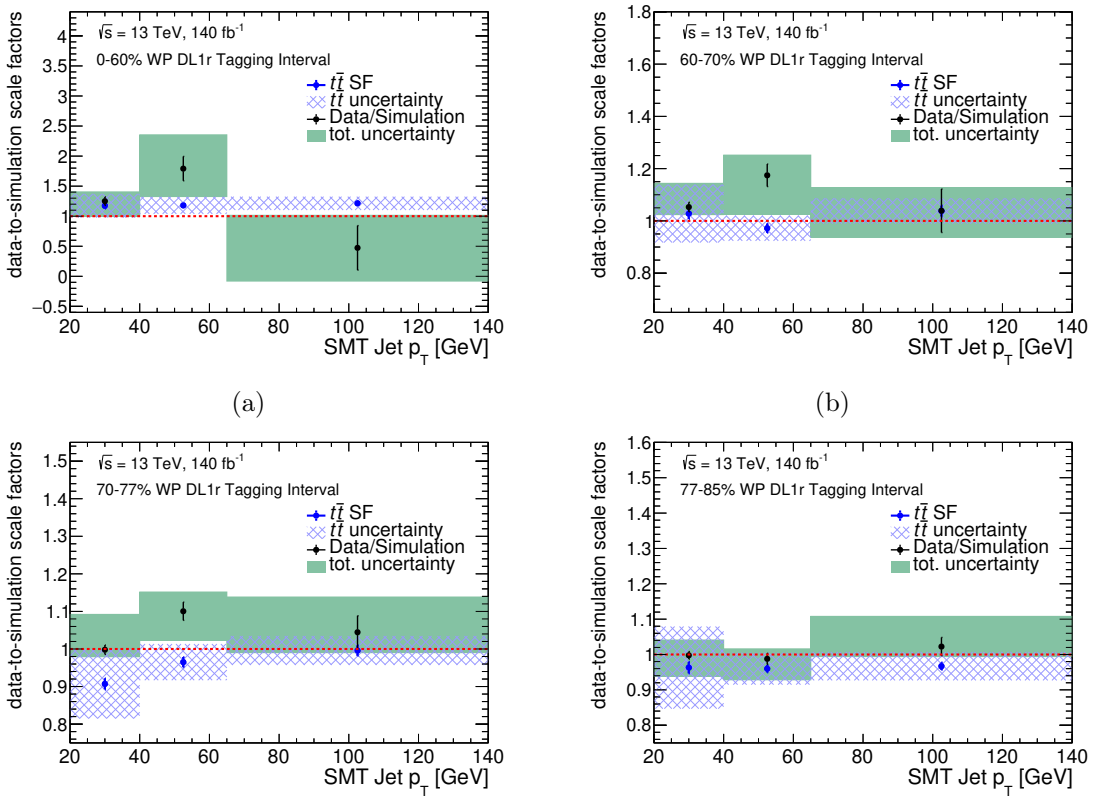

Figure 7.21: Comparison of the SFs obtained with the $t\bar{t}$ based standard calibration and the resulting PCBT data-to-MC scale factors from the W+c-jet calibration in all three p_{T} bins for (a) 0-60% tag-weight bin, (b) 60-70% tag-weight bin, (c)70-77% tag-weight bin and (d) 77-85% tag-weight bin. The black dots show the mean value of the SFs from the W+c-jet method with the black bars indicating the statistical uncertainty. The green boxes illustrate the total uncertainty of the SFs from the W+c-jet method, which is statistical and systematic uncertainties added in quadrature. The blue dots represent the SFs obtained with the $t\bar{t}$ method, with the blue bars representing the statistical uncertainty, and the blue, shaded band showing the total uncertainty.

8 Interpretation of single-top-quark *t*-channel cross section measurement

The parameters of the CKM matrix are free parameters of the SM. They are fundamental in understanding and describing interactions between quarks due to the electroweak interaction. Since there are no theoretical predictions for the values of the CKM matrix elements, they need to be measured experimentally. Therefore, a precise determination of the entries of the CKM matrix is important. At the LHC, top-quarks are produced with a large cross section and the semileptonic decay mode enables a clean decay reconstruction. However, distinguishing between decays involving a down quark or a strange quark, and thus, a precise measurement of $|V_{td}|$ and $|V_{ts}|$, is very challenging. There is no s-tagging algorithm available to date in ATLAS, which would allow for a distinction between top-quark decays into a d-quark or a s-quark, which complicates measurements. Currently, $|V_{td}|$ and $|V_{ts}|$ are determined from $B^0 - \bar{B}^0$ mixing processes, which are dominated by box Feynman diagrams involving top-quarks. Theoretical uncertainties, mainly from lattice QCD calculation, limit the current determinations of $|V_{td}|$ and $|V_{ts}|$. Details on current determinations of $|V_{td}|$ and $|V_{ts}|$ are outlined in Chapter 2.2 and Ref. [19].

An interpretation of the established single-top-quark t-channel cross section analysis, with the goal to measure all three top -quark involved CKM matrix elements, is presented in this Chapter. The single-top-quark t-channel process provides a great opportunity for studies and measurements related to different top-quark production and decay modes, due to its distinct detector signature. Current top-quark analyses, such as the measurement of the single-top-quark t-channel cross section are based on the assumption that $|V_{tb}| = 1$, with event selections optimized for the dominant $t \to Wb$ decay channel. Building on this inclusive cross section measurement an interpretation of the results is performed in order to measure $|V_{tb}|$ and put constraints on the suppressed CKM elements, $|V_{td}|$ and $|V_{ts}|$.

8.1 Overview cross section measurement

The aforementioned single-top-quark t-channel cross section measurement itself using $140\,\text{fb}^{-1}$ of pp collision data collected with the ATLAS experiment was performed by Joshua Reidelstürz et al from the ATLAS group in Wuppertal. The measurement was used for an interpretation for top-quark involved CKM elements, which was performed as part of this thesis. The presented analysis, including the CKM interpretation, was published in a peer reviewed journal [1].

8.1.1 Event selection

The cross section measurement targets the leptonic decay channel of the top-quark, $t \to W^+b$, and top-antiquark, $\bar{t} \to W^-\bar{b}$, respectively, as shown in the example Feynman diagrams in Figure 8.1. Therefore, a charged lepton and a neutrino from the W-boson are expected in the final state, besides a b-quark from the top-quark decay. Another characteristic signature of the t-channel top-quark process, is a spectator quark in forward direction of the detector, $|\eta| < 4.5$, along the top-quark.
An event selection is applied with the aim to maximize the signal contribution, while suppressing background activity. Events are selected with exactly one charged lepton, (ℓ), either an electron or a muon, which is required to have a $p_{\mathrm{T}} > 28\,\mathrm{GeV}$. Further, this charged lepton has to match the lepton object which fired the used single-lepton trigger. The selected lepton is expected to come directly from the hard scattering process, but it can also come from leptonically decying τ leptons. Events with any additional lepton with $p_{\mathrm{T}} > 10\,\mathrm{GeV}$ are rejected in order to reduce contributions from dileptonic $t\bar{t}$ events. At least two jets are required in each event, requiring exactly two jets with $p_{\mathrm{T}} > 30\,\mathrm{GeV}$ and $|\eta| < 4.5$. These two jets are assumed to correspond to the b-quark in the top-quark decay and the spectator quark, respectively. Thus, exactly one jet in the event must be b-tagged at the 60% WP of the `DL1r` tagging algorithm, which needs to be within $|\eta| < 2.5$ since the ID that is required for b-tagging covers that range. For jets with $2.3 < |\eta| < 4.5$, the p_{T} requirement is increased to $p_{\mathrm{T}} > 35\,\mathrm{GeV}$ to prevent known mis-modelling issues in the simulation of the transition region between the central and forward calorimeter.
Due to the expected neutrino from the W-boson decay, a requirement of $E_{\mathrm{T}}^{\mathrm{miss}} > 30\,\mathrm{GeV}$ is placed on the missing transverse momentum in each event. A cut on the transverse W-boson mass, $m_{\mathrm{T}}^{W} > 50\,\mathrm{GeV}$, is included to reduce the multijet background. For the same reason, an additional requirement is set on the p_{T} of the charged lepton, which removes events with a low lepton p_{T} depending on the difference of the azimuthal angle, Φ, between the lepton and the jet with the highest p_{T} in the event:

$$p_{\mathrm{T}}^{\ell} > 40 \cdot \frac{|\Delta\Phi(j,\ell)|}{\pi}. \tag{8.1}$$

To suppress events in which the top-quark is not produced on-shell, a requirement on the invariant mass of the charged lepton and the b-tagged jet, $m_{\ell,b}$ is used. This is important as the theoretical cross section prediction is defined for on-shell top-quarks and does not account for virtual contributions. Based on the relation $m_{\ell,b}^2 = m_t^2 - m_W^2$ for on-shell top-quarks, events are required to fullfil $m_{\ell,b} < 160\,\mathrm{GeV}$. Two separate SRs are constructed afterwards, depending on the electric charge of the lepton. Using both regions allows for an increased sensitivity to both, top-quark and top-antiquark processes. The sensitivity arises from differences in the proton PDFs, which differ for top-quark and top-antiquark production and can be accessed by the properties of the final state particles. Further, six CRs are constructed for a data-driven estimate of the multijet background [1], separately for barrel electrons, endcap electrons, and muons. Similar to the SRs, the CRs are also split by the charge of the reconstructed lepton, but differ by one inverted selection criterion. For electrons, the $E_{\mathrm{T}}^{\mathrm{miss}}$ requirement is inverted, while for muons the requirement defined in Equation (8.1) is inverted. After the selection, the main background process in the

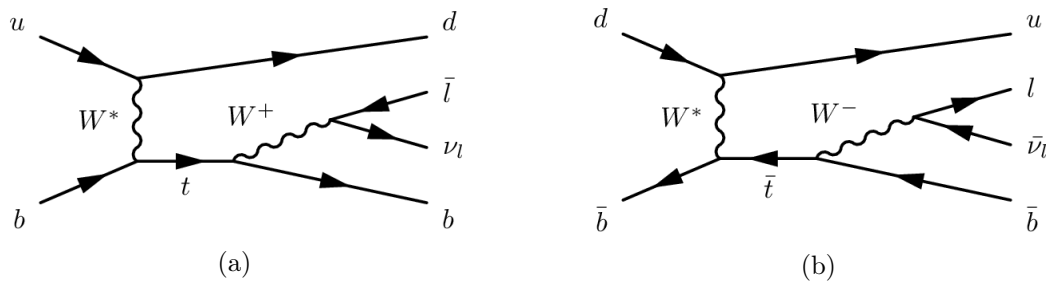

Figure 8.1: Example Feynman diagrams of (a) single-top-quark production and (b) single-top-antiquark production, both via the t-channel exchange of a virtual W boson at LO in perturbation theory [1].

cross section measurement is $t\bar{t}$. These events are selected if either in the semileptonic decay mode just two jets fulfill the selection criteria or in the dileptonic decay mode in which only one lepton survives the object selection. Due to its large cross section, many $t\bar{t}$ events are selected in the SRs. The resulting event yields for all processes in both SRs after the statistical analysis are listed in Figure 8.2.

Process	SR `plus`	SR `minus`
tq	169 000 ± 6000	150 ± 150
$\bar{t}q$	90 ± 90	109 000 ± 4000
$tW + \bar{t}W, t\bar{b} + \bar{t}b$	51 000 ± 4000	49 000 ± 4000
$t\bar{t}$	265 000 ± 14 000	265 000 ± 14 000
W+$b\bar{b}$	198 000 ± 21 000	159 000 ± 17 000
W+$c(\bar{c})$	60 000 ± 13 000	49 000 ± 11 000
Z+jets, diboson	21 000 ± 4000	19 000 ± 4000
Multijet	50 000 ± 10 000	50 000 ± 10 000
Total	814 000 ± 2100	698 800 ± 2000
Observed	814 185	698 845

Figure 8.2: Event yields after the statistical analysis in both used SRs. The cited uncertaintes include all statistical and systematic uncertainties present in the analysis. The event yields are rounded according to the Particle Data Group (PDG) rounding rules. The sum of the single processes do not add up to the total sum given because of correlations in the fit. Taken from Ref. [1].

8.1.2 Event classification using Neural Networks

An artificial feed-forward NN[1] was developed for both SRs to further distinguish between the signal and remaining background events after the selection [1]. A single NN is trained

[1] A more detailed overview on NNs is given in Chapter 9.2.

No.	Symbol	Description
1.	$m(jb)$	Invariant mass of the untagged jet (j) and the b-tagged jet (b)
2.	$\|\eta(j)\|$	Absolute value of the pseudorapidity of the untagged jet
3.	$\|\Delta p_{\mathrm{T}}(W, jb)\|$	Absolute value of the difference in transverse momentum between the reconstructed W boson and the jet pair
4.	$\|\Delta\phi(W, jb)\|$	Absolute value of the difference in azimuthal angle between the reconstructed W boson and the jet pair
5.	$m(t)$	Invariant mass of the reconstructed top quark
6.	$\|\Delta\eta(\ell, j)\|$	Absolute value of the difference in pseudorapidity between the charged lepton (ℓ) and the untagged jet
7.	$\Delta R(\ell, j)$	Angular distance of the charged lepton and the untagged jet
8.	$\|\Delta\eta(b, \ell)\|$	Absolute value of the difference in pseudorapidity between the b-tagged jet and the charged lepton
9.	$m_{\mathrm{T}}(W)$	Transverse mass of the W boson
10.	$m(\ell b)$	Invariant mass of the charged lepton and the b-tagged jet
11.	$H_{\mathrm{T}}(\ell, \text{jets}, E_{\mathrm{T}}^{\text{miss}})$	Scalar sum of the transverse momenta of the charged lepton and the jets and $E_{\mathrm{T}}^{\text{miss}}$
12.	$\|\Delta\eta(b, j)\|$	Absolute value of the difference in the pseudorapidity of the two jets
13.	$\|\Delta\phi(j, t)\|$	Absolute value of the difference in the azimuthal angle between the untagged jet and the reconstructed top quark
14.	$\cos\theta^*(\ell, j)$	Cosine of the angle θ^* between the charged lepton and the untagged jet in the rest frame of the reconstructed top quark
15.	$\|\eta(\ell)\|$	Absolute value of the pseudorapidity of the charged lepton
16.	S	Sphericity defined as the sum of the 2nd and 3rd largest eigenvalues of the sphericity tensor multiplied by 3/2
17.	$\|\Delta p_{\mathrm{T}}(\ell, j)\|$	Absolute value of the difference in transverse momentum of the charged lepton and the untagged jet

Figure 8.3: List of the 17 variables constructed and used for the NN training sorted by their discriminating power. The sphericity tensor is defined as $S^{\alpha\beta} = \sum_i p_i^\alpha p_i^\beta / \sum_i |\vec{p}_i|^2$. Here, α and β correspond to the spatial components x, y, and z of the three-momenta, $\vec{p}_i$, of the reconstructed jets, charged lepton and reconstructed neutrino. Taken from Ref. [1].

in both regions combined, as the kinematic distribution of top-quark and top-antiquark events are very similar and a scenario with two separate NNs for each SR gave a similar sensitivity. The NN is implemented using the `NeuroBayes` package [188] [189]. One hidden layer with 22 nodes is used between the input node and the output node. The output node gives a continuous output in the interval $(-1, +1)$, which is linearly scaled to the interval $(0, 1)$. In the training, all considered backgrounds, weighted accordingly to their expected number of events, are trained against. An equal number of signal and background events is used in the training. The NN uses 17 input variables, constructed from various kinematic quantities of the final state objects. In Figure 8.3, the input variables are listed ordered by their importance to the NN training. The reconstruction of the top-quark is needed for variables used in the NN, e.g. its invariant mass, and is conducted using the

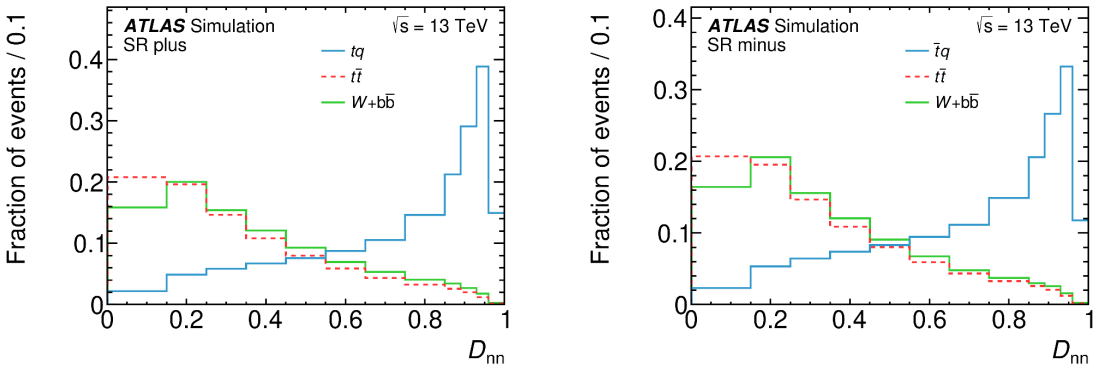

(a) (b)

Figure 8.4: Probability densities of the NN discriminants (a) for the tq and (b) for the $t\bar{t}q$ signal processes, and for the largest background contributions, $t\bar{t}$ and $W + b\bar{b}$, in the respective SRs. Taken from Ref. [1].

four-momenta of its decay products [190]. The reconstruction procedure is necessary since the top-quark decays before it reaches the detector and therefore, its properties need to be reconstructed from detected final-state particles. Hereby, the four-momenta of the charged lepton and the b-tagged jet are precisely determined, whereas for the four-momentum of the neutrino only the transverse components, p_x and p_y, are known as it is assumed to be measured as $E_{\mathrm{T}}^{\mathrm{miss}}$. The determination of the p_z of the neutrino is done using the pole mass of the W-boson, $m_W = 80.4\,\mathrm{GeV}$, as a constraint. Using this constraint leads to a quadratic equation for p_z, which therefore yields two possible solutions. The smaller of these two solutions is selected. In cases, where the reconstructed W-boson mass in the calculation is less than m_W used in the constraint a complex solution is obtained. This can happen due to resolution uncertainties of the $E_{\mathrm{T}}^{\mathrm{miss}}$ measurement or if there are no on-shell W-bosons in an event. To avoid these complex solutions, a correction procedure is applied [191]. Here, p_x and p_y are adjusted to maintain the mass constraint of the W-boson. Two new solutions are obtained. In the end, the smaller solution that minimizes the difference between the measured and the modifited values of p_x and p_y is selected which keeps the transverse energy of the neutrino close to the measured $E_{\mathrm{T}}^{\mathrm{miss}}$. To reconstruct the top-quark, the four-momenta of the W-boson, calculated by adding the four-momenta of the neutrino and charged lepton, and the b-jet are added.
The normalized NN output distributions for both SRs are shown in Figure 8.4. The NN is able to distinguish well between the single-top-quark signal and the two largest background sources, $t\bar{t}$ and W+heavy flavor jets. The probability densities of the NN in both SRs are used in a profile likelihood fit procedure in which the t-channel cross sections of both, single-top-quark and top-antiquark are determined. As this procedure is also used by the CKM interpretation and subsequently in the developed analysis presented in Chapter 9.5, it is described in detail here.

8.1.3 Profile likelihood fit procedure

The statistical analysis of the single-top-quark t-channel cross section measurement is performed using a binned profile likelihood fit. In the fit the simulated events are compared with the measured data using a likelihood, $L(\mathbf{k}|\mathbf{x})$, defined as

$$L(\tilde{\mathbf{k}}|\vec{x}) = \prod_i P\left(x_i|\vec{k}\right). \tag{8.2}$$

Here, x_i correspond to the data with $\vec{k}$ being parameters on which the predictions from simulation depend. The result of a fit using this likelihood approach are the estimated values $\hat{\vec{k}}$ which maximize the likelihood, hence the method is called the maximum likelihood method.

In ATLAS, the `HistFactory` [192] model is employed for binned template fits, which utilizes simulation-based template histograms for the predictions. The `HistFactory` model assumes a counting experiment, thus the likelihood is build from Poissonian probability densities including the predicted event yields and the measured data. Neglecting any systematic or MC statistical uncertainties, the likelihood can be expressed as

$$\mathcal{L}(\mathbf{n}|\mu) = \prod_{i\in\text{bins}} \text{Pois}(n_i|v_i(\mu)), \tag{8.3}$$

where n_i denotes the number of measured data events in bin i and $v_i(\mu)$ the number of predicted events in bin i, with μ representing the parameters of interest (POIs) in the likelihood. In this cross section measurement, v_i is defined as

$$v_i(\mu) = \mu_{tq} S_i^{tq} + \mu_{\bar{t}q} S_i^{\bar{t}q} + \sum_j B_{ij}. \tag{8.4}$$

The predicted number of t-channel events for single-top-quark and single top-antiquark production, S_i^{tq} and $S_i^{\bar{t}q}$, are scaled by the respective signal strength parameters, $\mu_{tq}, \mu_{\bar{t}q}$. The signal strength is defined as

$$\mu = \frac{\sigma_P^{\text{measured}}}{\sigma_P^{\text{SM}}}, \tag{8.5}$$

i.e. the ratio of the measured cross section and the SM prediction for a process P. The expected number of each contributing background process, j, is denoted by B_{ij}.
Adding systematic uncertainties, which affect the simulated events, yields in an auxiliary term in the likelihood function.

$$\mathcal{L}(\mathbf{n}, \theta^0|\mu, \theta) = \prod_{i\in\text{bins}} \text{Pois}(n_i|v_i(\mu)) \prod_j \text{Gauss}(\theta^0|\theta_j, \Delta\theta_j) \tag{8.6}$$

Systematic uncertainties are incorporated as nuisance parameters (NPs), θ, into the likelihood. The auxiliary term is a Gaussian probability density function in which the auxiliary measurement on a corresponding NP is implemented. The convention is that

each Gaussian has a mean value $\theta^0 = 0$ and a standard deviation of $\Delta\theta = 1$. A value of $\theta_j = 0$ corresponds to the nominal prediction, while $\theta_j = \pm 1$ correspond to the upper and lower 1σ bounds of the auxiliary measurement (*up* and *down* variation). Thus, a prediction for three values of θ is obtained, and an interpolation between these values and extrapolation beyond them is done to obtain model predictions for any value of θ. Each systematic uncertainty can impact either the shape of the nominal distributions or the normalization or both. Distributions are split into a pure shape component and a pure normalization component, as there are different interpolation and extrapolation strategies for each. The shape component uses bin-by-bin linear interpolation, which is defined as

$$\sigma_{b,p}(\alpha) = \sigma^0_{b,p} + I_{b,p,\text{lin}}, \tag{8.7}$$

with

$$I_{b,p,\text{lin}} = \begin{cases} \alpha \left(I^+_{b,p} - I^0_{b,p} \right) & \alpha \geq 0, \\ \alpha \left(I^0_{b,p} - I^-_{b,p} \right) & \alpha < 0. \end{cases} \tag{8.8}$$

Here, $I^+_{b,p}, I^-_{b,p}$ and $I^0_{b,p}$ denote the expected event yields for $\theta = -1, 0, +1$, respectively, for a process p in a histogram bin b. In contrast, a polynomial interpolation and an exponential extrapolation is used for the normalization component:

$$\eta_p(\alpha) = \begin{cases} \left(\frac{I^+_p}{I^0_p} \right)^{\alpha} & \alpha \geq 1, \\ 1 + \sum_{i=1}^{6} a_i \alpha^i & |\alpha| < 1, \\ \left(\frac{I^-_p}{I^0_p} \right)^{-\alpha} & \alpha \leq -1. \end{cases} \tag{8.9}$$

Hereby, t he interpolation factor, a_i, is fixed such that it matches the boundary conditions $\eta(\alpha = \pm 1)$, $\mathrm{d}\eta/\mathrm{d}\alpha|_{\alpha=\pm 1}$ and $\mathrm{d}^2\eta/\mathrm{d}\alpha^2|_{\alpha=\pm 1}$. This choice can result in negative values for the extrapolation, however, in practical applications this was found to not be the case. On the contrary, this approach avoids discontinuous first and second derivatives of η which can cause numerical instabilities during the minimization.
The input templates for the $\theta = \pm 1$ varied nuisance parameters can be affected by statistical fluctuations, as can the nominal prediction. The correlation between the statistical uncertainties of the nominal prediction and the varied templates depends on how the templates were generated. Moreover, the statistical uncertainty in the varied templates themselves is not directly included in the fit procedure. Instead, it affects the estimation of the uncertainties in the measured parameters μ. In order to mitigate the impact of statistical fluctuations in the variation templates on the measurement and the convergence of the fit, a *smoothing* algorithm is applied. For the t-channel cross section measurement a custom algorithm is applied [193] [194]. It uses two main steps, a rebinning step to decrease the statistical fluctuations and a smoothing step to interpolate the results back to the original binning. In the rebinning step, adjacent bins are merged under rules depending on the bin-wise ratios of the original template and the rebinned template. Afterwards, the rebinned ratio template build in the first step, is smoothed by the `TH1::SMOOTH()` algorithm of the `ROOT` [195] library in multiplie steps, described in Ref. [196]. Smoothing

is only applied to the nuisance parameters that were found to be constrained, i.e. whose post-fit uncertainties are substantially reduced compared to their pre-fit uncertainites.
There are cases in which both input template histograms for a systematic uncertainties are very asymmetric around the nominal prediction, or that there is just a one-sided variation. In such cases, a *symmetrization* is applied, in which the average of both variation is taken or the one-sided variation, respectively, and symmetrized around the nominal distribution to obtain the other variation.
Another factor in the stability of the fit procedure is the overall number of NPs, which can get very large depending on the number of physics objects used and their respective uncertainties. To reduce the number of NPs, a *pruning* step is done. During this step, systematic uncertainties which are considered to have a negligible impact on the uncertainties of the POI are removed. For this purpose, the effect on the fit is calculated as $|\text{variation}/(\text{nominal} - 1)| < \text{X}\%$ for the normalization component of a systematic uncertainty and $|\text{variation}/(\text{nominal} - 1)| < \text{Y}\%$ in all bins for the shape component after the variation is normalized to the same overall integral. In this analysis, a normalization component is then removed if the effect on the fit is smaller than 0.5% and a shape component is pruned if the effects are smaller than 0.5% in each bin. This procedure is done per region and per MC sample present in the fit.

In addition to systematic uncertainties, the statistical uncertainties due to the finite number simulated MC events are incorporated into the likelihood by the `HistFactory` model employing another set of dedicated NPs, which are described by, γ_i [192]. The whole procedure follows the prescription given by Barlow and Beeston in Ref. [197]. Contrary to the systematic uncertainties, a Poisson constraint term, $\text{Pois}(m_b|\gamma_b\tau_b)$ is used here. The event yields for the nominal prediction in a bin b are given by $m_b = \left(\delta_b/v_b^{\text{MC}}\right)^2$ with δ_b being the total statistical uncertainty. v_b^{MC} is the number of predicted MC simulated events where the statistical uncertainty need to be accounted for. The effective number of predicted events in bin b are given by $\tau_b = \left(v_b^{\text{MC}}/\delta_b\right)^2$ and is treated as a fixed value. The NP is labeled as γ_b, which acts as a scale factor to all yields in a bin b. This approach is chosen, as assigning individual γ factors for each process would increase the number of additional parameters in the likelihood significantly. That could affect the numerical stability of the fit procedure. Hence, for each bin a single constraint term is assigned to all processes.

The complete likelihood becomes

$$\mathcal{L}(\mathbf{n}, \theta^0|\mu, \theta, \gamma) = \prod_{i\in\text{bins}} \text{Pois}(n_i|v_i(\mu)) \prod_j \text{Gauss}(\theta^0|\theta_j, \Delta\theta_j) \prod_k \text{Pois}(m_k|\gamma_k\tau_k). \quad (8.10)$$

In practice, the negative logarithm of the likelihood is minimized instead of just maximizing the likelihood in order to avoid instabilities because of numerical limitations. The minimization is carried out by using `MINUIT` with the `MIGRAD` algorithm [184]. The uncertainties on the profile likelihood parameters are determined using the `MINOS` algorithm.

Two fits are performed to obtain the results of the analysis. In the first fit, the cross sections of both, single-top-quark and single-top-antiquark, are obtained. In a second fit,

the ratio of both processes as well as the total t-channel cross section is determined. The POIs in the first fit correspond to the signal strengths of the single-top-quark process, μ_t, and the single-top-antiquark process, $\mu_{\bar{t}}$. Both are used to calculate the measured cross sections from the fit using

$$\sigma_t = \mu_t \cdot \sigma_t^{\mathrm{SM}}$$
$$\sigma_{\bar{t}} = \mu_{\bar{t}} \cdot \sigma_{\bar{t}}^{\mathrm{SM}}$$

Since the ratio of both cross sections, R_t, is also measured, a parametrization of the signal event normalization is determined for the second fit, allowing to utilize two different POIs, μ_{tch} and μ_{R_t}, in the likelihood fit [194]. The profile likelihood fit is done simultaneously in both SRs and the six CRs combined. In both SRs, the neural network output distribution is fitted.

The performed fit to data, yields in likelihood estimators for all nuisance parameters and POIs such that these maximize the likelihood given in Equation 8.10. Setting all parameters to these 'so called' *post-fit* values, they can be applied to the fitted distributions according to the used parametrization. The plots for the post-fit distributions of the NN output distributions in both SRs are shown in Figure 8.5. The resulting cross sections from the first fit are [1]

$$\sigma_t = 137^{+8}_{-8}\,\mathrm{pb},$$

and

$$\sigma_{\bar{t}} = 84^{+6}_{-5}\,\mathrm{pb}.$$

The NNLO predictions for these cross sections are in good agreement with the results from the measurement. The combined cross section is measured to be

$$\sigma_{t+\bar{t}} = 221^{+13}_{-13}\,\mathrm{pb},$$

with the ratio being determined as

$$R_t = 1.636^{+0.036}_{-0.034}.$$

Signal modelling uncertainties, related primarily to the choice of the parton shower and hadronization model, are the dominant sources of systematic uncertainties [1]. In general, the cross section measurement is limited in precision by systematic uncertainties. The impact of different groups of systematic uncertainties on the results is given in Figure 8.6. Several interpretations of this measurement have been performed in order to gain additional insights, e.g. about PDF sets at NNLO. These interpretations and their results are published in Ref. [1] as well but are not discussed further in this thesis. Within the scope of this thesis, an interpretation regarding the CKM matrix elements involving the top-quark has been conducted, that was included in the same publication. In the following chapter, this interpretation is presented in detail, including the methodology and results.

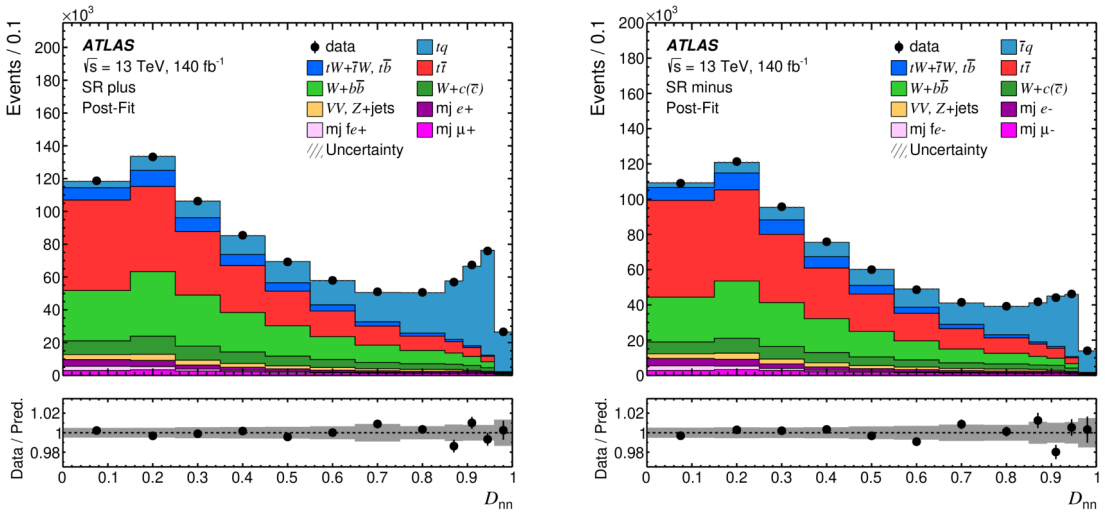

(a) (b)

Figure 8.5: Post-fit NN discriminant distributions (a) in the SRplus and (b) in the SRminus, for all predicted events and the measured data. The signal contribution is shown stacked on top of all considered background contributions. The ratio plot in the lower panel shows the ratio between data and the prediction. The hatched band around the prediction as well as the grey band in the ratio plot indicate the overall uncertainty from all sources considered in this measurement [1].

8.2 CKM interpretation

A determination of $f_{\mathrm{LV}} \cdot |V_{tb}|$ is done in the cross section measurement as the t-channel cross section is proportional to $f_{\mathrm{LV}}^2 \cdot |V_{tb}|^2$. Here, f_{LV} denotes the left-handed form factor, which is exactly one in the SM. It is introduced representing a potential non-standard gauge coupling at the Wtb vertex in Ref. [198]. BSM contributions could alter the value of f_{LV} significantly. An important assumption made for the determination is that $|V_{tb}| \gg |V_{td}|, |V_{ts}|$. The obtained result is the most precise result to date: $f_{\mathrm{LV}} \cdot |V_{tb}| = 1.015 \pm 0.031$ [1].

The above mentioned determination neglects all contributions due to Wts and Wtd vertices. To avoid this caveat, a more generalized CKM interpretation of the cross section measurement results is performed. Each possible single-top-quark and single-top-antiquark t-channel process, i.e. the three different production modes and the three different decay modes, are simulated. Thus, all possible combinations of Wtx vertices, with $x = b, d, s$, are considered. Additionally, all possible $t\bar{t}$ decay modes were also simulated in order to enhance the sensitivity to $|V_{td}|, |V_{ts}|$ in the interpretation. Schematic Feynman diagrams for the different single-top-quark t-channel processes and the different $t\bar{t}$ processes are shown in Figure 8.7. The details of the produced MC samples are described in Chapter 5.2.3. Other top-quark involved processes, e.g. tW and $t\bar{b}$ s-channel production, are neglected since the corresponding yields are much smaller than the yields for tq and $t\bar{t}$.
The same event selection as for the cross section measurement is applied to these samples.

Uncertainty group	$\Delta\sigma(tq)/\sigma(tq)$	$\Delta\sigma(\bar{t}q)/\sigma(\bar{t}q)$	$\Delta\sigma(tq+\bar{t}q)/\sigma(tq+\bar{t}q)$	$\Delta R_t/R_t$
Data statistics	+0.4 / −0.4	+0.5 / −0.5	+0.3 / −0.3	+0.6 / −0.6
Signal modelling	+4.9 / −4.5	+5.2 / −4.8	+5.0 / −4.6	+0.9 / −0.9
Background modelling	+1.8 / −1.6	+2.1 / −1.9	+1.8 / −1.6	+1.5 / −1.4
MC statistics	+1.0 / −1.0	+1.4 / −1.3	+1.1 / −1.0	+0.8 / −0.8
PDFs	+0.4 / −0.4	+1.2 / −1.0	+0.6 / −0.6	+0.9 / −0.8
Jets	+2.2 / −2.0	+3.0 / −2.7	+2.5 / −2.2	+1.0 / −0.9
b-tagging	+1.6 / −1.5	+1.7 / −1.5	+1.6 / −1.5	+0.2 / −0.1
Leptons	+1.1 / −1.0	+1.1 / −1.0	+1.1 / −1.0	+0.1 / −0.1
Luminosity	+0.9 / −0.8	+0.9 / −0.9	+0.9 / −0.8	< 0.1
Total	+5.9 / −5.5	+6.6 / −6.2	+6.1 / −5.7	+2.2 / −2.1

Figure 8.6: Impact of different groups of systematic uncertainties on single-top-quark and single-top-antiquark t-channel cross sections, respectively. as well as their combination and their ratio. Taken from Ref. [1].

Afterwards, the remaining events are evaluated with the NN. The NN output probabilities for each process are used in three different profile likelihood scan setups to obtain limits on the three CKM elements.

8.2.1 Effect of the event selection

The event selection with the requirement of exactly one b-tagged jet, represents one of the biggest challenges for the CKM interpretation. Especially looking for the suppressed top-quark decays into d- or s-quarks, this requirement has a large impact on the acceptance rate of these events. The acceptance rate is defined as the number of events passing the event

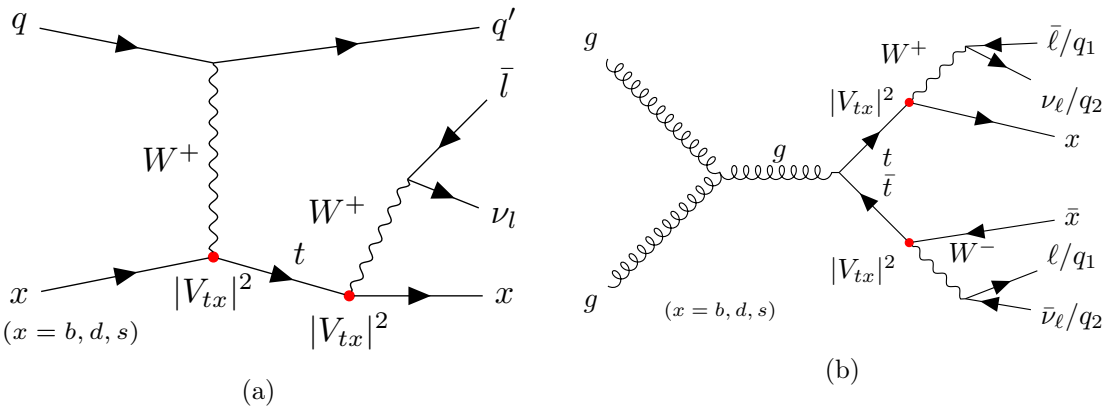

Figure 8.7: Schematic example Feynman diagrams of (a) single-top-quark t-channel production and (b) $t\bar{t}$ production. The red dot indicates the vertices with the different possible top-quark interactions.

selection divided by the number of events before the selection is applied. The acceptance rates and corresponding event yields for all single-top-quark and single-top-antiquark processes are shown in Table 8.1, while the acceptance rate for all $t\bar{t}$ processes are listed in Table 8.2. For the t-channel processes, the yields are calculated using the cross sections from Tables 5.2, which are calculated with the assumption of the CKM matrix element present in the top-quark and top-antiquark production being one. Hence, the most events passing the selection are for $d \to t$ production processes in the table. For the $t\bar{t}$ processes, the cross sections explained in Chapter 5.2.3 are used. Hence, for processes with both, the top-quark and the top-antiquark decaying into the same light quark, the event yields are higher after the selection. Using these assumptions simplifies the statistical analysis due to the parametrization calculated, which is explained in detail in the next chapter. The acceptance rates for both, t-channel and $t\bar{t}$ CKM processes, show an expected behavior with similar final states, e.g. light-quarks or b-quarks from the top-(anti)quark decays, resulting in similar acceptance values.
In Figure 8.8, the normalized NN output distributions for all single-top-quark processes in the inclusive SR (not divided by lepton charge) are shown. For the processes in which

Table 8.1: List of all acceptance rates and the corresponding expected reconstructed event yields for each single-top-quark and top-antiquark process added in the CKM interpretation for $\mathcal{L} = 140\text{fb}^{-1}$. The yields are calculated using the cross section calculations from Table 5.2, which suppose $|V_{tx}| = 1$ for $x = b, d, s$, respectively. The shown uncertainties are the statistical uncertainties.

Process	Acceptance	Event yields
$\bar{b} \to \bar{t}, \bar{t} \to \bar{d}$	0.0040	5000 ± 100
$b \to t, t \to d$	0.0039	8120 ± 160
$\bar{b} \to \bar{t}, \bar{t} \to \bar{s}$	0.0040	5000 ± 100
$b \to t, t \to s$	0.0039	8000 ± 500
$\bar{d} \to \bar{t}, \bar{t} \to \bar{b}$	0.0309	$170\,800 \pm 400$
$d \to t, t \to b$	0.0242	$353\,100 \pm 1200$
$\bar{d} \to \bar{t}, \bar{t} \to \bar{d}$	0.0002	1050 ± 40
$d \to t, t \to d$	0.0001	2600 ± 100
$\bar{d} \to \bar{t}, \bar{t} \to \bar{s}$	0.0002	1040 ± 40
$d \to t, t \to s$	0.0002	2700 ± 100
$\bar{s} \to \bar{t}, \bar{t} \to \bar{b}$	0.0309	$112\,770 \pm 280$
$s \to t, t \to b$	0.0280	$144\,100 \pm 500$
$\bar{s} \to \bar{t}, \bar{t} \to \bar{d}$	0.0002	620 ± 24
$s \to t, t \to d$	0.0002	880 ± 30
$\bar{s} \to \bar{t}, \bar{t} \to \bar{s}$	0.0002	630 ± 24
$s \to t, t \to s$	0.0002	960 ± 30

Table 8.2: List of all acceptance rates and the corresponding yields for each $t\bar{t}$ process added in the CKM interpretation for $\mathcal{L} = 140\text{fb}^{-1}$. This table includes both, the semileptonic decay modes and the dileptonic decay modes using the cross section calculations explained in Chapter 5.2.3. The shown uncertainties are the statistical uncertainties.

Process	Acceptance	Event yields
$t \to Wb, \bar{t} \to W\bar{d}$	0.00608	$89\,360 \pm 250$
$t \to Wb, \bar{t} \to W\bar{s}$	0.00617	$90\,720 \pm 260$
$t \to Wd, \bar{t} \to W\bar{b}$	0.00608	$89\,160 \pm 250$
$t \to Wd, \bar{t} \to W\bar{d}$	0.00008	4740 ± 90
$t \to Wd, \bar{t} \to W\bar{s}$	0.00008	1140 ± 40
$t \to Ws, \bar{t} \to W\bar{b}$	0.00617	$91\,120 \pm 260$
$t \to Ws, \bar{t} \to W\bar{d}$	0.00009	1200 ± 100
$t \to Ws, \bar{t} \to W\bar{s}$	0.00009	4930 ± 40

the top decays into a b-quark, the NN is able to assign it predominantly as signal. This is expected as many variables used in the NN training make use of b-tagging information and the signal process it was trained on has the same top-quark decay. Processes in which the top-quark originates from a b-quark from gluon splitting are categorized more often as a background. The reason for this is, that usually the jet formed from the second b-quark from the gluon splitting, which did not produce the top-quark, is tagged for these events. Due to this b-tagged jet not coming from the top-quark decay, the constructed variables with this jet used as input by the NN do match more closely these from background events. For all other processes, the NN output distribution is more flat, which shows that some events are classified as more signal-like, while others are more background like, which is expected since a jet in the event of processes with $t \to d, s$ needs to be mis-tagged as a b-jet. This does not need to be the jet from the top-quark decay, but it can also be the spectator jet or a jet from initial state radiation (ISR) or FSR, leading to kinematic distributions and constructed variables which do not exhibit the same characteristics as the ones from the signal process used in the training.
In Figure 8.9, the NN output distributions for all $t\bar{t}$ processes in the inclusive SR are shown, divided into dileptonic decay mode and semileptonic decay mode. It is visible that all $t\bar{t}$ processes are more often classified as background process by the NN, exactly as the nominal $t\bar{t}$ process. This is expected as, the purpose of the NN in the cross section analysis was the distinction of the signal process and the largest background contribution, which is $t\bar{t}$. The NN output distributions for each different process are very similar. Additionally, the latter ones are classified even more often as background than the events with a correctly tagged b-jet.
These NN output probabilities are utilized, on top of the NN output distributions of all other processes present in the analysis, to derive limits on the top-quark involved CKM elements. As a first step, the expected yields are parametrized based on the occuring CKM matrix elements.

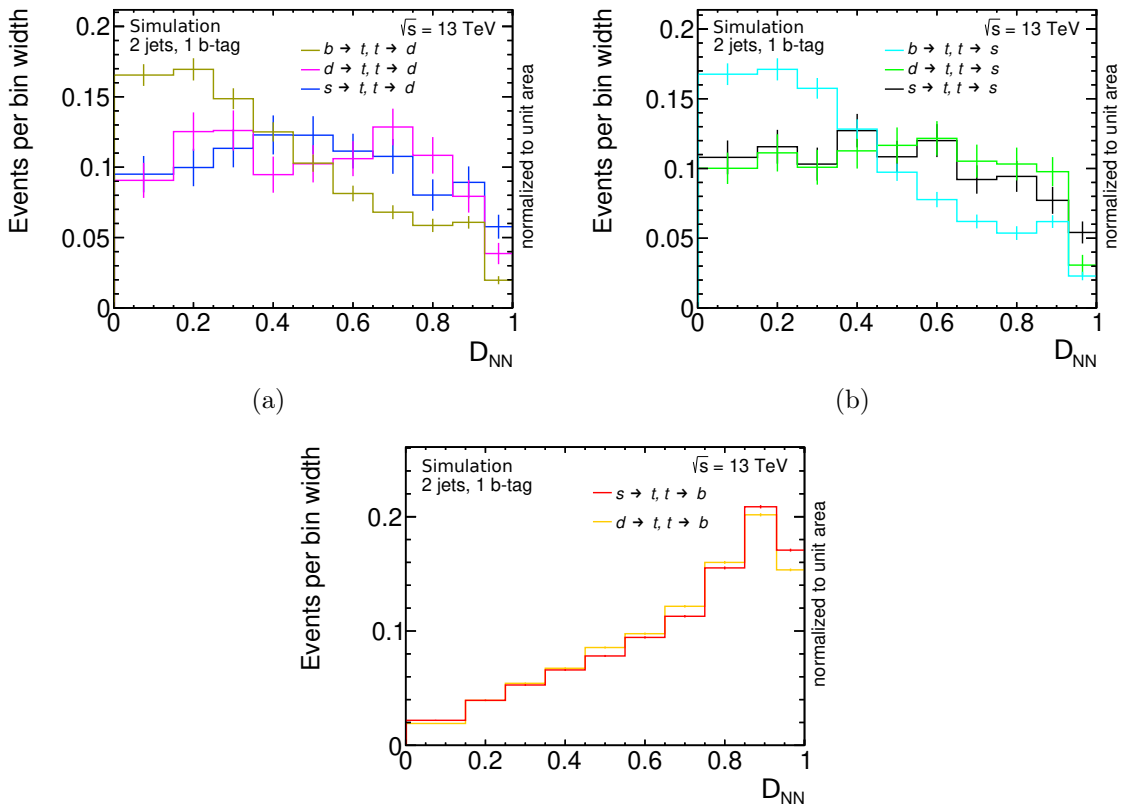

Figure 8.8: Normalized NN output probability distributions for all t-channel processes (a) with $t \to d$, (b) with $t \to s$ and (c) with $t \to b$. The uncertaintes correspond to the MC statistical uncertaintes.

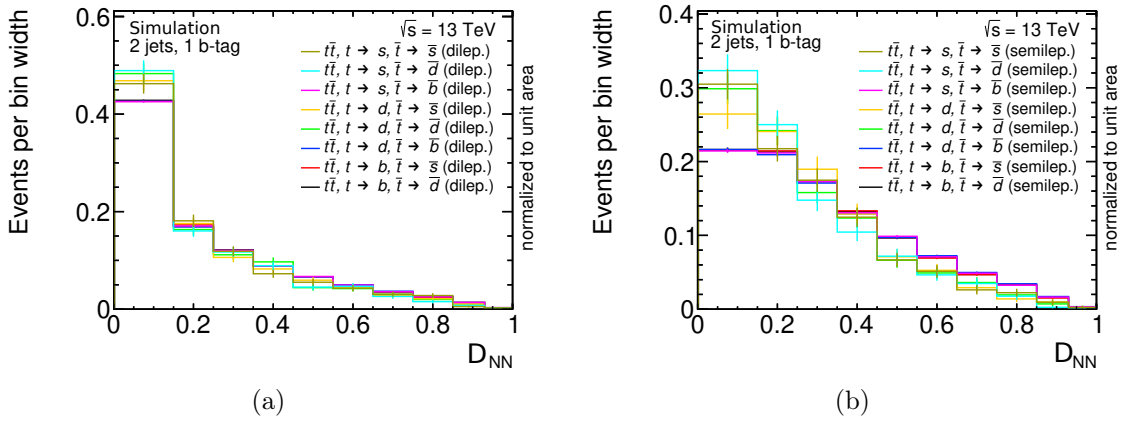

Figure 8.9: Normalized NN output probability distributions for all $t\bar{t}$-channel processes for the (a) dileptonic decay mode, and (b) the semileptonic decay mode.

8.2.2 Parametrization of signal CKM matrix elements

A parametrization of the overall number of expected single-top-quark t-channel events is used in order to access the CKM matrix elements. Here, the parametrization is shown for single-top-quark t-channel events in the SRplus, the respective parametrization of single-top-antiquark events in the SRminus, follows analogously. The overall number of events of all single-top-quark t-channel processes is expressed as:

$$N_{\mathrm{t-chan}} = \sum_{i=1}^{3}\sum_{j=1}^{3} N_{ij} \tag{8.11}$$

with

$$N_{ij} = \mathcal{L} \cdot \underbrace{\sigma_i^t |V_{ti}|^2}_{\text{prod.}} \cdot \underbrace{\mathcal{B}(t \to jW)}_{\text{decay}} \tag{8.12}$$

Hereby, the labels i, j denote all possible down-type quarks (b, d, s), such that there are nine summands. Each process can therefore be parametrized in terms of a production part and a decay part. For the production part, the respectively cross sections, σ_i^t for $V_{ti} = 1$ with $i = b, d, s$, are used, which are scaled with the occuring CKM matrix element as this quantity is the only difference between the production modes. For the decay part, the branching ratios are written as:

$$\begin{aligned}
\mathcal{B}(t \to bW) &\triangleq R = \frac{|V_{tb}|^2}{|V_{tb}|^2 + |V_{td}|^2 + |V_{ts}|^2} \\
\mathcal{B}(t \to dW) &\triangleq R_d = \frac{|V_{td}|^2}{|V_{tb}|^2 + |V_{td}|^2 + |V_{ts}|^2} \\
\mathcal{B}(t \to sW) &\triangleq R_s = \frac{|V_{ts}|^2}{|V_{tb}|^2 + |V_{td}|^2 + |V_{ts}|^2}
\end{aligned} \tag{8.13}$$

Again, the decay modes solely differ in the values of the occuring CKM matrix elements. With these, the full parametrization of the signal events becomes:

$$\begin{aligned}
N_{\mathrm{t-chan}} = \mathcal{L} \cdot R \Bigg[& \underbrace{\mu_b \cdot \sigma_b}_{\mathrm{b\to t,t\to b}} + \underbrace{\mu_d \cdot \sigma_d}_{\mathrm{d\to t,t\to b}} + \underbrace{\mu_s \cdot \sigma_s}_{\mathrm{s\to t,t\to b}} + \underbrace{\left(\frac{1-R-R_d}{R}\right) \cdot \mu_b \cdot \sigma_b}_{\mathrm{b\to t,t\to s}} + \underbrace{\left(\frac{1-R-R_s}{R}\right) \cdot \mu_b \cdot \sigma_b}_{\mathrm{b\to t,t\to d}} \\
& + \underbrace{\left(\frac{1-R-R_s}{R}\right) \cdot \mu_d \cdot \sigma_d}_{\mathrm{d\to t,t\to d}} + \underbrace{\left(\frac{1-R-R_s}{R}\right) \cdot \mu_s \cdot \sigma_s}_{\mathrm{s\to t,t\to d}} + \underbrace{\left(\frac{1-R-R_d}{R}\right) \cdot \mu_s \cdot \sigma_s}_{\mathrm{s\to t,t\to s}} \\
& + \underbrace{\left(\frac{1-R-R_d}{R}\right) \cdot \mu_d \cdot \sigma_d}_{\mathrm{d\to t,t\to s}} \Bigg],
\end{aligned} \tag{8.14}$$

using the signal strength parameters $\mu_b = {\mathrm{V_{tb}}}^2, \mu_d = {\mathrm{V_{td}}}^2, \mu_s = {\mathrm{V_{ts}}}^2$. Here, V_{tb}, V_{td} and V_{ts} denote the parameters for the according CKM matrix element involving the top-quark. The terms including the different branching ratios for $t \to d$ and $t \to s$ can be further simplified:

$$\begin{aligned}
\frac{1-R-R_d}{R} &= \frac{|\mathrm{V_{tb}}|^2 + |\mathrm{V_{td}}|^2 + |\mathrm{V_{ts}}|^2}{|\mathrm{V_{tb}}|^2} - 1 - \left(\frac{|\mathrm{V_{td}}|^2}{|\mathrm{V_{tb}}|^2 + |\mathrm{V_{td}}|^2 + |\mathrm{V_{ts}}|^2} \cdot \frac{|\mathrm{V_{tb}}|^2 + |\mathrm{V_{td}}|^2 + |\mathrm{V_{ts}}|^2}{|\mathrm{V_{tb}}|^2} \right) \\
&= \frac{|\mathrm{V_{ts}}|^2}{|\mathrm{V_{tb}}|^2}, \\
\frac{1-R-R_s}{R} &= \frac{|\mathrm{V_{td}}|^2}{|\mathrm{V_{tb}}|^2}.
\end{aligned}$$

These expression are incorporated into the full likelihood function, with three free parameters at this stage: $\mathrm{V_{tb}}, \mathrm{V_{td}}$ and $\mathrm{V_{ts}}$. Replacing the initial normalization factors in Equation 8.10 with these expressions and reparametrizing the likelihood function instead of directly constructing it with the formulae simplifies the implementation and thus ensures a more flexible adaptation.

For the $t\bar{t}$ events, the parametrization follows similarly. The expected number of events is parametrized as follows:

$$N_{\mathrm{tt}} = \mathcal{L} \cdot \sigma_{tt} \cdot \sum_{i=1}^{3} \sum_{j=1}^{3} \mathcal{B}(t \to iW) \cdot \mathcal{B}(\bar{t} \to jW) \tag{8.15}$$

The labels i, j denote all possible down type quarks (b, d, s), such that there are nine summands, one for each possible top-quark decay mode. Since the $t\bar{t}$ process occurs predominantly with gluon-gluon fusion at the energy at which the LHC is operating, the production cross section does not depend on any CKM matrix element and is therefore treated as a constant. The branching ratios of the top-quark and top-antiquark are parametrized as shown in Equation 8.13.
These parametrizations are used in order to derive limits on all CKM matrix elements involving the top-quark using a 2D profile likelihood scan, which is described in detail in the following chapter.

8.2.3 Profile Likelihood Scan procedure

A similar profile likelihood fit setup is used as for the nominal t-channel cross section measurement, but using the considered parametrizations mentioned above. Additionally, the NN output distributions for each CKM process are used in the SRs. All other distributions are used as they were in the nominal t-channel cross section measurement.
A binned profile likelihood fit using all processes with this parametrization turned out to be numerically too unstable as the fit never converged. Hence, a different interpretation strategy was developed, using a 2D profile likelihood scan. A 2D profile likelihood scan explores the dependence of the likelihood function on two parameters while profiling over all others. This involves systematically varying and fixing the two selected parameters and maximizing the likelihood with respect to the remaining nuisance parameters at each point.

Table 8.3: Parameter ranges of for the three investigated scenarios in the profile likelihood scans. For each scenario, the fixed parameter is set to the value in the nominal MC production, which all top-quark involved analyses use.

Parameter	**Scenario 1**	**Scenario 2**	**Scenario 3**
$\|V_{tb}\|$	$[0.93, 1.07]$	$[0.915, 1.065]$	1 (fixed)
$\|V_{td}\|$	$[0.0, 0.19]$	0 (fixed)	$[0.0, 0.15]$
$\|V_{ts}\|$	0 (fixed)	$[0.0, 0.45]$	$[0.0, 0.35]$

The resulting likelihood surface provides insights into correlations, allowed parameter regions, and the overall shape of the likelihood function in the chosen parameter space. The aim of this strategy is to set limits on two CKM matrix elements, while the third one is fixed to an arbitrary but meaningful value. This is $|V_{tb}| = 1$ and $|V_{td}|, |V_{ts}| = 0$ for the fixed CKM matrix elements in the respective scenarios, as these are the values set in the used nominal MC simulations. Therefore, three scenarios are investigated, which explore different ranges for the non-fixed elements of the CKM matrix, yielding in $|V_{tb}|$-versus-$|V_{td}|$, $|V_{tb}|$-versus-$|V_{ts}|$ and $|V_{td}|$-versus-$|V_{ts}|$ planes, respectively. The specific parameter constraints for each scenario are summarized in Table 8.3. Hereby, all three possible combinations of two of the tree free floating parameters in the fit, V_{tb}, V_{td} and V_{ts}, are scanned, with the third parameter being fixed. To balance computational efficiency and accuracy, the parameter ranges are discretized into 50 bins within each parameter interval. This choice ensures a sufficiently fine resolution while keeping the computational cost manageable. The interval boundaries itself are set based on the profile of the likelihood distribution in the 2D parameter space. The likelihood increases rapidly for parameter values beyond these limits, making further sampling unnecessary. By restricting the parameter space to these intervals, the focus is on the most relevant parameter space for the interpretation without introducing numerical instabilities or excessive computational costs.

8.2.4 Constraints on top-quark involved CKM matrix elements

For each scenario, the 2D profile likelihood scans are performed on data. The resulting 2D profile likelihood scans for each scenario are shown in Figure 8.10. In the first scenario, the $|V_{tb}|$-versus-$|V_{td}|$ plane, the minimum is found to be

$$f_{\mathrm{LV}}|V_{tb}| = 1.000 \pm 0.048, \tag{8.16}$$
$$f_{\mathrm{LV}}|V_{td}| = 0.000 \pm 0.133. \tag{8.17}$$

Similarily, in the second scenario, the $|V_{tb}|$-versus-$|V_{ts}|$ plane, the minimum is measured at

$$f_{\mathrm{LV}}|V_{tb}| = 0.990 \pm 0.048, \tag{8.18}$$
$$f_{\mathrm{LV}}|V_{ts}| = 0.144 \pm 0.162. \tag{8.19}$$

For the third scenario, the $|V_{ts}|$-versus-$|V_{td}|$ plane, the minimum is calculated to be

$$f_{\mathrm{LV}}|V_{td}| = 0.000 \pm 0.126, \tag{8.20}$$

$$f_{\mathrm{LV}}|V_{ts}| = 0.077 \pm 0.196. \tag{8.21}$$

All uncertainties given here correspond to the 2σ contour, which corresponds to the 95.45% confidence level (CL) in the 2D space. The likelihood function used in these scans includes all systematic uncertainties as in the nominal fit to determine the cross section, only neglecting the systematic variations for the CKM samples not including a V_{tb} vertex. These are excluded as the overall number of selected events is very small for the scanned parameter values of V_{td} and V_{ts}, making the estimation of systematic uncertainties unreliable. In regions with very few events, the statistical fluctuations within the systematic uncertainty templates become significant, leading to large relative uncertainties. This, in turn, can introduce an instability in the fit, as the impact of systematic variations is dominated by statistical noise rather than genuine physics effects.

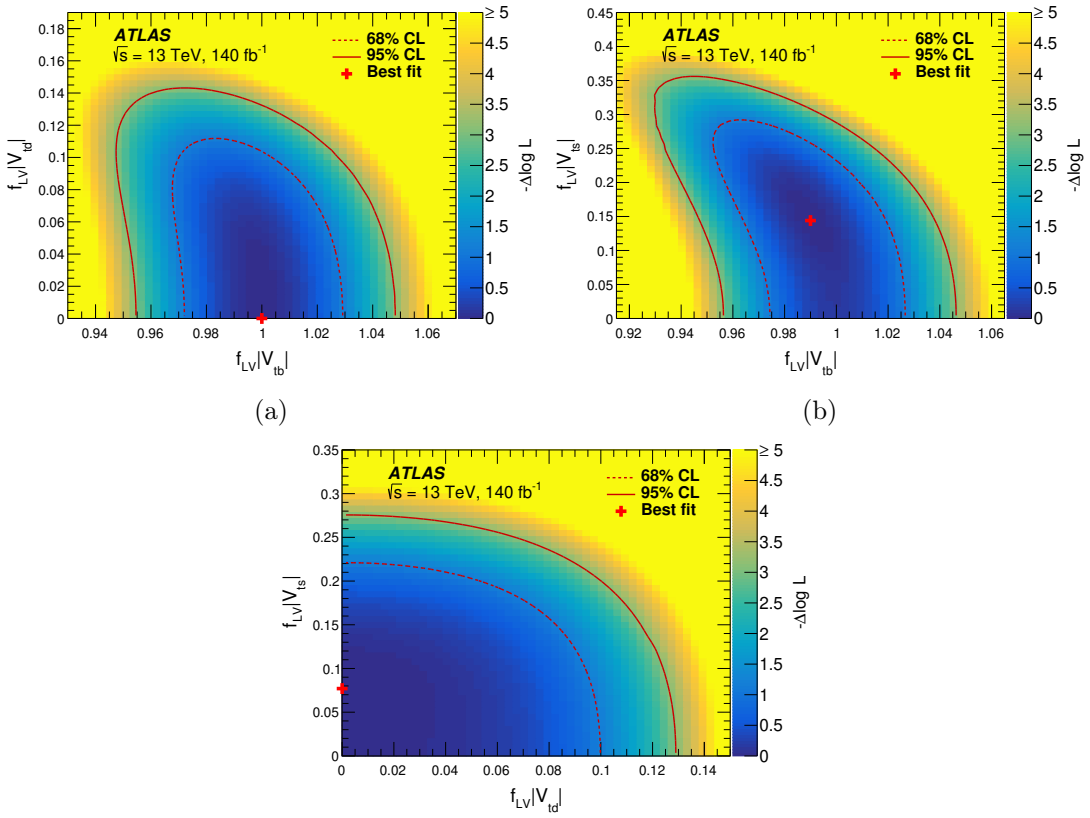

Figure 8.10: 2D profile Likelihood scans of two parameters each for the top-quark involved CKM matrix elements. The fits are performed on measured data. (a) shows the likelihood scan in the $|V_{tb}|$-versus-$|V_{td}|$ plane, (b) shows the likelihood scan in the $|V_{tb}|$-versus-$|V_{ts}|$ plane and (c) shows the likelihood scan in the $|V_{ts}|$-versus-$|V_{td}|$ plane. There are two contour lines shown in each plot, illustrating one σ and two σ contours, respectively. The red cross denotes the global minimum of the likelihood scan. Published in Ref. [1].

9 Towards a dedicated measurement of top-quark involved CKM matrix elements

The results of the CKM interpretation discussed in detail in the previous chapter are in agreement with the current best-fit measurements of the top-quark involved CKM matrix elements. However, the single-top-quark t-channel analysis targeted solely $t \to b$ decays and thus, events where the top-quark decays into a light quark are strongly suppressed. An attempt is made in this thesis to target all SM top-quark production and decay modes in order to measure $|V_{tb}|$, $|V_{td}|$ and $|V_{ts}|$ and additionally reduce the uncertainties in the measurement. The studies examined in the following provide insight if such a dedicated measurement is feasible and hightlights the remaining limitations.

9.1 Event selection

The resulting 2D limits in the CKM interpretation, examined in Chapter 8.2.4, were predominantly limited by MC statistical uncertainties due to the event selection, which was restricted to events containing exactly one b-tagged jet. Due to the good performance of the ATLAS flavor tagging algorithm, the mis-tag rate of jets originating from light quarks is very low (see Chapter 4.5.2), hence an improved event selection is needed in order to target all possible top-quark decay processes. In the first step, an event selection based on the one utilized in the t-channel analysis, described in Chapter 8.1.1, is implemented. All nine possible single-top t-channel processes are considered as the signal in these studies. The aim of the event selection is to enhance the sensitivity to all possible single-top-quark t-channel production and decay processes. Therefore, the criterion of exactly one b-tagged jet is removed in the event selection here. Additionally, the focus lies on reducing the $t\bar{t}$ contribution from the overall background events, as well as the now overwhelming W+jets background.
Again, semileptonic single-top-quark t-channel events are targeted and events are recorded using single lepton triggers, for either electrons or muons. Events with exactly one lepton, either an electron or a muon[1], with $p_{\mathrm{T}} > 28\,\mathrm{GeV}$ are selected, as for this transverse momentum the single lepton trigger efficiency reaches a plateau of close to 100%. Further, events are selected with $E_{\mathrm{T}}^{\mathrm{miss}} > 35\,\mathrm{GeV}$, due to the expected neutrinos

[1] Both can also originate from tau decays.

from the semileptonic top-quark decay.
As the semileptonic t-channel top-quark processes are characterized by a jet in forward direction and a jet from the top-quark decay, exactly two jets with $p_{\mathrm{T}} > 20\,\mathrm{GeV}$ and $|\eta| < 4.5$ are required. This requirement is tighter than the one previously used, leading to a reduction of the $t\bar{t}$ background contribution, which was the largest background in the t-channel analysis. The p_{T} requirement for jets with $2.3 < |\eta| < 4.5$ is increased to $p_{\mathrm{T}} > 35\,\mathrm{GeV}$. One of the two jets is required to be in forward direction in the detector, i.e. $2.5 < |\eta| < 4.5$, and is denoted as j_{fwd} in the following. The other jet needs to be in the central region of the detector ($|\eta| < 2.5$) and is denoted j_{central} in the following. Additionally, the pseudorapidity separation between both jets is required to fulfill $\Delta\eta(j_{\mathrm{central}}, j_{\mathrm{fwd}}) > 1.5$ to further reduce contributions from $t\bar{t}$ events. This requirement follows the approach in the t-channel analysis from ATLAS at $\sqrt{s} = 5.02\,\mathrm{TeV}$ [199]. The invariant mass of the central jet and the lepton, which are both expected to originate from the top-quark decay, has to fulfill $m_{\ell,b} < 160\,\mathrm{GeV}$, in order to suppress events with off-shell top-quarks. To reduce the contamination of events with fake leptons, the criterion on the transverse W-boson mass is $m_{\mathrm{T}}^{W} > 50\,\mathrm{GeV}$.
Due to the missing b-tagging requirement, the contribution of the W+jets background is expected to increase drastically, while the $t\bar{t}$ contribution is expected to be decreased. This increasing W+jets background is expected due to the large cross section of $W+$ any additional two jets compared to all other SM processes present. In order to decrease the W+jets contamination again, kinematic distributions were examined. In Figure 9.1, the normalized distributions of the sum of all transverse momenta in an event, H_{T}, and the difference in the azimuthal angle between $E_{\mathrm{T}}^{\mathrm{miss}}$ and the lepton, $\Delta\Phi(E_{\mathrm{T}}^{\mathrm{miss}}, \ell)$, are shown. For both variables, a clear difference in the shape of the distributions for W+jets and all

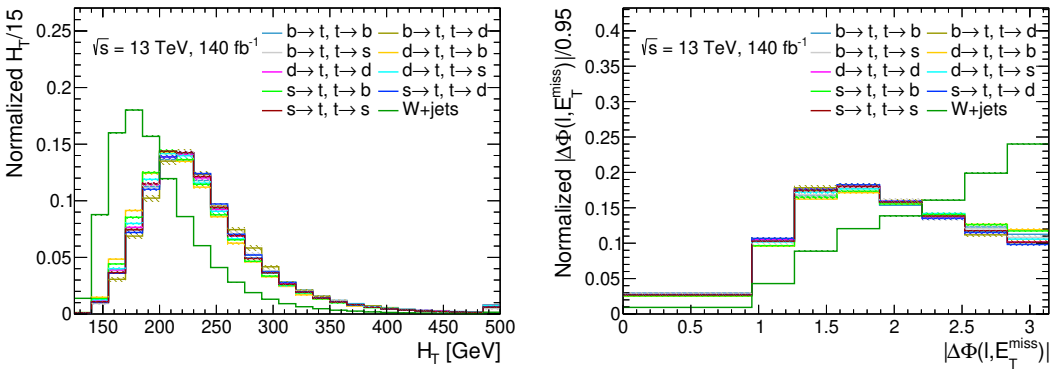

(a) (b)

Figure 9.1: Normalized distributions of (a) the sum of all transverse momenta in an event, H_{T}, and (b) the difference in azimuthal angle between $E_{\mathrm{T}}^{\mathrm{miss}}$ and the lepton. The nine single-top-quark t-channel signal processes and the largest background, W+jets, are compared. The shaded areas for each histogram depict the MC statistical uncertainty. Although these uncertainties may be too small to be resolved visually, they are nonetheless included.

signal processes is visible. Hence, two further selection criteria are applied in the final selection. Events are selected with $H_{\mathrm{T}} > 200\,\mathrm{GeV}$ and $\Delta\Phi(E_{\mathrm{T}}^{\mathrm{miss}}, \ell) < 2.2$. This selection reduces the W+jets contribution by about 80%, and at the same time only cuts away about 50% of the overall signal contribution.

In Table 9.1, the event yields for each considered process after the full selection is listed. The yields of the single-top processes with $|V_{td}|$ and/or $|V_{ts}|$ present are scaled to the SM prediction, using the current best measured values, $|V_{td}| = 8.6\times10^{-3}$ and $|V_{ts}| = 41.5\times10^{-3}$, taken from Ref. [19]. W+jets still emerges as the overwhelming background process after the selection, whereas $t\bar{t}$ is suppressed due to the applied criteria. A 10% difference between data and MC is observed. It has to be noted however that no systematic uncertainties are taken into account here, e.g. theoretical uncertainties on the cross sections are not accounted for in these studies. In particular, for W+jets typically, an additional uncertainty of 24% per additional jet is added in quadrature on top of the inclusive cross section uncertainty. This estimate is based on different merging schemes of LO MEs and PS [200]. Further, no fake lepton background estimation was performed as only feasability studies are presented in this work. Therefore, no direct comparison to data will be made beyond

Table 9.1: Number of events, N, in the signal region after applying the selection requirements described in detail in the text. "Total MC" denotes the sum of all individual processes, including the single-top-quark t-channel signal processes. The shown uncertainty is the MC statistical uncertainty. "Total Signal" and "Total Background" do not sum exactly to "Total MC" due to rounding effects.

Process	$N_{\text{signal region}}$
$b \to t, t \to b$	77 830 ± 280
$b \to t, t \to d$	5.7 ± 2.4
$b \to t, t \to s$	125 ± 11
$d \to t, t \to b$	30 ± 5
$d \to t, t \to d$	0.00 ± 0.05
$d \to t, t \to s$	0.06 ± 0.24
$s \to t, t \to b$	360 ± 20
$s \to t, t \to d$	0.03 ± 0.17
$s \to t, t \to s$	0.7 ± 0.8
Z+jets	85 220 ± 290
VV	3050 ± 60
$t\bar{t}$	23 240 ± 150
t, s-chan	2530 ± 50
W+jets	1 191 000 ± 1100
Total Signal	78 340 ± 280
Total Backgroud	1 305 000 ± 1100
Total MC	1 383 400 ± 1200
Data	1249439

Figure 9.2, in which six kinematic distributions comparing data and MC predictions are shown. In each plot, the predicted events overestimate the recorded data events. For the $E_{\mathrm{T}}^{\mathrm{miss}}$ distribution, a shape effect is visible for low values. This behaviour is expected, as this is the range in which events with fake leptons are expected to occur. Overall, the large offset is interpreted as a normalization effect, the origin might be a mismodelling in the huge W+jets background. Since no data are used in the following studies for this thesis no further investigation of this matter is made. Further distributions, including distributions for electrons, angular distributions for both jets and other calculated observables, are located in Appendix F, underlining the observations discussed here.
Cutflow distributions for all SM processes, excluding the t-channel CKM signal processes, are provided in Appendix G. In addition, cutflow distributions comparing all signal processes separately also to the W+jets process, are also in Appendix G. These cutflow plots illustrate the impact of the event selection on each process and, thus, demonstrate that background events are suppressed more strongly than the signal events, thereby supporting the aim of improving the signal purity in the final SR.
In order to further distinguish between the different signal processes and the W+jets background, a NN approach is utilized, similar to the analysis strategy employed in the t-channel analysis.

9.2 Event classification using Neural Networks

The main objective of the studies done in this thesis of measuring all top-quark involved CKM matrix elements is very challenging as the signal-over-background ratio with the current best SM estimation is small even with a dedicated event selection. Furthermore, the targeted signal consists of nine individual processes, each sensitive to at maximum two of the targeted CKM matrix elements. Therefore, in a first step a variable is constructed to separate the W+jets background from all signal processes. In a second step, the different signal processes need to be separated in order to achieve the best possible sensitivity to the corresponding CKM matrix elements. In the following, both, single-top-quark and single-top-antiquark processes are indicated by single-top-quark t-channel processes for simplicity.

The characteristics of single-top-quark t-channel processes, e.g. the presence of a jet in forward direction, is already exploited in the event selection. However, none of the available kinematic distributions and angular observables of final state objects do provide sufficient discrimination power, which would allow for cuts on these distributions to achieve a region mostly pure in signal events. Hence, a supervised machine-learning approach using an artificial NN for each step is employed that combines the information from several kinematic variables. The construction of the NN models utilized in these studies is outlined in the following, as well as their performance and optimization.

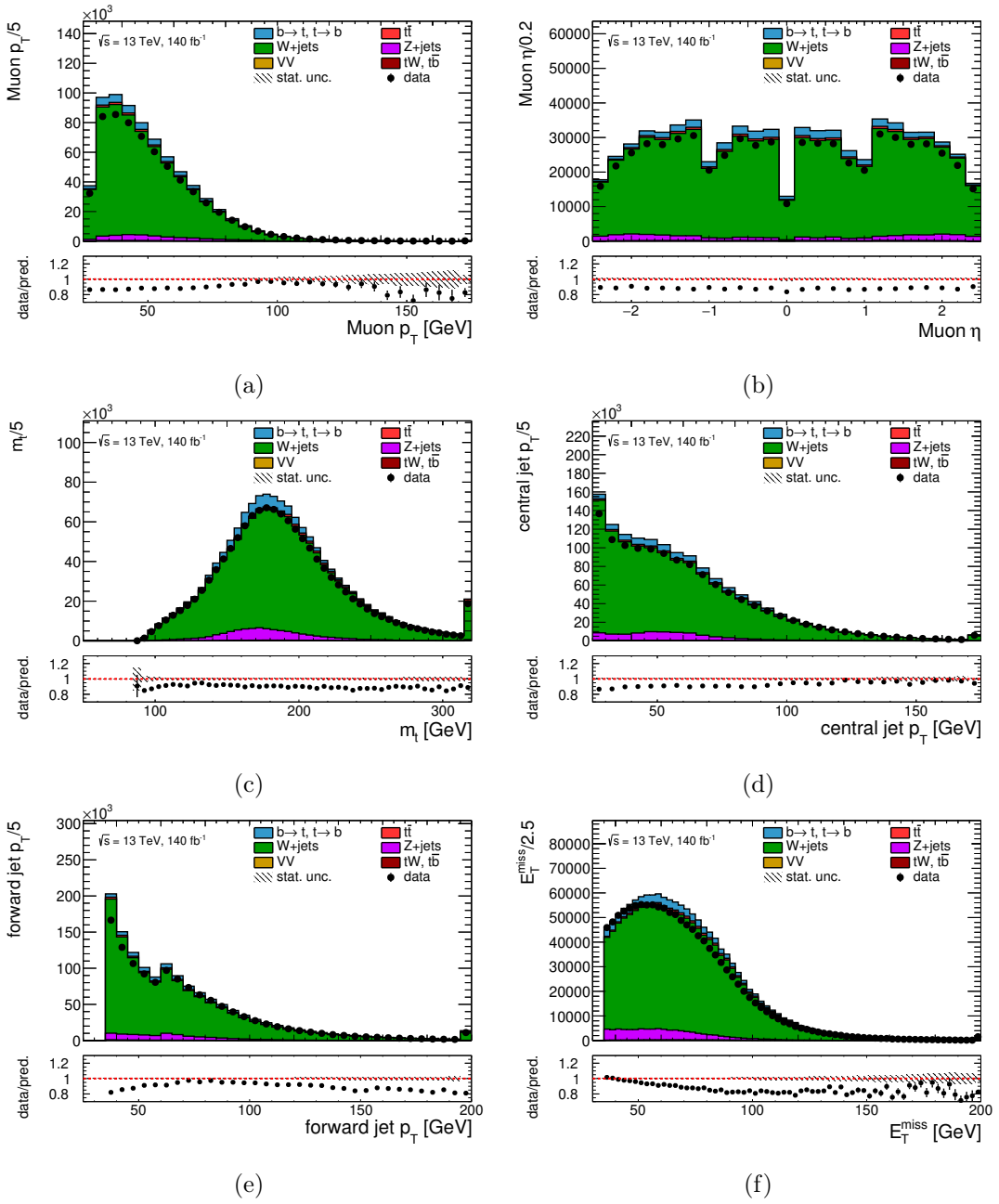

Figure 9.2: Kinematic distributions in the signal region after the event selection. Figure (a) and (b) show the p_{T} and η of the muon in an event, respectively. Figure (c) shows the invariant mass of the reconstructed top-quark. In (d) and (e) the p_{T} of the selected central jet and the selected forward jet is shown. In (f), the missing transverse momentum. The first and last bin of each distribution include the underflow and overflow bin, respectively. In the bottom panel of each plot, the ratio between observed and expected events is shown. All distributions show an offset between data and prediction. The depicted uncertainty bands indicate the MC statistical uncertainty, whereas the error bars on the black data points show the statistical uncertainty on the measurement of the recorded data.

Neural networks

Artificial NNs are a class of machine-learning models inspired by the structure and function of biological neurons. These types of machine-learning algorithms are designed to recognize patterns in given data. In this work, feed-forward NNs are employed to classify simulated events based on their kinematic properties. These networks consist of three different types of layers. Each layer consists of multiple nodes, which defines the size of the layer. The first layer is the input layer, whose size corresponds to the number of input variables, so-called input features, followed by layers with dense connections, and lastly an output layer. Each studied NN in this work contains fully-connected dense layers, where each neuron in a layer is connected to every neuron in the subsequent and preceding layer. Mathematically, each dense layer transforms an input vector of size n, $\vec{f}^{(k-1)} \in \mathbb{R}^n$, into an output vector, $\vec{f}^{(k)} \in \mathbb{R}^m$ of size m, as formulated in Equation (9.1). Hereby, k denotes the k-th dense layer. The transformation with a non-linear so-called *activation* function, ϕ, is given by

$$f_j^{(k)} = \phi\left(\sum_j W_{ij}\vec{f}^{(k-1)} + b_i\right), \forall i \in \mathbb{Z}. \tag{9.1}$$

The non-linear transformation is done for each element for each vector, with W being the *weight matrix* and b the bias vector. The chosen activation function for the NNs used in this thesis is the Rectified Linear Unit (ReLu) function,

$$\phi(x) = \max(0, x), \tag{9.2}$$

which is applied to all hidden layers. The choice of the activation function for the last layer, the output layer, depends on the classification problem. In this work the sigmoid function

$$\sigma(x) = \frac{1}{1 + e^{-x}} \tag{9.3}$$

is used for the binary classification problem. For the studied multiclass NN, the softmax activation function is chosen:

$$\sigma_i(\vec{x}) = \frac{e^{x_i}}{\sum_{j=1}^{m} e^{x_i}}, \quad i = 1, ..., m. \tag{9.4}$$

Each network is trained using supervised learning, where each event is assigned a target label depending on its category. For the binary classification, e.g. signal vs background events, the target variable is defined as

$$y = \begin{cases} 1, & \text{if the event belongs to the signal class,} \\ 0, & \text{if the event belongs to the background class.} \end{cases} \tag{9.5}$$

Subsequently, the sigmoid function returns a probability score $\hat{y}$, which can be interpreted as the likelihood of an event being signal. The predicted class is determined by applying a threshold, in case of this work $\hat{y} > 0.5$, for which an event is classified as signal and

otherwise classified as background if the condition is not met. In the case of multiclass classification, e.g. distinguishing between different signal processes, the target variable is a one-hot encoded vector, $\vec{y}$, which is given by

$$\vec{y} = (y_1, y_2, ..., y_m),\ y_i \in \{0, 1\},\ \sum_{i=1}^{m} y_i = 1, \tag{9.6}$$

where each class is represented by a unique index, i. Since the softmax activation function used in this case yields in class probabilities, the predicted class corresponds to the index with the highest probability, $\hat{y} = \arg\max_i \hat{y}_i$.
The training process of a NN is designed such that the model iteratively updates its parameters, $\vec{\theta}$, to minimize a predefined loss function, $l(\vec{\theta})$. Hereby, a function $f_{\vec{\theta}} : \mathbb{R}^n \to \mathbb{R}^m$ is approximated, which maps the aforementioned input feature vector $\vec{x} \in \mathbb{R}^n$ to an output vector $\widehat{\vec{y}} \in \mathbb{R}^m$. For a binary classifier, the output vector is one dimensional. Given the labeled dataset $\mathcal{D} = (\vec{x}^{(i)}, \vec{y}^{(i)})_{i=1}^{N}$, where $\vec{y}^{(i)}$ represents the true target values, the training procedure aims to find an optimal set of parameters, $\vec{\theta}^*$, that minimize $l(\vec{\theta})$. For the purpose of binary classification, the binary cross-entropy is chosen as the loss function, which is given by

$$l_1(\vec{\theta}) = -\frac{1}{N} \sum_{i=1}^{N} \left[y^{(i)} \log \hat{y}^{(i)} + \left(1 - y^{(i)}\right) \log \left(1 - y^{(i)}\right) \right]. \tag{9.7}$$

The corresponding cross-entropy function in case of the multiclass NN is the categorical cross-entropy loss, given by

$$l_2(\vec{\theta}) = -\frac{1}{N} \sum_{i=1}^{N} \sum_{j=1}^{m} y_j^{(i)} \log \hat{y}_j^{(i)}. \tag{9.8}$$

As indicated above, $y^{(i)}$ are the true labels, while $\hat{y}^{(i)}$ corresponds to the predicted probabilities by the NN. In order to minimize the respective $l(\vec{\theta})$, gradient based optimization algorithms are employed. These compute the gradient of the loss function with respect to each weight and updates the weights in the direction that reduces the loss in parameter space. Equation (9.9) defines the rule for updating the weights:

$$\vec{\theta}^{(t+1)} = \vec{\theta}^{(t)} - r \nabla_{\vec{\theta}} l(\vec{\theta}). \tag{9.9}$$

Here, t denotes the iteration, called *epoch*, and r is the learning rate which controls the size of the steps taken in the direction of the gradient in each iteration. The learning rate plays a crucial role during the training, as the parameter space can be high dimensional and very complex. A too large r may lead to missing the global minimum of the loss function by taking too large steps, causing the model to fail to converge, while a too small learning rate can result in slow convergence, requiring too many iterations to reach an optimal solution, or a convergence in a local minimum. All networks employed in these studies use the Adam optimizer [201], which is an extension of the standard gradient descent described here, that adapts the learning rate for each parameter based on estimates of the first and

second moments of the gradients. To propagate the updated weights from the output layer back to the input layer of a NN, the *backpropagation* algorithm is used. Backpropagation is based on the chain rule of calculus, as it calculates the gradient of the loss function with respect to each weight by recursively applying the chain rule starting from the output layer and propagating backwards through the network. These gradients indicate the direction in which the weights need to be adjusted to minimize the loss function. The derivatives of the loss function with respect to the weights are computed locally at each node in the network. These derivatives are then averaged over the entire input dataset. This allows the model to compute the gradient of the overall loss function by considering all input examples and adjusting weights accordingly. The process begins by calculating the gradient of the loss with respect to the output of the network, which is typically the error at the output layer. For each layer, the error is propagated backward through the network by recursively applying the chain rule. Once the errors for each layer are computed, the gradients of the loss function with respect to each weight are derived.

In order to perform the training of a model, i.e. the minimization of the loss function, a set of input data, a *training dataset*, is used. Further, to evaluate the performance and the generalization of a model, i.e. classification of data it never used to train on, during the training a *validation dataset*, is utilized, which consists of data not included in the training dataset. Usually a third dataset, the *test dataset* is utilized to provide an unbiased estimate of the performance after the full training is finished. Here, a slightly different approach is considered: All available MC events are used and a two-fold cross validation is employed for the training of the model. In the setup used in this work, the MC events are divided into two subsets based on the parity of the `eventNumber`[2]. Each of the two subsets is consequently split into a training set and a validation set. In the first fold, the model is trained and evaluated using all events with odd numbers, in the second fold the model uses all events with even numbers. In the following the model of the first fold is denoted as odd-model, while the model of the second fold is called even-model. For the training 80% of the events in a subset are used, while the remaining 20% are used in the validation dataset. This procedure ensures a precise control over the performance of the training process.

Overfitting occurs once a model recognizes not only the underlying patterns in the training dataset but also artefacts, e.g. noise or random fluctuations, leading to poor generalization to unseen data. To address this challenge and improve the generalizability of the model, regularization techniques are employed during the training process for the NN models in this thesis. First, L2 regularization [202], is applied to mitigate overfitting. The L2 regularization penalizes large weights by adding a term to the loss function, which prevents the NN from assigning excessively large values to the model parameters. In general, the regularized loss function is defined as:

$$l_{\text{reg}} = l + \lambda \sum_j \parallel W_j \parallel^2 . \tag{9.10}$$

[2]The eventNumber is a unique identifier assigned to each event in the simulation, used to distinguish events within the dataset.

Hereby, W represents the aforementioned weight matrix of the model with $\| W_j \|^2$ being the squared Frobenius norm, which is the sum of the squares of all entries of the matrix. By including the regularization term, the model is penalized when applying large weights, thereby, guiding it to smaller, more generalizable weights. The λ parameter controls the strength of the regularization. A large value of λ leads to stronger regularization, potentially resulting in the opposite effect, i.e. underfitting the model. In contrast, a small value of λ might not sufficiently constrain the chosen weights of the model.

Parameters introduced above that control the training process, e.g. the learning rate or the number of layers and nodes in each layer, are so called *hyperparameters* of the NN. Also, regularization parameters of a network, e.g. λ, are included. Hyperparameters are set before the training process begins and are not learned or updated from the data. The performance of a model is heavily impacted by the choice of the hyperparameters, since the convergence and generalization is influenced by their set values.
Although the number of possible hyperparameter combinations is theoretically infinite, in practice they are constrained by the number of events in the training dataset. Therefore, typically, hyperparameter optimization is performed using systematic approaches with different best-guessed combinations of hyperparameters being evaluated based on their performance on the validation dataset, aiming for the set of hyperparameters that yields the best model performance - performance measures for a NN are discussed in Chapter 9.3.2. However, in the scope of this work, a manual approach is employed with a finite set of hyperparameter values. The number of hidden layers and nodes in each layer, a learning rate scheduler and r itself were varied. The learning rate scheduling technique employs a reduction of r over time to improve the efficiency of the training process and avoid missing the global minimum by having a too large value of r. The common learning rate plateau strategy is applied, where r is decreased once the validation loss values do not improve for a given number of epochs. This allows the model to fine-tune the remaining parameters more precisely as it approaches convergence. The learning rate decay formula is given by

$$r(t) = r_0 \cdot D^{\frac{t}{d_e}}. \tag{9.11}$$

The decay factor, D, in Equation (9.11) is a constant factor by which r gets reduced, while d_s is the number of epochs after that the learning rate is updated.

One individual NN model is constructed for both steps explained in the first paragraph of Chapter 9.2. The chosen hyperparameters for each NN were selected based on their ability to balance model performance and training efficiency. In the first step, a NN with a single output node is used for the discrimination of signal and background events (*binary classifier*). For the second step, which involves the discrimination between different signal processes, the output layer consists of up to six nodes, corresponding to a multiclass NN approach, as well as another binary classifier. All models employed in this work are implemented using `Keras` [203] with the `Tensorflow` [204] backend.

9.3 Distinguishing between single-top-quark t-channel and W+jets events

The training described in the following is aimed at separating the signal process from the W+jets background.

9.3.1 Input features and preprocessing

In the single-top-quark t-channel cross section analysis, the NN was trained using high-level features as input variables. These were derived from lower-level features such as information from the four-vectors of individual physics objects. A NN architecture with one hidden layer is designed to achieve a sufficient separation between signal and background events. In principle, a NN that has a large enough structure should be able to extract these high-level information directly from the lower-level input features during training. Hence, for the NN trained for this thesis, mostly lower-level variables are used. The following kinematic variables are used from each event:

- p_{T}, η and ϕ for both jets,
- p_{T}, η, ϕ and electric charge for the charged lepton.

Since the ϕ distributions are flat and also periodic between 0 and 2π, the $\sin(\phi)$ and $\cos(\phi)$ are used as input parameters to capture the effects and mitigating the discontinuity of the ϕ values. Additionally, since no energy values are given to the NN in order to prevent the algorithm to learn masses itself, the transverse W-boson mass, m_{T}^{W}, and the reconstructed top-quark mass, m_{top}, are calculated in each event and also used as an input feature. The reconstruction of the W-boson and consequently the top-quark, explained in Chapter 8.1.1, is applied with a simplification: In the case a complex solution is obtained, the real part of that solution is taken as the solution instead of applying a correction procedure. For the single-top-quark t-channel events, the reconstructed top-quark mass is expected to be centered around the top-quark mass used in the MC simulations, while for the W+jets background it is expected to be shifted and the distribution to be broader. Studies were also done by training a network with high-level variables such as distances in the detector between objects, but no improvement in the performance was observed. Hence, the approach with the low level variables plus m_{T}^{W} and m_{top} was followed.

In Figure 9.3, the shape of the normalized p_{T} and η distributions for both, the central jet and the forward jet, are shown for all signal processes separated and for the W+jets process. In both, the p_{T} spectra of the central jet and the forward jet, it is visible, that the W+jets distributions are softer. Additionally, the p_{T} spectra of processes with $t \to b$ are also slightly softer than the distributions of the $t \to d, s$ processes. In the η distributions shown in Figure 9.3(b), no trend is observed. In contrast, Figure 9.3(d) indicates that the $|\eta|$ of the forward jets of the signal processes tend to be higher than the ones from W+jets events.
The shape of the normalized p_{T} and η distributions of the electron and muon, for all

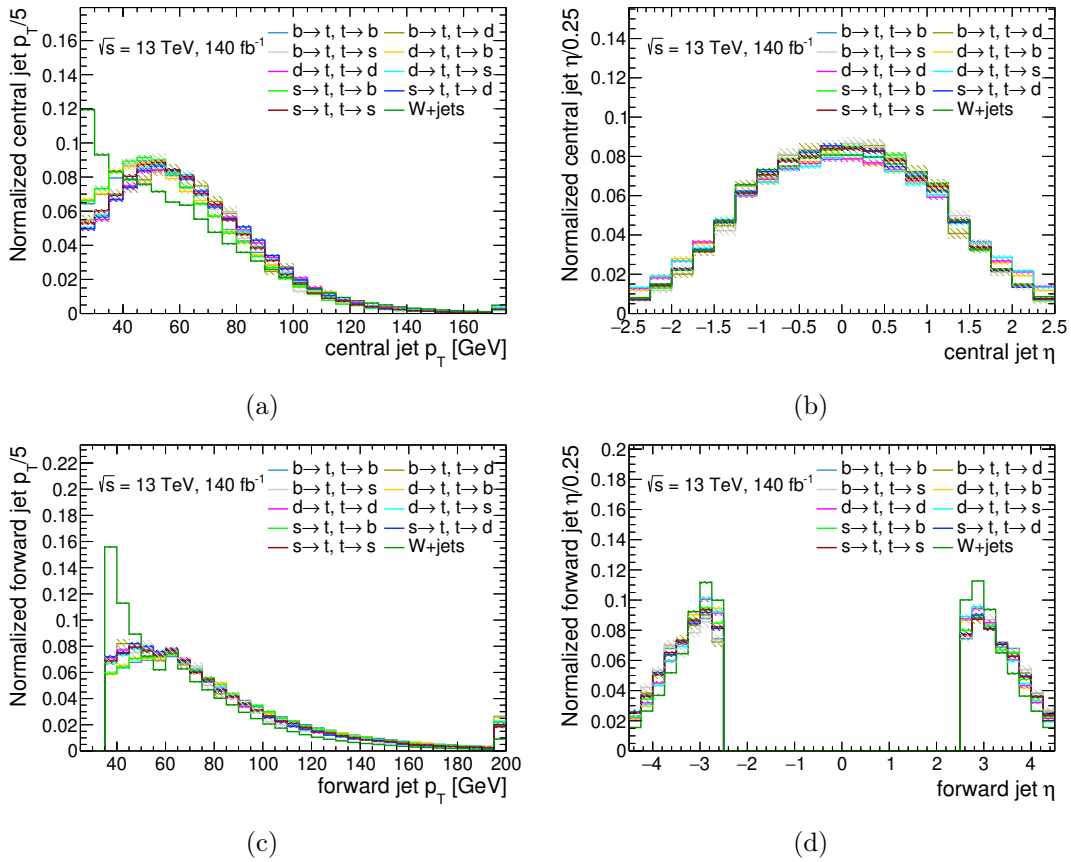

Figure 9.3: Shape of normalized distributions for all individual signal processes and the W+jets background. In (a) and (b) the p_{T} and η, respectively, of the central jet is shown. In (c) and (d) the p_{T} and η, respectively, of the forward jet is shown. The hashed areas denote the MC statistical uncertainty.

signal processes combined and for the W+jets process are displayed in Figure 9.4. Small differences are observed in both lepton η distributions between W+jets and the signal processes, as the lepton is detected more centrally for background process. No differences are observed in the p_{T} spectra of both leptons for W+jets and all signal processes.

The electric charge of the electron and muon, as well as m_{T}^{W} and m_{top} are shown in Figure 9.5. In both charge distributions, it is observed that for W+jets the distribution is more symmetric than for the signal processes. This is expected, as the cross section for W^{+}+jets is slightly larger as for W^{-}+jets due to the quark content of the proton. Further, it is expected to observe more positively electric charged leptons for the top-quark t-channel processes, as the cross section for top-quark production is larger than for top-antiquark production. The m_{T}^{W} distribution shows a harder spectrum for the W+jets process. While for m_{top} the distributions peak around the input top-quark mass of 172.5 GeV for the t-channel processes, the W+jets distribution is shifted and being smeared out further.
Even though some distributions only show small separation between signal and background

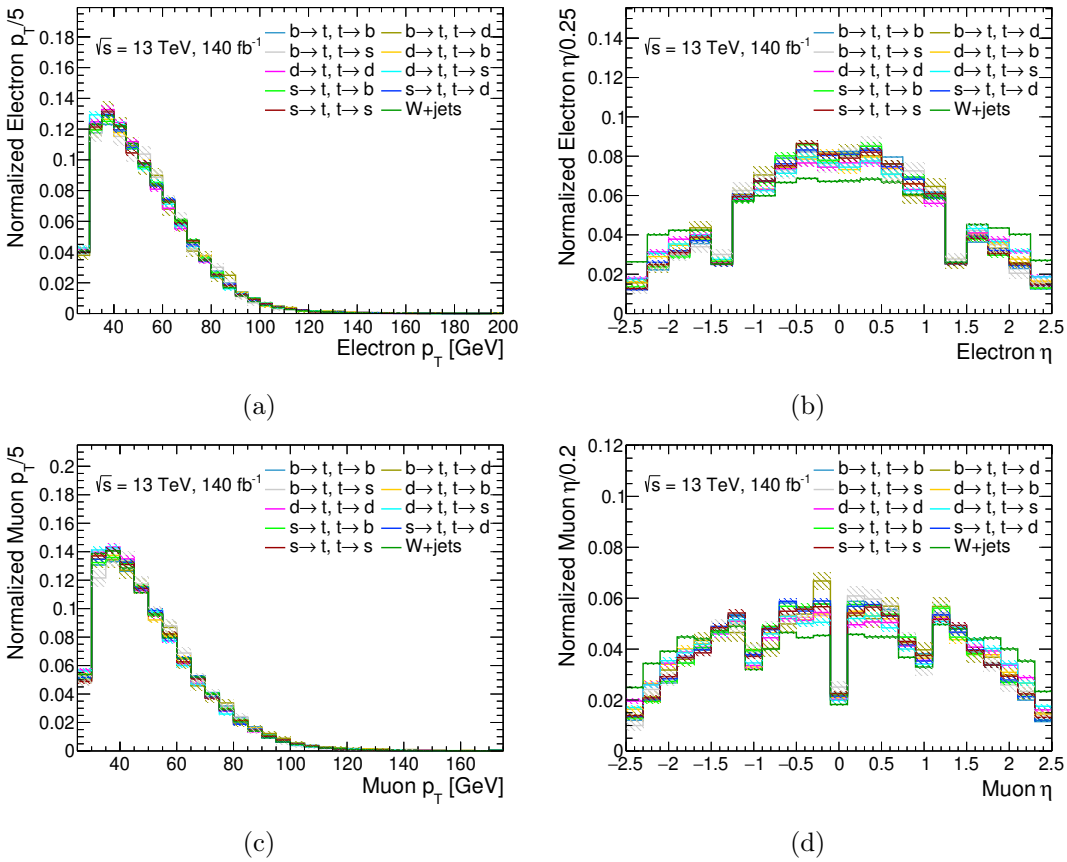

Figure 9.4: Shape of normalized distributions for all individual signal processes and the W+jets background. In (a) and (b) the p_{T} and η, respectively, of the electron is shown. In (c) and (d) the p_{T} and η, respectively, of the muon is shown. The hashed areas denote the MC statistical uncertainty.

events, the NN can potentially exploit hidden features of different quantities in an event and thus, including these distribution in the training can be important. On the other hand, having only a few distributions with noticeable differences does indicate that a separation of signal and W+jets events is a challenging task.

NNs are sensitive to features with vastly different scales, as the model may prioritize features with larger ranges or values compared to those with smaller ranges. Since the values and ranges of the input features differ, it is important to scale them to ensure consistent treatment during training to reduce the probability of landing in a local minimum. Therefore, the `MinMaxScaler` is utilized. This scaler transforms each value of an input feature, x, to a fixed range, typically $[0, 1]$, via:

$$x_{\mathrm{scaled}} = \frac{x - x_{\mathrm{min}}}{x_{\mathrm{max}} - x_{\mathrm{min}}}. \tag{9.12}$$

Here, x_{min} and x_{max} denotes the minimum and the maximum value of the feature.

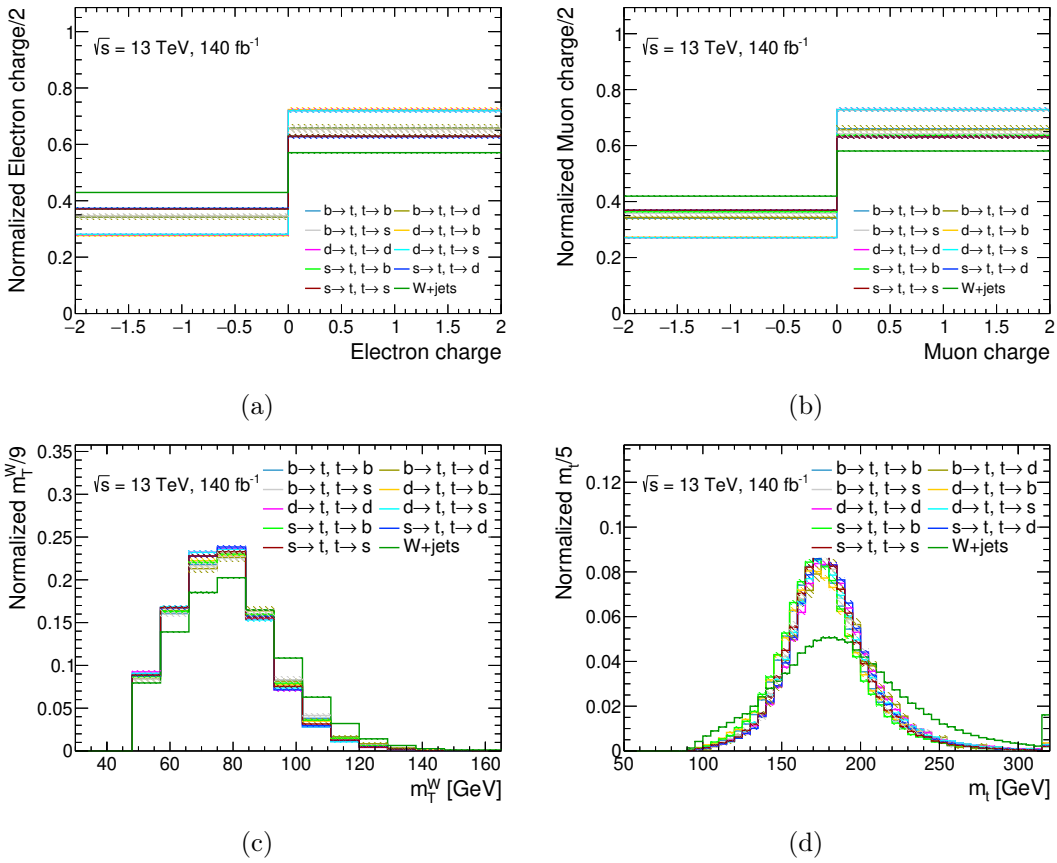

Figure 9.5: Shape of normalized distributions for all individual signal processes and the W+jets background. In (a) and (b) the electric charge of the electron and muon is shown, respectively. In (c) the m_{T}^{W} distributions are shown and in (d) the reconstructed m_{top} is shown. The hashed areas denote the MC statistical uncertainty.

For the combined signal, there are 2.5 M MC simulated events in the training set and 1.07 M events in the validation set, while for W+jets, there are 3.1 M and 1.3 M events, respectively. Both, the combined signal and W+jets events are weighted for the training with the usual MC weights and normalization to the cross section of each process and the measured luminosity is applied as a weight for each input feature. In order to avoid any bias towards one process during the NN training, another weight is computed to compensate any difference in the sum of all weights between the combined signal and the W+jets background.
All procedures described above are executed for both NNs in the odd-even cross validation and the corresponding input datasets.

9.3.2 Training and evaluation

The chosen NN architecture is a model with five hidden layers with the following number of nodes in descending order: $32, 16, 8, 4$, and 2. For the training, a learning rate of $r = 0.0005$ and batch size of 256 events was chosen. The training process was run for 200 epochs. The learning rate scheduler was implemented to scale r with a factor of 0.95 after every 10 epochs during which the validation loss did decrease. After each adjustment of r, a cooldown period of 5 epochs was set. The best model, indicated by the smallest validation loss, was saved during the training and used for the further steps in this work.

As mentioned above, a NN with the same settings is used for the odd-even cross validation procedure. In the following part, all plots shown correspond to the training of both, the NN model trained on the odd dataset, and the NN model trained on the even dataset, respectively. In Figure 9.6, the loss and the accuracy as function of the epoch are shown. The differences between the loss and accuracy curves of both networks are minor, indicating the odd-even cross validation did not introduce any bias. The curves for the validation dataset show a more uneven behavior. This effect is caused by the low number of events in the dataset, compared to the training dataset[3]. In order to evaluate the model and the training further, the Receiver operating characteristic (ROC)-curve is examined. The ROC curve is a graphical representation of a classifier's performance, illustrating the trade-off between the true positive rate (TPR) and the false positive rate (FPR), both defined in Equation (9.13), across different classification thresholds. The TPR, also called sensitivity or recall, is the proportion of actual positives, i.e. signal events here, that are correctly identified by the model, while the FPR is the proportion of actual negatives, i.e. W+jets events in this case, that are incorrectly classified as positives. These fractions are given by

$$\begin{aligned} \text{TPR} &= \frac{\text{True Positives}}{\text{True Positives} + \text{False Negatives}}, \\ \text{FPR} &= \frac{\text{False Positives}}{\text{False Positives} + \text{True Negatives}}. \end{aligned} \tag{9.13}$$

The ROC curve depicts the TPR against the FPR for different threshold values, illustrating the performance of the model as the decision threshold is varied. In Figure 9.7, the ROC curve for both NNs used for the cross validation are shown. The ROC curves for both NNs do not show any visible differences. Additionally, the area under the ROC curve (AUC) is used as a summary measure of the ability of a NN model to distinguish between two classes, with a value of 1 indicating perfect classification and a value of 0.5 indicating random guessing. For both NNs, the AUC score is comparable, with the odd NN yielding 0.732 and the even model NN yielding 0.734. Again, no bias towards one NN is observed. Here, both value indicate a good but not optimal separation power of the NN, as it nearly reaches the mean between a random guessing classifier and a perfect classifier. This result underlines, how challenging the task is with the input variables available.

[3] In order to estimate uncertainties on the different metrics to validate the applied cross-validation mathematically, one would need bootstrapping methods. These studies were beyond the scope of this work.

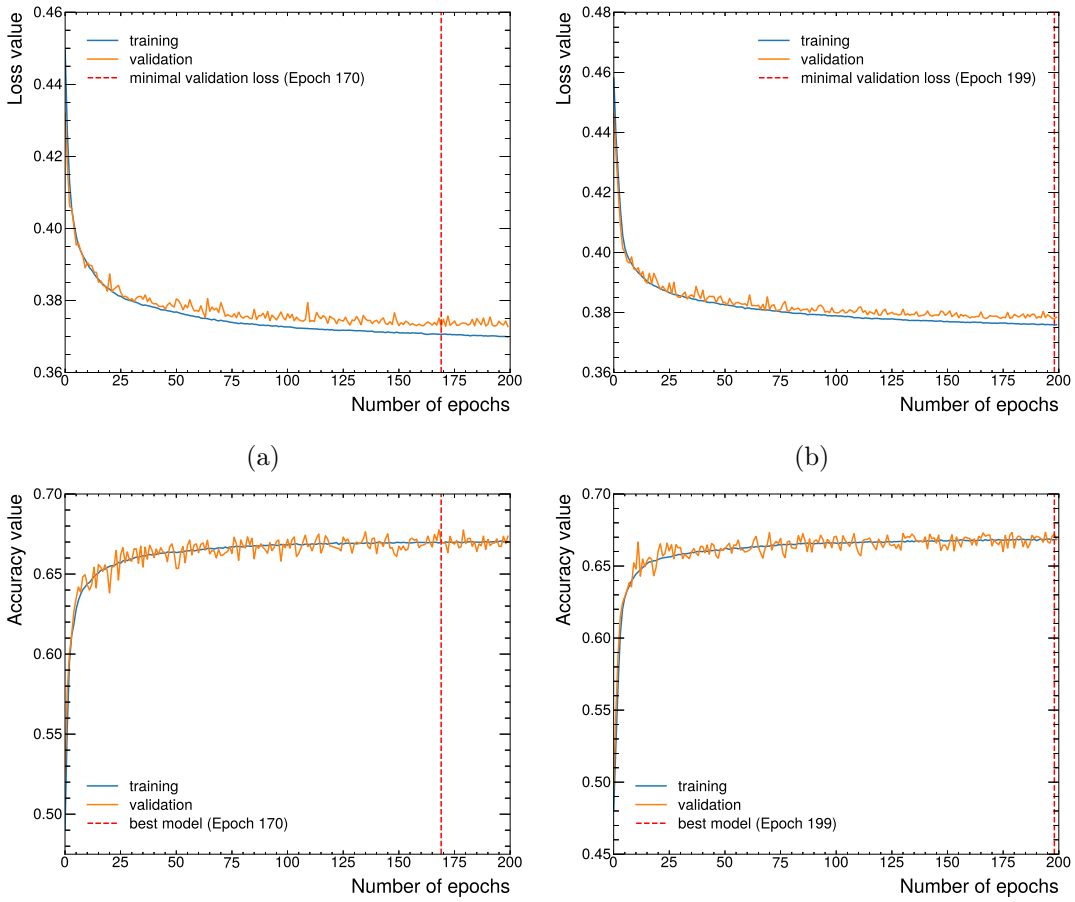

Figure 9.6: The loss curve and the accuracy curve for the odd model are shown in (a) and (c), respectively. The loss curve and the accuracy curve for the even model are shown in (b) and (d), respectively. The blue curve depicts the training dataset, while the orange curve shows the validation dataset. The red dashed line shows the best epoch saved at the end of the training.

Additionally, the NN output distributions for the saved best model are examined with regards to signs of possible overfitting. In Figure 9.8, the NN output distributions for both NNs are illustrated. The distributions are normalized such that the sum of all bin entries, divided by the number of bins yields one. No signs of overfitting are observed, as indicated by the ratio plots in both distributions. For both, true signal and true background events, the events of the validation dataset are classified very similar to the ones of the training dataset. Further, the output distributions for both NNs show a very similar shape indicating that the training on odd and even data set performed equally well.

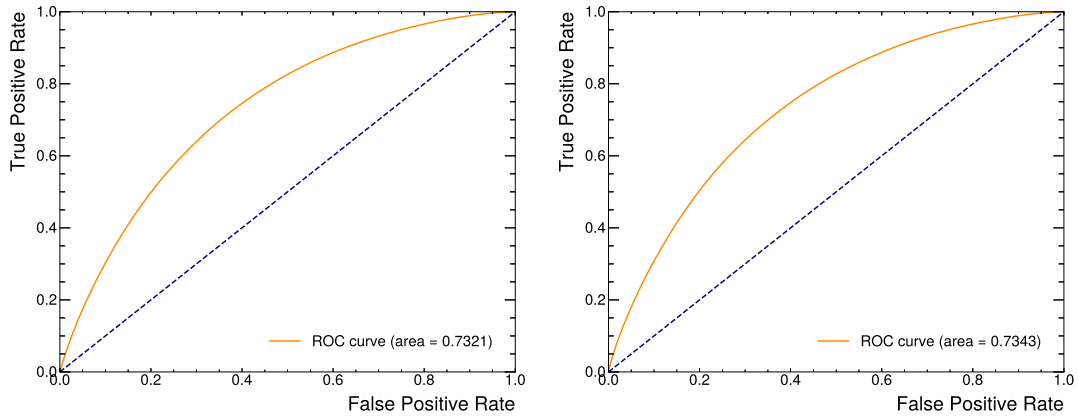

(a) (b)

Figure 9.7: The ROC curve for the odd model is shown in (a), while ROC curve for the even model is illustrated in (b). The dashed blue line depicts a classifier that guesses randomly.

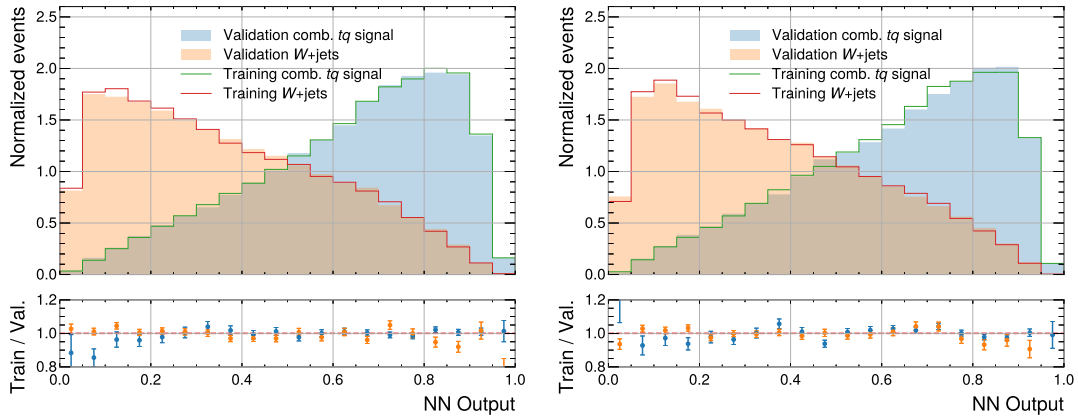

(a) (b)

Figure 9.8: Normalized NN output distributions for the best saved odd model are shown in (a), while same distributions for the best saved even model are shown in (b). The solid lines show the distributions for the training dataset, while the filled histograms depict the distributions for the validation dataset. The bottom plot shows the ratio between the entries of the training dataset and the validation dataset in each bin.

Application of NN model

After ensuring that the training was performed correctly, the NN models need to be applied to the dataset which it was not trained and evaluated on in order to assure that no bias was introduced. Hence, all plots shown in this section correspond to the NN model trained on the odd dataset applied to the even data set, and the NN model trained on the even dataset applied to the odd data set, respectively. In addition, both models are also applied to the minor backgrounds, Z+jets, top-quark s-channel and tW, VV and $t\bar{t}$. The normalized NN output distributions for the combined signal and combined background is shown in Figure 9.9. In both plots, both NN output distributions look very similar to the ones obtained from the training of the network. Hence, both NNs did generalize the learned information sufficiently. Further, the shape of the corresponding distributions to the background events and the signal events in both plots in Figure 9.9 shows only minor differences. The same distribution, but for the combined signal, W+jets and the minor backgrounds are presented in Figure 9.10. First, it is visible, that the minor background are also separated well from the signal. Secondly, the distributions for both, the odd model applied to the even dataset and vice versa, have a very similar shape, also for the background contributions not used in any training or validation dataset. Again, this observation indicates that both NNs were able to generalize learned information during the training. Both NNs classify diboson events (orange), single-top-quark s-channel[4] events (pink) and $t\bar{t}$ events (red) as more background like, while for Z+jets (magenta) it shows a broad distribution with a small peak in the middle, indicating that the kinematic information of these events do not exhibit a clear signal- or background-like structure.
In Figure 9.11, the NN output distribution for the combined signal, W+jets with and without the minor backgrounds are displayed, with the single-top-quark t-channel events being scaled by their SM prediction, i.e. the value from the global fit [19], $|V_{td}| = 8.6 \times 10^{-3}$ and $|V_{ts}| = 41.5 \times 10^{-3}$. Even though the NN is able to distinguish W+jets and single-top-quark events well - and comparable to the NN used in the t-channel cross section measurement in Figure 8.4 - the background yields are still overwhelming the signal yields. Further, Z+jets also shows a sizeable contribution in the more signal-like regions of the NN output in the range closer to one.
In order to find a trade-off between a quite pure region in t-channel events and a sufficiently large number of MC events, a cut value on the NN output distribution is chosen, with all events having a score higher than that cut value being used in the next step. Figure 9.12 illustrates the ratio of signal events over background events, S/B, as a function of the cut value on the NN output distribution. Processes including V_{td} and V_{ts} are scaled again to their current SM estimations. It is visible that using that scaling only $b \to t, t \to b$ has a sizeable contribution with respect to the background contamination. Based on these plots, the cut value on the NN output distribution to continue the studies presented here is chosen to be $NN_{\text{out}} > 0.8$. At this value, it is ensured that a sufficient amount of MC events is available in the next steps. In the following, only events with a NN output score larger than 0.8 are utilized. In Table 9.2, the expected event yields for all processes are

[4] In this Chapter real s-channel events and tW events are combined and therefore called s-channel for the rest of the chapter.

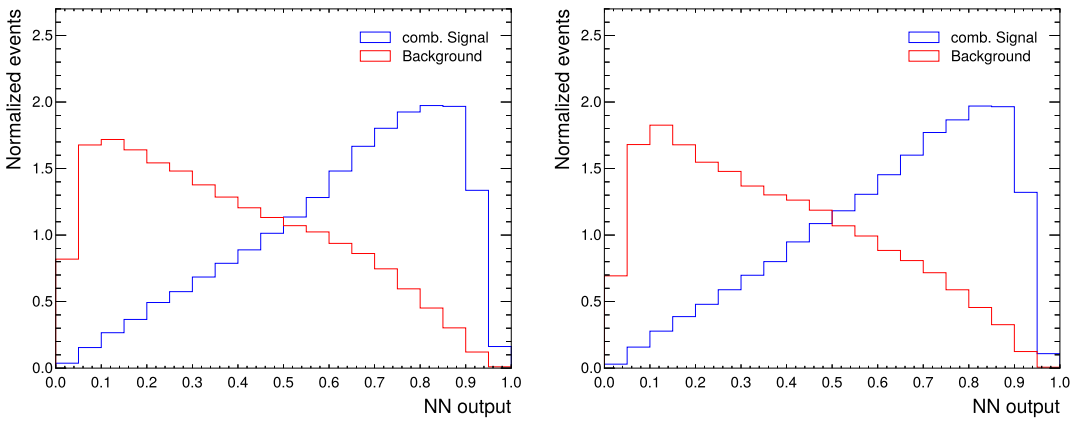

(a) (b)

Figure 9.9: Normalized NN output distributions for the best saved odd model applied to even dataset are shown in (a), while the same distributions for the best saved even model applied to the odd dataset are shown in (b). The blue line displays the combined signal, while the dark green line denotes the background events.

listed including the MC statistical uncertainty. Here, the single-top-quark CKM processes are again scaled to their SM prediction. Therefore, the number of W+jets events is still large compared to all signal events. The overall S/B ratio is 0.36, with a combined signal efficiency of $\approx 27\%$, which is the ratio of all signal yields after the cut on the NN of 0.8

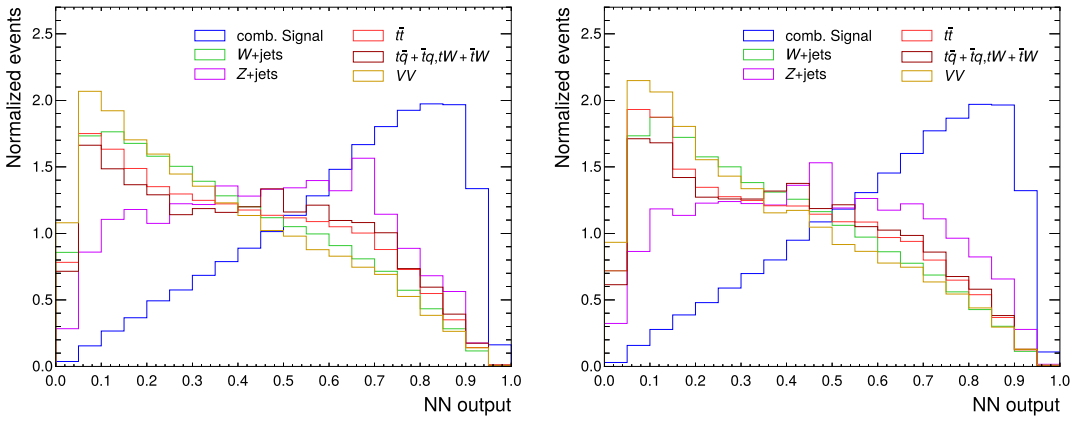

(a) (b)

Figure 9.10: Normalized NN output distributions for the best saved odd model applied to even dataset are shown in (a), while the same distributions for the best saved even model applied to the odd dataset are shown in (b). The blue line displays the combined signal, while the green line denotes the dominant W+jets events. All other backgrounds are also shown.

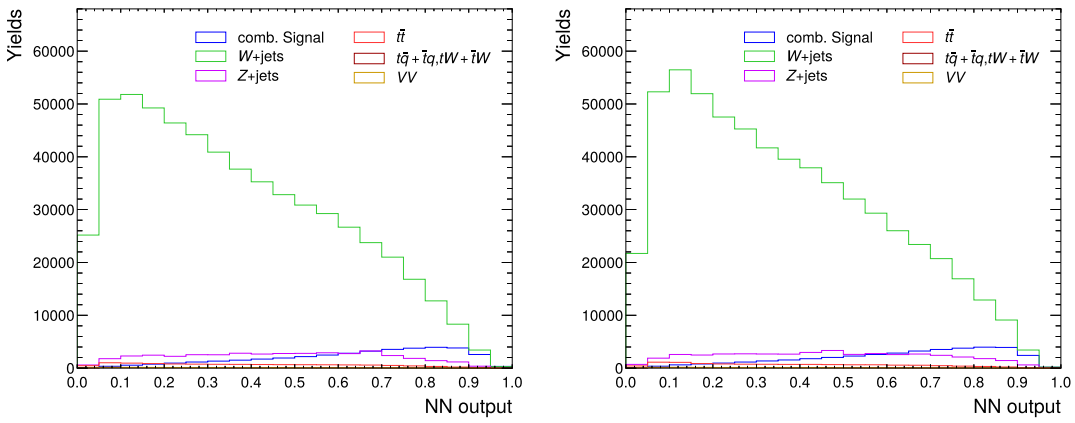

(a) (b)

Figure 9.11: NN output distributions for the best saved odd model applied to even dataset are shown in (a), while the same distributions for the best saved even model applied to the odd dataset are shown in (b). The blue line displays the combined signal, while the green line denotes the dominant W+jets events. All other backgrounds are also shown. The signal processes including V_{td} and V_{ts} are scaled to their corresponding SM prediction, using $|V_{td}| = 8.6 \times 10^{-3}$ and $|V_{ts}| = 41.5 \times 10^{-3}$ [19].

and all signal yields.

In order to improve the distinction between W+jets and single-top-quark t-channel events even further, other NN architectures like graph NNs or transformer-based NNs could be used, which might better capture the complex correlations and global event features.
In Figure 9.13, the feature importance is illustrated for both, the odd model and the even model trained. The feature importance is quantitatively defined as the impact of a given input variable on the performance of a NN model. The importance of a specific input feature is evaluated after training using a permutation-based approach. This is done by applying the trained model to the entire dataset while randomly shuffling the values of the feature under investigation. In this work, this procedure is performed twice, due to the large dataset[5]. Afterwards, the performance of the NN is compared to the performance before. A significant drop in the accuracy indicates that the feature is important, as the model strongly relies on it for classification, whereas small differences between the accuracy values before and after the permutation indicate less importance. As expected, for both NNs, the importance of different input features is very similar. The six most important variables are the same for both NNs, indicating that the events of both folds do not introduce any bias in the networks. The most important variable is the lepton η for both networks. Additionally, the p_{T} of the forward jet as well as the η distributions of both jets and the reconstructed top-quark mass have the largest impact on the training

[5]The probability to end up with the correct value at the correct event from before the shuffling is negligible.

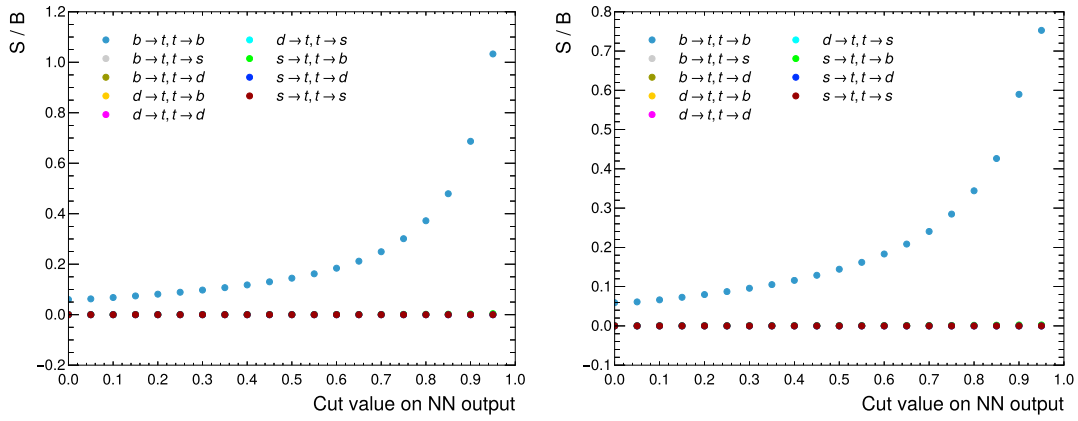

(a) (b)

Figure 9.12: S/B ratio as a function of the cut value on the NN output distribution (a) for the best saved odd model applied to even dataset, and (b) for the best saved even model applied to the odd dataset. The signal processes including V_{td} and V_{ts} are scaled to their corresponding current SM estimations, using $|V_{td}| = 8.6 \times 10^{-3}$ and $|V_{ts}| = 41.5 \times 10^{-3}$ [19].

Table 9.2: Number of events, N, for events with an $\mathrm{NN_{out}} > 0.8$. "Total MC" denotes the sum of all individual processes, including the single-top-quark t-channel signal processes. The shown uncertainty is the MC statistical uncertainty. "Total Signal" is the sum of all t-channel events and "Total Background" the sum of all other events. Both might not summarize exactly due to rounding effects.

Process	$N_{\text{signal region}}$
$b \to t, t \to b$	21 000 ± 140
$b \to t, t \to d$	1.4 ± 1.2
$b \to t, t \to s$	30 ± 6
$d \to t, t \to b$	8.3 ± 2.9
$d \to t, t \to d$	0.00 ± 0.03
$d \to t, t \to s$	0.02 ± 0.13
$s \to t, t \to b$	90 ± 9
$s \to t, t \to d$	0.01 ± 0.09
$s \to t, t \to s$	0.2 ± 0.4
Z+jets	6850 ± 80
VV	127 ± 11
$t\bar{t}$	1210 ± 30
t, s-chan	140 ± 12
W+jets	50 360 ± 220
Total Signal	21 120 ± 150
Total Backgroud	58 700 ± 240

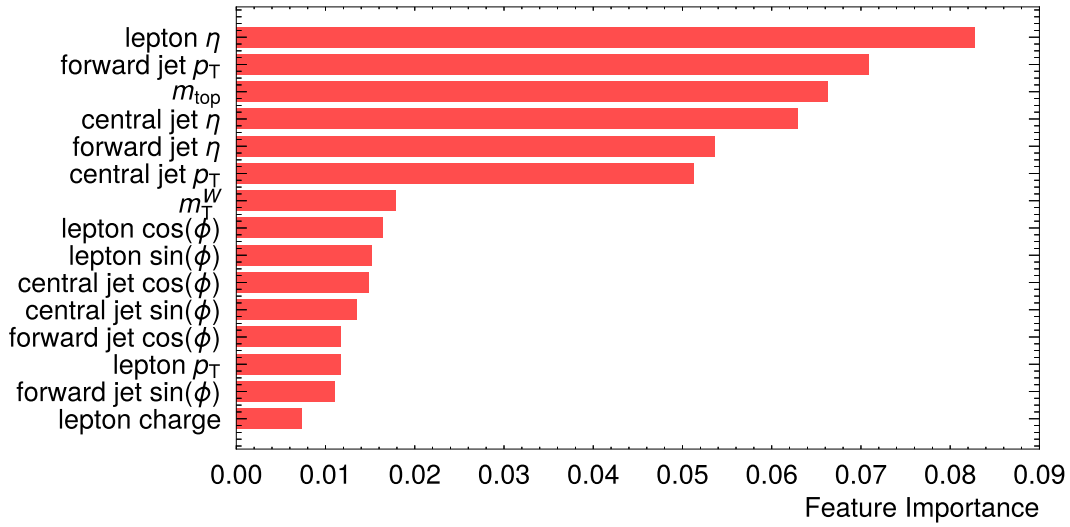

(a)

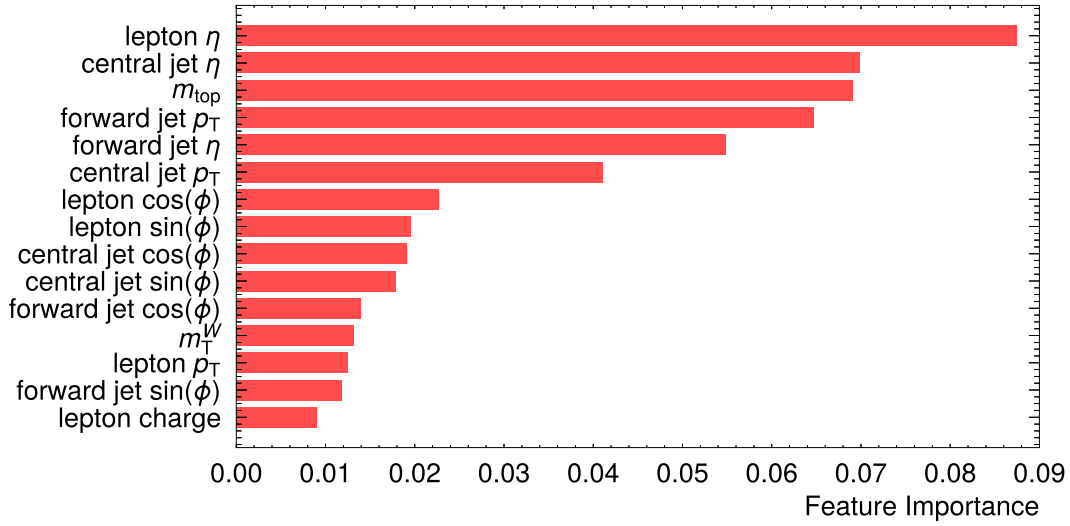

(b)

Figure 9.13: Feature importance for (a) the best saved odd model and (b) for the best saved even model. The higher the value for a feature, the more important the variable is for the training, i.e. the correct classification of training events.

of the NNs. Features with less helpful information include the p_T of the lepton, as well as all ϕ distributions and the lepton charge. Further, studies were done using the same variables as the NN in the top-quark t-channel cross section measurement. Using these high-level variables, constructed from four momenta of the final states does not improve the training or the results. Hence, it is assumed that the NN used in these studies is able to learn the relations during the training from the given input features. Concluding these studies, adding variables which incorporate information regarding particle tracks might

be suitable for this task. Adding b-tagging information could be tested as well, however, since top-quark events without b-quarks are part of the signal processes, this might still not lead to a better performance overall for the aim of signal and background separation. Further studies regarding track information and b-tagging information at this stage were beyond the scope of this thesis.

9.4 Distinguishing between different single-top-quark *t*-channel processes

In order to gain sensitivity to the different top-quark involved CKM matrix elements, an attempt is made to separate different single top-quark t-channel processes. The aim is to create different analysis regions, tailored to one or more specific CKM matrix elements. Further, exploiting possible differences between different production modes is assumed to increase the sensitivity. In a first step, information about the `DL1r` tag-weight bin of the central jet in each jet is added to the input features. As explained in the calibration procedure in Chapter 7.1, jets are assigned to a tag-weight bin depending on their `DL1r` score. Therefore, it is expected that this addition will boost the classification of the NN. Furthermore, the p_{T} and the η distribution of the reconstructed top-quark and the NN output score of the previous signal-background network are added to the input features. In addition, the reconstructed top-quark mass is dropped from the input vector, as in studies with and without this feature, no differences were observed in the training or performance of the networks described in the following.

9.4.1 Multiclass Neural Network for all top-quark processes

In a first setup, the single-top-quark t-channel processes are grouped into six categories, based on the production and decay vertices. Hereby, processes in which the top-quark decays into a d-quark or s-quark are grouped together in one category, as a distinction between light flavor jets originating from a d- or s-quark is currently not achievable in ATLAS. Therefore, the six categories are

- 1: $b \to t, t \to b$;
- 2: $b \to t, t \to d$,$b \to t, t \to s$;
- 3: $d \to t, t \to b$;
- 4: $d \to t, t \to d$,$d \to t, t \to s$;
- 5: $s \to t, t \to b$;
- 6: $s \to t, t \to d$,$s \to t, t \to s$;

with the process(es) being denoted by the top-quark production and decay included after the colon. Analogously as for the discrimination between signal and background, an odd-even cross validation procedure is done. The NN models for both folds are trained to distinguish different all processes and classify the simulated events into the dedicated categories. Hence, multi-class feed-forward NNs are used for these studies. For the training, all events are assigned a true value between 1 and 6 depending on the corresponding true class. Training and evaluation procedures are done comparable to the NN setup described in the previous chapter. The NN architecture consists of five hidden layers with the following number of nodes: $128, 64, 32, 16, 8$. The learning rate is set to $r = 0.00005$ for the training. The learing rate scheduler is implemented to scale r with a factor of 0.95 after every 10 epochs during which the validation loss did decrease. After each adjustment of r a cooldown period of 5 epochs is set. A batch size of 256 events is used, and the training is run for 500 epochs in total. Analogously to the NN used in the signal background classification, the best model, indicated by the lowest validation loss, is saved during the training and used for the further steps in this work.

Figure 9.14 shows the loss functions and the accuracies for the training and the validation dataset for both NNs. For both used networks, the accuracy curve as a function of the epoch shows the same behavior. During training, the accuracy initially increases rapidly, reaching approximately 0.5 after around 80 epochs. However, instead of continuing to improve, it decreases over the next $80 - 100$ epochs before stabilizing at a plateau around 0.4. In contrast, the loss for both networks monotonically decreases throughout training. One possible explanation for this behavior is that, in the early training phase, the model learns simple patterns from the input dataset that allow it to distinguish between classes more effectively. However, as training progresses, the model begins to capture more complex structures in the data. This process can lead to overfitting to specific features that do not generalize well, causing a degradation in the classification accuracy. While the model continues to optimize the loss function, the learned decision boundaries may shift in a way that reduces overall accuracy. Another contributing factor could be class confusion. In a multiclass classification setting, the model might initially find clear separations for some classes. As the NN refines its decision boundaries, it may inadvertently increase misclassification rates for certain categories, leading to a decline in accuracy despite a decreasing loss. This effect suggests that the model is minimizing uncertainty in its predictions rather than improving class separability.

In order to investigate the observations further, the output of the multiclass NN is examined. Since a multi-class approach with six classes is used, the output distribution is a six-dimensional vector. An event is labeled as correctly identified if the predicted class equals the true class for an event, i.e. if the corresponding entry in the output vector is the largest value in the output vector.
The different distributions for each output vector entry for the odd NNs, comparing the correctly classified true class and the true events of all other classes in the training dataset, is shown in Figure 9.15. The output vector entry distributions of the even NNs show qualitatively a very similar pattern compared to those of the odd NNs as well. For none of the classes, events are assigned a probability above 0.4, indicating the difficulty of distinguishing between different signal processes using the NN. Moreover, the distributions

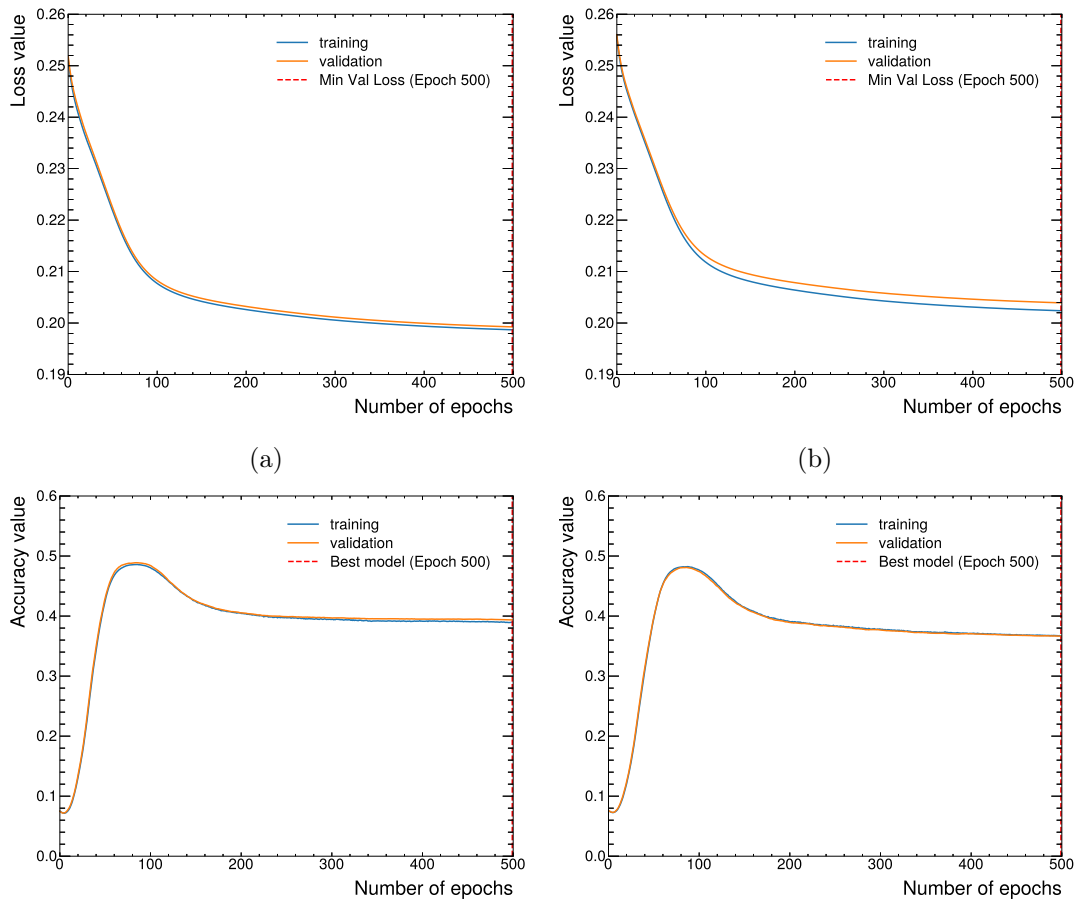

Figure 9.14: The loss curve and the accuracy curve for the odd model are shown in (a) and (c), respectively. The loss curve and the accuracy curve for the even model are shown in (b) and (d), respectively. The blue curve depicts the training dataset, while the orange curve shows the validation dataset. The red dashed line shows the best epoch saved at the end of the training.

of the output probabilities for both the events that are part of the true class and the events belonging to other classes exhibit a significant overlap. This suggests that the model fails to assign distinctly higher probabilities to the correct class, leading to a lack of separation in the classification. Additionally, no clear trend or systematic deviation is observed, further reinforcing the observation that the network does not differentiate well between classes.

Further analysis of the classification of both NNs is performed by inspecting the confusion matrices. The confusion matrix provides a detailed evaluation of the model's classification performance by summarizing the number of correctly and incorrectly predicted events for each class. Each row represents the true class, while each column corresponds to

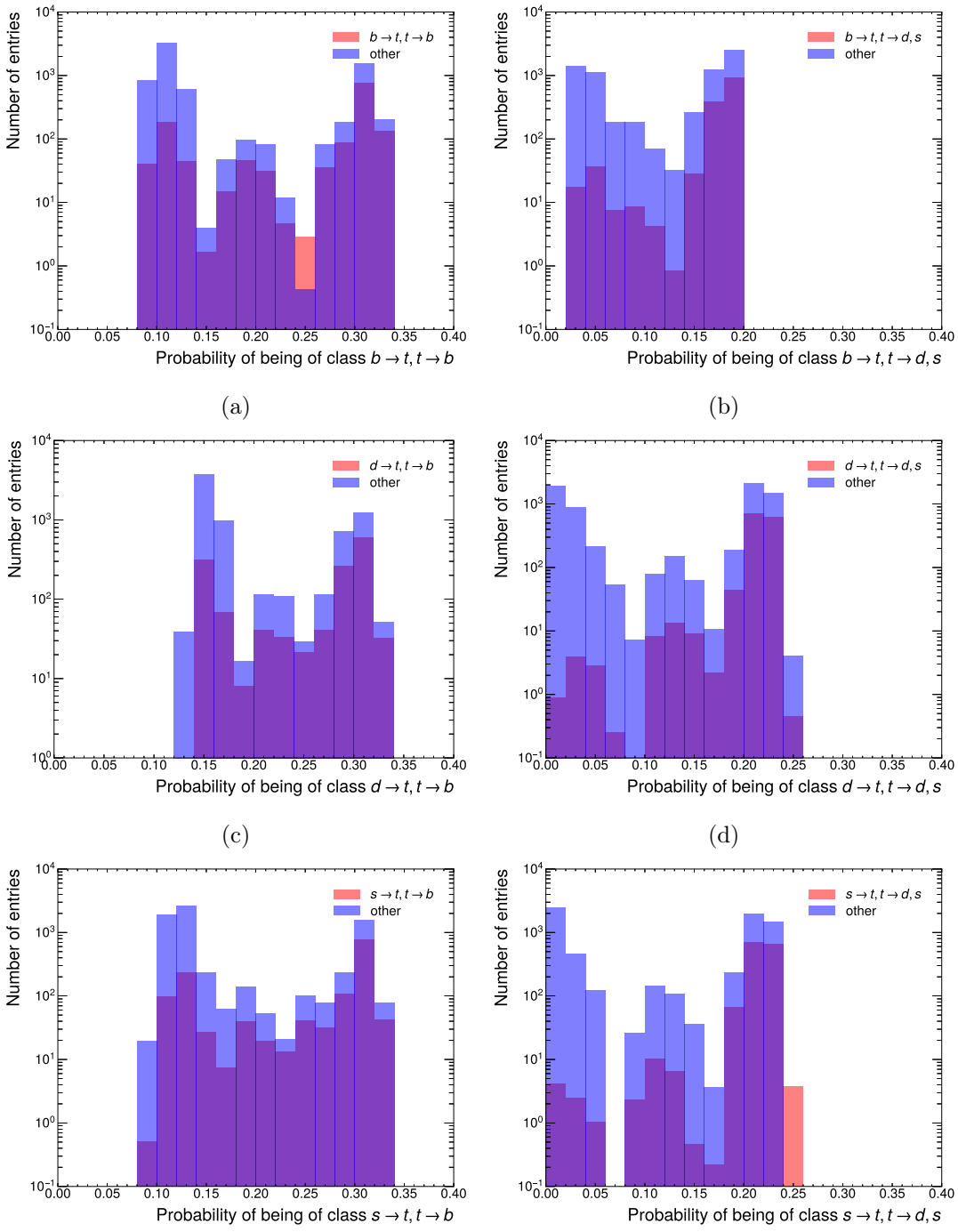

Figure 9.15: Distributions for each output vector entry for the odd NNs. The probability of an event being classified for class 1 is shown in (a), for class 2 in (b), for class 3 in (c), for class 4 in (d), for class 5 in (e) and for class 6 in (f). The red histogram in each plot denotes the true class, while the blue histogram depicts the events of all other classes.

the predicted class, allowing for an analysis of misclassification patterns. For a perfect classifier, the confusion matrix would be diagonal.
In Figure 9.16, the normalized confusion matrices for the training and validation dataset are shown. For both networks, the same trend is observed in both, training and validation datasets. For events where top-quarks decay into light quarks, no event is assigned to class 2 ($b \to t, t \to b$). Instead, the network classifies all such events into either class 4 or class 6, suggesting that it does not distinguish well between these two categories. For top-quarks decaying into b-quarks, the network predominantly assigns events to class 1 ($b \to t, t \to b$). However, even in this case, a non-negligible fraction of more than 10% of events is misclassified into each other class per true class. This indicates again that the network struggles to effectively separate the six individual processes, likely due to overlapping input feature distributions and insufficiently distinct patterns in the input space. The confusion matrix show, that the added b-tagging information helps the networks to distinguish between events with $t \to b$ and $t \to d, s$, but other differences related to the different initial states are not distinguishable for the NN.

This multi-class study indicates, that a simple feed-forward NN is not able to distinguish properly between processes with different single-top-quark production and decay modes. As mentioned for the binary classifier in Chapter 9.3.2, information about track properties could also be used in the multiclass networks to improve their performance.

9.4.2 Multiclass Neural Network for groups of top-quark processes

As the next step, a simpler NN architecture is chosen. Instead of six classes, four classes are utilized. Targeting differences in the final state objects from altering probability density functions (pdfs) of the initial state quarks, processes are grouped as follows:

- 1: $s, b \to t, t \to d, s$;
- 2: $d \to t, t \to d, s$;
- 3: $s, b \to t, t \to b$;
- 4: $d \to t, t \to b$;

The training process and evaluation is done analogously to the six class network described in the previous section. The same NN architecture was chosen as for the multiclass classifier utilized in the previous chapter, as well as the same input features.

Figure 9.17 shows the loss functions and the accuracies for the training and the validation dataset for both trained NNs. Similarily to the previous multiclass network, the accuracy curve exhibits a non-monotonic behavior throughout training. Initially, the accuracy increases rapidly, reaching approximately 0.45 within the first 20 epochs. However, during the next 20 epochs, a decline is observed, indicating a temporary degradation in classification performance. Following this drop, the accuracy gradually recovers over the next 100 epochs before stabilizing at a slowly increasing plateau ending just above 50% after the complete training of 500 epochs. This behavior suggests that the network initially

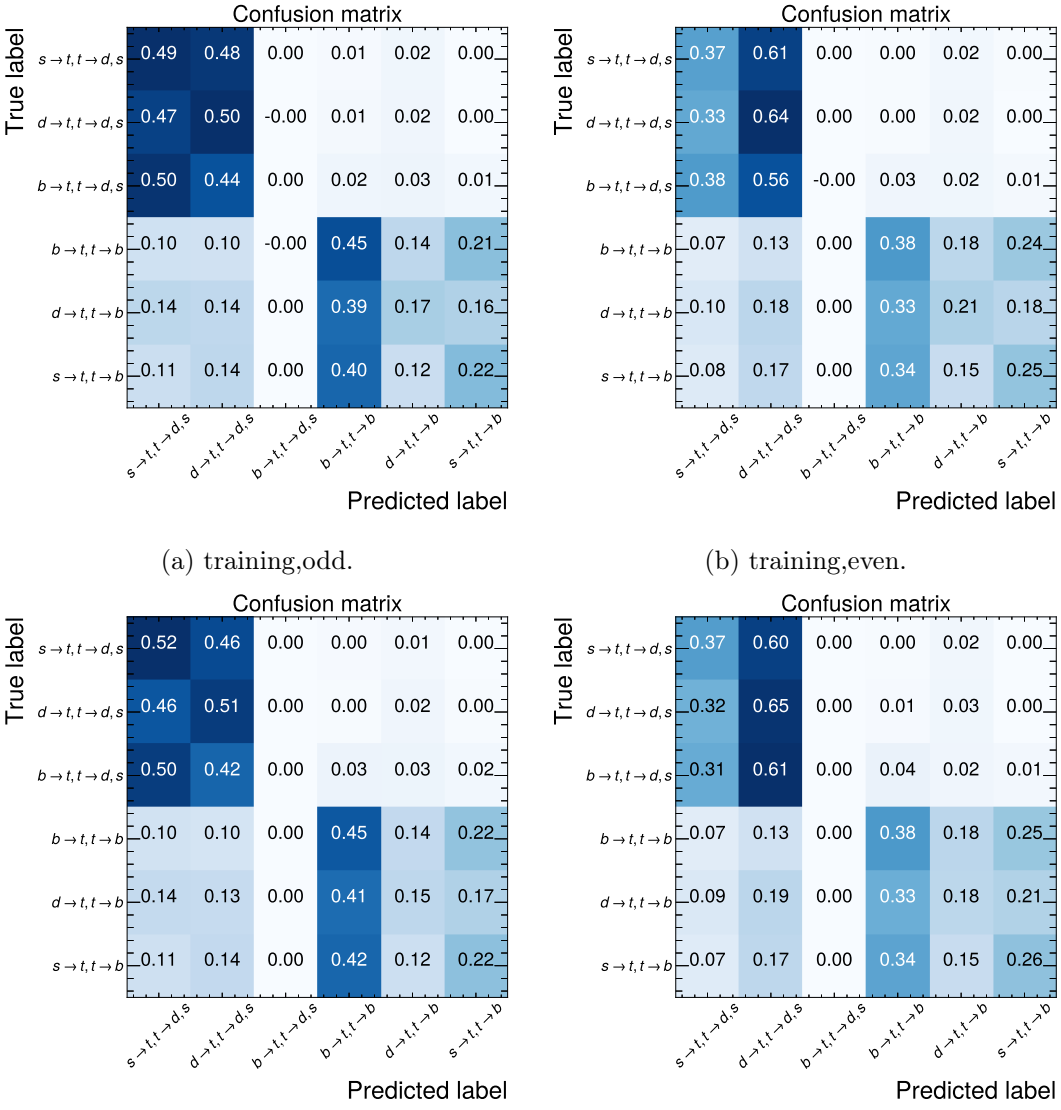

(a) training,odd.

(b) training,even.

(c) validation,odd.

(d) validation,even.

Figure 9.16: Confusion matrices for both models of the two-fold cross-validation for the NN with six output classes, illustrating the classification accuracy. (a) and (c) show the confusion matrices for the training and validation datasets of the odd-fold model, respectively. (b) and (d) show the confusion matrices for the training and validation datasets of the even-fold model, respectively. The diagonal elements represent the number of correctly classified events for each class, while off-diagonal elements indicate misclassifications.

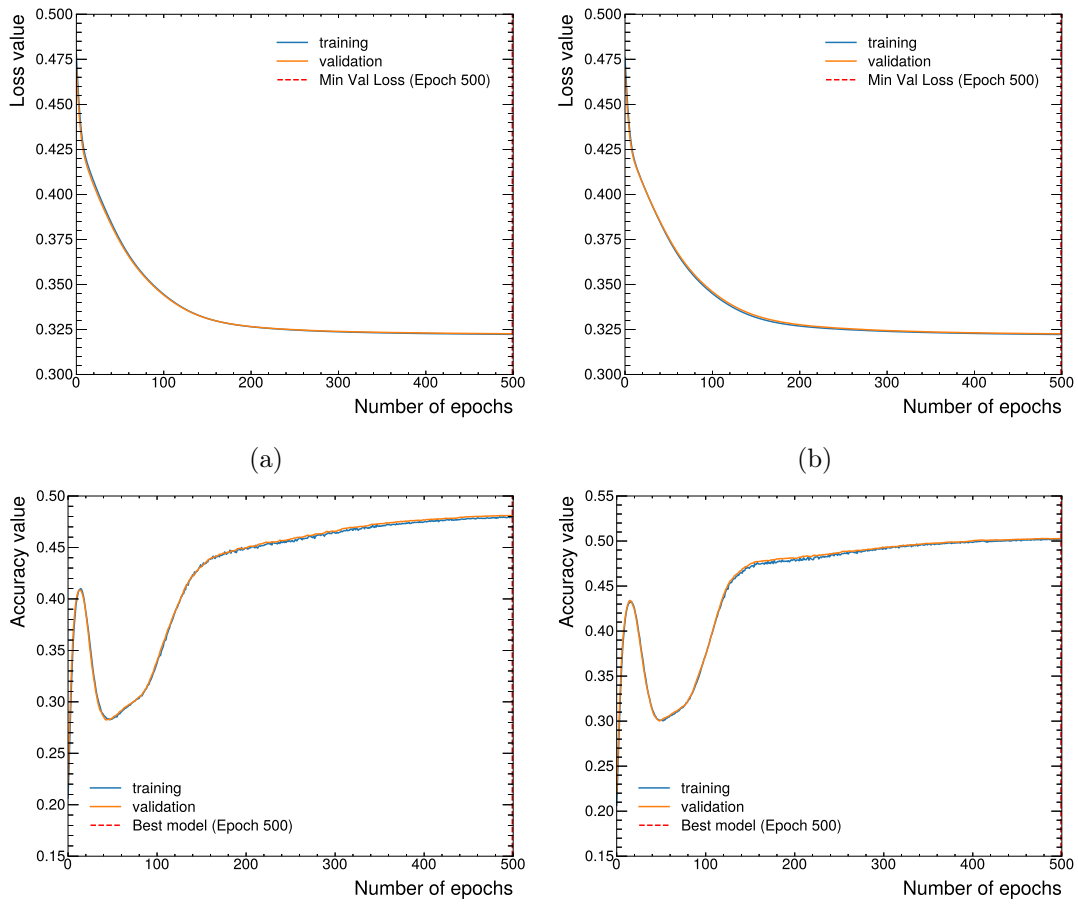

Figure 9.17: The loss curve and the accuracy curve for the odd model are shown in (a) and (c), respectively. The loss curve and the accuracy curve for the even model are shown in (b) and (d), respectively. The blue curve depicts the training dataset, while the orange curve shows the validation dataset. The red dashed line shows the best epoch saved at the end of the training.

learns simple patterns that improve classification, but as training progresses, adjustments to the decision boundaries lead to a temporary performance drop. The subsequent slow recovery points to the network continuing to refine its classifications, albeit with diminishing improvements in feature separability, indicating to the same observations made for the six class NN.

The fact that the validation loss reaches its lowest value in the final epoch, even if it remains on a plateau, suggests that the model has reached a stable state without signs of significant overfitting. This indicates that additional training epochs or fine-tuning of hyperparameters, such as the learning rate schedule, could potentially yield further improvements. However, major further improvements are unlikely as the model has effectively learned to extract the relevant features from the data given the observations

described in the following.

The output of this multiclass NN is a four-dimensional vector. Analogously to the previous multiclass network, an event is labeled as correctly identified if the predicted class equals the true class for an event, i.e. if the corresponding entry in the output vector is the largest value in the output vector. In Figure 9.18, the confusion matrices for both NNs for both, the training and validation dataset, are shown. Again, for both networks, the same trend is observed. Events with a b-quark in the final state and those without are well separated by the network. However, distinctions between classes with the same final state are still unclear, especially in the case of events with a b-quark in the final state. Furthermore, events with jets originating from b-quarks that are not tagged as b-jets lead to a non-negligible number of events from $t \to b$ being misclassified into categories without a b-quark in the final state.

Further analysis of the classification of both NNs can be performed by inspecting the output vector entries, similarily to the six classes multiclass NN. The different distributions for each output vector entry, comparing the correctly classified true class and the true events of all other classes in the training dataset, are located in Appendix H. The output vector entries show a very similar behavior to the ones observed for the network using six classes, indicating the same challenges leading to low separation power between the different classes as the previous NN.

Again, the same conclusions as for the network with six output classes are drawn. The differences in the pdfs for each top-quark process are not accessible at the detector level, and therefore, the networks are not able to distinguish processes where the top-quark originates from the b-, d-, or s-quark. Further, differences in the final state are also not fully captured due to expected challenges using b-tagged jets. Exploiting track information might help in that regard. As mentioned before, track information was not available. Hence, this limitation impacts the model's performance.

9.4.3 Binary classifier to distinguish $t \to d, s$ and $t \to b$

In order to be able to separate the different top-quark decay processes, a binary classifier is implemented. Since kinematic differences between the single-top-quark production processes were not sufficiently large to enable the multiclass networks to distinguish between different processes, two classes are constructed, depending on the top-quark decay:

- 0: $b \to t, t \to b$, $d \to t, t \to b$,$s \to t, t \to b$;
- 1: $b \to t, t \to d$,$b \to t, t \to s$, $d \to t, t \to d$,$d \to t, t \to s$,$s \to t, t \to d$,$s \to t, t \to s$;

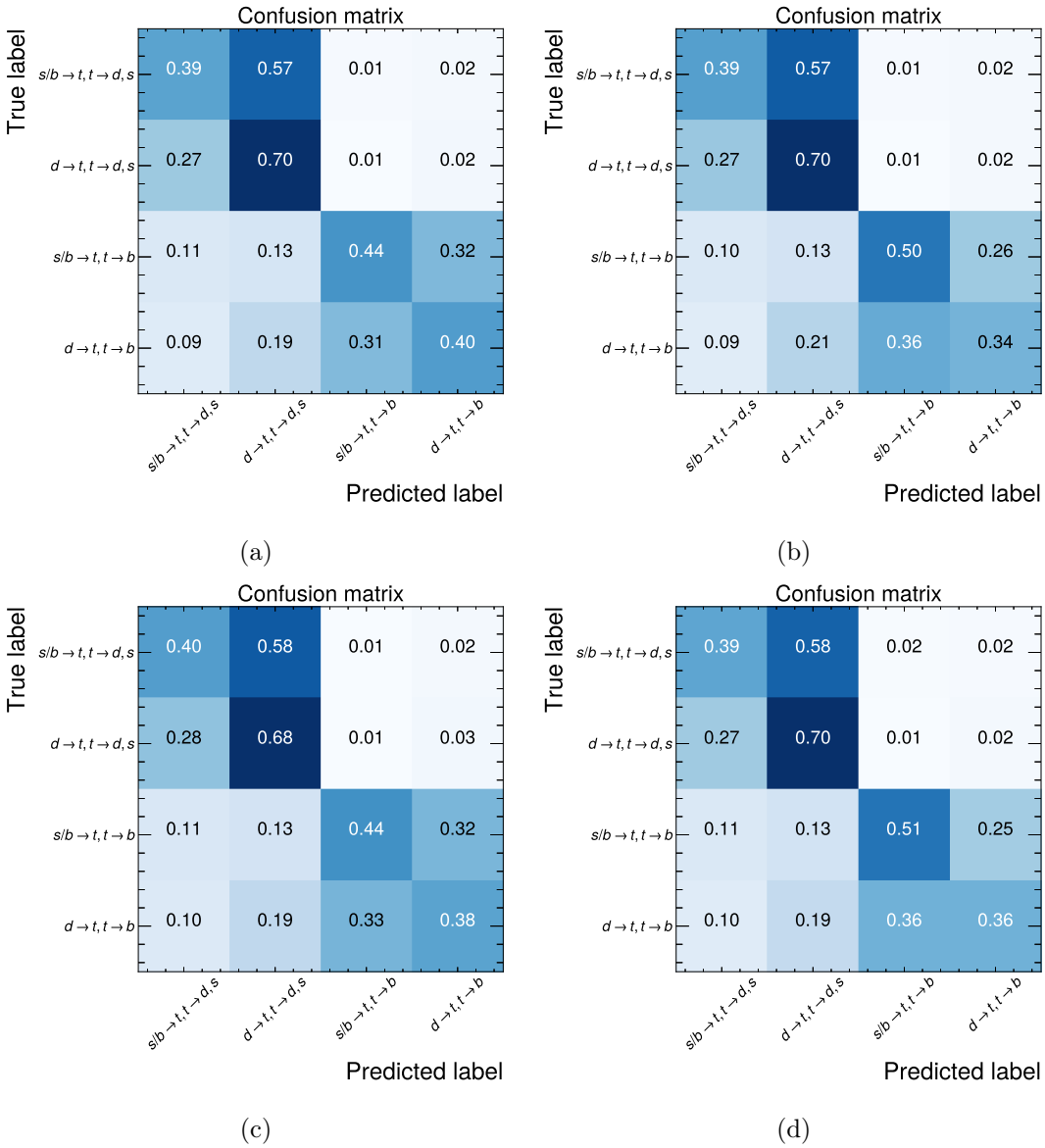

Figure 9.18: Confusion matrices for both models of the two-fold cross-validation for the NN with four output classes, illustrating the classification accuracy. (a) and (c) show the confusion matrices for the training and validation datasets of the odd-fold model, respectively. (b) and (d) show the confusion matrices for the training and validation datasets of the even-fold model, respectively. The diagonal elements represent the number of correctly classified events for each class, while off-diagonal elements indicate misclassifications.

Therefore, all top-quark events are assigned either a true value of 0 or 1 in the training, depending on the top-quark decay process. A binary classifier similar to the one utilized for the classification of all signal processes against W+jets is utilized. The chosen NN architecture is a network with 5 layers with the following number of nodes in descending order: 32, 16, 8, 4, 2. The same learning rate as for the signal-background-classifier is used, $r = 0.0005$. A batch size of 256 is applied for the training, which is performed for 150 epochs.

In Figure 9.19, the evaluation metrics for the training, the loss functions and the accuracy, are shown for the odd-fold model and the even-fold model. The loss functions do not indicate any sign of overfitting, with both the loss curves for the training and validation

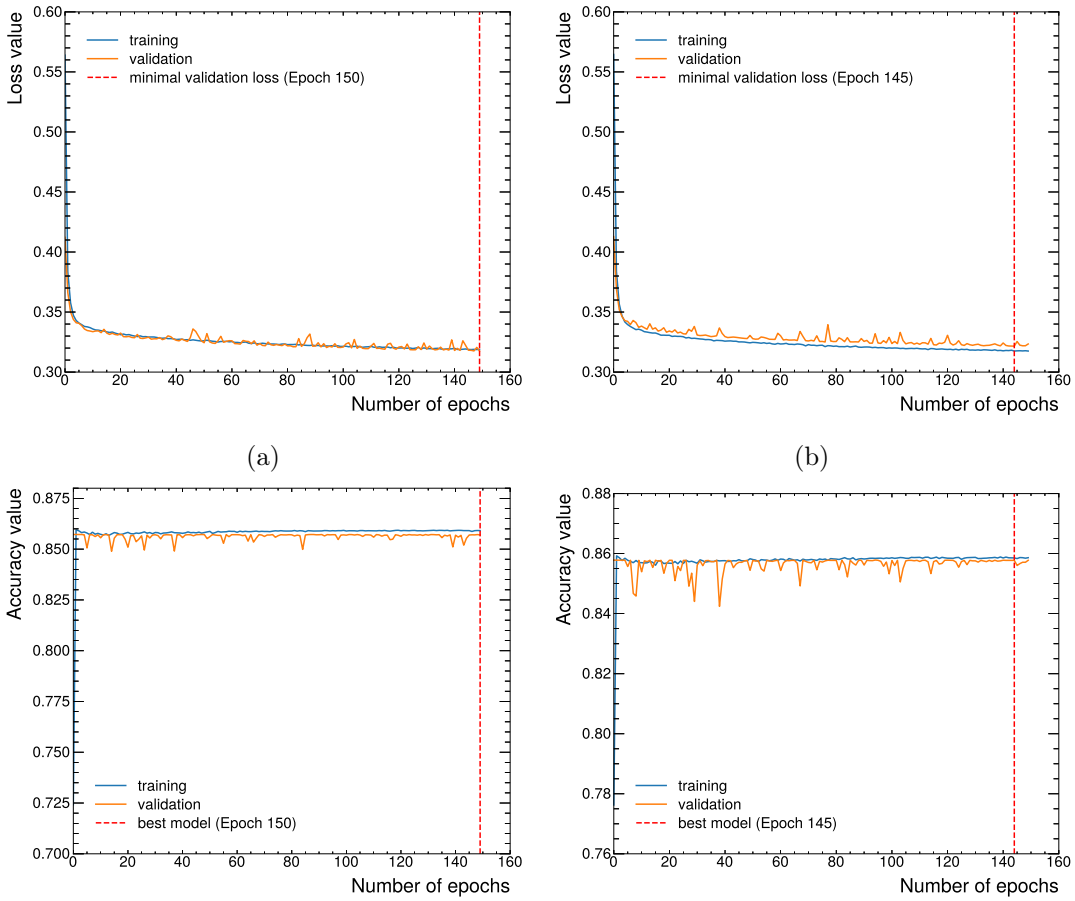

Figure 9.19: The loss curve and the accuracy curve for the odd model are shown in (a) and (c), respectively. The loss curve and the accuracy curve for the even model are shown in (b) and (d), respectively. The blue curve depicts the training dataset, while the orange curve shows the validation dataset. The red dashed line shows the best epoch saved at the end of the training.

datasets, showing a steep declinde at the beginning and a plateau at the end. The accuracy curves are also very similiar, both in terms of shape and accuracy values for both networks. The network performs similarily on both, the training and the validation datasets.

The ROC curve and the corresponding AUC score are illustrated in Figure 9.20. The ROC curve for the model shows a sharp increase in the TPR at the beginning, with a nearly constant FPR until approximately 0.2. The TPR reaches a value of around 0.95 at this point. Afterwards, the curve flattens, for both, TPR and FPR torwards one. The corresponding AUC scores are 90.58 and 90.66, indicating strong classification performance and no bias in either NN.
This shape suggests that the model is very effective in correctly classifying the majority of positive events early on, with a relatively low number of false positives. However, the flattening of the curve as it approaches the top-right corner (TPR = 1, FPR = 1) implies that the model struggles to maintain a balance between identifying true positives and controlling false positives when the decision threshold becomes more stringent. This could indicate that the model is potentially overfitting to certain patterns or input features.

The NN output distributions after the training procedure are shown in Figure 9.21. Most events with $t \to b$ are classified accordingly to their true class to the left side of the plot. However, a small subset of events from these processes are classified more to the right part of the output distribution. This is expected, as not all jet originating from b-quarks are expected to be tagged. Additionally, another even smaller subset of events has a NN output score around 0.2 to 0.4, indicating that these events are neither strongly resembling events with either top-quark decay for the network. Consequently, the NN is also able to mostly classify events with $t \to d, s$ to the right side of the distribution. Nevertheless, the majority of events are not as strongly classified as those from other class, with the NN output distribution for these events peaking around 0.8, and no events being classified

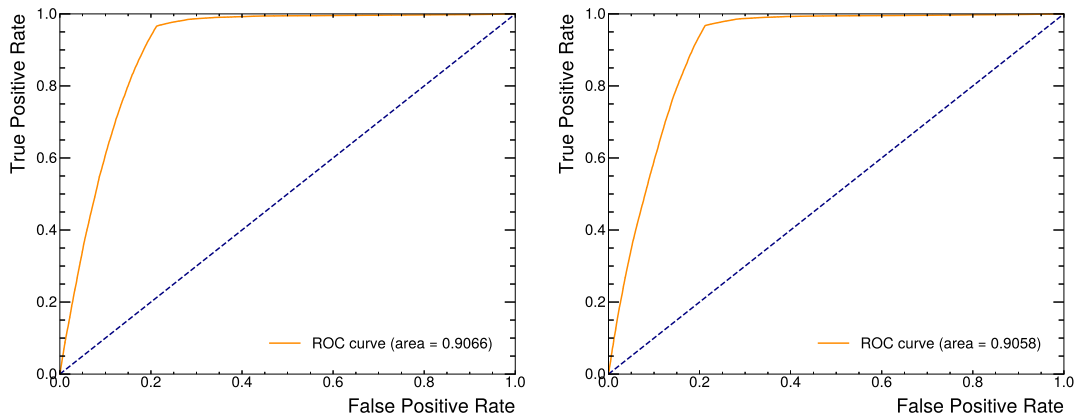

(a) (b)

Figure 9.20: The ROC curve for the odd model is shown in (a), while ROC curve for the even model is illustrated in (b). The dashed blue line depicts a classifier that guesses randomly.

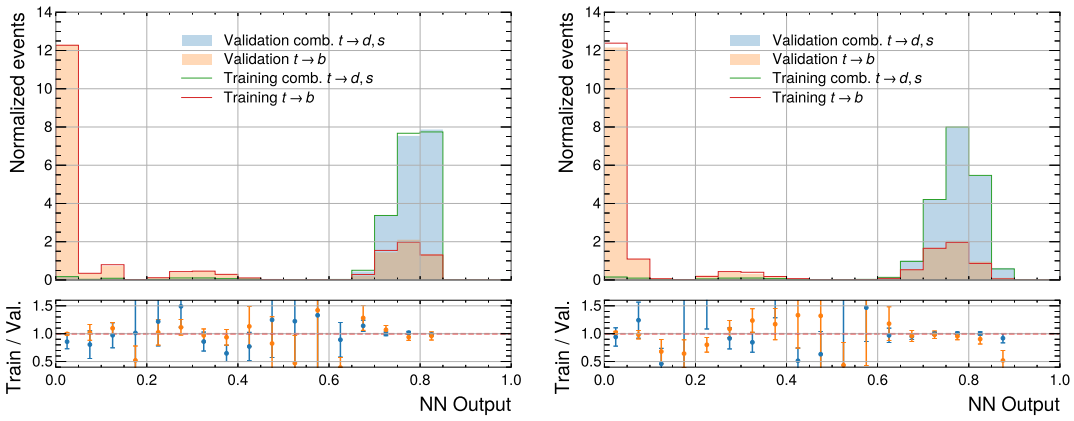

(a) (b)

Figure 9.21: Normalized signal-versus-signal NN output distributions for the best saved odd-fold model are shown in (a), while same distributions for the best saved even-fold model are shown in (b). The solid lines show the distributions for the training dataset, while the filled histograms depict the distributions for the validation dataset. The bottom plot shows the ratio between the entries of the training dataset and the validation dataset in each bin.

with a NN score of 0.9 or larger. This observation can be attributed to the contribution of $t \to b$ events being mis-classified as $t \to d, s$ events, which makes it difficult for the NN to distinguish between them. Therefore, assigning higher NN output score values to events with $t \to d, s$ is not achieved.

The feature importance plot, depicted in Figure 9.22, reinforces the statement, that the addition of the b-tagging weight bin for the central jet in an event to the input features is highly crucial for the network's performance and primarily determines which events receive which NN output scores: The feature importance is calculated as explained in Chapter 9.3.2. No other feature than the associated tag-bin of the `DL1r` algorithim of the central jet is important to classify the events. This further demonstrates, that the differences in the kinematic distributions between the different top-quark processes are almost negligible. This underlines the necessity to include track-based variables for such measurements in the future.

In a next step, the odd-model is applied to the dataset with the even number and vice versa. The corresponding normalized NN output distributions are depicted in Figure 9.23. Most of the background events are classified very similar to the $t \to d, s$ events. Since W+jets and Z+jets make up the majority of background events, this is expected.
The NN output distribution for all events is utilized further in the final step, the statistical analysis.

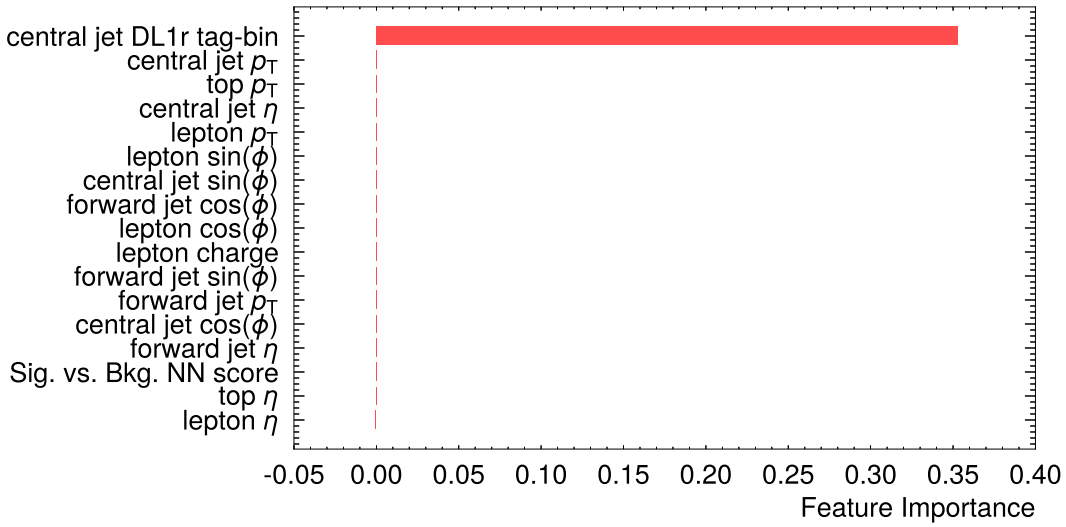

(a)

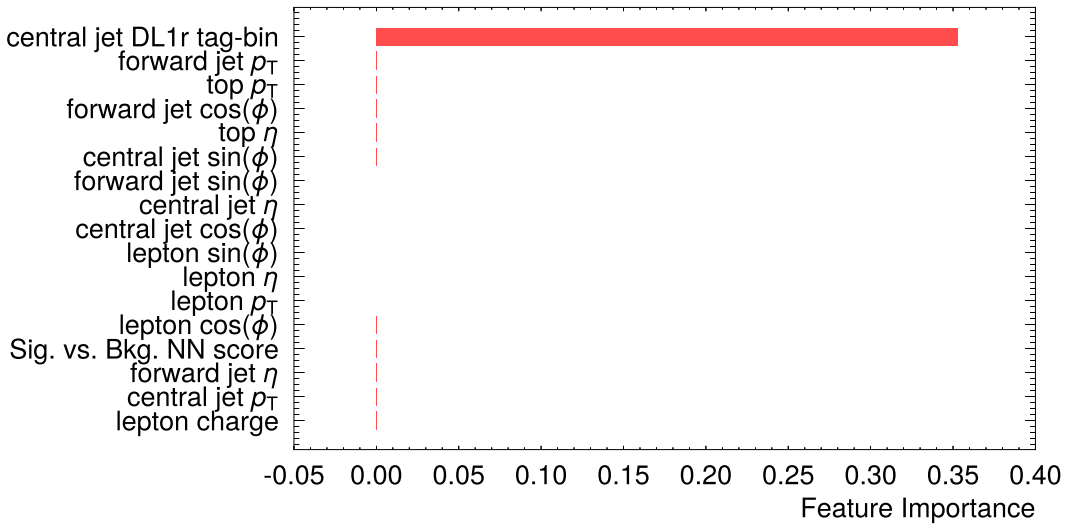

(b)

Figure 9.22: Feature importance for (a) the best saved odd model and (b) for the best saved even model. The higher the value for a feature, the more important the variable is for the training, i.e. the correct classification of training events.

9.5 Profile Likelihood fit procedure

The final step is performing the statistical analysis. This step is again not examined using data due to the missing fake lepton background. The best NN model obtained in the binary classifier between different signal processes described in the previous chapter is used in a profile likelihood fit setup. The NN model is applied to all background events

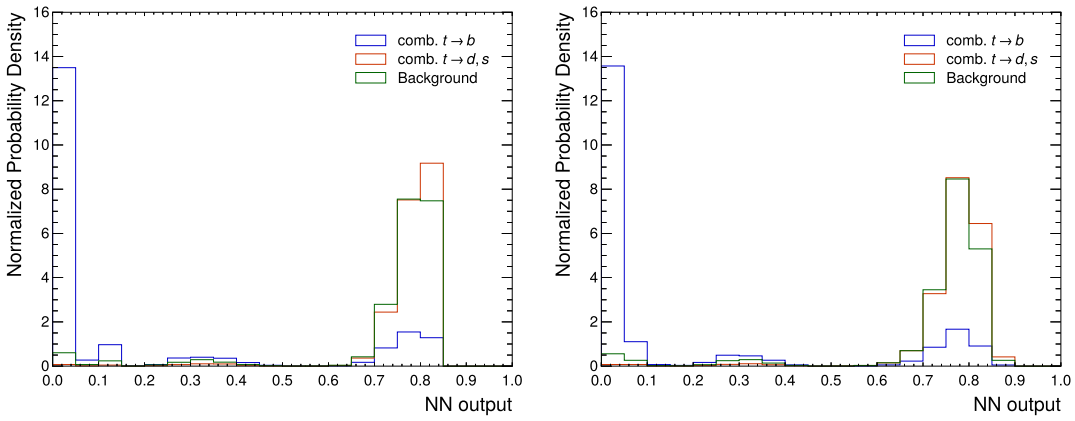

(a) (b)

Figure 9.23: Normalized NN output distributions for the best saved odd model applied to even dataset are shown in (a), while the same distributions for the best saved even model applied to the odd dataset are shown in (b). The blue and red line display the two signal classes, respectively, while the green line denotes the background events.

passing the cut from the NN trained for signal versus background classification. Hereby, all events with an odd number are evaluated using the even model and vice versa. All events are used together in the end to obtain one combined distribution.

The events are parametrized in the fit setup as explained in Chapter 8.2.2 of this thesis. Since $t\bar{t}$ is a negligible background, none of the $t\bar{t}$ CKM samples with all possible top-quark and top anti-quark decay modes are used for these studies. Consequently, three free floating parameters, the POIs, are introduced in the fit: Vtb, Vtd and Vts. Each parameter acts on the single-top-quark t-channel processes as described in detail in Chapter 8.2.2.

The final goal in these studies is to determine if a fit setup is sensitive to all three CKM matrix elements, in one fit instead of having to rely on 2D likelihood scans. Therefore, a binned profile likelihood fit using an Asimov dataset is performed. An Asimov dataset is a simulated dataset functioning as a pseudo-dataset where each bin of an utilized distribution contains exactly the predicted number of events from a given model, i.e. the expected yields from the MC predictions. Hence, the maximum likelihood estimate of all parameters matches the set value. The Asimov dataset is used to evaluate the expected statistical precision of a fit regarding expected uncertainties, limits or other quantities of interest.

The pre-fit and post-fit Asimov distributions are shown in Figure 9.24. The binning was optimized by hand in order to avoid empty bins, i.e. bin without predicted MC events. Further, the bin width was chosen such that it is approximately constant for the whole distribution and merge together bins with small but non-zero yields. It is visible, that the majority of the W+jets background is classified to the right side by the NN. This is expected as W+light flavor jets are expected to account for the largest contribution of this background. The other backgrounds only have small contributions, with Z+jets being

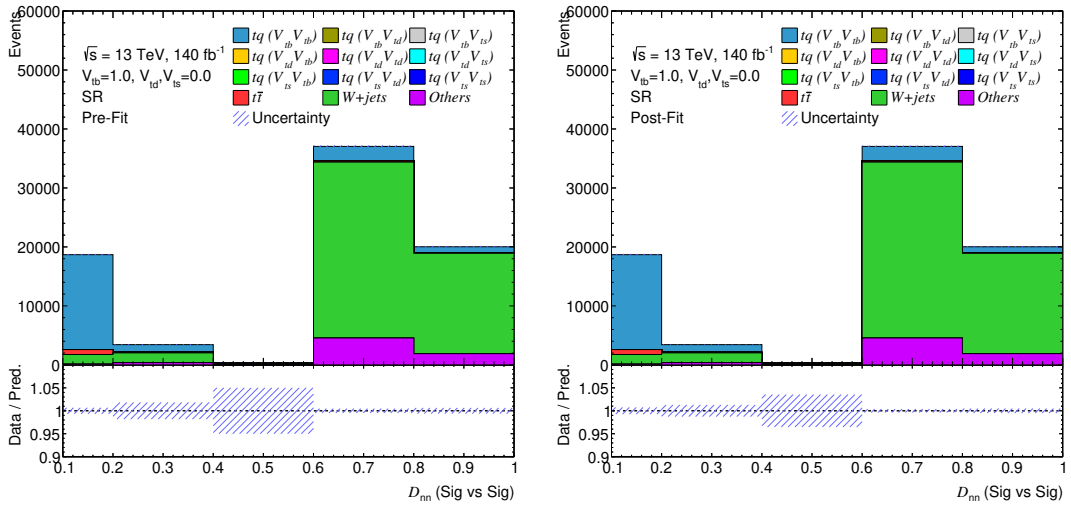

(a) (b)

Figure 9.24: Pre-fit (a) and Post-fit (b) distributions of the NN output distribution used in the Asimov fit to test the feasability of one fit determining V_{tb}, V_{td} and V_{ts}. The ratio plot usually shows the ratio between data and predictions. Since no data was used, only the MC statistical uncertainty is shown as a hashed band.

classified almost exclusively to the right side of the distribution and $t\bar{t}$ being classified to the left side of the distribution. The overall uncertainties are shown in the ratio plots in Figure 9.24. Since no systematic uncertainties are utilized, only the MC statistical uncertainty is illustrated. As expected, in the post-fit plot the uncertainties are reduced due to correlation between the POIs. The values of the POIs obtained from the Asimov profile likelihood fit are

$$\text{Vtb} = 1.00^{+0.01}_{-0.03}, \tag{9.14}$$

$$\text{Vtd} = -0.01^{+0.13}_{-0.11}, \tag{9.15}$$

$$\text{Vts} = 0.00^{+0.13}_{-0.13}. \tag{9.16}$$

The results differ from the expectations, that in an ideal case, the profile likleihood fit to the Asimov dataset should return the exact pre-fit parameter values (one for Vtb, and zero for Vtd and Vts) with symmetric uncertainties. However, the fitted value for Vtd deviates from that expectation, as well as the uncertainites of Vtd and Vtb. In order to understand the asymmetric uncertainties on Vtb and Vtd in Equation (9.14) and (9.15), respectively, as well as the non-zero mean value of Vtd, further measures are examined. The correlation matrix is depicted in Figure 9.25, together with one dimensional likelihood scans for each POI. The covariance matrix values should be interpreted with caution, as the 1D scans of the three parameters reveal that Vtb exhibits a highly asymmetric distribution, while Vts and Vtd appear to have a nearly flat distributions around zero, transitioning to a quadratic shape at larger values. This non-Gaussian behavior indicates that the covariance

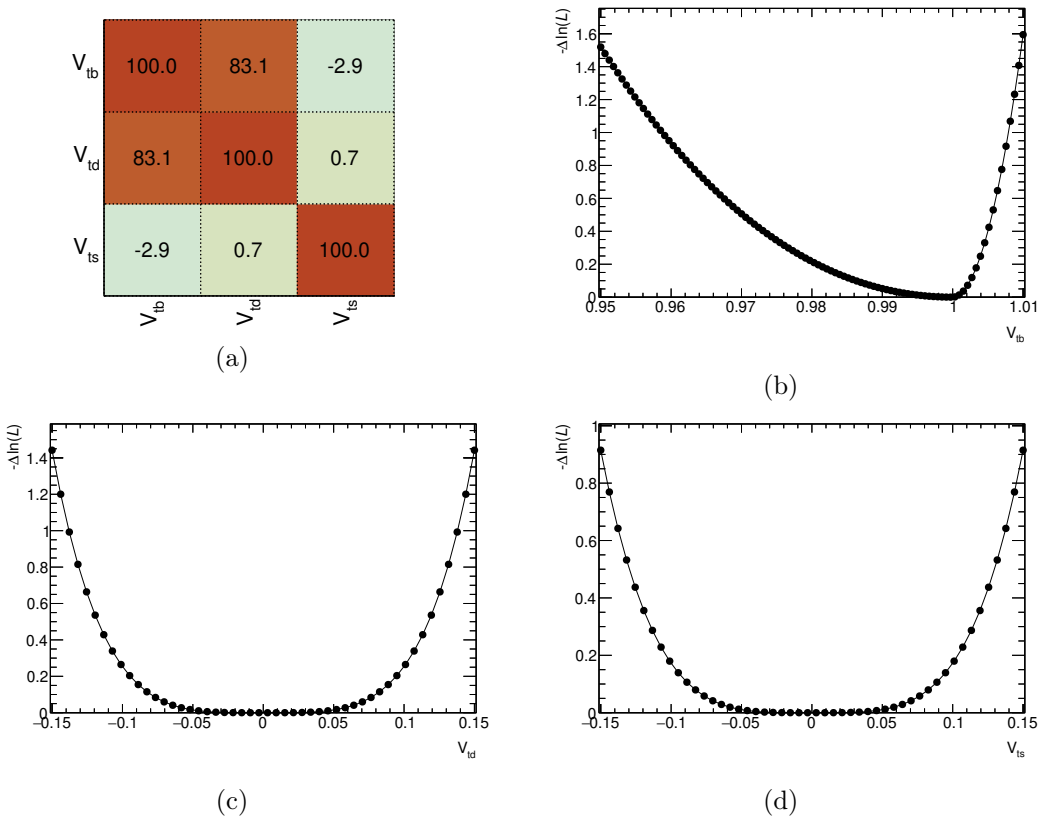

Figure 9.25: In (a) the correlation matrix between the three different free floating parameters in the fit is shown. In (b)-(d), the 1D likelihood scans for Vtb, Vtd and Vts is shown, respectively.

matrix derived under the assumption of a quadratic log-likelihood approximation does not correctly describe the parameter uncertainties, as the correlations between parameters deviate from a linear regime. Hence, the standard Hessian approximation, which assumes a parabolic likelihood around the best-fit point, may not be valid. Consequently, the correlation structure observed may not be a reliable indicator of the true relationships between the parameters, as it could be influenced by the non-linear and asymmetric nature of the distributions. Given these complications, it is worth considering whether Wilks' theorem remains valid in this case. The assumptions of the validity of Wilks' theorem are important to correctly assess the statistical uncertainties of the parameters in this study.

In conclusion, a dedicated CKM analysis using single-top-quark t-channel samples requires more information regarding reconstructed objects, e.g. track properties, a better rejection of the W+jets background and a better separation of this background and the signal processes. The distinction between different signal processes also needs more information, such as track properties of jets. Without a dedicated s-tagger, the distinction between jets of d-quarks and s-quarks will remain impossible.

10 Conclusion

The SM is one of the most extensively tested theories in physics, even though it is not considered a complete theory as it does not include phenomena such as dark matte, neutrino masses, or the gravitational interaction. In the search for a more fundamental theory beyond the SM, proton-proton collision experiments at the LHC are performed in order to probe the SM predictions and search for potential deviations that could hint at BSM physics. Furthermore, the SM incorporates various parameters, for that no theoretical predictions exist, requiring precise experimental measurements. The three angles and one phase of the CKM matrix are such free parameters and play a crucial role in understanding quark mixing and CP violation in the SM. Therefore, measuring the elements of the CKM matrix is important to probe the SM. As the heaviest known elementary particle, the top-quark plays a crucial role in the SM. Consequently, studying the top-quark is a key aspect of the physics program at the ATLAS experiment, both for testing SM predictions and exploring possible signs of new physics, making precise measurements of its properties essential.

In this thesis, two measurements of the top-quark involved CKM matrix elements were presented. In a first measurement, an interpretation was performed of the single-top-quark t-channel cross section measurement using the full Run 2 dataset recorded with the ATLAS detector corresponding to an integrated luminosity of $140\,\text{fb}^{-1}$. All different top-quark and top-antiquark t-channel production modes, $b \to t$, $b \to t$ and $b \to t$, and all different top-quark and top-antiquark decay modes, $t \to b$, $t \to d$ and $t \to s$, were considered in the interpretation. Additionally, due its large background contamination in the cross section measurement, $t\bar{t}$ events with all possible top-quark and top-antiquark decay modes were considered for the semileptonic as well as for the dileptonic channel. For this purpose, dedicated simulations of these processes were produced. A parametrization of all included single-top-(anti)quark t-channel events was developed and subsequently used in a profile likelihood fit setup. For this purpose, the NNs developed in each SR of the analysis were applied to the t-channel and $t\bar{t}$ CKM events, and the output distributions were used in the fit. Limits on all three CKM matrix elements, $|V_{tx}|$ with $x = d, s, b$, were obtained in three different scenarios. Each scenario includes one top-quark involved CKM matrix element being set to a fixed value, which corresponds to the current used value in the nominal MC simulations used for top-quark processes. Consequently, a 2D profile likelihood scan was performed for each scenario. The three scenarios and the resulting limits at 95% CL are

1) $V_{td} = 0$; $f_{LV} \cdot |V_{tb}| < 1.038$, $f_{LV} \cdot |V_{ts}| < 0.306$,

2) $V_{ts} = 0$; $f_{LV} \cdot |V_{tb}| < 1.048$, $f_{LV} \cdot |V_{td}| < 0.133$,

3) $V_{tb} = 1$; $f_{LV} \cdot |V_{td}| < 0.126$, $f_{LV} \cdot |V_{ts}| < 0.273$,

Hereby, f_{LV} corresponds to the left-handed form factor, which is one in the SM. The interpretation is more sensitive to $|V_{td}|$, as due to the event selection, differences in the event kinematics exploited by the used NN were mostly from differences in the initial state, i.e. the PDFs. This interpretation was published in Ref. [1].

A major challenge in this interpretation arises from the event selection used in the cross section measurement, as it requires exactly one b-tagged jet expected to originate from the top-quark decay. Thus, events where the top-quark decays into light-quarks (d or s) were selected with very low efficiency. To improve the obtained results, a proof-of-concept analysis was conducted to target all possible top-quark production and decay modes. As a first step, an event selection was developed which relaxed the b-tagging requirement while simultaneously reducing the contribution from $t\bar{t}$ production. The latter aspect also allows the focus to be placed solely on the single-top-quark t-channel processes as the signal processes in these studies, since the $t\bar{t}$ contribution becomes negligible. However, after the selection, W+jets emerges as the dominant background, due to its significantly larger production cross section compared to top-quark processes. To define a signal region that enhances the sensitivity to the targeted signal processes, a feed-forward NN was employed to distinguish between W+jets and the signal events. The NN output distribution shows a clear separation between signal and background events, and events were further selected if their NN output score exceeds a value of 0.8. This selection criterion ensures a sufficiently large number of MC simulated events for further analysis, while also defining a signal region with improved purity. Nevertheless, due to the large cross section, W+jets events still contribute dominantly in the selected events compared to the SM prediction of the signal processes. In a next step, additional NNs were developed and tested to further enhance the separation between the different signal processes and thus, different production and decay modes. A binary classifier was trained to distinguish between events where the top-quark decays into light-quark and those where it decays into a b-quark. A multi-class approach did not yield in an improvement. Finally, a profile likelihood fit was performed on an Asimov dataset to demonstrate the feasibility of the analysis. The fit employs the same parametrization for the signal processes as used in the interpretation and includes three free parameters, one for each relevant CKM matrix element. For simplicity, systematic uncertainties were not included at this stage. The observed asymmetry in the uncertainties arises from the non-quadratic behavior of the fit parameters, as seen in one-dimensional scans of the individual parameters. While these studies indicate the feasibility of using single-top-quark t-channel events to measure and constrain the top-quark involved CKM matrix elements, they emphasize, more notably, the significant challenges associated with the different steps of the analysis. Moreover, a direct comparison e.g. with the results from the interpretation is inherently limited, as no systematic uncertainties were considered in these studies.

To further enhance the sensitivity of such an analysis, dedicated control regions for the W+jets background, could be defined based on the flavor composition of the additional jets. Additionally, incorporating track-based information could help in developing NNs that not only improve the discrimination between signal and background events but especially

enhance the separation between the different signal processes. Exploring alternative NN types, such as graph neural networks or transformers, may further increase the sensitivity to the various top-quark production and decay modes. An interesting observation in this study was the non-quadratic behavior of the fit parameters in one-dimensional likelihood scans. This could be influenced by the choice of discriminating variable used in the fit, i.e. the NN output score. Investigating alternative NNs and their output scores or employing a multi-dimensional fit approach might help stabilize the parameter behavior.
In this context, employing an s-tagging algorithm, analogous to the existing b-tagging algorithm in ATLAS, would greatly improve the selection of events with $t \to s$ decays, thereby increasing the sensitivity to V_{ts}. Under the assumption of unitarity, an improved measurement of V_{ts} would simultaneously refine the constraints on V_{td} and V_{tb} and simultaneously therefore increase the sensitivity to V_{td} and V_{tb}, respectively. In ATLAS, an approach to develop s-tagging was found to be limited by systematic uncertainties [205]. The obtained constraints were weaker for V_{td} but showed slight improvements for V_{ts}, demonstrating the potential of an s-tagging algorithm in enhancing the sensitivity to V_{ts}. A recent publication [206], introduced a new transformer-based deep learning approach for s-jet tagging, which was found to improve the sensitivity to V_{ts}, particularly in the high-luminosity (HL)-LHC era.

Flavor tagging is a crucial part in top-quark physics, enabling the identification of jets originating from heavy-flavor quarks. Accurate flavor tagging algorithms were essential not only for top-quark analyses but also for many other precision measurements in ATLAS, e.g. including those involving Higgs bosons.
In this thesis, an alternative calibration of the flavor tagging algorithm used in Run 2 in ATLAS was presented.

The calibration was performed for both a direct cut on the tagging output discriminant (SingleWP) and for pseudo-continuous b-tagging (PCBT). For this purpose, W+c-jet events were used as the signal process, where the c-jet was identified by the presence of a soft muon inside the jet. Hence, semileptonically decaying c-Hadron events were used to obtain data-to-MC SFs that correct for potential mismodelling in the MC simulations.
Events were selected with a pair of muons in the final state. Since the signal process is expected to predominantly contain opposite-sign muon pairs, the signal region was defined at the histogram level, by subtracting events with a same-sign muon pair from those with an opposite-sign muon pair. This selection yielded a signal purity of 89%. The selected events were categorized according to their tagging score and the p_{T} of the jet containing the soft muon for both calibration strategies.
A likelihood fit setup was employed to determine the SFs ensuring a proper treatment of the uncertainties as well as preventing unphysical negative SFs. The resulting SFs show reduced uncertainties in the low p_{T} region (up to 40 GeV) compared to the SFs obtained with the nominal calibration method based on $t\bar{t}$ events. Most of the obtained SFs were in agreement with those from the nominal calibration. However, for soft-muon-tagged jets in the p_{T} range of 40 to 65 GeV, a trend was observed that the SFs in the presented calibration were systematically larger than unity. The calibration is limited by systematic uncertainties, particularly by uncertaintes related to JES and JER.

To generalize the resulting SFs for all c-jets, an extrapolation was performed using $t\bar{t}$ events, following the event selection strategy of the nominal calibration. Jets in these events were first classified based on their p_{T} and then categorized according to their tagging score and whether they contain a soft muon. The goal was to derive SFs that quantify the differences between jets matched to a soft muon and those that were not. A profile likelihood fit was used to determine the extrapolation SFs, incorporating several systematic uncertainties, including lepton-related uncertainties and uncertainties regarding known mismodeling effects for different jet flavors. The obtained extrapolation SFs show a similar trend to the SFs obtained in the calibration: The nominal values were closer to unity for jets tagged at looser WPs and those with lower p_{T}. The largest deviations were observed for jets tagged at the 60% and 70% WP.

In order to further investigate the observed differences, variables that were sensitive to the jet flavor, such as the secondary vertex mass, could provide valuable insights. The calibration itself would benefit from using events with $W \to e\nu_e$ as well, as these would increase the available number of MC simulated events, thereby reducing the MC statistical uncertainties. This effect would be particularly relevant in phase space regions with lower event counts, such as for tighter WPs or higher p_{T} jets. This approach would be especially advantageous for the calibration of the flavor tagging algorithm in Run 3, as the rejection rate of non-b-jets is even higher, making the mis-tag calibration analyses even more challenging. Furthermore, including the electron channel would allow for a direct comparison with the results obtained using only the muon channel, providing further validation of the SFs.

Overall, the precise measurement of free parameters of the SM remains a high priority in high-energy physics. Improving the performance and calibration of key analysis tools, such as flavor tagging algorithms, is essential - especially in Run3 and forward, where increasing data events provide new opportunities for precision measurements. As more data is recorded, a major challenge is the reduction of systematic uncertainties, which ultimately limits the sensitivity of measurements, even already to date. Optimizing the (mis-tag) calibration strategies for the utilized flavor tagging algorithms, such as the alternative approach presented in this thesis, contribute to this goal by improving the accuracy of the physics analyses.
Additionally, achieving higher precision in measurements of top-quark properties enables stringent tests of the SM. With future improvements in detector performance, analysis techniques, e.g. machine learning-based approaches as tested in this thesis, these measurements will continue to play a crucial role in advancing the understanding of the elementary particles and their interactions.

Bibliography

[1] ATLAS Collaboration, *Measurement of t-channel production of single top quarks and antiquarks in pp collisions at* 13 *TeV using the full ATLAS Run 2 data sample*, JHEP **05** (2024) 305, arXiv: 2403.02126 [hep-ex], Erratum: JHEP **06** (2025) 024.

[2] E. Noether, *Invariante Variationsprobleme*, ger,
Nachrichten von der Gesellschaft der Wissenschaften zu Göttingen,
Mathematisch-Physikalische Klasse **1918** (1918) 235,
URL: http://eudml.org/doc/59024.

[3] G. 't Hooft and M. Veltman, *Regularization and renormalization of gauge fields*, Nucl. Phys. A **44** (1972) 189, ISSN: 0550-3213.

[4] S. Weinberg, *New Approach to the Renormalization Group*,
Phys. Rev. D **8** (10 1973) 3497.

[5] S. Weinberg, *Non-Abelian Gauge Theories of the Strong Interactions*,
Phys. Rev. Lett. **31** (7 1973) 494.

[6] H. D. Politzer, *Reliable Perturbative Results for Strong Interactions?*,
Phys. Rev. Lett. **30** (26 1973) 1346.

[7] D. J. Gross and F. Wilczek, *Ultraviolet Behavior of Non-Abelian Gauge Theories*,
Phys. Rev. Lett. **30** (26 1973) 1343.

[8] H. Fritzsch, M. Gell-Mann, and H. Leutwyler,
Advantages of the color octet gluon picture, Phys. Lett. B **47** (1973) 365,
ISSN: 0370-2693.

[9] S. L. Glashow, *Partial-symmetries of weak interactions*, Nucl. Phys. **22** (1961) 579,
ISSN: 0029-5582.

[10] S. Weinberg, *A Model of Leptons*, Phys. Rev. Lett. **19** (21 1967) 1264.

[11] A. Salam, *Weak and Electromagnetic Interactions*,
Conf. Proc. C **680519** (1968) 367.

[12] S. L. Glashow, J. Iliopoulos, and L. Maiani,
Weak Interactions with Lepton-Hadron Symmetry, Phys. Rev. D **2** (7 1970) 1285.

[13] F. Englert and R. Brout, *Broken Symmetry and the Mass of Gauge Vector Mesons*,
Phys. Rev. Lett. **13** (9 1964) 321.

[14] P. W. Higgs, *Spontaneous Symmetry Breakdown without Massless Bosons*,
Phys. Rev. **145** (4 1966) 1156.

[15] G. S. Guralnik, C. R. Hagen, and T. W. B. Kibble,
Global Conservation Laws and Massless Particles,
Phys. Rev. Lett. **13** (20 1964) 585.

[16] S. Elitzur, *Impossibility of spontaneously breaking local symmetries*,
Phys. Rev. D **12** (12 1975) 3978.

[17] ATLAS Collaboration, *Observation of a new particle in the search for the Standard Model Higgs boson with the ATLAS detector at the LHC*,
Phys. Lett. B **716** (2012) 1, arXiv: `1207.7214 [hep-ex]`.

[18] CMS Collaboration, *Observation of a new boson with mass near* 125 *GeV in pp collisions at* $\sqrt{s} = 7$ *and* 8 *TeV*, JHEP **06** (2013) 081, arXiv: `1303.4571 [hep-ex]`.

[19] S. Navas et al., *Review of particle physics*, Phys. Rev. D **110** (2024) 030001.

[20] C. Burgard and D. Galbraith, *Model-Physics*,
`https://texample.net/model-physics/`, [Accessed: 05-03-2025], 2021.

[21] N. Cabibbo, *Unitary Symmetry and Leptonic Decays*,
Phys. Rev. Lett. **10** (12 1963) 531.

[22] M. Kobayashi and T. Maskawa,
CP-Violation in the Renormalizable Theory of Weak Interaction,
Prog. Theor. Phys. **49** (1973) 652, ISSN: 0033-068X.

[23] L.-L. Chau and W.-Y. Keung,
Comments on the Parametrization of the Kobayashi-Maskawa Matrix,
Phys. Rev. Lett. **53** (19 1984) 1802.

[24] L. Wolfenstein, *Parametrization of the Kobayashi-Maskawa Matrix*,
Phys. Rev. Lett. **51** (21 1983) 1945.

[25] A. J. Buras, M. E. Lautenbacher, and G. Ostermaier, *Waiting for the top quark mass,* $K^+ \to \pi^+ \nu\nu^-$, B_s^0-B_s^0 *mixing, and CP asymmetries in B decays*,
Phys. Rev. D **50** (5 1994) 3433.

[26] J. Charles et al., *CP violation and the CKM matrix: assessing the impact of the asymmetric B factories.*, Eur. Phys. J. C **41** (2005) 1, ISSN: 1434-6052.

[27] C. Jarlskog, *Commutator of the Quark Mass Matrices in the Standard Electroweak Model and a Measure of Maximal* CP *Nonconservation*,
Phys. Rev. Lett. **55** (10 1985) 1039.

[28] S. W. Herb et al., *Observation of a Dimuon Resonance at 9.5 GeV in 400-GeV Proton-Nucleus Collisions*, Phys. Rev. Lett. **39** (1977) 252.

[29] DØ Collaboration, *Observation of the Top Quark*,
Phys. Rev. Lett. **74** (14 1995) 2632.

[30] CDF Collaboration, *Observation of Top Quark Production in* $\overline{p}p$ *Collisions with the Collider Detector at Fermilab*, Phys. Rev. Lett. **74** (14 1995) 2626.

[31] M. Jeżabek and J. Kühn, *QCD corrections to semileptonic decays of heavy quarks*,
Nucl. Phys. A **314** (1989) 1, ISSN: 0550-3213.

[32] ATLAS Collaboration, *Inclusive and differential cross-sections for dilepton $t\bar{t}$ production measured in $\sqrt{s} = 13$ TeV pp collisions with the ATLAS detector*, JHEP **07** (2023) 141, arXiv: 2303.15340 [hep-ex].

[33] CMS Collaboration, *Measurement of differential $t\bar{t}$ production cross sections in the full kinematic range using lepton+jets events from proton–proton collisions at $\sqrt{s} = 13$ TeV*, Phys. Rev. D **104** (2021) 092013, arXiv: 2108.02803 [hep-ex].

[34] M. Czakon, P. Fiedler, and A. Mitov, *Total Top-Quark Pair-Production Cross Section at Hadron Colliders Through $\mathcal{O}(\alpha_S^4)$*, Phys. Rev. Lett. **110** (2013) 252004, arXiv: 1303.6254 [hep-ph].

[35] ATLAS Collaboration, *Measurement of single top-quark production in the s-channel in proton–proton collisions at $\sqrt{s} = 13$ TeV with the ATLAS detector*, JHEP **06** (2023) 191, arXiv: 2209.08990 [hep-ex].

[36] CMS Collaboration, *Measurement of inclusive and differential cross sections for single top quark production in association with a W boson in proton–proton collisions at $\sqrt{s} = 13$ TeV*, JHEP **07** (2023) 046, arXiv: 2208.00924 [hep-ex].

[37] J. Wess and B. Zumino, *A lagrangian model invariant under supergauge transformations*, Phys. Lett. B **49** (1974) 52, ISSN: 0370-2693.

[38] S. P. Martin, *A Supersymmetry Primer*, Perspectives on Supersymmetry (1998) 1, ISSN: 1793-1339.

[39] C. T. Hill and E. H. Simmons, *Strong dynamics and electroweak symmetry breaking*, Phys. Rept. **381** (2003) 235, ISSN: 0370-1573.

[40] A. Azatov and J. Galloway, *Light custodians and Higgs physics in composite models*, Phys. Rev. D **85** (5 2012) 055013.

[41] J. F. Gunion, H. E. Haber, G. L. Kane, and S. Dawson, *The Higgs Hunter's Guide*, vol. 80, Frontiers in Physics, Westview Press, 1990.

[42] M. Carena, H. E. Haber, I. Low, N. R. Shah, and C. E. M. Wagner, *Complementarity between nonstandard Higgs boson searches and precision Higgs boson measurements in the MSSM*, Phys. Rev. D **91** (3 2015) 035003.

[43] M. Carena, H. E. Haber, I. Low, N. R. Shah, and C. E. M. Wagner, *Alignment limit of the NMSSM Higgs sector*, Phys. Rev. D **93** (3 2016) 035013.

[44] J. F. Gunion and H. E. Haber, *CP-conserving two-Higgs-doublet model: The approach to the decoupling limit*, Phys. Rev. D **67** (7 2003) 075019.

[45] O. S. Brüning et al., *LHC Design Report*, CERN Yellow Reports: Monographs, Geneva: CERN, 2004, URL: https://cds.cern.ch/record/782076.

[46] O. S. Brüning et al., *LHC Design Report*, CERN Yellow Reports: Monographs, Geneva: CERN, 2004, URL: https://cds.cern.ch/record/815187.

[47] M. Benedikt, P. Collier, V. Mertens, J. Poole, and K. Schindl, *LHC Design Report*, CERN Yellow Reports: Monographs, Geneva: CERN, 2004, URL: https://cds.cern.ch/record/823808.

[48] E. Mobs, *The CERN accelerator complex in 2019*, CERN-GRAPHICS-2019-002-1, 2019, URL: https://cds.cern.ch/record/2684277.

[49] R. Bruce, N. Fuster-Martínez, A. Mereghetti, D. Mirarchi, and S. Redaelli, *Review of LHC Run 2 Machine Configurations*, 2019 187, URL: https://cds.cern.ch/record/2750415.

[50] ATLAS Collaboration, *The ATLAS Experiment at the CERN Large Hadron Collider*, JINST **3** (2008) S08003.

[51] CMS Collaboration, *The CMS Experiment at the CERN LHC*, JINST **3** (2008) S08004.

[52] The LHCb Collaboration, *The LHCb Detector at the LHC*, JINST **3** (2008) S08005.

[53] The ALICE Collaboration, *The ALICE experiment at the CERN LHC*, JINST **3** (2008) S08002.

[54] ATLAS Collaboration, *Luminosity determination in pp collisions at $\sqrt{s} = 8$ TeV using the ATLAS detector at the LHC*, Eur. Phys. J. C **76** (2016) 653, arXiv: 1608.03953 [hep-ex].

[55] ATLAS Collaboration, *Peak luminosity per fill*, accessed: 30.09.2024, 2018, URL: https://atlas.web.cern.ch/Atlas/GROUPS/DATAPREPARATION/PublicPlots/2018/DataSummary/figs/peakLumiByFill.png.

[56] ATLAS Collaboration, *Luminosity determination in pp collisions at $\sqrt{s} = 13$ TeV using the ATLAS detector at the LHC*, Eur. Phys. J. C **83** (2023) 982, arXiv: 2212.09379 [hep-ex].

[57] S. Fartoukh et al., *LHC Configuration and Operational Scenario for Run 3*, CERN-ACC-2021-0007, 2021, URL: https://cds.cern.ch/record/2790409.

[58] ATLAS Collaboration, *ATLAS Inner Detector: Technical Design Report, Volume 1*, ATLAS-TDR-4; CERN-LHCC-97-016, 1997, URL: https://cds.cern.ch/record/331063.

[59] ATLAS Collaboration, *ATLAS Inner Detector: Technical Design Report, Volume 2*, ATLAS-TDR-5, CERN-LHCC-97-017, 1997, URL: https://cds.cern.ch/record/331064.

[60] ATLAS Collaboration, *ATLAS Central Solenoid: Magnet Project Technical Design Report, Volume 4*, ATLAS-TDR-9; CERN-LHCC-97-021, CERN, 1997, URL: https://cds.cern.ch/record/331067.

[61] ATLAS Collaboration, *ATLAS Pixel Detector: Technical Design Report*, ATLAS-TDR-11; CERN-LHCC-98-013, 1998, URL: https://cds.cern.ch/record/381263.

[62] ATLAS Collaboration,
ATLAS Inner Tracker Pixel Detector: Technical Design Report,
ATLAS-TDR-030; CERN-LHCC-2017-021, 2017,
URL: https://cds.cern.ch/record/2285585.

[63] ATLAS Collaboration,
ATLAS Inner Tracker Strip Detector: Technical Design Report,
ATLAS-TDR-025; CERN-LHCC-2017-005, 2017,
URL: https://cds.cern.ch/record/2257755.

[64] ATLAS Collaboration, *ATLAS Insertable B-Layer: Technical Design Report*,
ATLAS-TDR-19; CERN-LHCC-2010-013, 2010,
URL: https://cds.cern.ch/record/1291633,
Addendum: ATLAS-TDR-19-ADD-1; CERN-LHCC-2012-009, 2012, URL:
https://cds.cern.ch/record/1451888.

[65] B. Abbott et al., *Production and integration of the ATLAS Insertable B-Layer*,
JINST **13** (2018) T05008, arXiv: 1803.00844 [physics.ins-det].

[66] ATLAS Collaboration, *Performance of the ATLAS Transition Radiation Tracker in Run 1 of the LHC: tracker properties*, JINST **12** (2017) P05002,
arXiv: 1702.06473 [hep-ex].

[67] ATLAS Collaboration, *ATLAS Calorimeter Performance: Technical Design Report*,
ATLAS-TDR-1; CERN-LHCC-96-040, 1996,
URL: https://cds.cern.ch/record/331059.

[68] ATLAS Collaboration, *ATLAS Liquid Argon Calorimeter: Technical Design Report*,
ATLAS-TDR-2; CERN-LHCC-96-041, 1996,
URL: https://cds.cern.ch/record/331061.

[69] ATLAS Collaboration, *ATLAS Tile Calorimeter: Technical Design Report*,
ATLAS-TDR-3; CERN-LHCC-96-042, 1996,
URL: https://cds.cern.ch/record/331062.

[70] ATLAS Collaboration,
ATLAS Liquid Argon Calorimeter Phase-I Upgrade: Technical Design Report,
ATLAS-TDR-022; CERN-LHCC-2013-017, 2013,
URL: https://cds.cern.ch/record/1602230.

[71] ATLAS Collaboration,
ATLAS LAr Calorimeter Phase-II Upgrade: Technical Design Report,
ATLAS-TDR-027; CERN-LHCC-2017-018, 2017,
URL: https://cds.cern.ch/record/2285582.

[72] ATLAS Collaboration,
ATLAS Tile Calorimeter Phase-II Upgrade: Technical Design Report,
ATLAS-TDR-028; CERN-LHCC-2017-019, 2017,
URL: https://cds.cern.ch/record/2285583.

[73] ATLAS Collaboration, *ATLAS Muon Spectrometer: Technical Design Report*,
ATLAS-TDR-10; CERN-LHCC-97-022, CERN, 1997,
URL: https://cds.cern.ch/record/331068.

[74] ATLAS Collaboration,
ATLAS Muon Spectrometer Phase-II Upgrade: Technical Design Report,
ATLAS-TDR-026; CERN-LHCC-2017-017, 2017,
URL: https://cds.cern.ch/record/2285580.

[75] ATLAS Collaboration,
ATLAS Barrel Toroid: Magnet Project Technical Design Report, Volume 2,
ATLAS-TDR-7; CERN-LHCC-97-019, 1997,
URL: https://cds.cern.ch/record/331065.

[76] ATLAS Collaboration,
ATLAS End-Cap Toroids: Magnet Project Technical Design Report, Volume 3,
ATLAS-TDR-8; CERN-LHCC-97-020, CERN, 1997,
URL: https://cds.cern.ch/record/331066.

[77] ATLAS Collaboration, *ATLAS New Small Wheel: Technical Design Report*,
ATLAS-TDR-020; CERN-LHCC-2013-006, 2013,
URL: https://cds.cern.ch/record/1552862.

[78] ATLAS Collaboration, *ATLAS Level-1 Trigger: Technical Design Report*,
ATLAS-TDR-12; CERN-LHCC-98-014, 1998,
URL: https://cds.cern.ch/record/381429.

[79] ATLAS Collaboration, *ATLAS High-Level Trigger, Data Acquisition and Controls: Technical Design Report*, ATLAS-TDR-16; CERN-LHCC-2003-022, 2003,
URL: https://cds.cern.ch/record/616089.

[80] ATLAS Collaboration,
ATLAS TDAQ System Phase-I Upgrade: Technical Design Report,
ATLAS-TDR-023; CERN-LHCC-2013-018, 2013,
URL: https://cds.cern.ch/record/1602235.

[81] ATLAS Collaboration, *ATLAS TDAQ Phase-II Upgrade: Technical Design Report*,
ATLAS-TDR-029; CERN-LHCC-2017-020, 2017,
URL: https://cds.cern.ch/record/2285584.

[82] ATLAS Collaboration, *Approved Plots DAQ*,
https://twiki.cern.ch/twiki/bin/view/AtlasPublic/ApprovedPlotsDAQ,
visited on: 09.10.2024.

[83] *The Grid: A system of tiers*, (2012),
URL: https://cds.cern.ch/record/1997396.

[84] ATLAS Collaboration, *Performance of the ATLAS track reconstruction algorithms in dense environments in LHC Run 2*, Eur. Phys. J. C **77** (2017) 673,
arXiv: 1704.07983 [hep-ex].

[85] ATLAS Collaboration, *Performance of the ATLAS Silicon Pattern Recognition Algorithm in Data and Simulation at* $\sqrt{s} = 7$ *TeV*, ATLAS-CONF-2010-072, 2010,
URL: https://cds.cern.ch/record/1281363.

[86] R. Frühwirth, *Application of Kalman filtering to track and vertex fitting*,
Nucl. Instrum. Meth. A **262** (1987) 444, ISSN: 0168-9002.

[87] ATLAS Collaboration,
A neural network clustering algorithm for the ATLAS silicon pixel detector,
JINST **9** (2014) P09009, arXiv: 1406.7690 [hep-ex].

[88] ATLAS Collaboration,
Training and validation of the ATLAS pixel clustering neural networks,
ATL-PHYS-PUB-2018-002, 2018, URL: https://cds.cern.ch/record/2309474.

[89] G. Piacquadio, K. Prokofiev, and A. Wildauer,
Primary vertex reconstruction in the ATLAS experiment at LHC, J. Phys. Conf. Ser. **119** (2008) 032033, ed. by R. Sobie, R. Tafirout, and J. Thomson.

[90] ATLAS Collaboration, *Reconstruction of primary vertices at the ATLAS experiment in Run 1 proton–proton collisions at the LHC*,
Eur. Phys. J. C **77** (2017) 332, arXiv: 1611.10235 [physics.ins-det].

[91] ATLAS Collaboration,
Vertex Reconstruction Performance of the ATLAS Detector at $\sqrt{s} = 13$ *TeV*,
ATL-PHYS-PUB-2015-026, 2015, URL: https://cds.cern.ch/record/2037717.

[92] W. Waltenberger, R. Frühwirth, and P. Vanlaer, *Adaptive vertex fitting*,
J. Phys. G **34** (2007) 343.

[93] ATLAS Collaboration,
Secondary vertex finding for jet flavour identification with the ATLAS detector,
ATL-PHYS-PUB-2017-011, 2017, URL: https://cds.cern.ch/record/2270366.

[94] ATLAS Collaboration, *Electron and photon performance measurements with the ATLAS detector using the 2015–2017 LHC proton–proton collision data*,
JINST **14** (2019) P12006, arXiv: 1908.00005 [hep-ex].

[95] ATLAS Collaboration,
Electron reconstruction and identification in the ATLAS experiment using the 2015 and 2016 LHC proton–proton collision data at $\sqrt{s} = 13$ *TeV*,
Eur. Phys. J. C **79** (2019) 639, arXiv: 1902.04655 [physics.ins-det].

[96] ATLAS Collaboration,
Performance of electron and photon triggers in ATLAS during LHC Run 2,
Eur. Phys. J. C **80** (2020) 47, arXiv: 1909.00761 [hep-ex].

[97] ATLAS Collaboration, *Topological cell clustering in the ATLAS calorimeters and its performance in LHC Run 1*, Eur. Phys. J. C **77** (2017) 490,
arXiv: 1603.02934 [hep-ex].

[98] W. Lampl et al., *Calorimeter Clustering Algorithms: Description and Performance*,
ATL-LARG-PUB-2008-002, 2008, URL: https://cds.cern.ch/record/1099735.

[99] ATLAS Collaboration, *Electron and photon energy calibration with the ATLAS detector using 2015–2016 LHC proton–proton collision data*,
JINST **14** (2019) P03017, arXiv: 1812.03848 [hep-ex].

[100] ATLAS Collaboration, *Muon reconstruction and identification efficiency in ATLAS using the full Run 2 pp collision data set at* $\sqrt{s} = 13$ *TeV*,
Eur. Phys. J. C **81** (2021) 578, arXiv: 2012.00578 [hep-ex].

[101] ATLAS Collaboration, *Muon reconstruction performance of the ATLAS detector in proton–proton collision data at $\sqrt{s} = 13$ TeV*, Eur. Phys. J. C **76** (2016) 292, arXiv: 1603.05598 [hep-ex].

[102] ATLAS Collaboration, *Performance of the ATLAS muon triggers in Run 2*, JINST **15** (2020) P09015, arXiv: 2004.13447 [physics.ins-det].

[103] ATLAS Collaboration, *Jet reconstruction and performance using particle flow with the ATLAS Detector*, Eur. Phys. J. C **77** (2017) 466, arXiv: 1703.10485 [hep-ex].

[104] M. Cacciari, G. P. Salam, and G. Soyez, *The anti-k_t jet clustering algorithm*, JHEP **04** (2008) 063, arXiv: 0802.1189 [hep-ph].

[105] M. Cacciari, G. P. Salam, and G. Soyez, *FastJet user manual*, Eur. Phys. J. C **72** (2012) 1896, arXiv: 1111.6097 [hep-ph].

[106] ATLAS Collaboration, *Reconstruction of hadronic decay products of tau leptons with the ATLAS experiment*, Eur. Phys. J. C **76** (2016) 295, arXiv: 1512.05955 [hep-ex].

[107] ATLAS Collaboration, *Jet energy scale and resolution measured in proton–proton collisions at $\sqrt{s} = 13$ TeV with the ATLAS detector*, Eur. Phys. J. C **81** (2021) 689, arXiv: 2007.02645 [hep-ex].

[108] ATLAS Collaboration, *Determination of the jet energy scale and resolution at ATLAS using Z/γ-jet events in data at $\sqrt{s} = 8$ TeV*, ATLAS-CONF-2015-057, 2015, URL: https://cds.cern.ch/record/2059846.

[109] ATLAS Collaboration, *TeV-scale jet energy calibration using multijet events including close-by jet effects at the ATLAS experiment*, ATLAS-CONF-2013-003, 2013, URL: https://cds.cern.ch/record/1504740.

[110] ATLAS Collaboration, *Tagging and suppression of pileup jets with the ATLAS detector*, ATLAS-CONF-2014-018, 2014, URL: https://cds.cern.ch/record/1700870.

[111] ATLAS Collaboration, *Forward jet vertex tagging using the particle flow algorithm*, ATL-PHYS-PUB-2019-026, 2019, URL: https://cds.cern.ch/record/2683100.

[112] I. Neutelings, *B tagging jets*, accessed: 20.10.2024, URL: https://tikz.net/jet_btag/.

[113] F. Renner, *A new Soft Muon Tagger for b-tagging evaluated with the DL1d tagger in ATLAS*, ATL-COM-SOFT-2022-013, 2022, URL: https://cds.cern.ch/record/2814375.

[114] ATLAS Collaboration, *ATLAS flavour-tagging algorithms for the LHC Run 2 pp collision dataset*, Eur. Phys. J. C **83** (2023) 681, arXiv: 2211.16345 [physics.data-an].

[115] ATLAS Collaboration, *Optimisation and performance studies of the ATLAS b-tagging algorithms for the 2017-18 LHC run*, ATL-PHYS-PUB-2017-013, 2017, URL: https://cds.cern.ch/record/2273281.

[116] ATLAS Collaboration, *Identification of Jets Containing b-Hadrons with Recurrent Neural Networks at the ATLAS Experiment*, ATL-PHYS-PUB-2017-003, 2017, URL: https://cds.cern.ch/record/2255226.

[117] ATLAS Collaboration, *Topological b-hadron decay reconstruction and identification of b-jets with the JetFitter package in the ATLAS experiment at the LHC*, ATL-PHYS-PUB-2018-025, 2018, URL: https://cds.cern.ch/record/2645405.

[118] ATLAS Collaboration, *ATLAS b-jet identification performance and efficiency measurement with $t\bar{t}$ events in pp collisions at $\sqrt{s} = 13$ TeV*, Eur. Phys. J. C **79** (2019) 970, arXiv: 1907.05120 [hep-ex].

[119] ATLAS Collaboration, *Measurement of the c-jet mistagging efficiency in $t\bar{t}$ events using pp collision data at $\sqrt{s} = 13$ TeV collected with the ATLAS detector*, Eur. Phys. J. C **82** (2022) 95, arXiv: 2109.10627 [hep-ex].

[120] ATLAS Collaboration, *Calibration of the light-flavour jet mistagging efficiency of the b-tagging algorithms with Z+jets events using 139 fb^{-1} of ATLAS proton–proton collision data at $\sqrt{s} = 13$ TeV*, Eur. Phys. J. C **83** (2023) 728, arXiv: 2301.06319 [hep-ex].

[121] ATLAS Collaboration, *The performance of missing transverse momentum reconstruction and its significance with the ATLAS detector using 140 fb^{-1} of $\sqrt{s} = 13$ TeV pp collisions*, (2024), arXiv: 2402.05858 [hep-ex].

[122] ATLAS Collaboration, *ATLAS data quality operations and performance for 2015–2018 data-taking*, JINST **15** (2020) P04003, arXiv: 1911.04632 [physics.ins-det].

[123] G. Avoni et al., *The new LUCID-2 detector for luminosity measurement and monitoring in ATLAS*, JINST **13** (2018) P07017.

[124] ATLAS Collaboration, *The ATLAS Simulation Infrastructure*, Eur. Phys. J. C **70** (2010) 823, arXiv: 1005.4568 [physics.ins-det].

[125] S. Agostinelli et al., GEANT4 – *a simulation toolkit*, Nucl. Instrum. Meth. A **506** (2003) 250.

[126] T. Sjöstrand, S. Mrenna, and P. Skands, *A brief introduction to PYTHIA 8.1*, Comput. Phys. Commun. **178** (2008) 852, arXiv: 0710.3820 [hep-ph].

[127] ATLAS Collaboration, *The Pythia 8 A3 tune description of ATLAS minimum bias and inelastic measurements incorporating the Donnachie–Landshoff diffractive model*, ATL-PHYS-PUB-2016-017, 2016, URL: https://cds.cern.ch/record/2206965.

[128] NNPDF Collaboration, R. D. Ball, et al., *Parton distributions with LHC data*, Nucl. Phys. B **867** (2013) 244, arXiv: 1207.1303 [hep-ph].

[129] ATLAS Collaboration, *Measurement of the Inelastic Proton–Proton Cross-Section at $\sqrt{s} = 13$ TeV with the ATLAS Detector at the LHC*, ATLAS-CONF-2015-038, 2015, URL: https://cds.cern.ch/record/2045064.

[130] T. Sjöstrand et al., *An introduction to PYTHIA 8.2*, Comput. Phys. Commun. **191** (2015) 159, arXiv: 1410.3012 [hep-ph].

[131] ATLAS Collaboration, *ATLAS Pythia 8 tunes to 7 TeV data*, ATL-PHYS-PUB-2014-021, 2014, URL: https://cds.cern.ch/record/1966419.

[132] D. J. Lange, *The EvtGen particle decay simulation package*, Nucl. Instrum. Meth. A **462** (2001) 152.

[133] S. Frixione, G. Ridolfi, and P. Nason, *A positive-weight next-to-leading-order Monte Carlo for heavy flavour hadroproduction*, JHEP **09** (2007) 126, arXiv: 0707.3088 [hep-ph].

[134] P. Nason, *A new method for combining NLO QCD with shower Monte Carlo algorithms*, JHEP **11** (2004) 040, arXiv: hep-ph/0409146.

[135] S. Frixione, P. Nason, and C. Oleari, *Matching NLO QCD computations with parton shower simulations: the POWHEG method*, JHEP **11** (2007) 070, arXiv: 0709.2092 [hep-ph].

[136] S. Alioli, P. Nason, C. Oleari, and E. Re, *A general framework for implementing NLO calculations in shower Monte Carlo programs: the POWHEG BOX*, JHEP **06** (2010) 043, arXiv: 1002.2581 [hep-ph].

[137] NNPDF Collaboration, R. D. Ball, et al., *Parton distributions for the LHC run II*, JHEP **04** (2015) 040, arXiv: 1410.8849 [hep-ph].

[138] ATLAS Collaboration, *Studies on top-quark Monte Carlo modelling for Top2016*, ATL-PHYS-PUB-2016-020, 2016, URL: https://cds.cern.ch/record/2216168.

[139] R. Frederix, E. Re, and P. Torrielli, *Single-top t-channel hadroproduction in the four-flavour scheme with POWHEG and aMC@NLO*, JHEP **09** (2012) 130, arXiv: 1207.5391 [hep-ph].

[140] M. Beneke, P. Falgari, S. Klein, and C. Schwinn, *Hadronic top-quark pair production with NNLL threshold resummation*, Nucl. Phys. B **855** (2012) 695, arXiv: 1109.1536 [hep-ph].

[141] M. Cacciari, M. Czakon, M. Mangano, A. Mitov, and P. Nason, *Top-pair production at hadron colliders with next-to-next-to-leading logarithmic soft-gluon resummation*, Phys. Lett. B **710** (2012) 612, arXiv: 1111.5869 [hep-ph].

[142] P. Bärnreuther, M. Czakon, and A. Mitov, *Percent-Level-Precision Physics at the Tevatron: Next-to-Next-to-Leading Order QCD Corrections to $q\bar{q} \to t\bar{t} + X$*, Phys. Rev. Lett. **109** (2012) 132001, arXiv: 1204.5201 [hep-ph].

[143] M. Czakon and A. Mitov, *NNLO corrections to top-pair production at hadron colliders: the all-fermionic scattering channels*, JHEP **12** (2012) 054, arXiv: 1207.0236 [hep-ph].

[144] M. Czakon and A. Mitov, *NNLO corrections to top pair production at hadron colliders: the quark-gluon reaction*, JHEP **01** (2013) 080, arXiv: 1210.6832 [hep-ph].

[145] M. Czakon and A. Mitov, *Top++: A program for the calculation of the top-pair cross-section at hadron colliders*, Comput. Phys. Commun. **185** (2014) 2930, arXiv: 1112.5675 [hep-ph].

[146] M. Bähr et al., *Herwig++ physics and manual*, Eur. Phys. J. C **58** (2008) 639, arXiv: 0803.0883 [hep-ph].

[147] J. Bellm et al., *Herwig 7.2 release note*, Eur. Phys. J. C **80** (2020), arXiv: 1912.06509 [hep-ph].

[148] S. Frixione, E. Laenen, P. Motylinski, and B. R. Webber, *Angular correlations of lepton pairs from vector boson and top quark decays in Monte Carlo simulations*, JHEP **04** (2007) 081, arXiv: hep-ph/0702198.

[149] P. Artoisenet, R. Frederix, O. Mattelaer, and R. Rietkerk, *Automatic spin-entangled decays of heavy resonances in Monte Carlo simulations*, JHEP **03** (2013) 015, arXiv: 1212.3460 [hep-ph].

[150] S. Alioli, P. Nason, C. Oleari, and E. Re, *NLO single-top production matched with shower in POWHEG: s- and t-channel contributions*, JHEP **09** (2009) 111, arXiv: 0907.4076 [hep-ph], Erratum: JHEP **02** (2010) 011.

[151] E. Re, *Single-top Wt-channel production matched with parton showers using the POWHEG method*, Eur. Phys. J. C **71** (2011) 1547, arXiv: 1009.2450 [hep-ph].

[152] S. Frixione, E. Laenen, P. Motylinski, C. White, and B. R. Webber, *Single-top hadroproduction in association with a W boson*, JHEP **07** (2008) 029, arXiv: 0805.3067 [hep-ph].

[153] N. Kidonakis, *Two-loop soft anomalous dimensions for single top quark associated production with a W^- or H^-*, Phys. Rev. D **82** (2010) 054018, arXiv: 1005.4451 [hep-ph].

[154] N. Kidonakis, *Top Quark Production*, Proceedings of the Helmholtz International Summer School on Physics of Heavy Quarks and Hadrons (HQ2013), JINR, Dubna, Russia (2013) 139, Presented at HQ2013, July 15–28, 2013, arXiv: 1311.0283 [hep-ph].

[155] M. Aliev et al., *HATHOR – HAdronic Top and Heavy quarks crOss section calculatoR*, Comput. Phys. Commun. **182** (2011) 1034, arXiv: 1007.1327 [hep-ph].

[156] P. Kant et al., *HatHor for single top-quark production: Updated predictions and uncertainty estimates for single top-quark production in hadronic collisions*, Comput. Phys. Commun. **191** (2015) 74, arXiv: 1406.4403 [hep-ph].

[157] L. Wolfenstein, *Parametrization of the Kobayashi-Maskawa Matrix*, Phys. Rev. Lett. **51** (21 1983) 1945.

[158] E. Bothmann et al., *Event generation with Sherpa 2.2*, SciPost Phys. **7** (2019) 034, arXiv: 1905.09127 [hep-ph].

[159] T. Gleisberg and S. Höche, *Comix, a new matrix element generator*, JHEP **12** (2008) 039, arXiv: 0808.3674 [hep-ph].

[160] F. Buccioni et al., *OpenLoops 2*, Eur. Phys. J. C **79** (2019) 866, arXiv: 1907.13071 [hep-ph].

[161] F. Cascioli, P. Maierhöfer, and S. Pozzorini, *Scattering Amplitudes with Open Loops*, Phys. Rev. Lett. **108** (2012) 111601, arXiv: 1111.5206 [hep-ph].

[162] A. Denner, S. Dittmaier, and L. Hofer, COLLIER*: A fortran-based complex one-loop library in extended regularizations*, Comput. Phys. Commun. **212** (2017) 220, arXiv: 1604.06792 [hep-ph].

[163] C. Anastasiou, L. Dixon, K. Melnikov, and F. Petriello, *High-precision QCD at hadron colliders: Electroweak gauge boson rapidity distributions at next-to-next-to leading order*, Phys. Rev. D **69** (2004) 094008, arXiv: hep-ph/0312266.

[164] S. Schumann and F. Krauss, *A parton shower algorithm based on Catani–Seymour dipole factorisation*, JHEP **03** (2008) 038, arXiv: 0709.1027 [hep-ph].

[165] S. Höche, F. Krauss, M. Schönherr, and F. Siegert, *A critical appraisal of NLO+PS matching methods*, JHEP **09** (2012) 049, arXiv: 1111.1220 [hep-ph].

[166] S. Höche, F. Krauss, M. Schönherr, and F. Siegert, *QCD matrix elements + parton showers. The NLO case*, JHEP **04** (2013) 027, arXiv: 1207.5030 [hep-ph].

[167] S. Catani, F. Krauss, B. R. Webber, and R. Kuhn, *QCD Matrix Elements + Parton Showers*, JHEP **11** (2001) 063, arXiv: hep-ph/0109231.

[168] S. Höche, F. Krauss, S. Schumann, and F. Siegert, *QCD matrix elements and truncated showers*, JHEP **05** (2009) 053, arXiv: 0903.1219 [hep-ph].

[169] ATLAS Collaboration, *Modelling and computational improvements to the simulation of single vector-boson plus jet processes for the ATLAS experiment*, JHEP **08** (2022) 089, arXiv: 2112.09588 [hep-ex].

[170] ATLAS Collaboration, *Simulation-based extrapolation of b-tagging calibrations towards high transverse momenta in the ATLAS experiment*, ATL-PHYS-PUB-2021-003, 2021, URL: https://cds.cern.ch/record/2753444.

[171] ATLAS Collaboration, *Electron and photon energy calibration with the ATLAS detector using LHC Run 2 data*, JINST **19** (2024) P02009, arXiv: 2309.05471 [hep-ex].

[172] ATLAS Collaboration, *Studies of the muon momentum calibration and performance of the ATLAS detector with pp collisions at* $\sqrt{s} = 13$ *TeV*, Eur. Phys. J. C **83** (2023) 686, arXiv: 2212.07338 [hep-ex].

[173] W. Buttinger, *Using Event Weights to account for differences in Instantaneous Luminosity and Trigger Prescale in Monte Carlo and Data*, ATL-COM-SOFT-2015-119, 2015, URL: https://cds.cern.ch/record/2014726.

[174] J. C. Collins, D. E. Soper, and G. Sterman, *Factorization of Hard Processes in QCD*, 2004, arXiv: hep-ph/0409313 [hep-ph].

[175] J. Butterworth et al., *PDF4LHC recommendations for LHC Run II*, J. Phys. G **43** (2016) 023001, arXiv: 1510.03865 [hep-ph].

[176] B. R. Webber, *A QCD Model for Jet Fragmentation Including Soft Gluon Interference*, Nucl. Phys. B **238** (1984) 492.

[177] T. Sjöstrand, *Jet fragmentation of multiparton configurations in a string framework*, Nucl. Phys. B **248** (1984) 469.

[178] B. Andersson, G. Gustafson, G. Ingelman, and T. Sjöstrand, *Parton fragmentation and string dynamics*, Phys. Rept. **97** (1983) 31.

[179] ATLAS Collaboration, *Search for flavour-changing neutral-current interactions of a top quark and a gluon in pp collisions at $\sqrt{s} = 13$ TeV with the ATLAS detector*, Eur. Phys. J. C **82** (2022) 334, arXiv: 2112.01302 [hep-ex].

[180] ATLAS Collaboration, *b-jet tagging calibration on c-jets containing D^{*+} mesons*, ATLAS-CONF-2012-039, 2012, URL: https://cds.cern.ch/record/1435193.

[181] ATLAS Collaboration, *Calibration of the performance of b-tagging for c and light-flavour jets in the 2012 ATLAS data*, ATLAS-CONF-2014-046, 2014, URL: https://cds.cern.ch/record/1741020.

[182] ATLAS Collaboration, *Calibration of the b-tagging efficiency for c jets with the ATLAS detector using events with a W boson produced in association with a single c quark*, ATLAS-CONF-2013-109, 2013, URL: https://cds.cern.ch/record/1640162.

[183] ATLAS Collaboration, *Calibration of the b-tagging efficiency on charm jets using a sample of $W + c$ events with $\sqrt{s} = 13$ TeV ATLAS data*, ATLAS-CONF-2018-055, 2018, URL: https://cds.cern.ch/record/2652195.

[184] F. James and M. Roos, *Minuit - a system for function minimization and analysis of the parameter errors and correlations*, Comput. Phys. Commun. **10** (1975) 343, ISSN: 0010-4655.

[185] K. Olive et al., *Review of particle physics*, Chin. Phys. C **38** (2014) 1.

[186] E. Lohrmann, *A Summary of Charm Hadron Production Fractions*, 2011, arXiv: 1112.3757 [hep-ex].

[187] J. Erdmann et al., *A likelihood-based reconstruction algorithm for top-quark pairs and the KLFitter framework*, Nucl. Instrum. Meth. A **748** (2014) 18, ISSN: 0168-9002.

[188] M. Feindt, *A Neural Bayesian Estimator for Conditional Probability Densities*, (2004), arXiv: physics/0402093 [physics.data-an].

[189] M. Feindt and U. Kerzel, *The NeuroBayes neural network package*, Nucl. Instrum. Meth. A **559** (2006) 190, Proceedings of the X International Workshop on Advanced Computing and Analysis Techniques in Physics Research, ISSN: 0168-9002.

[190] P. Sturm, *Studies for the Measurement of Single-Top-Quark-Events with the CMS-Experiment.*, Karlsruhe U., 2008, URL: https://cds.cern.ch/record/1311220.

[191] T. Chwalek, *Measurement of the W boson helicity in top-antitop quark events with the CDF II experiment*, 2006, URL: https://www.osti.gov/biblio/911839.

[192] K. Cranmer, G. Lewis, L. Moneta, A. Shibata, and W. Verkerke, *HistFactory: A tool for creating statistical models for use with RooFit and RooStats*, CERN-OPEN-2012-016, 2012, URL: https://cds.cern.ch/record/1456844.

[193] ATLAS Collaboration, *SystematicSmoothingTool*, https://gitlab.cern.ch/atlas/statistics/SystematicSmoothingTool/-/blob/master/doc/algorithm_description.md, accessed: 23.01.2025, 2025.

[194] J. A. Reidelsturz, *Measurement of t-channel single top-quark production in proton-proton collisions at a center-of-mass energy of 13 TeV using the full ATLAS Run 2 dataset*, Presented 22 05 2024, Wuppertal U., 2024, URL: https://cds.cern.ch/record/2901310.

[195] R. Brun and F. Rademakers, *ROOT – An object oriented data analysis framework*, Nucl. Instrum. Meth. A **389** (1997) 81, ISSN: 0168-9002.

[196] *Proceedings of the 1974 CERN School of Computing: Godøysund, Norway 11 - 24 Aug 1974. 3rd CERN School of Computing*, CERN, Geneva: CERN, 1974, URL: https://cds.cern.ch/record/186223.

[197] R. Barlow and C. Beeston, *Fitting using finite Monte Carlo samples*, Comput. Phys. Commun. **77** (1993) 219.

[198] G. L. Kane, G. A. Ladinsky, and C. .-P. Yuan, *Using the top quark for testing standard-model polarization and* CP *predictions*, Phys. Rev. D **45** (1 1992) 124.

[199] ATLAS Collaboration, *Measurement of t-channel single-top-quark production in pp collisions at $\sqrt{s} = 5.02$ TeV with the ATLAS detector*, Phys. Lett. B **854** (2024) 138726, arXiv: 2310.01518 [hep-ex].

[200] J. Alwall et al., *Comparative study of various algorithms for the merging of parton showers and matrix elements in hadronic collisions*, Eur. Phys. J. C **53** (2007) 473, ISSN: 1434-6052, arXiv: 0706.2569 [hep-ph].

[201] D. P. Kingma and J. Ba, *Adam: A Method for Stochastic Optimization*, 2017, arXiv: 1412.6980 [cs.LG].

[202] C. Cortes, M. Mohri, and A. Rostamizadeh,
L2 Regularization for Learning Kernels, 2012, arXiv: 1205.2653 [cs.LG].

[203] M. Abadi et al.,
TensorFlow: Large-Scale Machine Learning on Heterogeneous Distributed Systems,
2015, URL: https://www.tensorflow.org.

[204] F. Chollet et al., *Keras*, 2015, URL: https://keras.io.

[205] S. V. Zeißner, *Development and calibration of an s-tagging algorithm and its application to constrain the CKM matrix elements |Vts| and |Vtd| in top-quark decays using ATLAS Run-2 Data*,
Dissertation: Technische Universität Dortmund, 2021,
URL: https://doi.org/10.17877/DE290R-22226.

[206] J. Heo et al., *Improving the Direct Determination of $|V_{ts}|$ using Deep Learning*,
2025, arXiv: 2502.02918 [hep-ph].

Appendix

A Additional kinematic distributions for $W+c$ calibration

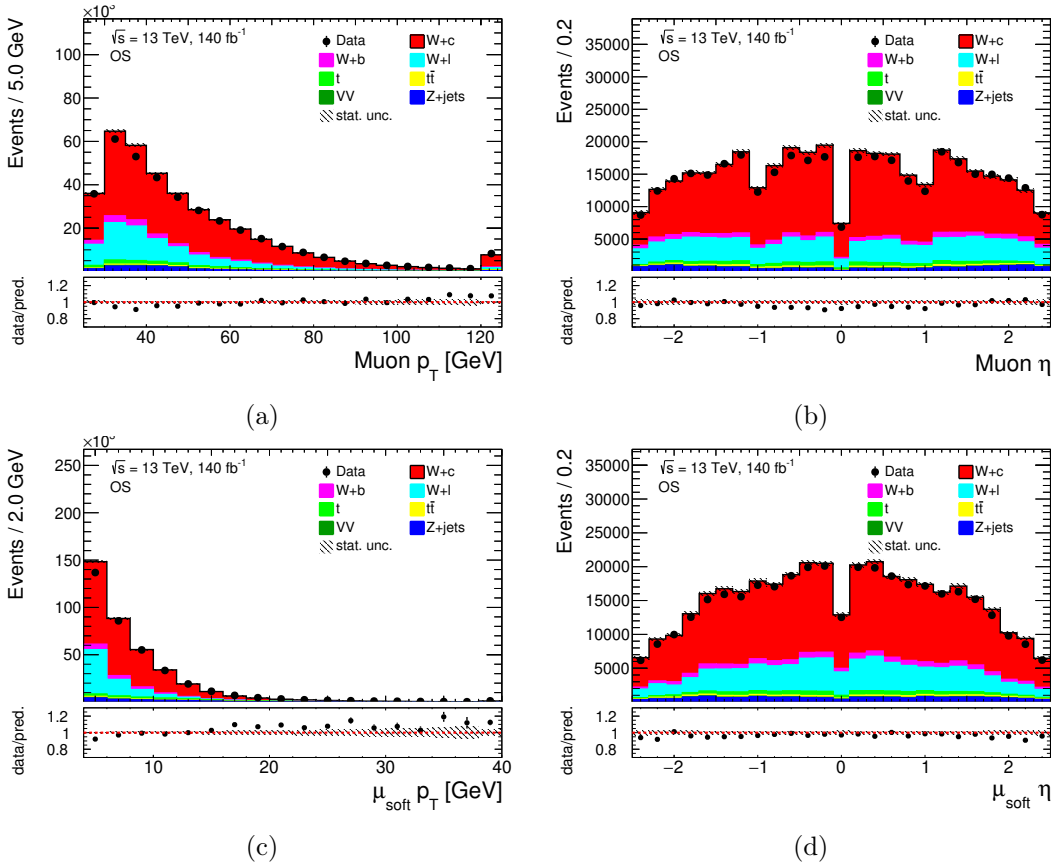

Figure A.1: Kinematic distributions in the OS region. (a) shows the p_{T} and (b) the pseudorapidity of the prompt muon in an event, respectively. (c) and (d) show the p_{T} and the pseudorapidity of the soft muon, respectively. The first and last bin of each distribution include the underflow and overflow bin, respectively. In the bottom panel of each plot, the ratio between observed and expected events is shown. All distributions show a good agreement between data and simulation. The depicted uncertainty bands indicate the MC statistical error, whereas the error bars on the black data points show the statistical uncertainty on the recorded data.

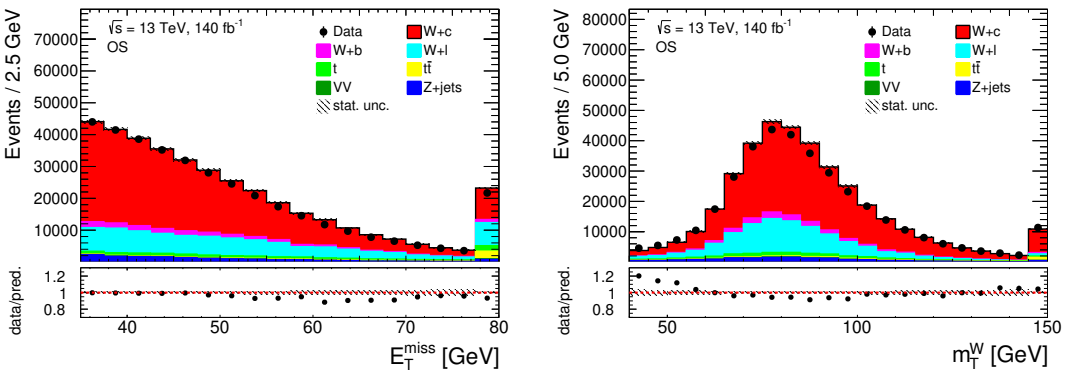

(a) (b)

Figure A.2: Kinematic distributions in the OS region. In (a) the missing transverse momentum is shown and in (b) the transverse W-boson mass. The first and last bin of each distribution include the underflow and overflow bin, respectively. In the bottom panel of each plot, the ratio between observed and expected events is shown. All distributions show a good agreement between data and simulation. The depicted uncertainty bands indicate the MC statistical error, whereas the error bars on the black data points show the statistical uncertainty on the recorded data.

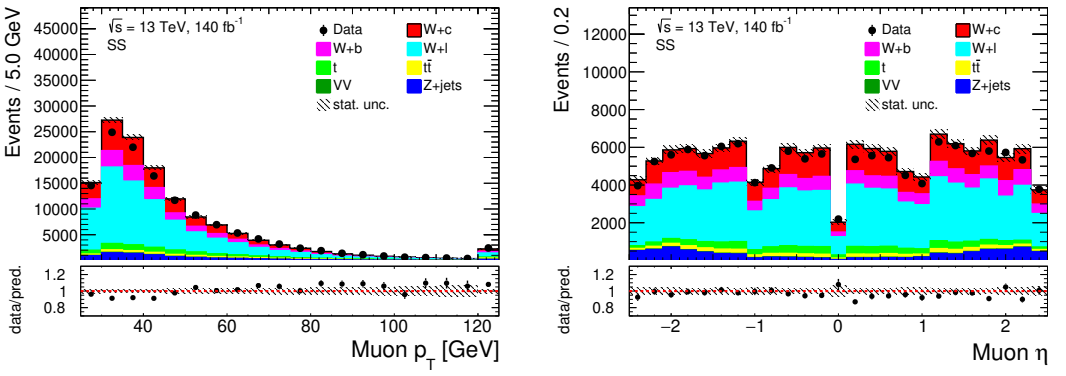

(a) (b)

Figure A.3: Kinematic distributions in the SS region. (a) shows the p_{T} and (b) the pseudorapidity of the prompt muon in an event, respectively. The first and last bin of each distribution include the underflow and overflow bin, respectively. In the bottom panel of each plot, the ratio between observed and expected events is shown. All distributions show a good agreement between data and simulation. The depicted uncertainty bands indicate the MC statistical error, whereas the error bars on the black data points show the statistical uncertainty on the recorded data.

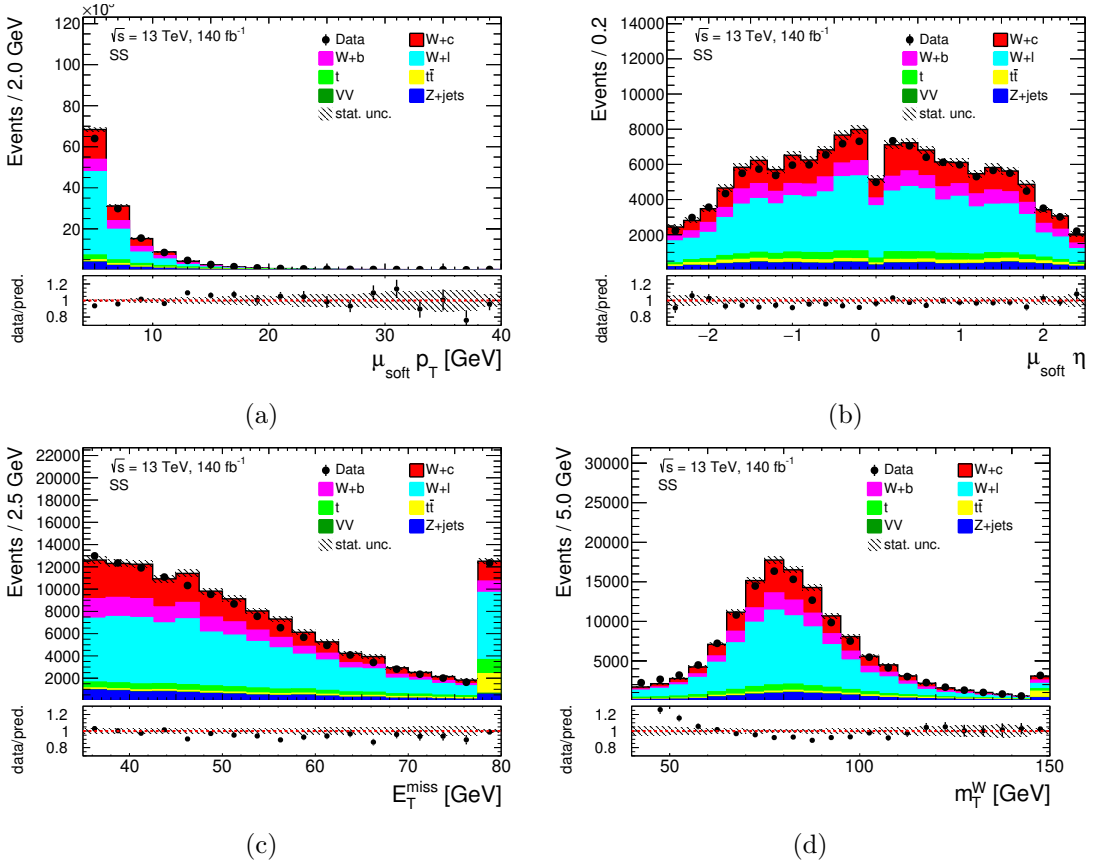

Figure A.4: Kinematic distributions in the SS region. (a) and (b) show the p_{T} and the pseudorapidity of the soft muon, respectively. In (c) the missing transverse momentum is shown and in (d) the transverse W-boson mass. The first and last bin of each distribution include the underflow and overflow bin, respectively. In the bottom panel of each plot, the ratio between observed and expected events is shown. All distributions show a good agreement between data and simulation. The depicted uncertainty bands indicate the MC statistical error, whereas the error bars on the black data points show the statistical uncertainty on the recorded data.

B Pre-fit and post-fit distributions for additional WPs in SingleWP fit for $W+c$ calibration

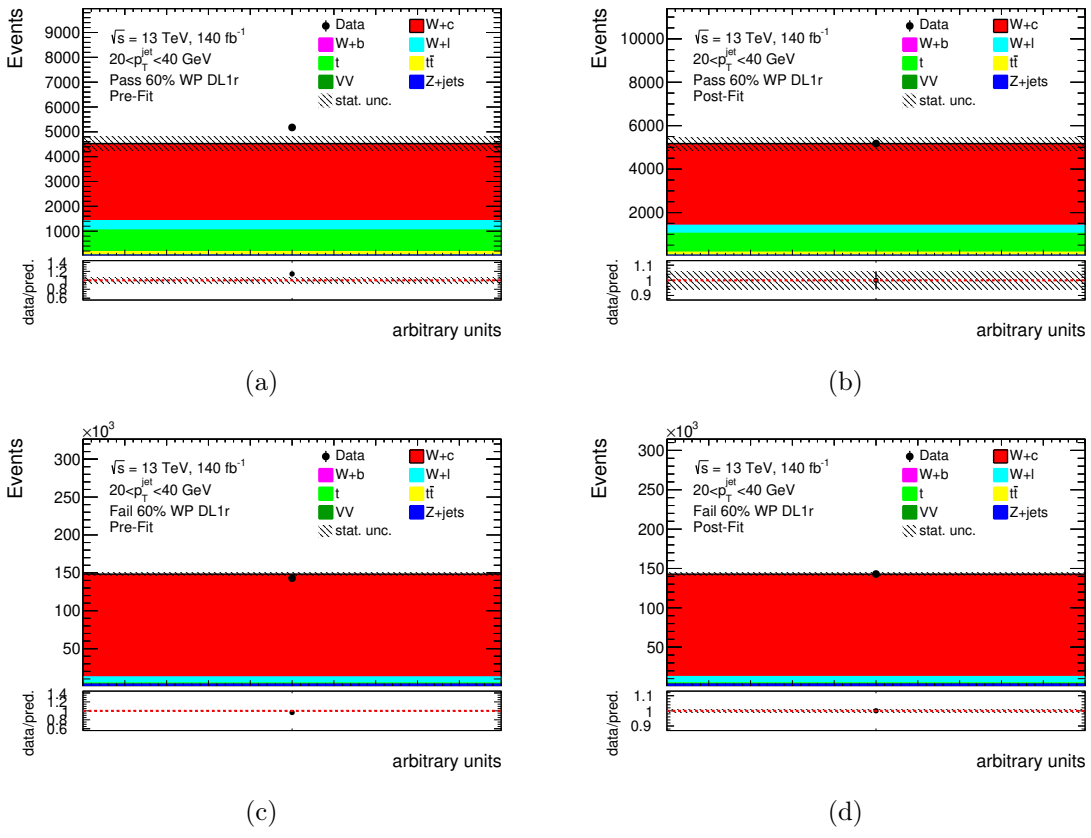

Figure B.1: Pre-fit and post-fit plots for events in the OS-SS region with the p_{T} of the jet being within 20 and 40 GeV for the SingleWP calibration. (a) and (b) show the events with the jet being tagged at the 60% efficiency WP of the `DL1r` algorithm, whereas the events with the jet not being tagged are shown in (c) and (d). In the bottom panel in each plot, the ratio between data and simulated events is shown. The MC statistical uncertainty is indicated by the black, shaded error band.

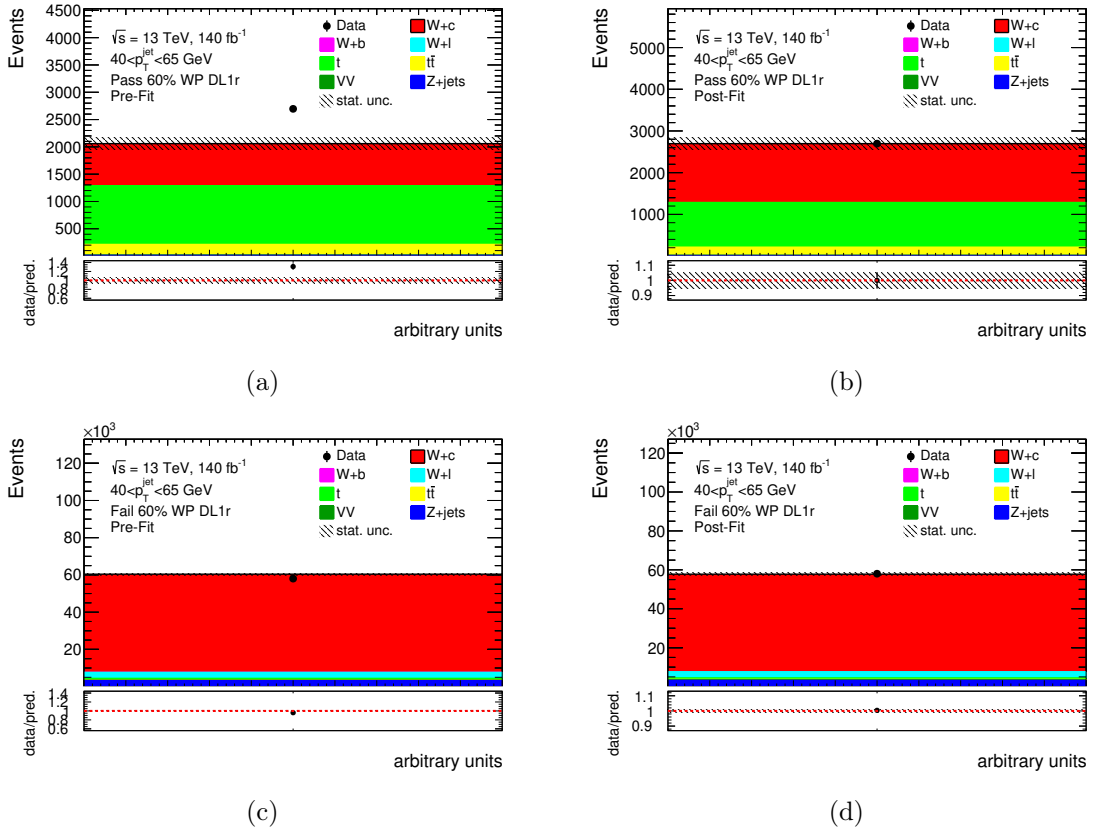

Figure B.2: Pre-fit and post-fit plots for events in the OS-SS region with the p_{T} of the jet being within 40 and 65 GeV for the SingleWP calibration. (a) and (b) show the events with the jet being tagged at the 60% efficiency WP of the `DL1r` algorithm, whereas the events with the jet not being tagged are shown in (c) and (d). In the bottom panel in each plot, the ratio between data and simulated events is shown. The MC statistical uncertainty is indicated by the black, shaded error band.

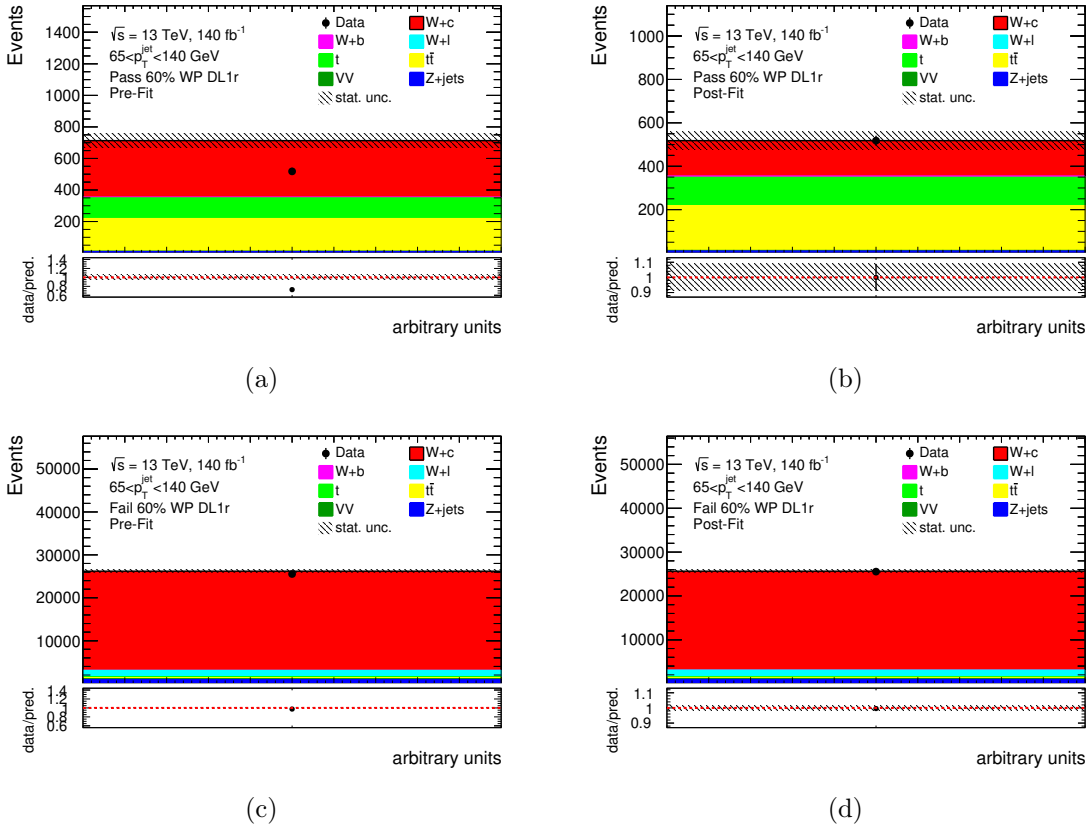

Figure B.3: Pre-fit and post-fit plots for events in the OS-SS region with the p_{T} of the jet being within 65 and 140 GeV for the SingleWP calibration. (a) and (b) show the events with the jet being tagged at the 60% efficiency WP of the `Dl1r` algorithm, whereas the events with the jet not being tagged are shown in (c) and (d). In the bottom panel in each plot, the ratio between data and simulated events is shown. The MC statistical uncertainty is indicated by the black, shaded error band.

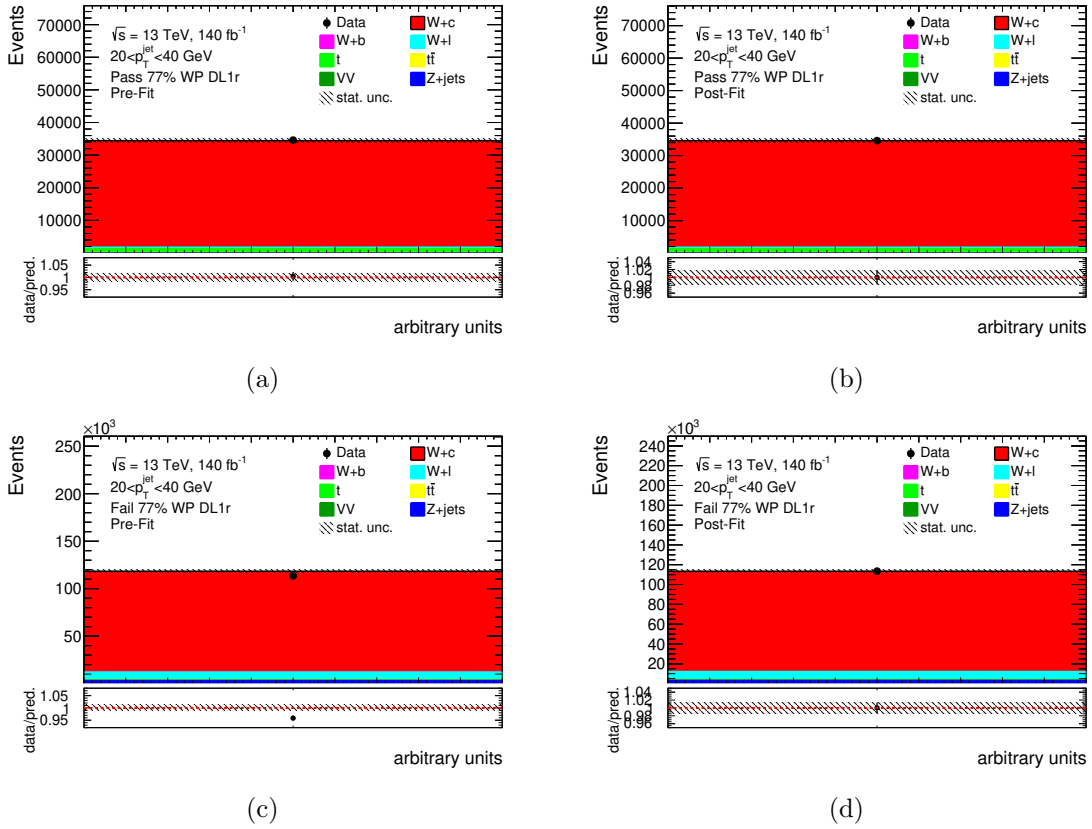

Figure B.4: Pre-fit and post-fit plots for events in the OS-SS region with the p_{T} of the jet being within 20 and 40 GeV for the SingleWP calibration. (a) and (b) show the events with the jet being tagged at the 77% efficiency WP of the `DL1r` algorithm, whereas the events with the jet not being tagged are shown in (c) and (d). In the bottom panel in each plot, the ratio between data and simulated events is shown. The MC statistical uncertainty is indicated by the black, shaded error band.

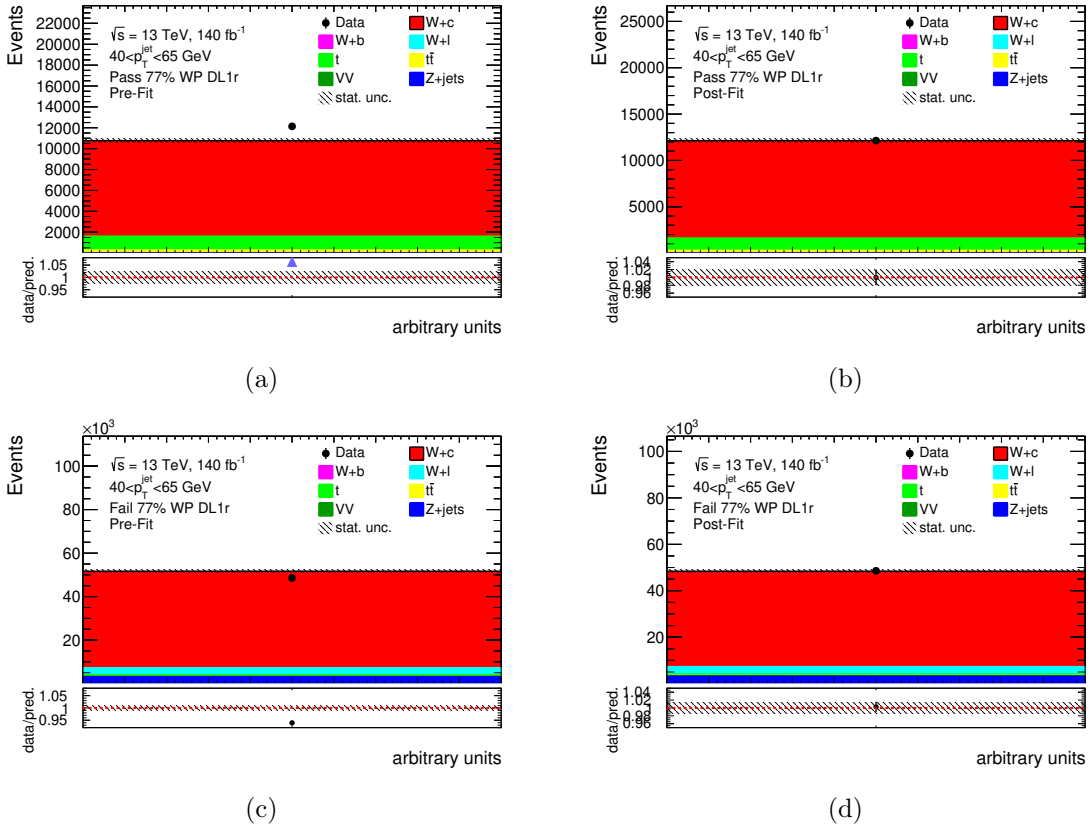

Figure B.5: Pre-fit and post-fit plots for events in the OS-SS region with the p_{T} of the jet being within 40 and 65 GeV for the SingleWP calibration. (a) and (b) show the events with the jet being tagged at the 77% efficiency WP of the `DL1r` algorithm, whereas the events with the jet not being tagged are shown in (c) and (d). In the bottom panel in each plot, the ratio between data and simulated events is shown. The MC statistical uncertainty is indicated by the black, shaded error band.

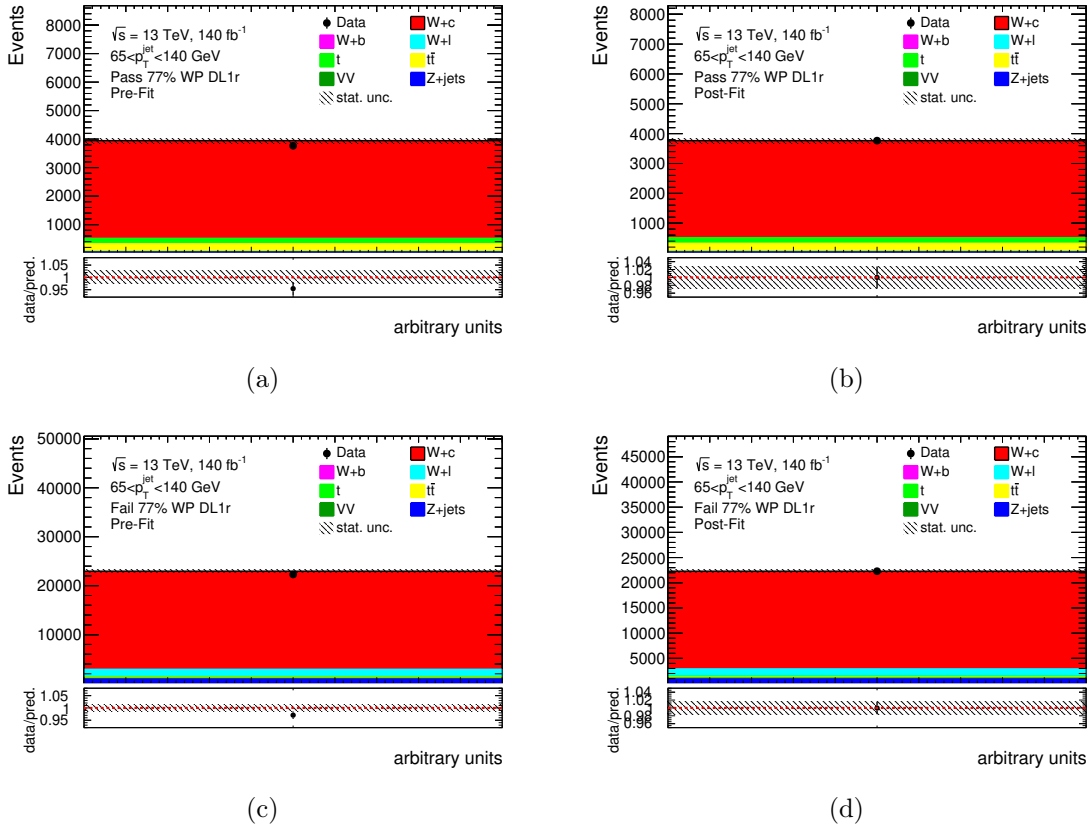

Figure B.6: Pre-fit and post-fit plots for events in the OS-SS region with the p_{T} of the jet being within 65 and 140 GeV for the SingleWP calibration. (a) and (b) show the events with the jet being tagged at the 77% efficiency WP of the `DL1r` algorithm, whereas the events with the jet not being tagged are shown in (c) and (d). In the bottom panel in each plot, the ratio between data and simulated events is shown. The MC statistical uncertainty is indicated by the black, shaded error band.

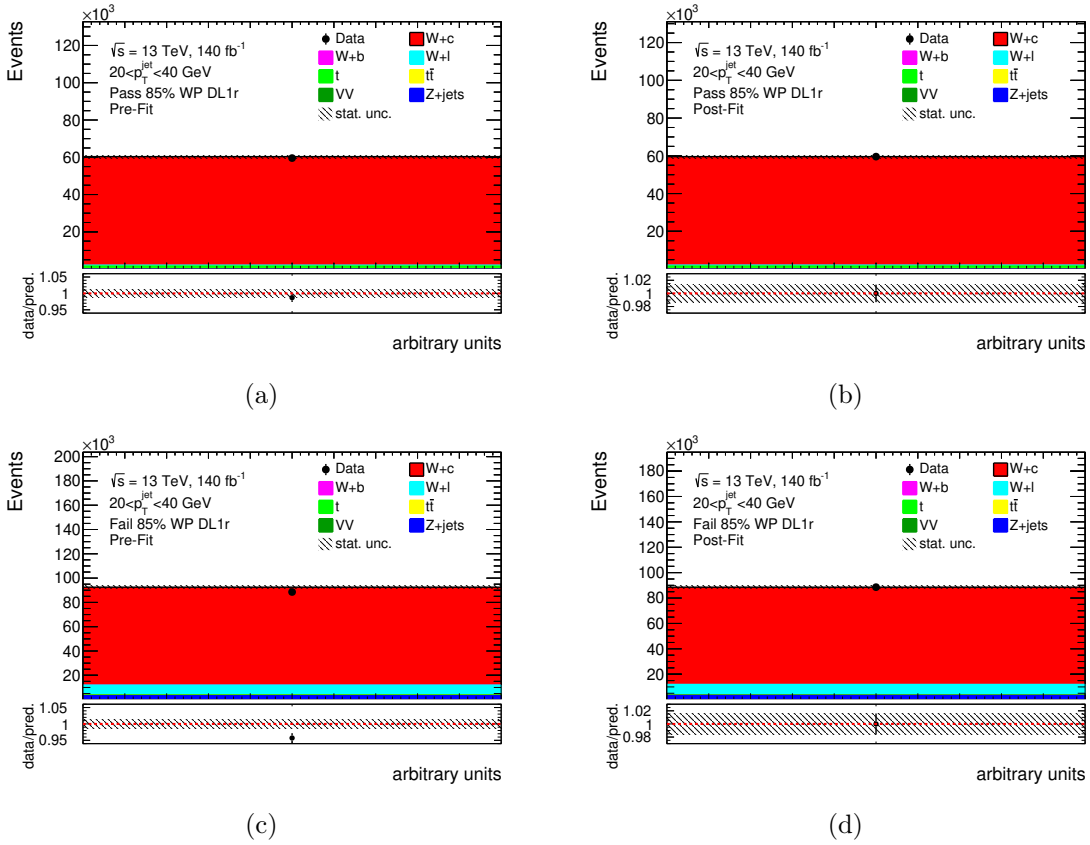

Figure B.7: Pre-fit and post-fit plots for events in the OS-SS region with the p_{T} of the jet being within 20 and 40 GeV for the SingleWP calibration. (a) and (b) show the events with the jet being tagged at the 85% efficiency WP of the `Dl1r` algorithm, whereas the events with the jet not being tagged are shown in (c) and (d). In the bottom panel in each plot, the ratio between data and simulated events is shown. The MC statistical uncertainty is indicated by the black, shaded error band.

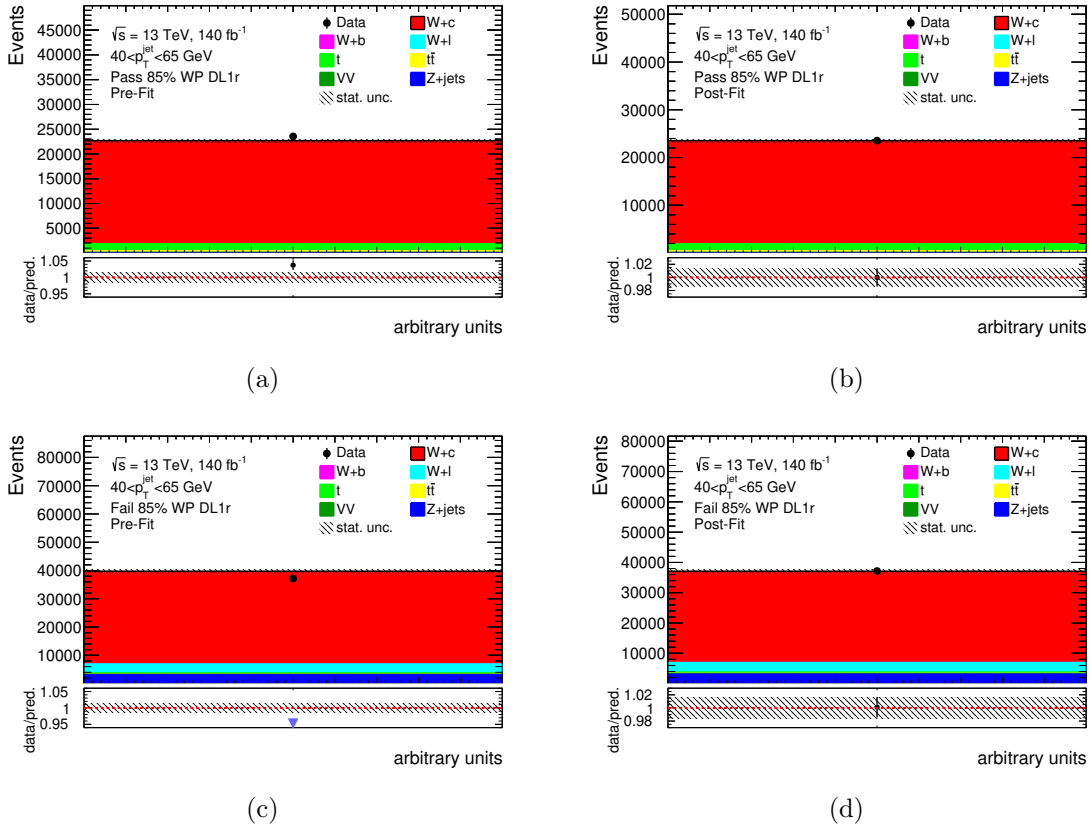

Figure B.8: Pre-fit and post-fit plots for events in the OS-SS region with the p_{T} of the jet being within 40 and 65 GeV for the SingleWP calibration. (a) and (b) show the events with the jet being tagged at the 85% efficiency WP of the `DL1r` algorithm, whereas the events with the jet not being tagged are shown in (c) and (d). In the bottom panel in each plot, the ratio between data and simulated events is shown. The MC statistical uncertainty is indicated by the black, shaded error band.

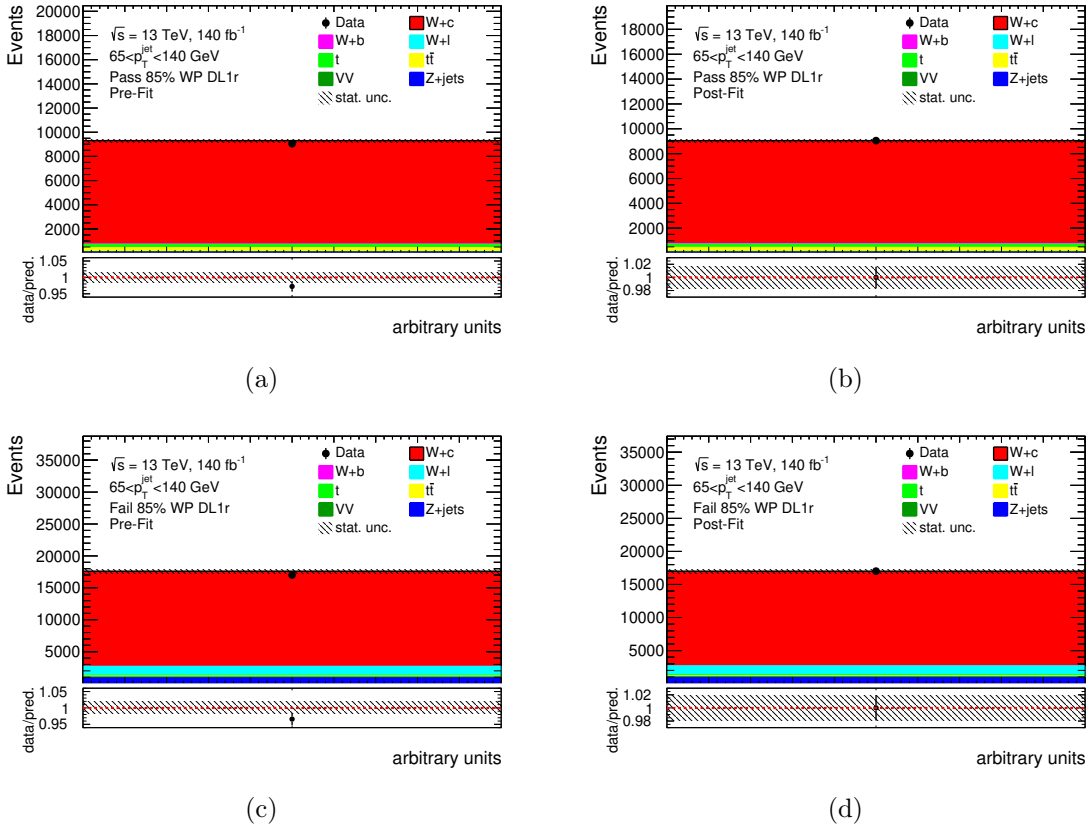

Figure B.9: Pre-fit and post-fit plots for events in the OS-SS region with the p_{T} of the jet being within 65 and 140 GeV for the SingleWP calibration. (a) and (b) show the events with the jet being tagged at the 85% efficiency WP of the `Dl1r` algorithm, whereas the events with the jet not being tagged are shown in (c) and (d). In the bottom panel in each plot, the ratio between data and simulated events is shown. The MC statistical uncertainty is indicated by the black, shaded error band.

C Additional pre-fit and post-fit distributions in PCBT fit

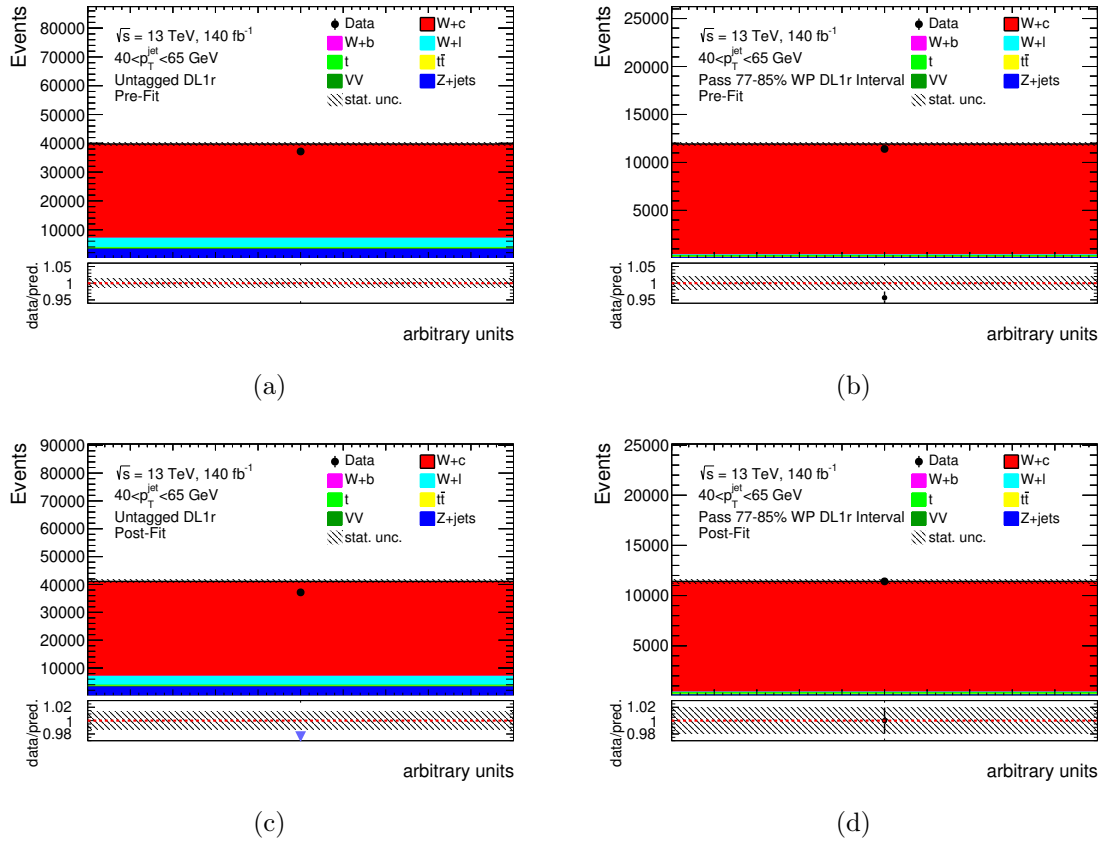

Figure C.1: Pre-fit (left) and post-fit (right) plots for events in the OS-SS region with the p_{T} of the jet being within 40 and 65 GeV for the PCBT calibration. (a) and (b) first tag-weight bin (85%-100%), (c) and (d) second tag-weight bin. In the bottom panel in each plot, the ratio between data and simulated events is shown. The MC statistical uncertainty is indicated by the black, shaded error band.

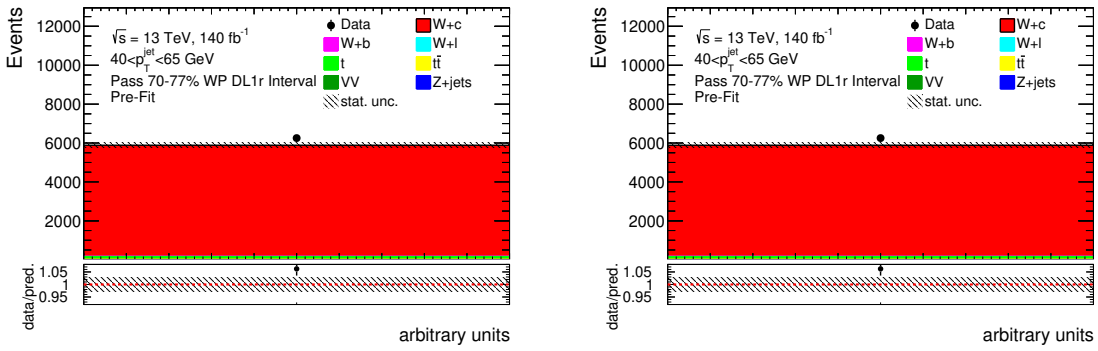

(a)

(b)

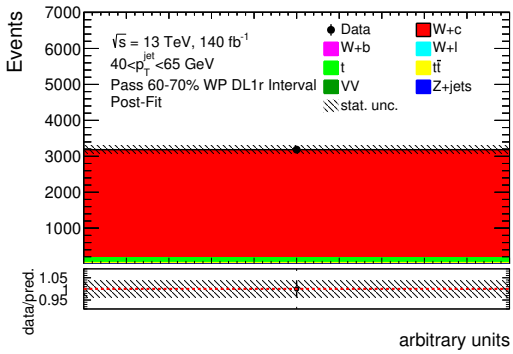

(c)

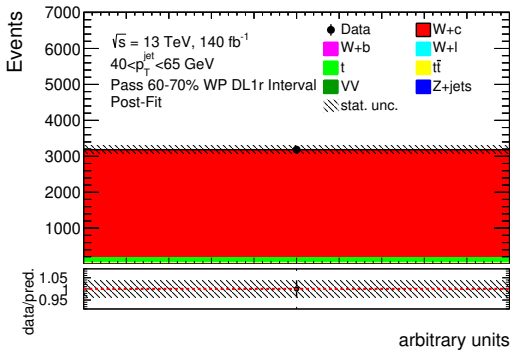

(d)

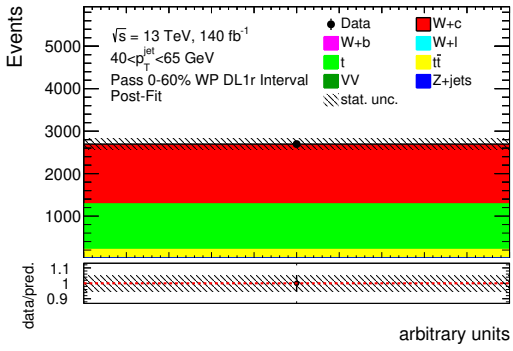

(e)

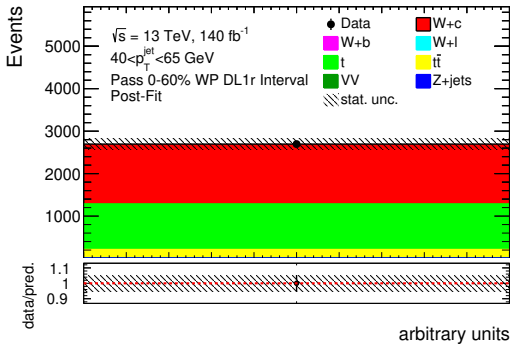

(f)

Figure C.2: Pre-fit (left) and post-fit (right) plots for events in the OS-SS region with the p_{T} of the jet being within 40 and 65 GeV for the PCBT calibration. (a) and (b) third tag-weight bin, (c) and (d) fourth tag-weight bin, (e) and (f) fifth tag-weight bin. In the bottom panel in each plot, the ratio between data and simulated events is shown. The MC statistical uncertainty is indicated by the black, shaded error band.

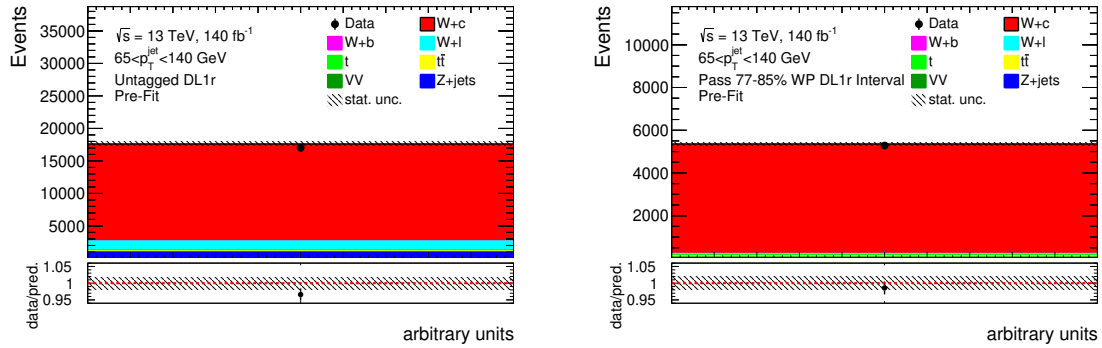

(a)

(b)

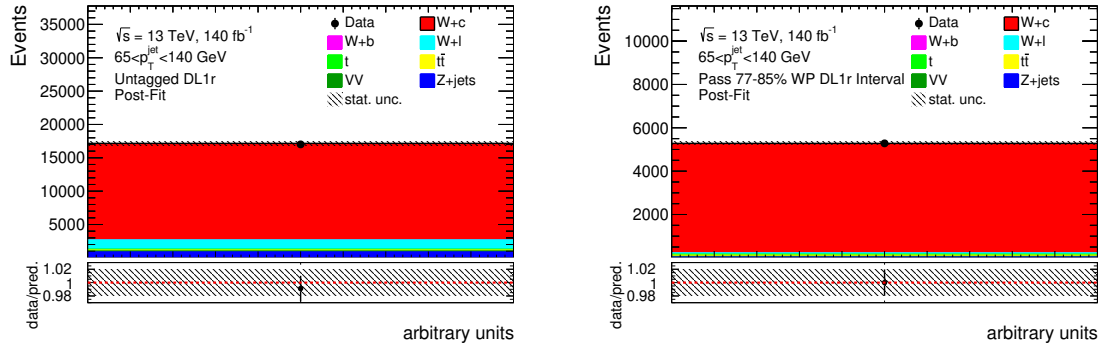

(c)

(d)

Figure C.3: Pre-fit (left) and post-fit (right) plots for events in the OS-SS region with the p_{T} of the jet being within 65 and 140 GeV for the PCBT calibration. (a) and (b) first tag-weight bin (85%-100%), (c) and (d) second tag-weight bin. In the bottom panel in each plot, the ratio between data and simulated events is shown. The MC statistical uncertainty is indicated by the black, shaded error band.

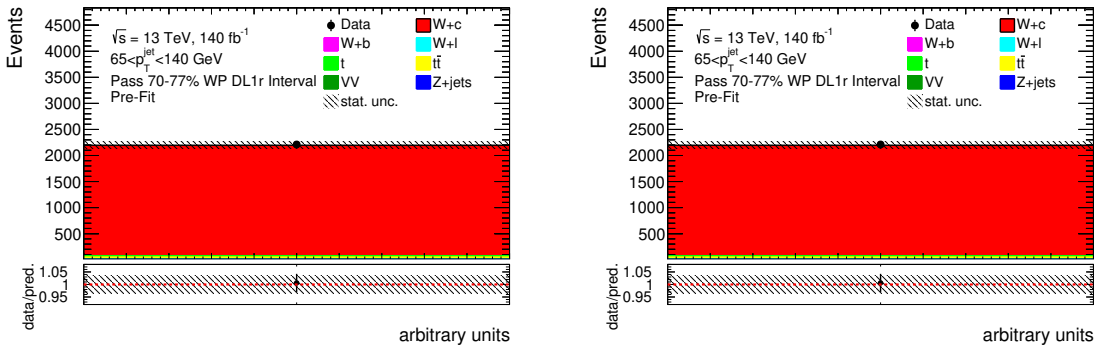

(a)

(b)

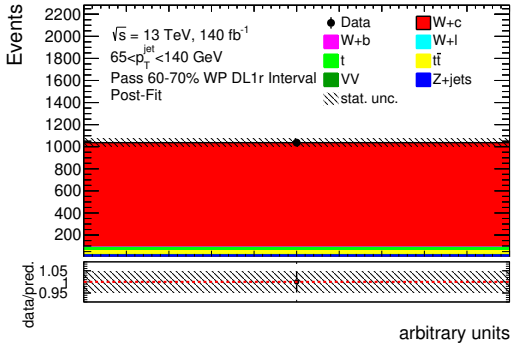

(c)

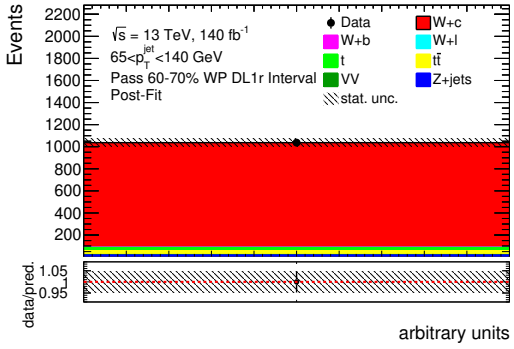

(d)

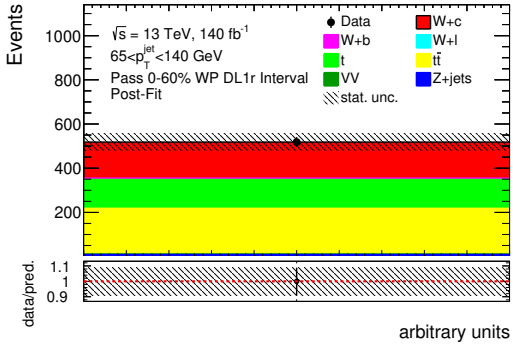

(e)

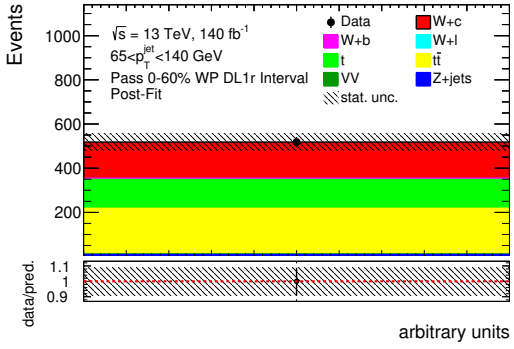

(f)

Figure C.4: Pre-fit (left) and post-fit (right) plots for events in the OS-SS region with the p_{T} of the jet being within 65 and 140 GeV for the PCBT calibration. (a) and (b) third tag-weight bin, (c) and (d) fourth tag-weight bin, (e) and (f) fifth tag-weight bin. In the bottom panel in each plot, the ratio between data and simulated events is shown. The MC statistical uncertainty is indicated by the black, shaded error band.

D Uncertainty breakdown for 85 – 100% WP tag-weight bin for $W+c$ calibration

Table D.1: Summary of the systematic and the statistical uncertainty contribution to the PCBT data-to-MC scale factor calculation for the 85 – 100% tag-weight bin in all three p_{T} bins. All values are given in percent difference from the nominal result. The combined overall uncertainty is calculated by adding in quadrature the corresponding sources. If up and down variation of a source differ, the larger one is quoted here. No systematic uncertainties were symmetrized, hence why adding up the uncertainties of each column might not result in the overall uncertainty quoted here. The "Experimental" category includes JVT, luminosity and pileup. If the impact is less than 0.05% it is shown as 0.0%.

	85-100% WP		
Source	20-40 GeV	40-65 GeV	65-140 GeV
JES	1.0	2.9	1.7
JER	2.7	1.6	2.9
Muons	0.4	0.4	0.1
Electrons	0.0	0.0	0.0
$E_{\mathrm{T}}^{\mathrm{miss}}$	0.4	0.7	0.5
Experimental	0.1	0.2	0.2
Cross section	0.2	0.3	0.1
PDF	0.1	0.1	0.1
α_S variation	0.1	0.1	0.0
Scale	0.1	0.2	0.1
EW corrections	0.0	0.1	0.0
ISR / FSR	0.0	0.0	0.0
All systematic	2.8	3.4	3.4
Statistical	0.6	1.0	1.5

E Additional pre-fit and post-fit distributions for $W+c$ extrapolation

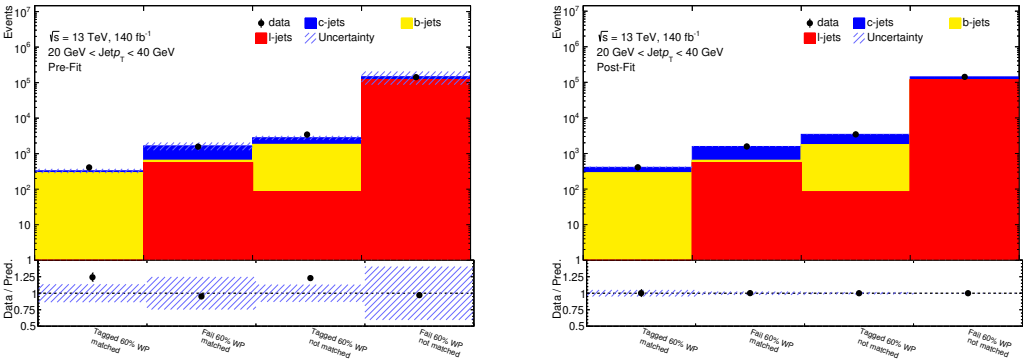

(a) (b)

Figure E.1: Pre-fit (a) and post-fit (b) plots for events with $20 <$ jet $p_{\mathrm{T}} < 40\,\mathrm{GeV}$ for the inclusive c-hadron extrapolation in the SingleWP case for the 60% WP. In the bottom panel in each plot, the ratio between data and simulated events is shown. The overall uncertainty is indicated by the blue, shaded error band.

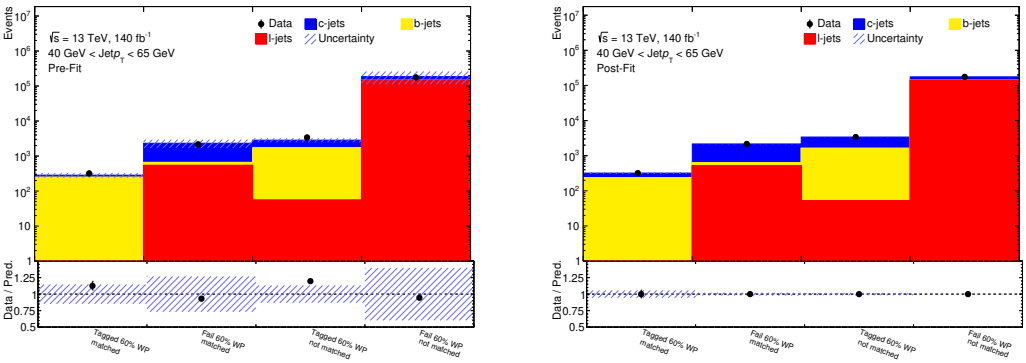

(a) (b)

Figure E.2: Pre-fit (a) and post-fit (b) plots for events with $40 <$ jet $p_{\mathrm{T}} < 65\,\mathrm{GeV}$ for the inclusive c-hadron extrapolation in the SingleWP case for the 60% WP. In the bottom panel in each plot, the ratio between data and simulated events is shown. The overall uncertainty is indicated by the blue, shaded error band.

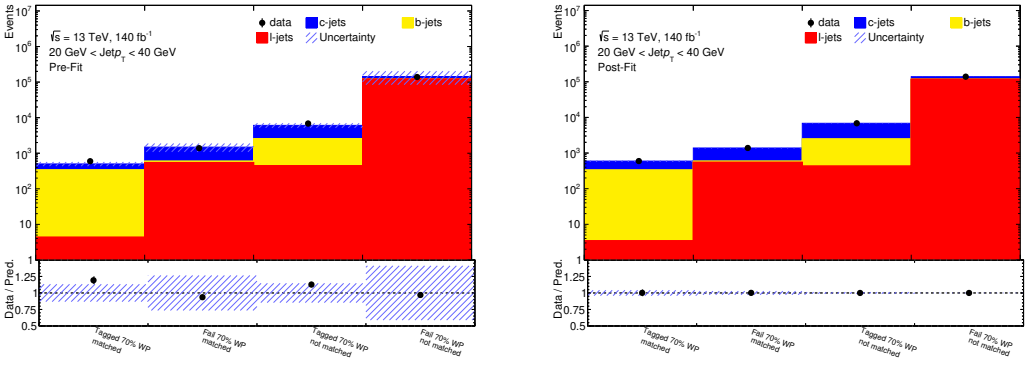

(a) (b)

Figure E.3: Pre-fit (a) and post-fit (b) plots for events with $20 <$ jet $p_{\mathrm{T}} < 40\,\mathrm{GeV}$ for the inclusive c-hadron extrapolation in the SingleWP case for the 70% WP. In the bottom panel in each plot, the ratio between data and simulated events is shown. The overall uncertainty is indicated by the blue, shaded error band.

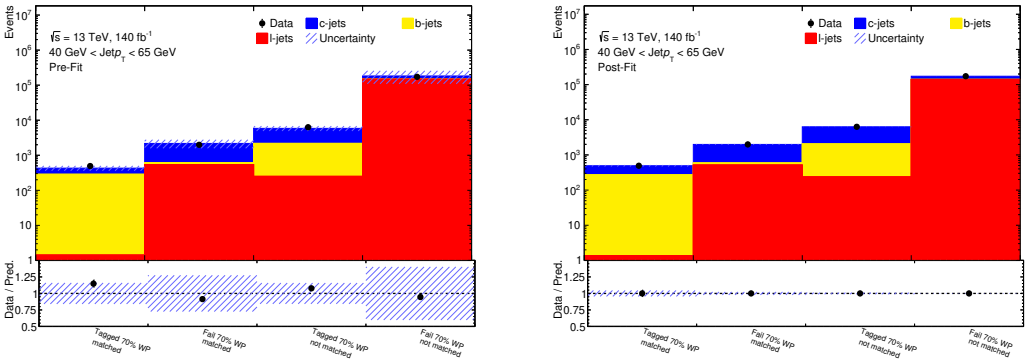

(a) (b)

Figure E.4: Pre-fit (a) and post-fit (b) plots for events with $40 <$ jet $p_{\mathrm{T}} < 65\,\mathrm{GeV}$ for the inclusive c-hadron extrapolation in the SingleWP case for the 70% WP. In the bottom panel in each plot, the ratio between data and simulated events is shown. The overall uncertainty is indicated by the blue, shaded error band.

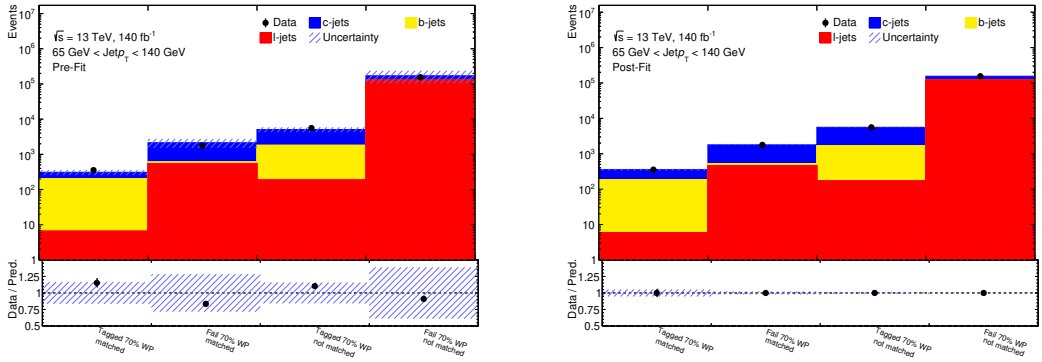

(a) (b)

Figure E.5: Pre-fit (a) and post-fit (b) plots for events with $65 <$ jet $p_{\mathrm{T}} < 140\,\mathrm{GeV}$ for the inclusive c-hadron extrapolation in the SingleWP case for the 70% WP. In the bottom panel in each plot, the ratio between data and simulated events is shown. The overall uncertainty is indicated by the blue, shaded error band.

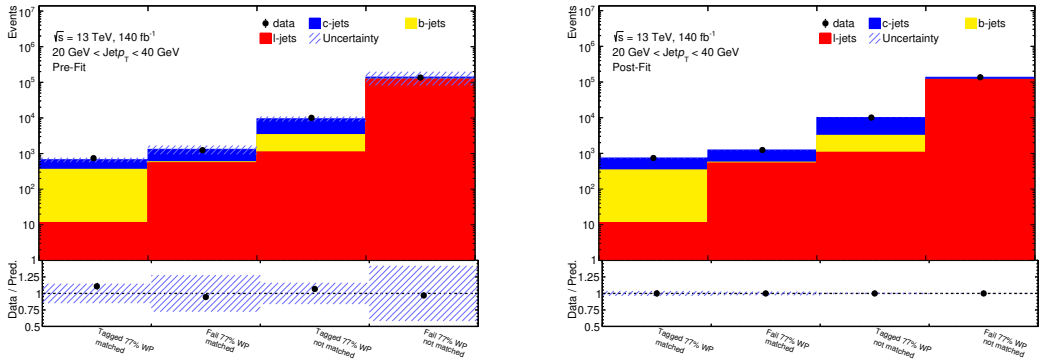

(a) (b)

Figure E.6: Pre-fit (a) and post-fit (b) plots for events with $20 <$ jet $p_{\mathrm{T}} < 40\,\mathrm{GeV}$ for the inclusive c-hadron extrapolation in the SingleWP case for the 77% WP. In the bottom panel in each plot, the ratio between data and simulated events is shown. The overall uncertainty is indicated by the blue, shaded error band.

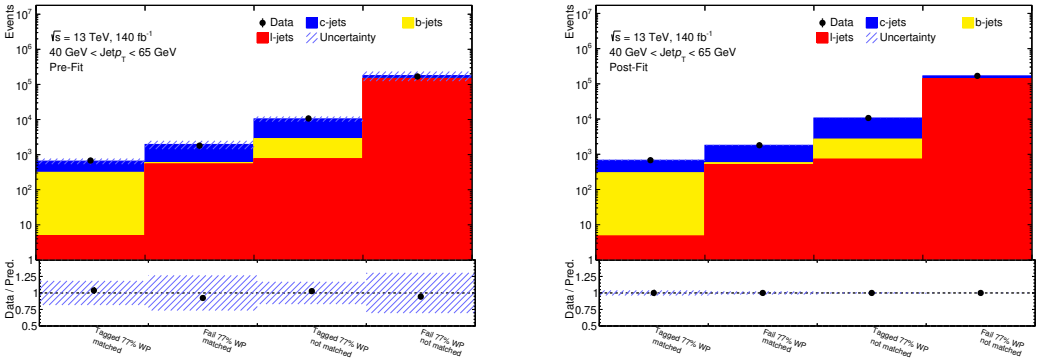

(a) (b)

Figure E.7: Pre-fit (a) and post-fit (b) plots for events with $40 <$ jet $p_{\mathrm{T}} < 65\,\mathrm{GeV}$ for the inclusive c-hadron extrapolation in the SingleWP case for the 77% WP. In the bottom panel in each plot, the ratio between data and simulated events is shown. The overall uncertainty is indicated by the blue, shaded error band.

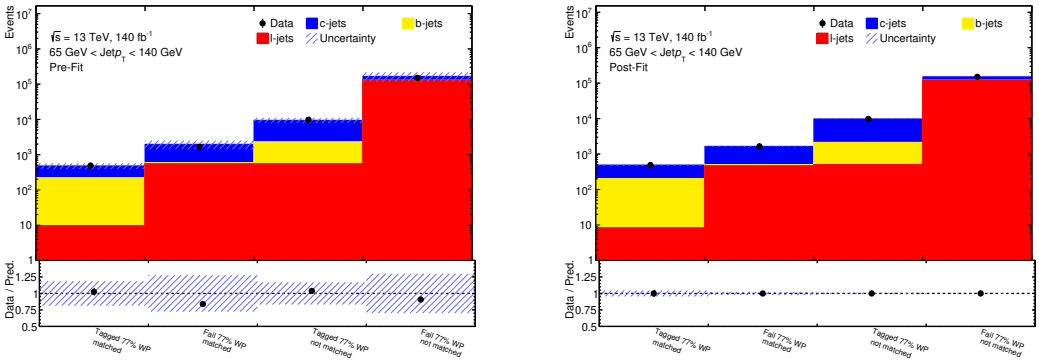

(a) (b)

Figure E.8: Pre-fit (a) and post-fit (b) plots for events with $65 <$ jet $p_{\mathrm{T}} < 140\,\mathrm{GeV}$ for the inclusive c-hadron extrapolation in the SingleWP case for the 77% WP. In the bottom panel in each plot, the ratio between data and simulated events is shown. The overall uncertainty is indicated by the blue, shaded error band.

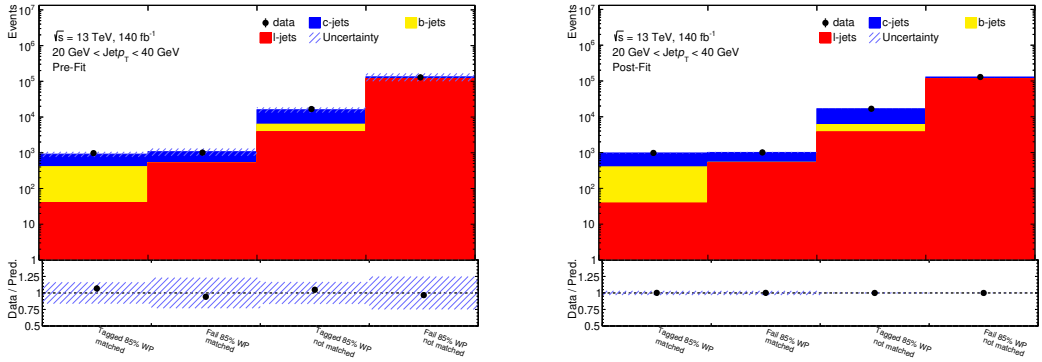

(a) (b)

Figure E.9: Pre-fit (a) and post-fit (b) plots for events with $20 <$ jet $p_{\mathrm{T}} < 40\,\mathrm{GeV}$ for the inclusive c-hadron extrapolation in the SingleWP case for the 85% WP. In the bottom panel in each plot, the ratio between data and simulated events is shown. The overall uncertainty is indicated by the blue, shaded error band.

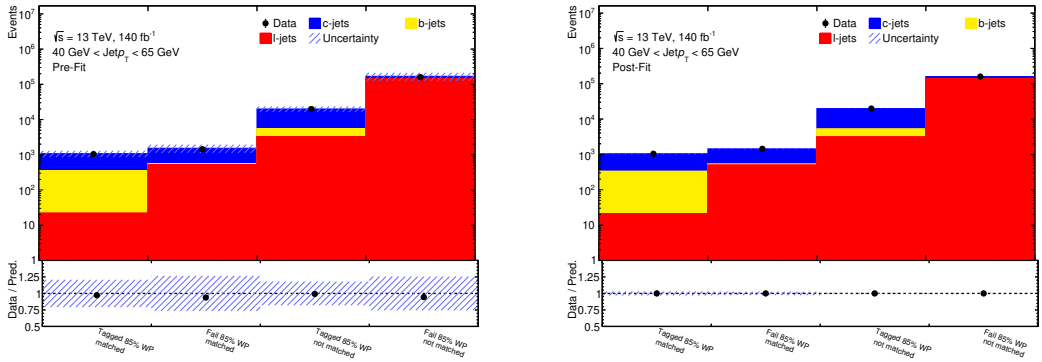

(a) (b)

Figure E.10: Pre-fit (a) and post-fit (b) plots for events with $40 <$ jet $p_{\mathrm{T}} < 65\,\mathrm{GeV}$ for the inclusive c-hadron extrapolation in the SingleWP case for the 85% WP. In the bottom panel in each plot, the ratio between data and simulated events is shown. The overall uncertainty is indicated by the blue, shaded error band.

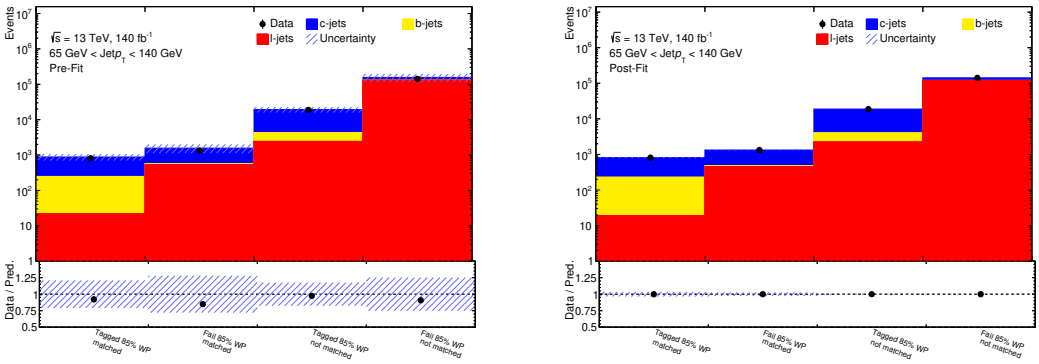

(a) (b)

Figure E.11: Pre-fit (a) and post-fit (b) plots for events with 65 < jet $p_{\mathrm{T}} < 140\,\mathrm{GeV}$ for the inclusive c-hadron extrapolation in the SingleWP case for the 85% WP. In the bottom panel in each plot, the ratio between data and simulated events is shown. The overall uncertainty is indicated by the blue, shaded error band.

F Additional kinematic distributions in studies towards a dedicated CKM analysis

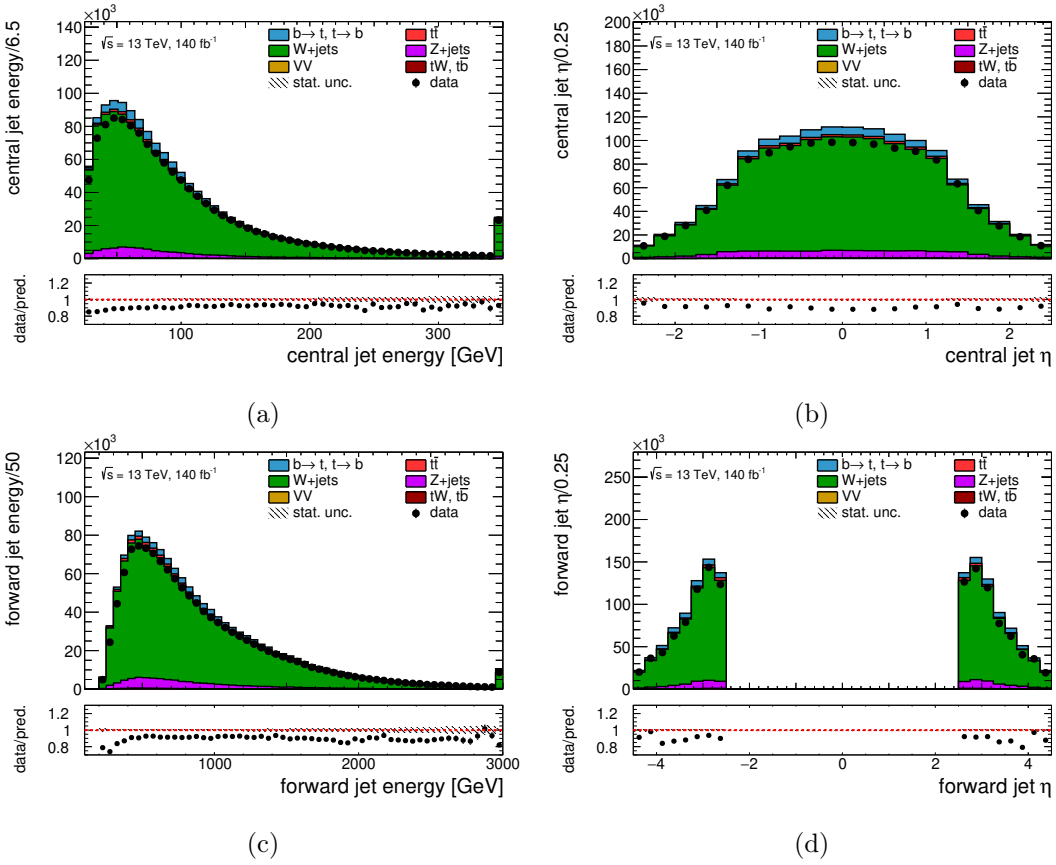

(a) (b)

(c) (d)

Figure F.1: Kinematic distributions in the signal region after the event selection. (a) and (b) show the energy and η of the central jet, respectively. (c) and (d) show the energy and η of the forward jet, respectively. The first and last bin of each distribution denote the underflow and overflow bin, respectively. In the bottom panel of each plot, the ratio between observed and expected events is shown. The depicted uncertainty bands indicate the MC statistical uncertainty, whereas the error bars on the black data points show the statistical uncertainty on the measurement of the recorded data.

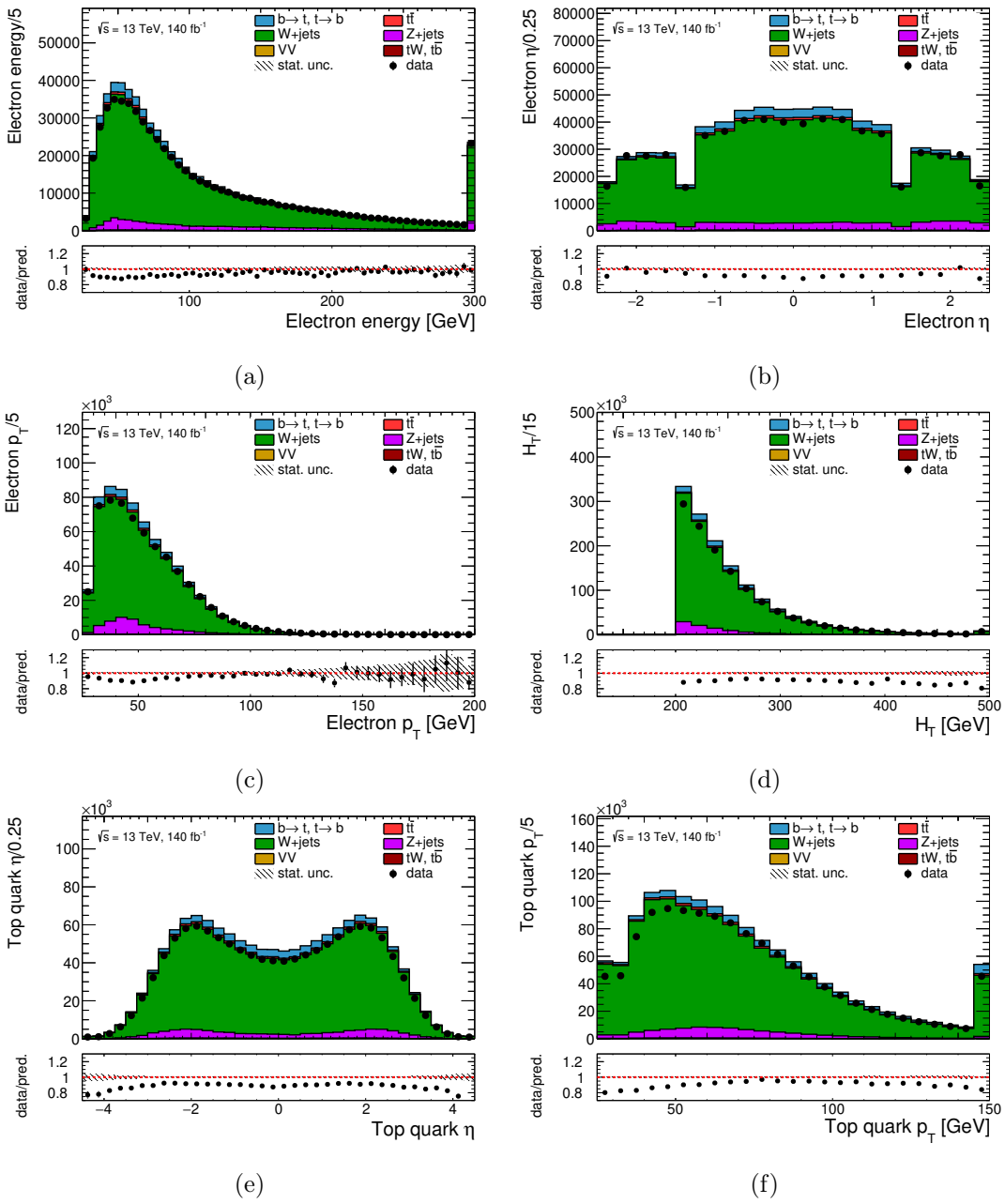

Figure F.2: Kinematic distributions in the signal region after the event selection. (a), (b) and (c) show the energy, η and p_{T} of the electron. (d) depicts H_{T}. (e) shows the η and (f) the p_{T} of the reconstructed top quark. The first and last bin of each distribution denote the underflow and overflow bin, respectively. In the bottom panel of each plot, the ratio between observed and expected events is shown. All distributions show an offset between data and prediction. The depicted uncertainty bands indicate the MC statistical uncertainty, whereas the error bars on the black data points show the statistical uncertainty on the measurement of the recorded data.

G Cutflows in studies towards a dedicated CKM analysis

The cutflow distributions for all SM processes are shown in Figure G.1. The plot uses a logarithmic y-axis. All background contributions are affected larger by each cut, than the single top t-channel process, which is one of the signal processes. Further, it is visible that the last two cuts suppress the main background, W+jets, stronger than the signal process, as expected.

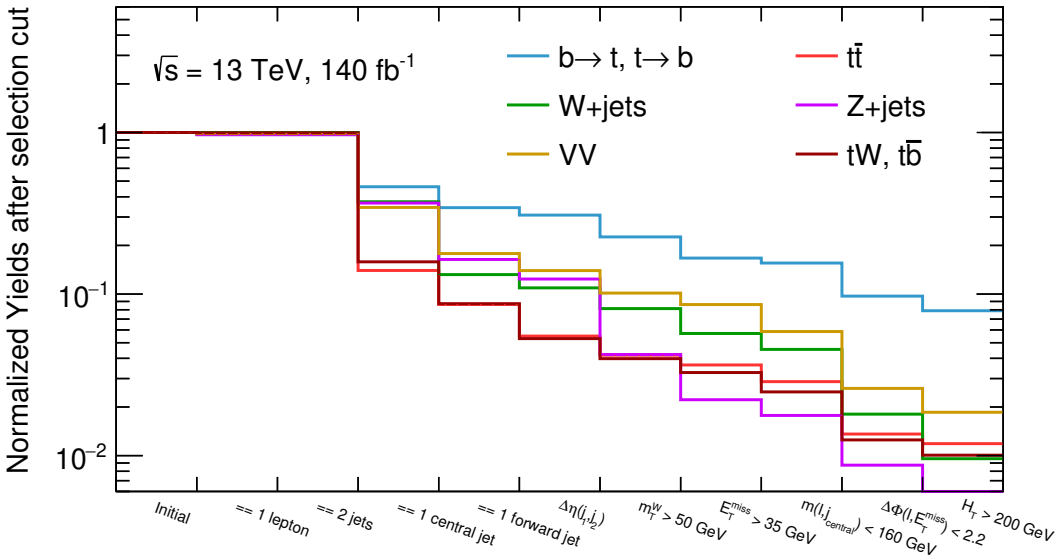

Figure G.1: Normalized cutflow distributions in the signal region after the event selection for all SM processes, excluding the single top quark t-channel CKM processes, with a logarithmic y-axis. The depicted uncertainty bands indicate the MC statistical uncertainty.

The cutflow distributions for all signal processes and the main background, W+jets, are shown in Figure G.2. The plot uses a logarithmic y-axis. The W+jets contribution is affected larger by each cut, than the signal processes, as expected.

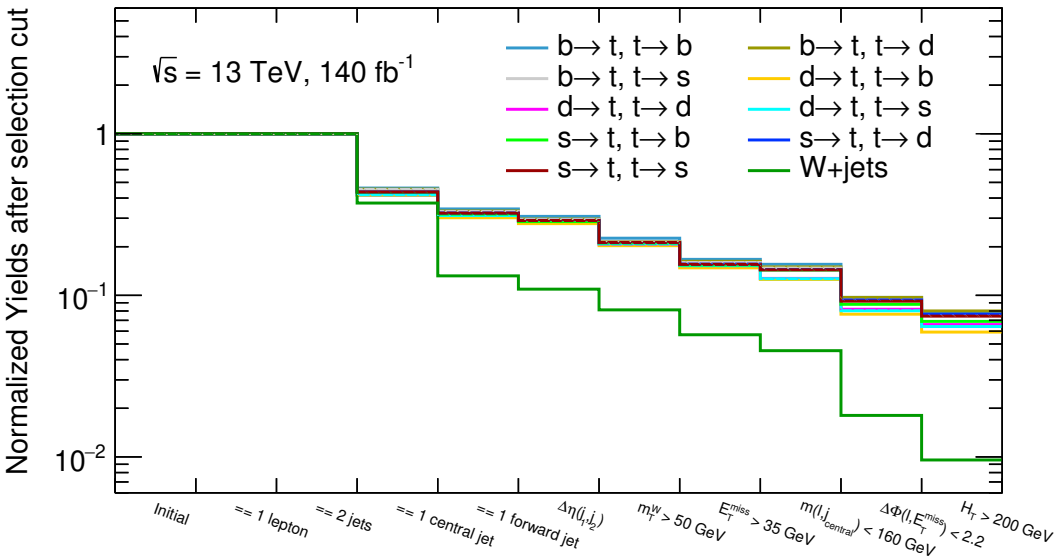

Figure G.2: Normalized cutflow distributions in the signal region after the event selection for all signal processes and W+jets with a logarithmic y-axis. The depicted uncertainty bands indicate the MC statistical uncertainty.

H Output vector entries for multiclass NN in studies towards a dedicated CKM analysis

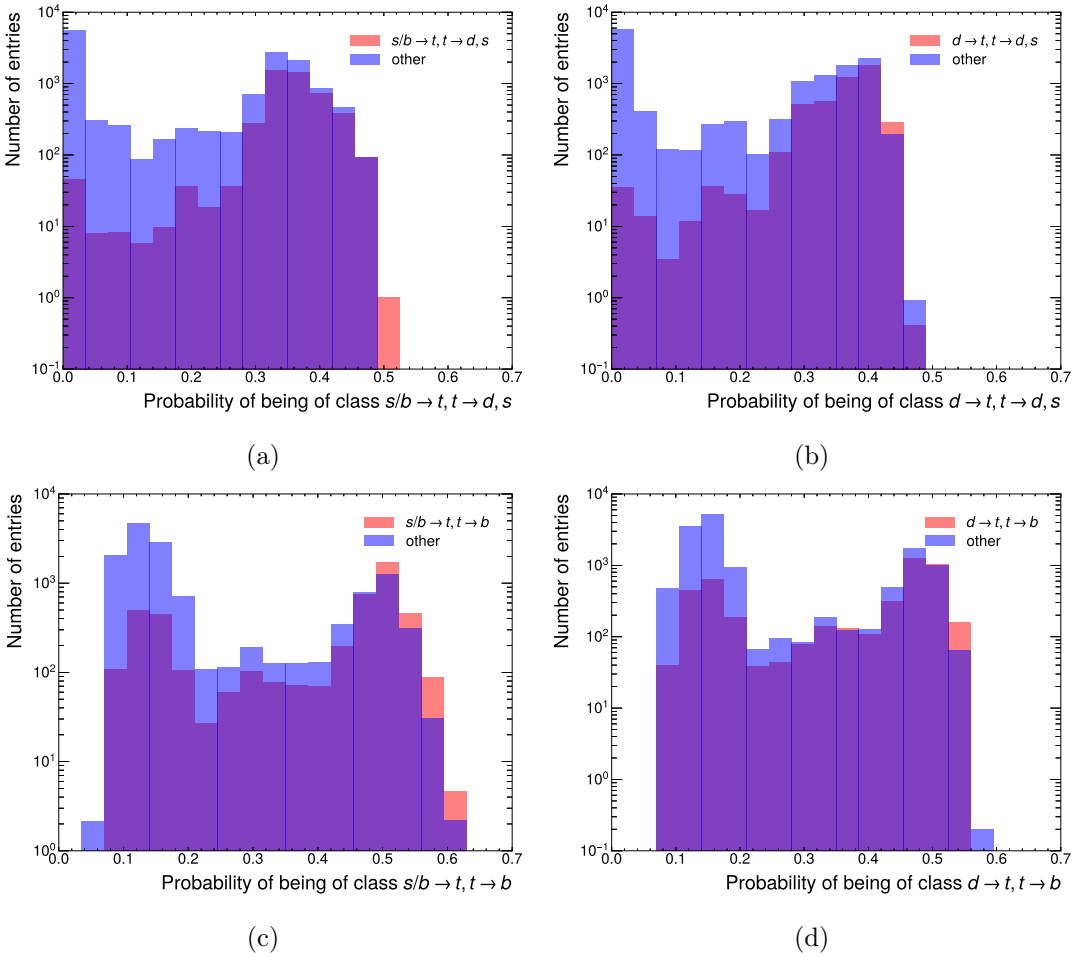

Figure H.1: Distributions for each output vector entry for the even NNs. The probability of an event being classified for class 1 in (a), for class 2 in (b), for class 3 in (c) and for class 4 in (d). The red histogram in each plot denotes the true class, while the blue histogram depicts the events of all other classes.

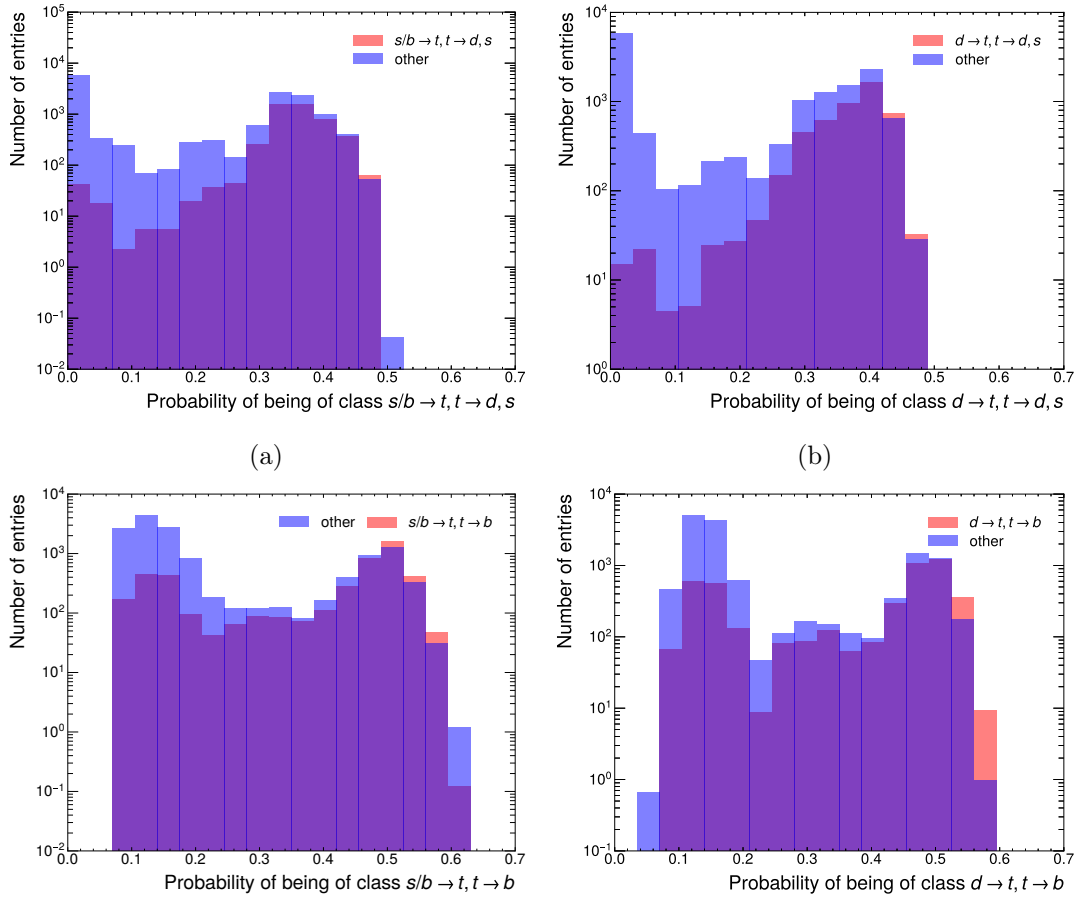

Figure H.2: Distributions for each output vector entry for the odd NNs. The probability of an oddt being classified for class 1 in (a), for class 2 in (b), for class 3 in (c) and for class 4 in (d). The red histogram in each plot denotes the true class, while the blue histogram depicts the oddts of all other classes.

Acknowledgements

At this point it is time to look back and to express my gratitude to everyone who made this achievement possible. First of all I thank Prof. Dr. Kevin Kröninger for giving me the opportunity to pursue my PhD at his working group and also for serving as the first reviewer. Further, I want to thank you for the opportunities given during this time, e.g. schools and conferences. I also thank Prof. Dr. Johannes Albrecht for serving as the second reviewer. In addition, I need to thank Prof. Dr. Johannes Erdmann for encouraging and enabling me to do the PhD in the same group in which I already completed my Bachelor's and Master's degrees. I thank Dr. Olaf Nackenhorst for his supervision for the CKM interpretation and the fruitful discussions and feedback. A huge Thank you to PD Dr. Andrea Knue. Ever since you arrived in Dortmund your guidance and support were invaluable for the success and completion of my thesis. Another huge Thank you to Dr. Tomas Dado. I can basically repeat myself, ever since you joined the working group, I benefited a lot from your huge wealth of knowledge, so I learned a lot from you. Also, thank you for the six months we spent together in an office at CERN, I had an enjoyable and memorable time.
Another special thank you to Dr. Chris Delitzsch. I was not part of your working group, but regardless, you always took the time for a chat - even if it wasn't work-related - or when I needed a reality check to counter my pessimistic outlooks. Thank you to Dr. Carsten Burgard for always answering my questions whenever I had them and the helpful discussions during the analysis meetings.

I want to thank the whole ATLAS Top working group for their support through the years with the t-channel analysis and CKM interpretation. I would especially like to thank the Wuppertal group for welcoming me to the analysis team and helping shape the CKM interpretation - and helping with software questions regarding your framework, this was much appreciated. Thank you Prof. Dr. Wolfgang Wagner, Dr. Dominic Hirschbühl, Dr. Joshua Reidelstürz and also Maren Stratmann!
I also would like to thank the ATLAS Flavor Tagging group. Especially Dr. Valerio Dao for your technical supervision during my qualification task, for your help in performing the charm mis-tag calibration and constructing the fit setup. Thank you to Dr. Valentina Vecchio for your efforts especially for the extrapolation but also in finalizing the whole calibration, first as calibration group convener and later as Flavor Tagging group convener. Furthermore, I want to thank the $W+c$ cross section measurement team and especially Dr. Francesco Giuli. Your help, efforts and MC samples were an integral part of the charm mis-tag calibration.

Looking back, I am very thankful for all the years now in the AG Kröninger (I think, somehow, it will always be E4 for me.). So, thank you to everyone in E4 over the years. A special thank you to Andrea Teichmann for always being available to answer my countless questions (mostly regarding travel expenses) and also for the many nice conversations along the way. And of course, to all the colleagues I spent time with in the office: Thank you, Salvatore, Donna, Ramona, Michael and Lars. Every one of you contributed in part to the success of this thesis, be it through helpful discussions or some conversations away

from work, but also by keeping my motivation up. Thank you, Aaron for your support regarding machine learning and also for the chats in between (and the ride back from Frankfurt after a DPG)! And a huge thank you to Christopher, Lucas and Nils: Whenever there was a problem or question regarding our infrastructure you Admins were able to help quickly.

My PhD time wasn't just work - even though it felt like that way too many times... - and there are a lot of people I need to thank outside academia. First, the biggest Thank you belongs to my parents and my sister. The unconditional love and support kept me going, even during times when I felt like everything was too much for me. I think I cannot thank you enough for being an important part of my support system that I needed, without you this thesis would not have been possible. I also want to thank my entire family for their support and interest in my work.

Last but definitely not least, Thank you to Dominik, Moritz, Saskia and Mariam. I am just grateful that I met you during my time as an undergraduate student. You always took the time to listen to my complaints, and we supported each other mentally and emotionally as much as we could. You always found the right words, the right motivation - or even sometimes the right solutions for problems I was facing. Also, without you this thesis would probably not exist now - Thank you!